Title
Dynamics of Ocean Circulation in Glacial Fjords and Ice-Shelf Cavities

Author
Zhao, Ken

Publication Date
2021

Peer reviewed|Thesis/dissertation

UNIVERSITY OF CALIFORNIA

Los Angeles

Dynamics of Ocean Circulation in Glacial Fjords and Ice-Shelf Cavities

A dissertation submitted in partial satisfaction

of the requirements for the degree

Doctor of Philosophy in Atmospheric and Oceanic Sciences

by

Ken Zhao

2021

ABSTRACT OF THE DISSERTATION

Dynamics of Ocean Circulation in Glacial Fjords and Ice-Shelf Cavities

by

Ken Zhao
Doctor of Philosophy in Atmospheric and Oceanic Sciences
University of California, Los Angeles, 2021
Professor James C. McWilliams, Co-Chair
Professor Andrew L. Stewart, Co-Chair

Melting at the submerged faces of marine-terminating glaciers at the fringes of Antarctica and Greenland has increased dramatically in recent decades. This acceleration has been driven in part by the ocean circulation within ice-shelf cavities and fjords through the increased access of warm, salty water masses and a presumed amplification of the heat flux towards these glaciers. However, the dynamics of the ocean circulation within fjords and ice-shelf cavities are poorly understood and require the representation of scales of motion that range seven orders of magnitude, from 100s of kilometers (circulation on the adjacent coastal shelves) down to centimeters (at the ice-ocean inner boundary layer interface). This presents unique challenges for existing models, which underpredict melt rates by an order of magnitude compared to recent observations at vertical glacial faces.

The work in this dissertation seeks to improve the agreement of models and theory with observations and provide a better understanding of the dynamical processes within fjords and ice-shelf cavities. To accomplish this, a series of high-resolution numerical simulations of increasing complexity is presented. In Chapters 2 and 3, 2- and 3-layer isopycnal model

configurations with idealized geometry and forcing are used; subsequently in Chapters 4 and 5, z-coordinate models with idealized and semi-realistic regional configurations are used. Inspired by the simplest models, theories of the overturning and horizontal recirculation (the two primary bulk measures of circulation strength within fjords and ice-shelf cavities,) are developed and tested and used to make predictions for the glacial melt rate. These theories are then tested in increasingly complex models, which reveal new features and factors that also should be taken into account. Three important features presented in this dissertation include the identification of cavity/fjord geometry as a critical constraint on heat transport, melt-circulation feedbacks in fjords, and the existence of standing eddies, which can both further amplify glacial melt rates.

This work advances the understanding of the dynamics within fjords and ice-shelf cavities and many promising avenues of future work have emerged as a result. Future work will likely continue to provide critical improvements to our understanding of ocean circulation near the margins of ice sheets and improve our projections of future sea level rise and glacial retreat in a changing climate.

The dissertation of Ken Zhao is approved.

Marcelo Chamecki

Eric J. Rignot

Andrew L. Stewart, Committee Co-Chair

James C. McWilliams, Committee Co-Chair

University of California, Los Angeles

2021

To future oceanographers, may you be stalwart stewards of our oceanic homeworld.

"You know the fjords in Norway? I got a prize for creating those, you know."

– Slartibartfast (The Hitchhiker's Guide to the Galaxy)

TABLE OF CONTENTS

LIST OF FIGURES

LIST OF TABLES

ACKNOWLEDGMENTS

The research presented in this dissertation is the product of collaborative work with my thesis advisors Andrew Stewart and Jim McWilliams. I am grateful for their mentorship and guidance throughout this work and the additional guidance from Ian Fenty and Eric Rignot on the work presented in Chapter 5.

Chapter 2 is reproduced from Zhao et al. (2019), Chapter 3 is reproduced from Zhao et al. (2021a), Chapter 4 is reproduced from Zhao et al. (2021b) (in review for Geophysical Research Letters), and Chapter 5 is reproduced from Zhao et al. (2021c) (preliminary version, not yet submitted). Material from the chapters that have been published are reproduced with permission from the publishers.

Chapter 2 is based in part upon work supported by the National Science Foundation under Grant Number PLR-1543388. For Chapter 2, I would like to thank Pierre St-Laurent for allowing the use of the open source code BEOM and insightful comments and Tore Hatterman for extensive feedback, and two anonymous reviewers for helpful comments. The model source code used in this study is available at *www.nordet.net/beom.html*.

Chapter 3 is based in part upon work supported by the National Science Foundation under Grants PLR-1543388 and OCE-1751386. I would again like to thank Pierre St-Laurent for helpful comments.

Chapter 4 is based in part upon work supported by the NASA FINESST Fellowship under Grant 80NSSC20K1636, the National Science Foundation under Grant OCE-1751386, and the Extreme Science and Engineering Discovery Environment (XSEDE, Towns et al. 2014), supported by National Science Foundation grant number ACI-1548562. The MITgcm model configuration, test case, and modified plume parameterization (a slightly modified version of Cowton et al. 2015) is available at: *https://github.com/zhazorken/MITgcm_FJ*.

Chapter 5 is based in part upon work supported by the NASA FINESST Fellowship under Grant 80NSSC20K1636 and the National Science Foundation under Grant OCE-1751386.

I would like to thank Ian Fenty and Eric Rignot for very helpful comments during the conceptualization of the work contained in this chapter.

VITA

2007–2011 BS in Mathematics, New York University

2007–2011 BE in Mechanical Engineering, Stevens Institute of Technology

2011–2013 MS in Applied Mathematics, Columbia University

2016–2018 MS in Atmospheric and Oceanic Sciences, The University of California, Los Angeles

PUBLICATIONS

K. X. Zhao, A. L. Stewart, and J. C. McWilliams. Sill-Controlled Circulation in Ice Shelf Cavities. *Journal of Physical Oceanography, Jan. 2019.*

K. X. Zhao, A. L. Stewart, and J. C. McWilliams. Dynamical Controls of Fjord Circulation. *Journal of Physical Oceanography, Apr. 2021.*

K. Cohanim[a], **K. X. Zhao**, and A. L. Stewart. Dynamics of Eddies Generated by Sea Ice Leads. *Journal of Physical Oceanography, Aug. 2021.*

K. X. Zhao, A. L. Stewart, and J. C. McWilliams. Linking Overturning, Recirculation, and Melt in Glacial Fjords. *Submitted to Geophysical Research Letters.*

[a]Student Advisee

K. X. Zhao, A. L. Stewart, J. C. McWilliams, I. Fenty, and E. Rignot. Roles of Geometry and Standing Eddies in Mediating Fjord-Shelf Exchange. *In Preparation for Journal of Physical Oceanography, late 2021 (anticipated).*

CHAPTER 1

Introduction and Background

1.1 Prologue: Why I decided to study ocean dynamics near ice

The brief answer to why I was drawn to this field of study is that there is an abundance of interesting and fundamental fluid dynamics problems spanning over 7 orders of magnitude (from over 100s of kilometers to centimeters) at the ice-ocean margins, many of which have significant ramifications for the understanding of our rapidly melting ice sheets. As such, I believe this is both a particularly timely and time-sensitive area of study.

As I am submitting this document for consideration as a Doctor of *Philosophy*, I will use this opportunity to offer a few reflections on the motivation, vision, and experimental design choices made throughout this work. First, however, I will provide some context with an informal summary of the ongoing global efforts to delay the looming climate catastrophe and where we seem to be headed from the perspective of a young scientist.

As of the submission of this thesis (December, 2021), the 2021 United Nations Climate Change Conference held in Glasgow, Scotland has recently concluded. This was the 26th Conference of the Parties (COP26) to the United Nations Framework Convention on Climate Change. This meeting set an expectation of member states to ramp up climate change mitigation commitments following the Paris Agreement, which formally required signatories to provide improved national pledges every five years (note that COP26 was delayed a year due to the ongoing COVID pandemic). The outcome was the Glasgow Climate Pact, which was the first climate resolution to explicitly commit to a reduction of coal as an energy

source, although the commitments in this pact have been perceived as disappointingly weak to many scientists and policymakers.

This also follows the recent release of the Sixth Assessment Report (AR6) of the United Nations Intergovernmental Panel on Climate Change (IPCC) (IPCC, 2021). The report provides updated estimates of our chances to achieve the target of limiting global mean temperatures to a 1.5 ^{o}C increase since the pre-industrial era (circa 1850). The report finds that unless immediate, rapid, and large-scale reductions in greenhouse gas emissions are put into place (so far, the resolutions made during COP26 do not appear to meet these expectations), there is high confidence that global temperature will exceed 1.5 ^{o}C over the next 20 to 30 years. So far, the anthropogenic contribution to greenhouse gas emissions have warmed the planet approximately 1.1 ^{o}C since the pre-industrial era.

One of the broader impacts of understanding ice-ocean interactions and specifically, ocean-driven glacial melt is how this seemingly inevitable anthropogenic warming translates to sea level rise. The IPCC report predicts sea level to rise 0.3 to 0.8 m by 2100 even if global temperatures can be limited to 1.5 ^{o}C. Importantly, there is great uncertainty in these projections and small variations in sea level may lead to significant impacts on coastal populations.

With the recent accelerated mass loss of the Antarctic and Greenland ice sheets, I expect that the topic of focus in this thesis, the ocean circulation near ice-ocean margins in fjords and ice-shelf cavities, will likely undergo drastic changes within the next few decades. Recent studies even anticipate the degree of ice-ocean interaction at the margins of Greenland to decrease substantially by the end of the century due to continued glacial retreat unless unexpected and truly groundbreaking reductions in greenhouse gas emissions occur in the next few decades (see references in IPCC 2019). Along with the potential for ice sheet instability and collapse around Antarctica over the next century, there are many model limitations that limit our confidence for existing projections, as discussed in the Special Report on the Ocean and Cryosphere in a Changing Climate (SROCC) (see references in

IPCC 2019).

In light of these reports and recent decisions, we are in the midst of an era of desperation given the limited progress in climate policy and mitigation as we continue to succumb to higher and higher global temperature targets. Because of this, I believe (with a healthy dose of youthful optimism) it is essential to not only continue forging ahead in the study of climate, but also to develop and be receptive to creative ways of climate mitigation and adaption as inspired by scientific advances (at least before we can sufficiently curb greenhouse gases emissions). I will present one such nascent idea in Chapter 6.4 that I believe is worthy of some consideration.

Finally, on a more personal note, I consider myself lucky to have embarked on this research journey with some flexibility of research topic. I spent valuable time in the beginning of my program exploring potential topics and repeated this process before the transition from ice-shelf cavity circulation to the related fjord circulation problems (in Chapters 3–5) as well. This transition was largely inspired by the new data from the NASA Oceans Melting Greenland campaign, which conducted an ambitious multi-year Greenland-wide assessment of fjord and shelf waters, which (conveniently for me) commenced at the beginning of my PhD studies in 2016. Although there is much to be understood about ocean circulation in fjords and cavities, I believe the experiences and skills that I have developed while completing the work will continue to guide my future work in this field.

1.2 Introduction and Background

In this section, I provide a brief and broad overview of the recent literature relevant to the thesis work. The individual chapters that follow will each provide additional introduction and background discussions relevant to each self-contained project.

In recent decades, warm ocean circulation near and within fjords and ice-shelf cavities has led to the accelerated melting and retreat of glaciers in Antarctica and Greenland often

through the transport of warm and salty waters towards the glaciers at depth (van den Broeke et al., 2016; Beckmann et al., 2018). This melting and glacial retreat, which is concentrated at the marine-terminating glaciers along the margins of the Antarctic and Greenland Ice Sheet, has important implications for future sea level rise (Enderlin et al., 2016; Holland et al., 2008).

In addition, the retreat and changes in freshwater fluxes from glaciers may also potentially influence large-scale ocean circulation and regional ocean and terrestrial ecosystems. Many existing CMIP (Climate Model Intercomparison Project) climate models do not currently include glacial and ice-shelf meltwater fluxes and others include this at the surface (Nowicki et al., 2016). Accurate representations of these fluxes as well as glacial melt rate relies on accurate submarine melt parameterizations. Therefore, improving the predictions for glacial melt is critical to improving global sea level rise estimates and assessing the effect of retreating glaciers on climate change.

The increased ocean-driven melt portion is partly due to increased access of warm waters from the off-shore shelf circulation to fjords and ice-shelf cavities around the margins of ice sheets, but the circulation (both the overturning and horizontal recirculation) within fjords/ice-shelf cavities controls the heat flux towards and freshwater away (a renewal process) from the ice-ocean boundary layer (Straneo and Cenedese, 2015). This internal circulation is primarily driven by subglacial discharge plumes (larger source of buoyancy flux, more relevant in Greenland's fjords) and meltwater plumes (relevant in most warm fjords/cavities) although other processes (winds, tides, coastal currents, and waves) are sometimes also important (Spall et al., 2017; Beckmann et al., 2018; Jackson et al., 2017; Straneo and Cenedese, 2015). The subglacial discharge is sourced from surface melt that flows out into the ocean from beneath the glacier, which creates buoyant plumes that entrain warmer water at depth. This melts ice at the ice-ocean boundary and generates a continuous source of meltwater plumes (Morlighem et al., 2016; Sutherland et al., 2019).

The current state-of-the-art boundary layer parameterizations at glacial faces that drive

the circulation dynamics generally involve plume parameterizations (Holland and Jenkins, 1999) and 3-equation thermodynamics (Hellmer and Olbers, 1989). These assume that ice is melting due to temperature and a shear boundary layer. However, existing ice-ocean boundary layer parameterizations underpredict observed glacial melt rates (derived from meltwater isotope tracer concentrations) by an order of magnitude with conventional, empirically-derived boundary layer turbulent transfer coefficients (Jackson et al., 2019); this points to either a limitation in ice-ocean parameterizations or missing physics ranging from the polar seas to the ice-ocean boundary. Many studies have investigated the ice-ocean boundary layer processes, buoyancy forcing at the surface (icebergs and surface melt), buoyancy forcing at depth (subglacial discharge), wind stresses, shelf currents, bathymetry, and mixing processes (Carroll et al., 2016, 2017; Cowton et al., 2015; Fenty et al., 2016; Gladish et al., 2015), but so far, none of these have resolved this conundrum of melt rate mismatch between observational and model results.

1.3 Science Questions and Objectives

For Chapters 2 and 3, the central question is how geometric and environmental controls the transfer of heat/tranport to and from glaciers. For Chapters 4 and 5, we tackle a major conundrum within the field, which is: *Why do existing ice-ocean parameterizations underpredict observed glacial melt rates by an order of magnitude?* This disagreement points to either a limitation in ice-ocean parameterizations or missing physics at scales ranging from the shelf seas to the ice-ocean boundary.

In addition, many aspects of the interaction between 3D fjord and ice-shelf cavity circulation and glacial melt are presently poorly understood. To address these gaps in understanding and make incremental progress towards resolving the central questions above, we target the following science questions:

Primary Science Questions:

- What are the relevant parameters in constraining the overturning circulation that brings warm water masses towards and away from marine-terminating glaciers? (Chapters 2, 3)
- What are the most important physical/dynamical processes in shelf-fjord and shelf-cavity exchange? (Chapters 2, 3)
- What are the relevant submesoscale phenomena within fjords/ice shelf cavities and what role do they play in the mixing and export of freshwater? (Chapter 4)
- Are there significant feedbacks between fjord circulation and glacial melt rate due to stratification and subglacial plume entrainment and how do these vary over the relevant parameter regimes? (Chapter 4)
- How does realistic geometry in fjords influence circulation and glacial melt rate and does this lead to any new dynamical phenomena? (Chapter 5)

1.4 Outline

First, I make some general remarks on the overall philosophical approach in the following series of studies that constitute Chapter 2–5. Chapter 2 and 3 start from first principles motivated by the simplest yet sufficiently robust models of ice-shelf cavities and fjords to develop basic theories of their circulation. These chapters also provide a basic inventory of the different dynamical features observed in simple geometries. In Chapter 4 and 5, these models and theories are developed into increasingly complex and realistic models of fjord circulation and predictions of ocean-driven glacial melt.

In Chapter 2, we investigate the importance of bathymetric sills in the ocean-filled cavities beneath a few fast-retreating ice shelves in West Antarctica and northern Greenland. These sills can be high enough to obstruct the cavity circulation and thereby modulate glacial melt rates. This chapter focuses on the idealized problem of diabatically-driven, sill-constrained

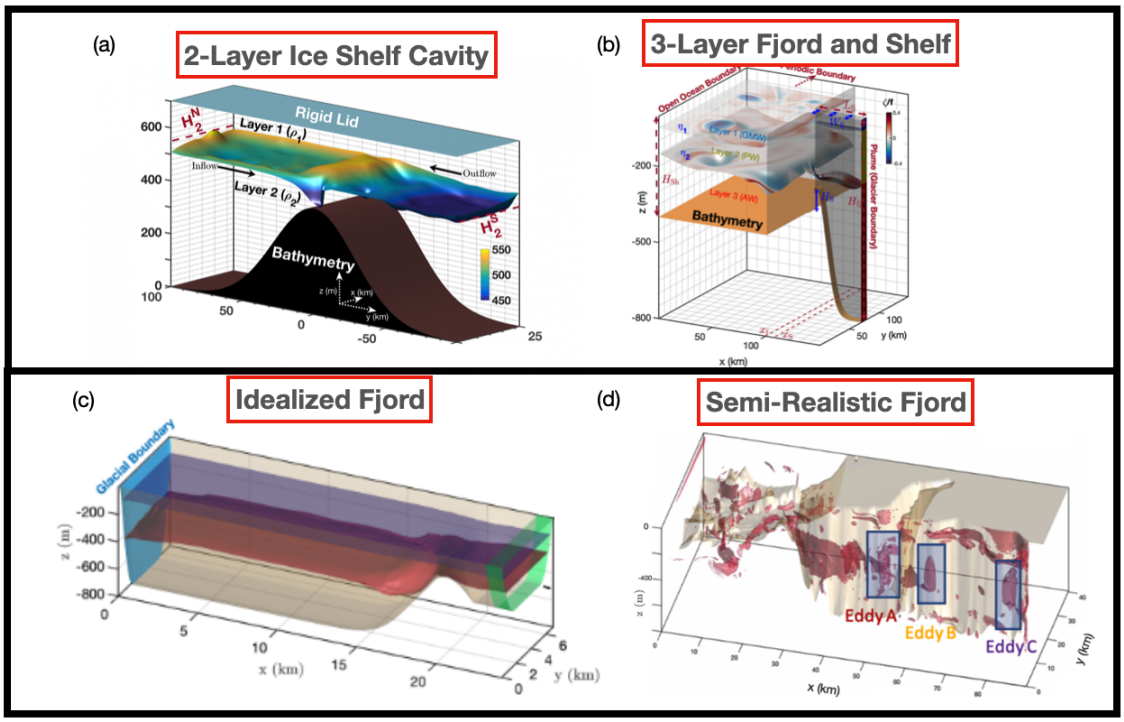

Figure 1.1: A synthesis diagram showing an overview of the models used in this thesis: (a) an idealized 2-layer isopycnal model of an ice-shelf cavity used in Chapter 2, an idealized 3-layer isopycnal model of a fjord-shelf domain used in Chapter 3, a z-coordinate model of an idealized fjord with bathtub geometry used in Chapter 4, and a z-coordinate model of a semi-realistic fjord used in Chapter 5.

overturning circulation in a cavity. We use a two-layer isopycnal hydrostatic model (Fig. 1.1a) to study the cross-sill exchange of these waters in ice shelf cavities wide enough to be rotationally-dominated. Results from the model simulations demonstrate the key parameters controlling the overturning transport and its variability are the sill height relative to the bottom layer thickness and the strength of the frictional drag. By varying these two key parameters, we simulate a diversity of flow phenomena. We present theoretical ideas to explain the characteristics of the different flow regimes observed using this model.

In Chapter 3, we discuss how the connections between tidewater glaciers and the continental shelf waters are modulated and controlled by fjords that are geometrically complex

with both internal and external drivers of variability. A strong overturning circulation driven by near-glacier buoyancy forcing transports heat towards the glaciers and meltwater away and is postulated to control the ocean-driven melt of glaciers in Antarctica and Greenland. To understand the parameters that influence the overturning circulation, we conduct idealized numerical simulations (see Fig. 1.1b) using the same isopycnal model from Chapter 2 with domains consisting of continental shelves and fjords representative of those in Greenland and the West Antarctic Peninsula.

In Chapter 4, we investigate how the overturning and horizontal recirculation in fjords discussed in Chapter 3 are driven by both subglacial discharge plumes and distributed meltwater plumes and how this leads to a feedback between the glacial melt and fjord circulation. In this study, we use high-resolution z-coordinate model to conduct numerical simulations of idealized glacial fjords (see Fig. 1.1c) to demonstrate that recirculation strength controls melt, which feeds back on overturning and recirculation. The overturning circulation strength is well predicted by existing plume models for face-wide melt and subglacial discharge, while relationships between the overturning, recirculation, and melt rate are well predicted by vorticity balance, reduced-order melt parameterizations, and empirical scaling arguments. These theories allow improved predictions of fjord overturning, recirculation, and glacial melt by taking intrafjord dynamics into account.

In Chapter 5, we investigate the complex three-dimensional circulation in three realistic fjord geometries. In this chapter, we present high-resolution numerical simulations (see Fig. 1.1d) of three glacial fjords (Ilulissat, Sermilik, and Kangerdlugssuaq), which exhibit along-fjord overturning circulations similar to previous studies. However, multiple standing eddies emerge in each of the simulated fjords and owe their existence to realistic fjord geometry. These standing eddies are long-lived, take months to spin up and prefer locations over the widest regions of deep-water fjords, with some that periodically merge with other eddies. The residence time within these eddies are significantly larger than waters outside of the eddies. These eddies are most significant for two reasons: (1) they account for a majority of the

vorticity dissipation required to balance the vorticity generated by discharge and meltwater plume entrainment and act to spin down the overall recirculation; (2) if the eddies prefer locations near the ice face, their azimuthal velocities can significantly increase melt rates. Therefore, the existence of standing eddies are an important factor to consider in glacial fjord circulation and melt rates and should be taken into account in models and observations.

Finally, in Chapter 6, we summarize the advances presented in this thesis. We also review recent, ongoing, and both short-term and long-term goals for future research inspired by this work.

CHAPTER 2

Circulation in Idealized Ice-Shelf Cavities

2.1 Introduction

In recent decades, warm ocean circulation within ice shelf cavities has led to the accelerated melting of glaciers in West Antarctica and northern Greenland (Schodlok et al. 2012, Mayer et al. 2000). This circulation contributes to glacial melting through the inward transport of warm, salty water masses and amplification of the ice-ocean heat flux through greater flow velocities and temperature gradients (Holland et al. 2008). Recent observations and modeling have also shown that as glaciers retreat past bathymetric maxima, the bathymetry has a leading-order effect on the glacial melt rates as subglacial cavities are shaped by oceanic circulations on the undersides of floating glaciers (Gudmundsson et al. 2012). This rapid retreat, postulated to be caused by the retrograde bathymetric slopes (increasing elevation in the direction of ice flow), has been observed using satellite radar interferometry to varying degrees in West Antarctic glaciers such as Pine Island, Thwaites, Smith, and Kohler glaciers (Rignot et al. 2014). Autosub cavity-transect measurements in the Pine Island Glacier (PIG) revealed a cavity that hosts the most prominent bathymetric sill yet observed and exhibits the fastest melt rate in the region (Jenkins et al. 2010, Kimura et al. 2016). Floating glaciers in northern Greenland such as the 79 North Glacier and Petermann Glacier have similar geometries and oceanic circulations (Cai et al. 2017, Schaffer 2017).

Previous studies have suggested that grounding lines retreating on a descending slope will ultimately lead to Marine Ice Sheet Instability, a dynamically-driven, runaway retreat

that can result in complete discharge of the ice stream (Schoof 2007, Gudmundsson 2013, Joughin et al. 2014). The bathymetric influence of many of the glaciers in the Amundsen Sea in West Antarctica, with the PIG as a prime example, are critical in understanding why this region is the fastest melting sector of Antarctica. Here, the melting occurs primarily at the ice-ocean interface and is predominantly forced by warm ocean circulation, as opposed to calving processes or surface melting leading to subglacial discharge (Mouginot et al. 2014, Konrad et al. 2017). The sill under the PIG is speculated to have a controlling effect on melt rates due to its modulation of intruding warm, salty Circumpolar Deep Water (CDW) into Pine Island Bay (De Rydt et al. 2014). Data and observations inside the cavity have been sparse, but diabatic processes deep inside such an ice shelf cavity lead to persistent differences between the water mass properties in the interior compared to the open ocean (Jacobs et al. 2011, Dutrieux et al. 2014).

Previous studies have investigated the dynamics using simplified models with idealized ice shelf geometries without sills (Little et al., 2008), and with sills (De Rydt et al. 2014, De Rydt and Gudmundsson 2016), as well as using more comprehensive regional ocean models with realistic bathymetry (Schodlok et al. 2012, Nakayama et al. 2014, St-Laurent et al. 2015, Seroussi et al. 2017). In these studies, the bathymetric sill was consistently found to act as a topographic barrier to the inflow of warm, salty CDW, provided that the CDW layer was sufficiently thin. These models all predict enhanced friction at the ice-ocean interface as a result of the sill, which leads to greater melt rates.

The problem of pressure-driven flow across a bathymetric obstruction has been widely studied in other oceanographic contexts, such as hydraulically-controlled flows (Whitehead et al. 1974, Gill 1977). However, this characterization is also appropriate for glaciers like the PIG and 79 North as bathymetrically-modulated exchange flows. The establishment of hydraulic control is a potential explanation for the sill's apparent role as an obstruction to CDW inflow mentioned in previous studies (De Rydt et al. 2014, Dutrieux et al. 2014), and is discussed in Sect. 7.

Under an ice shelf, a simple model for the leading-order dynamics is an exchange flow forced by negative buoyancy on the open-ocean side and a positive buoyancy in the far interior. This represents the common situation in West Antarctic and northern Greenland glaciers where a denser bottom layer is thicker on the open-ocean side than in the cavity, forcing an inflow at depth via a pressure head (Dutrieux et al., 2014). The oceanic buoyancy is then increased by freshening of the water mass through a transformation at the ice-ocean boundary occurring due to subglacial melting at the ice-ocean boundary in the far interior of the cavity, which establishes an overall isopycnal tilt along the length of the cavity.

Previous studies have placed less emphasis on the dynamical mechanisms via which the sill constrains the circulation. As a result, relatively little is understood about the flow regimes that manifest in cavity circulation and the important physical parameters that define these regimes and control the cross-sill transport. Using a high-resolution, minimal model, we simulate the circulation patterns over varying flow parameters to provide a qualitative and quantitative understanding of the transport and forms of variability that can be expected in real ice shelf cavities.

The outline of this chapter is as follows. In Sect. 2.2, we discuss the setup of a simplified 2-layer dynamical model and the details of the numerical methods used to study this problem. We also discuss the considerations for a robust posing of the idealized problem. In Sect. 2.3, we discuss the reasoning for partitioning the parameter space into three regimes based on the nondimensionalized sill height and friction velocity. In Sect. 2.4, we present solutions in the high-friction (HF) regime and explain this theoretically as a friction-dominated Stommel balance regime with equations for the boundary layer and a prediction for the flow structure. In Sect. 2.5, we present solutions in the low-friction, low-sill (LFLS) regime and discuss the emergence of gyres and eddies using potential vorticity (PV) and energy budgets. In Sect. 2.6, we present solutions in the low-friction, high-sill (LFHS) regime and discuss the phenomena of shocks, which are sharp interface gradients that appear due to wave propagation in critical flow, and layer-grounding, which occurs when the bottom layer thickness

reaches zero. In Sect. 2.7, we derive theoretical estimates of the cross-sill transport based on rotating hydraulic control theory with uniform PV, discuss their limitations, and compare with numerical results. We classify and discuss the analytical and numerical boundaries between the regimes as a function of friction and sill height. In Sect. 2.8, we summarize our findings and discuss the implications and caveats of the chapter. In Sect. 2.9, we conclude.

2.2 Idealized Cavity Flow

2.2.1 A 2-Layer Model

We pose the problem of sill-controlled circulation under an ice shelf as a 2-layer exchange flow with bathymetry (see Fig. 2.1 for reference geometry). Our shallow water momentum and continuity equations for $n = 1$, 2 on an f-plane are

$$\frac{\partial \mathbf{u}_n}{\partial t} + (\mathbf{u}_n \cdot \nabla)\mathbf{u}_n + f\hat{\mathbf{z}} \times \mathbf{u}_n = \upsilon \mathbf{S}_n - \frac{r}{h_n}\mathbf{u}_n - \nabla \phi_n \,, \tag{2.1}$$

$$\frac{\partial h_n}{\partial t} + \nabla \cdot (h_n \mathbf{u}_n) = \varpi_n \,, \tag{2.2}$$

where u is the cross-channel velocity (in the x-direction), v is the along-channel velocity (in the y-direction), and the layer thicknesses are $h_1 = H_1^M - \eta$ and $h_2 = H_2^M + \eta - h_B$, with $\eta(x, y)$ as the elevation of the interface between the layers. The reference thicknesses of the top and bottom layer are H_1^M and H_2^M, and $h_B(y)$ is the bathymetric height. We use a linear friction velocity r (m/s) that is equal for both the top and bottom layers. In numerical calculations, we control grid-scale energy and enstrophy using a thickness-weighted biharmonic eddy viscosity term $\upsilon \mathbf{S}_n$, for which $S_n^x = h^{-1}[\partial_x(hF^x) + \partial_y(hF^y)]$, $S_n^y = h^{-1}[\partial_x(hF^y) - \partial_y(hF^x)]$, where $F_n^x = \partial_x \nabla^2 u_n - \partial_y \nabla^2 v_n$, $F_n^y = \partial_x \nabla^2 v_n + \partial_y \nabla^2 u_n$ (Griffies and Hallberg, 2000). The Montgomery potential is defined as $\phi_1 = p_T/\overline{\rho}$, $\phi_2 = p_T/\overline{\rho} + g'\eta$, where p_T is the rigid lid surface pressure, $g' = g(\rho_2 - \rho_1)/\overline{\rho}$, and $\eta = H_1^M - h_1 = h_2 - H_2^M + h_B$.

The layer thicknesses at the North and South boundaries are linearly restored toward prescribed reference thicknesses, providing a simplistic representation of processes that occur

outside of the cavity and the interior. The water mass transformation near ice shelves can be significant wherever ocean waters with temperatures above the local freezing point are in contact with the ice shelf. Melting is typically enhanced near grounding lines, which for Antarctic ice shelves are partly due to the greater depths for which the pressure-dependent freezing point is reduced to lower temperatures (Joughin et al., 2012). Also, in some warm water cavities such as the PIG, which has relatively warm (i.e. above surface freezing temperature) intrusions, the location at which the ice is in contact with the warmest water is primarily concentrated at the grounding line (Dutrieux et al., 2014).

Our simplification is valid only for glaciers where the sill maximum is not located near the primary source of water mass transformation. For more general lock-exchange applications, this water mass transformation, which effectively fixes the stratification, represents any external processes that do not occur near the topographic sill as long as it leads to a relatively steady across-sill pressure head.

We model the 2-layer channel flow problem purely dynamically and do not include interior diabatic mixing or thermal fluxes between layers or to the ice shelf and bottom boundary, except for a simplified representation of water mass transformation at the northern and southern boundaries. This means that although we are motivated by a flow under an ice shelf cavity, the work presented in this chapter is not specific to ice-ocean interactions and the results also apply to channel flows in general. Due to this simplified dynamical framework, we do not make any predictions for the PIG melt rate, but a total transport can be used to constrain melt rate estimates via the water mass transformation. Instead, we focus on the circulation patterns that emerge and the bathymetric and geometric constraints on these patterns and the resulting transport. Also, the depth-distribution of the water mass transformation/diabatic forcing is an important topic, but not addressed in the present chapter, and would be better addressed with more complete vertical resolution than in the 2-layer model here.

In the posing of this problem, there is a range of possible choices for upstream and down-

stream boundary conditions including two extremes: a specified water mass transformation or nudging to a fixed stratification. We select the latter, since it allows Q to be an emergent property of the solution (except in the high-sill limit discussed in Sect. 2.6) and it also allows the isopycnal heights at the boundaries to be effectively fixed to specified values. This translates into an effective water mass transformation between the two layers at the boundaries via

$$\varpi_n = \begin{cases} -\tau_h^{-1}(h_n - H_n^N), & \text{for } \mathbf{x} \in A_N, \\ -\tau_h^{-1}(h_n - H_n^S), & \text{for } \mathbf{x} \in A_S, \\ 0, & \text{otherwise}, \end{cases} \tag{2.3}$$

with each layer n being restored to H_n^N and H_n^S (where $H_n^M = (H_n^N + H_n^S)/2$) at the northern and southern nudging region A_N and A_S, defined as 12 km-wide regions adjacent to the northern and southern boundaries. We choose the nudging timescale to be $\tau_h = 1$ day at the domain edges, with a nudging strength $\propto \tau_h^{-1}$ that decreases linearly to zero in the interior edge of the nudging zone. By construction, specifying the boundary thickness nudging H_n^N and H_n^S sets the diapycnal velocities in the two layers to be equal and opposite, $\varpi_2 = -\varpi_1$. We experimentally selected the nudging timescale to be large enough to minimize spurious high-frequency noise and small enough that the thicknesses at the boundaries remain close to (i.e. 90-95% of) the nudged values. Since we choose $H_2^N > H_2^S$, there is an upwelling $\varpi_2 > 0$ in the northern nudged region $\mathbf{x} \in A_N$, which drives an overturning circulation that inflows in the bottom layer and outflows in the top layer from the open-ocean (northern) boundary.

The cavity has dimensions $W \times L \times H = 50$ km $\times$ 200 km $\times$ 700 m, based on an idealization of bathymetry and glacier geometry of the PIG cavity in Dutrieux et al. (2014). We choose a computational domain that is twice as long (in y) as the PIG cavity to cleanly separate the North/South boundary forcing effects from the flow dynamics over the sill. The flow in the neighborhood of the sill is essentially insensitive to further increases in L. The domain coordinate system is defined as $(x, y, z) =$ [-25:25 km, -100:100 km, 0:700 m].

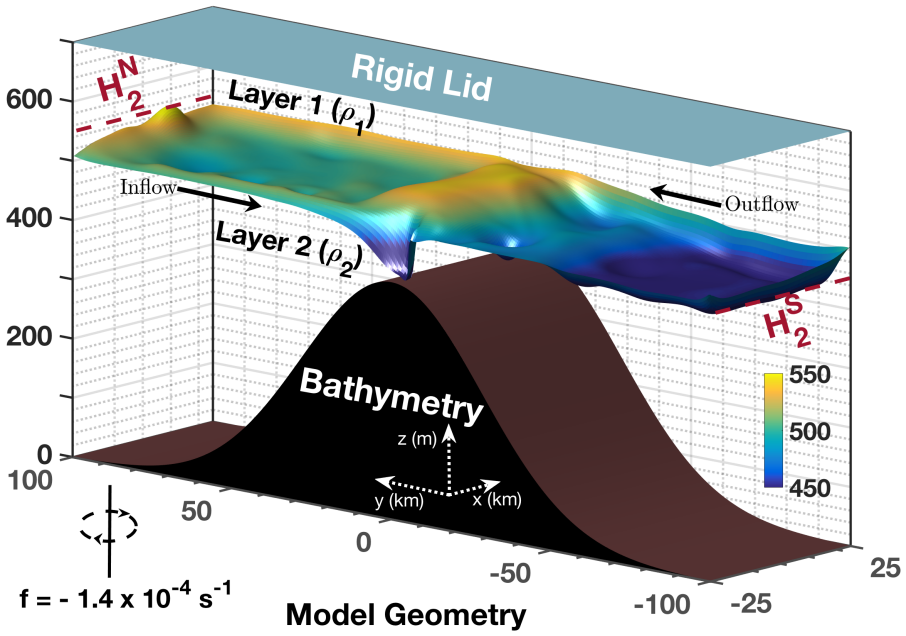

Figure 2.1: A representative geometry of a low-friction, high-sill case, with a snapshot of the interface elevation η for case $S_{400}r_5F_{100}$ ($r = 5 \times 10^{-5}$ m/s, $H_{\text{Sill}} = 400$ m, $\Delta H_2 = H_2^N - H_2^S = 100$ m; see Table 2.1 for the case notation definition). The flow exhibits geostrophic boundary currents with substantial mesoscale variability and a shock just downstream of the sill maximum along the western boundary.

In this chapter, we define the internal baroclinic deformation radius as

$$L_d(h_1, h_2) = \left(\frac{g' h_1 h_2}{f^2 (h_1 + h_2)} \right)^{1/2}, \text{ where } L_d^N = L_d(H_1^N, H_2^N)\,, \tag{2.4}$$

for H_1^N and H_2^N defined as the forced top and bottom layer thicknesses at the northern boundary. The deformation radius L_d varies throughout the domain and for each run primarily due to differences in bathymetry and the southern boundary forcing, while the northern, open-ocean boundary condition allows L_d^N to be fixed as a constant for all runs. For the purpose of a scaling analysis, we make the simplifying approximation $L_d \approx L_d^N$.

We allow the sill height $H_{\text{Sill}} = \max(h_B)$ to vary between 0 – 450 m for the various cases. We prescribe the bathymetry as a Gaussian in y

$$h_B(y) = H_{\text{Sill}} \exp(-2y^2/L_{\text{Sill}}^2)\,, \tag{2.5}$$

for a chosen sill width scale $L_{\text{Sill}} = 80$ km that is fixed for all cases. L_{Sill} is the relevant scale used to approximate the bathymetric slope $H_{\text{Sill}}/L_{\text{Sill}}$. The definition of $h_B(y)$ approximates the shape of the bathymetry beneath the PIG (De Rydt et al., 2014). In our tests, results were insensitive to the width of the sill L_{Sill} for sills much wider than the deformation radius, $L_{\text{Sill}} \gg L_d$. Also, excluding the minor influences of top topography, we use a flat-topped rigid lid for our simulations. Top topography plays a minor role compared to the controlling effects of the sill. For further discussion on this, see Appendix A.

Using representative values for the PIG (Jacobs et al., 2011), the Coriolis parameter is $f = -1.41 \times 10^{-4}\, s^{-1}$ and the densities for the two layers are $(\rho_1, \rho_2) = (1027.47, 1027.75)$ kg/m^3, which corresponds to a reduced gravity $g' = 0.0027$ m^2/s and determines the deformation radius L_d and L_d^N in Eq. (2.4).

2.2.2 Numerical Methods

To run simulations of the channel flow problem, we use the Back of Envelope Ocean Model (BEOM), a publicly available Fortran code written by Pierre St-Laurent (St-Laurent, 2018). The numerical scheme is similar to the Hallberg Isopycnal Model (Hallberg and Rhines, 1996), but offers a special treatment of layer-grounding (isopycnal outcropping when layer thicknesses vanish) using a Salmon layer (Salmon, 2002). The Salmon layer introduces an artificial term added to the Montgomery potential that prevents numerical instability due to layer-grounding by raising the potential energy of the layer to infinity as its thickness approaches zero. PV is conserved in the continuous equations with the Salmon layer present.

We modify this code to include a rigid lid pressure solver, variable rigid lid elevation, friction against the rigid lid, and biharmonic viscosity. We assume equal top and bottom

friction velocities in this chapter. The model uses the generalized Forward-Backward scheme (Shchepetkin and McWilliams, 2005), which has been modified for compatibility with the rigid lid implementation and is discussed in Appendix B. The boundary conditions are free-slip and closed on all four boundaries (no normal flow), with thickness nudging at the North and South boundaries, as mentioned in Sect. 2.2.1. The model uses energy-conserving finite-differences (Sadourny, 1975) for momentum and 3rd-order upwinding (e.g. Shchepetkin and McWilliams 1998) for thickness advection on an Arakawa C-grid of uniform resolution $dl =$ 250 m (unless otherwise specified) chosen based on the convergence of key flow properties (see Appendix A for a discussion on resolution convergence). The runs in some cases require hundreds of days of model time to fully spin up due to the generation of eddies, so we choose a run duration of 1000 days to adequately achieve statistical equilibrium, classified as having small trends (less than 5% change in the last 100 days) in the domain-integrated mean and eddy energy reservoirs of kinetic energy and available potential energy (to be defined in Eqs. (2.27a) – (2.27d)).

All time-averaged results in the following discussions are derived from 100-day averages at the end of each simulation, which is approximately one residence timescale, defined by the cavity volume divided by the exchange rate ($\int h_1 v_1 \, \mathrm{d}x$).

2.2.3 Interface Nudging and Geostrophic Transport

With the boundary condition posing in Sect. 2.2.1, there is a fixed isopycnal tilt along the channel if a strong enough nudging is used. Assuming the end points of the stratification are essentially fixed by the nudging, we can make an estimate for the zonal geostrophic transport. Here zonal (cross-channel) geostrophic transport is used as a reference scale for the meridional (along-channel) geostrophic transport; generally all of the flow crosses the channel from West to East as it flows from North to South, due to topographic steering by the sill, so the zonal geostrophic transport and meridional geostrophic transport are approximately equal. This does not mean the cross-channel and along-channel pressure gradients need always be the

same, but the reference zonal transport is found to predict the net cross-sill exchange well in most of the experiments discussed in Sects. 2.4–2.7.

Assuming weak drag, viscosity, and tendency, the bottom layer geostrophic transport is

$$\begin{aligned} Q_{\mathrm{geo}} &= \int h_2 u_2 \,\mathrm{d}y' = \int h_2 \partial_y \phi_2 / |f| \,\mathrm{d}y' \\ &= \int (H_2^M + \eta - h_B) \partial_y (\phi_1 + g'\eta) / |f| \,\mathrm{d}y' \\ &= \int \Big[\underbrace{g'(H_2^M + \eta)\partial_y \eta / |f| + H_2^M \partial_y \phi_1 / |f|}_{\text{Pressure Head Transport}} \\ &\quad - \underbrace{h_B (g' \partial_y \eta + \partial_y \phi_1)/|f|}_{\mathrm{BFD}} + \underbrace{\eta \partial_y \phi_1 / |f|}_{-\mathrm{IFD}} \Big] \,\mathrm{d}y' \,, \end{aligned} \tag{2.6}$$

where BFD is the transport reduction due to bathymetric form drag and IFD is that due to interfacial form drag. Mass conservation implies that

$$\begin{aligned} -Q_{\mathrm{geo}} &= \int h_1 u_1 \,\mathrm{d}y' = \int h_1 \partial_y \phi_1 / |f| \,\mathrm{d}y' \\ &= \int H_1^M \partial_y \phi_1 / |f| \,\mathrm{d}y' - \int \eta \partial_y \phi_1 / |f| \,\mathrm{d}y' \,, \end{aligned} \tag{2.7}$$

which allows Eq. (2.6) to be rewritten as

$$Q_{\mathrm{geo}} = Q_{\mathrm{qg}} - \int \left[\mathrm{IFD} + \frac{H_1^M}{H_1^M + H_2^M} \mathrm{BFD} \right] \mathrm{d}y' \,, \tag{2.8}$$

where we define

$$\begin{aligned} Q_{\mathrm{qg}} &= \frac{g' H_1^M}{|f|(H_1^M + H_2^M)} \int (H_2^M + \eta) \partial_y \eta \,\mathrm{d}y' \\ &\approx |f| L_d^2 \Delta H_2 \,. \end{aligned} \tag{2.9}$$

The simplified transport estimate Q_{qg} is chosen such that in the quasigeostrophic (QG) limit, $Q_{\mathrm{geo}} \to Q_{\mathrm{qg}}$ for L_d as defined in Eq. (2.4). The approximation in Eq. (2.9) is valid if $\eta^N \approx H_2^N - H_2^M$ and $\eta^S \approx H_2^S - H_2^M$, which is a reasonable approximation for all of our cases. The QG approximation (e.g. Vallis 2006) is valid for small Rossby number (Ro) and small thickness perturbations $\Delta h_n / H_n^M \sim \mathcal{O}(\mathrm{Ro})$, which is a reasonable assumption for most cases except the ones with the tallest sills or lowest friction velocities, for which BFD and IFD become non-negligible.

2.3 Regime Partitioning

For both our analytical and numerical study, we primarily examine the dynamics in a parameter regime relevant to the PIG, but our results also apply to the general class of nearly-geostrophic, wide-channel flows, in which the channel width is much larger than the deformation radius $W \gg L_d$, and the channel length is larger than the scale sill width $L \gg L_{\text{Sill}} \gtrsim W$. For the PIG, typical length scales are $L_d \approx 2 - 4$ km, $L_d^N \approx 4$ km, and $L_{\text{Sill}} \approx 80$ km.

We show a reference case in Fig. 2.1, which illustrates the geometry of the model and the interface elevation η for a case with sill height $H_{\text{Sill}} = 400$ m, isopycnal tilt (representing a pressure head) $\Delta H_2 = H_2^N - H_2^S = 100$ m, and North/upstream boundary forcing height $H_2^N = 550$ m. This case approximately matches the properties of the PIG (Jacobs et al., 2011). The imposed stratification in this case (and all our cases) has an internal baroclinic deformation radius $L_d^N = 4$ km. The regime classifications, which will be discussed in Sects. 2.4–2.6, are also directly applicable for any stratification as long as the deformation radius $L_d \lesssim L_d^N$ is less than half the width of the channel i.e. the boundary currents on opposite sides do not interact. The majority of the following figures will show the dynamics of the bottom layer mapped onto the xy-plane because the effects of bathymetry are stronger in the bottom layer.

We now determine the key parameters that control the dynamics of cross-sill exchange. The relevant dimensional parameters are W, L, H, L_{Sill}, H_{Sill}, r, H_2^N, ΔH_2, g', f, τ_h, and υ. We choose τ_h and υ such that the solutions are insensitive to modest changes, i.e. within a factor of 2. Furthermore, we choose W, L, H, H_2^N, and g' to resemble the PIG values, but in principle, we can vary and study these parameters for more general cases. Excluding these, only three parameters remain to be independently varied in this chapter: friction velocity r,

sill height H_{Sill}, and pressure head ΔH_2, which we nondimensionalize as

$$\hat{r} = \frac{r L_{\text{Sill}} H_2^N}{|f| L_d H_0 (H_2^N - H_0)}\,, \tag{2.10a}$$

$$\widehat{H}_{\text{Sill}} = H_{\text{Sill}} / H_2^N\,, \tag{2.10b}$$

$$\Delta \widehat{H}_2 = \Delta H_2 / H_2^N\,, \tag{2.10c}$$

where $H_0 = (H_2^N - H_2^S)/2 - H_{\text{Sill}}$ is an estimate for the bottom layer thickness at the sill maximum, assuming a linear isopycnal slope. We summarize these parameters in Table 2.1.

The chosen dimensionless $\hat{r}$ is based on a bulk estimate of friction PV modification in a cross-sill Stommel boundary layer, which we discuss in Sect. 2.4a. Recent microstructure friction velocity estimates from the PIG lie in the range $u^* = 1.5 - 3.7 \times 10^{-3}$ m/s (Kimura et al., 2016). Therefore, using $u^* = \sqrt{ru}$ for velocities in the range $.1 < u < 2$ m/s, we estimate the linear friction velocity to be in the range $r = 1$ x 10^{-6} to 1.4 x 10^{-4} m/s for the PIG.

To understand variations of the parameters controlling the circulation, we study the effects of varying nondimensionalized friction, sill height, and pressure head from Eqs. (2.10a) – (2.10c). We plot the mean and root mean square deviation (RMSD) of the transport as a function of these three variables in Fig. 2.2 in which each parameter is varied separately, relative to a reference state defined by $H_{\text{Sill}} = 300$ m, $r = 1 \times 10^{-5}$ m/s, and $\Delta H_2 = 100$ m (or named as $S_{300} r_1 F_{100}$ for S subscript denoting H_{Sill}, and F subscript denoting ΔH_2). This reference state was chosen such that deviations from this case qualitatively illustrate all of the sensitivities of the transport and its variability. We use a fixed dimensional friction for the sill height and pressure head parameter sweeps, since the mean transport is found to be insensitive to friction (discussed in Sect. 2.7). The RMSD is measured based on the last 100 days of the run using high temporal resolution calculations of the transport ($dt = 1/20$ day).

In these results, variations in friction cause a 100% change to the variability over the studied range, while sill height causes transport to drop to 25% of QG prediction at $\widehat{H}_{\text{Sill}} = .82$. Mean transport varies by less than 5% and variability varies by less than 30% when we vary

Name	*Parameter*	*Test Cases*	*PIG estimate*	*Units*
Friction Velocity	r	$[1, 3, 5, 10, 20, 50, 100, 500]$	$.1 - 14$	10^{-5} m/s
		$[r_1, r_3, r_5, r_{10}, ..., r_{500}]$		
Sill Height	H_{Sill}	[0:50:450]	400	m
		$[S_0, S_{50}, ..., S_{450}]$		
Pressure Head	ΔH_2	100, 150, 200	$\sim$ 100 - 200	m
		$[F_{100}, F_{150}, F_{200}]$		
Geometry	$W \times L \times H$	$50 \times 200 \times .7$	$50 \times 100 \times .7$	km
North Interface Height	H_2^N	550	$\sim 550 \pm 100$	m
Transport	Q	.1-.5	$\sim .4 \pm .1$	Sv

Table 2.1: Summary of key parameters for the numerical simulations and their corresponding estimates for the PIG. The sill height, friction velocity, and pressure head are varied independently in this chapter. The simulations will be referenced in the format $S_{\#}r_{\#}F_{\#}$, e.g. the simulation in Fig. 2.1 is $S_{400}r_5F_{100}$.

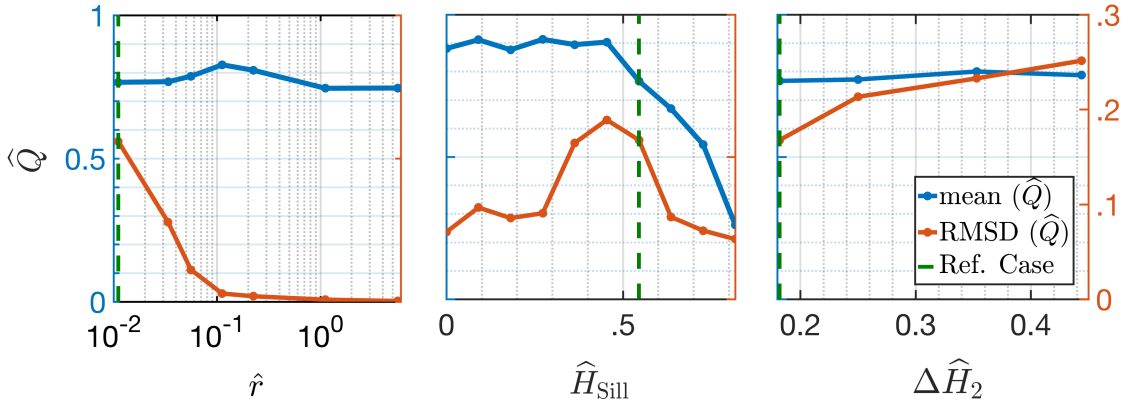

Figure 2.2: Mean and root mean square deviation (RMSD) of the nondimensionalized transport $\widehat{Q}$ as a function of friction $\hat{r}$, sill height $\widehat{H}_{\mathrm{Sill}}$, and pressure head $\Delta\widehat{H}_2$ (definitions in Eqs. (2.10a) – (2.10c)), perturbed about a reference case $S_{300}r_1F_{100}$ using results averaged over days 900-1000. Note that transport is primarily controlled by sill height while variability varies greatly with friction and peaks at an intermediate sill height due to development of critical flow (discussed in Sect. 2.6). The reference case is a low-friction, high-sill, weak pressure head case without layer-grounding, which would complicate the sensitivity of transport to the independent variables (further discussed in Sect. 2.6). The mean and RMSD transports are scaled by the geostrophic transport, given by Eq. (2.9). Note the different axis scale for RMSD transport on the right.

the pressure head. Therefore, once nondimensionalized, $\hat{r}$ and $\widehat{H}_{\text{Sill}}$ capture the important changes in mean transport and variability. These results suggest a reasonable partition of the parameters into three regimes: high-friction (HF) (including both low and high sills); low-friction, low-sill (LFLS); and low-friction, high-sill (LFHS). We do not distinguish between low and high sill in the HF regime because in HF, even for very high sills, transport decreases to no less than 80% of the geostrophic estimate.

In the next three sections, we discuss each of these regimes and describe the phenomena that emerge, both qualitatively and quantitatively.

2.4 High-Friction (HF) Regime ($\hat{r} = \mathcal{O}(1)$)

2.4.1 PV Balance

In this section, we discuss the numerical solutions in the high-friction regime. We present a solution in Fig. 2.3 for a high-friction case $S_{400}r_{500}F_{100}$, where we define the streamfunction and PV for each layer as

$$\psi_n = \int_{-W/2}^{x} v_n h_n \, \mathrm{d}x', \tag{2.11a}$$

$$q_n = (f + \zeta_n)/h_n. \tag{2.11b}$$

There is a western boundary current (i.e. at the edge of the domain toward which topographic Rossby waves would propagate) which narrows and strengthens as it approaches the steepest part of the sill, and a subsequent broadening near the sill maximum due to smaller bathymetric gradients. At the maximum, the bottom layer flow crosses the channel since topographic beta, defined as $\beta_{\text{topo}} = f\partial_y h_B/H_2^M$, changes sign due to a reversal of the bottom slope. Compared to the bottom layer, the sill exhibits a much weaker influence on the top layer. Overall, this solution is representative of the high-friction regime with a circulation that is steady in time and can be interpreted via a time-mean vorticity balance resembling Stommel boundary layer theory (Stommel, 1948).

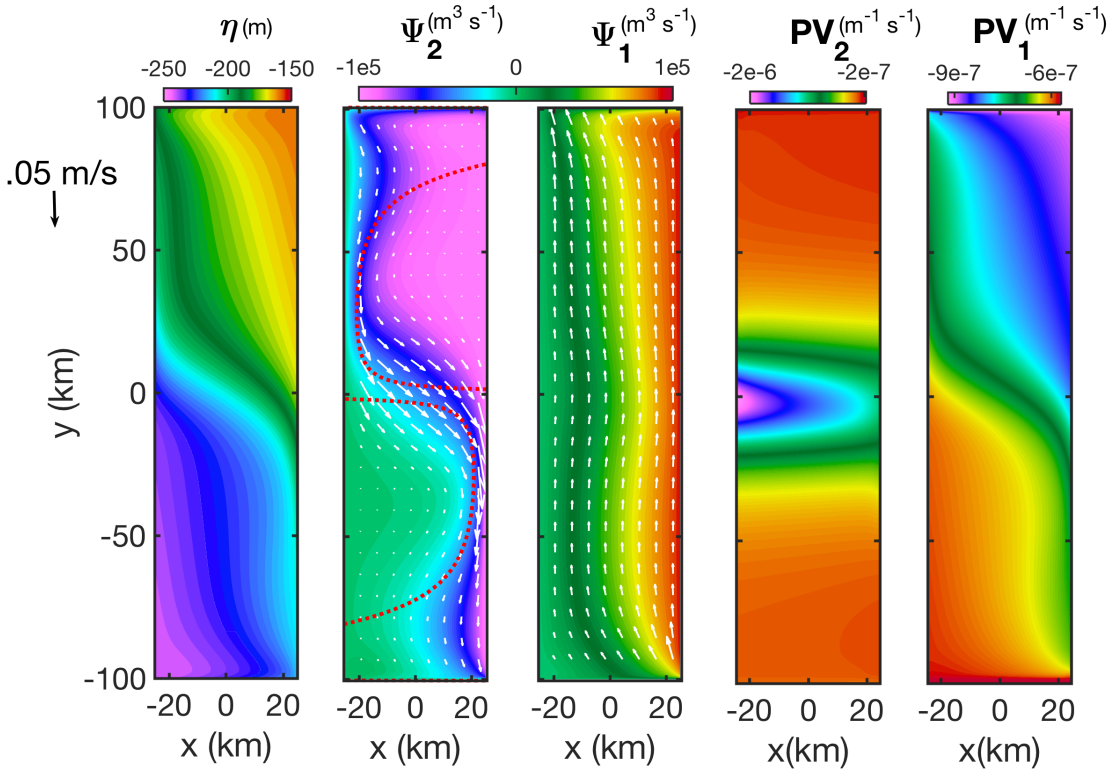

Figure 2.3: Numerical solution for the high-friction case $S_{400}r_{500}F_{100}$ showing the interface elevation η, top and bottom layer transport streamfunctions ψ_n, and top and bottom layer PV. We show the solution at day 1000, which remains steady and exhibits a Stommel-like boundary current (Stommel, 1948), crossing the channel along the sill maximum due to the sign change of β_{topo}. The thickness-weighted average velocity vectors are shown in white for each layer and the theoretical boundary layer width L_{St} from Eq. (2.18) is shown as a dotted red line in the ψ_2 panel.

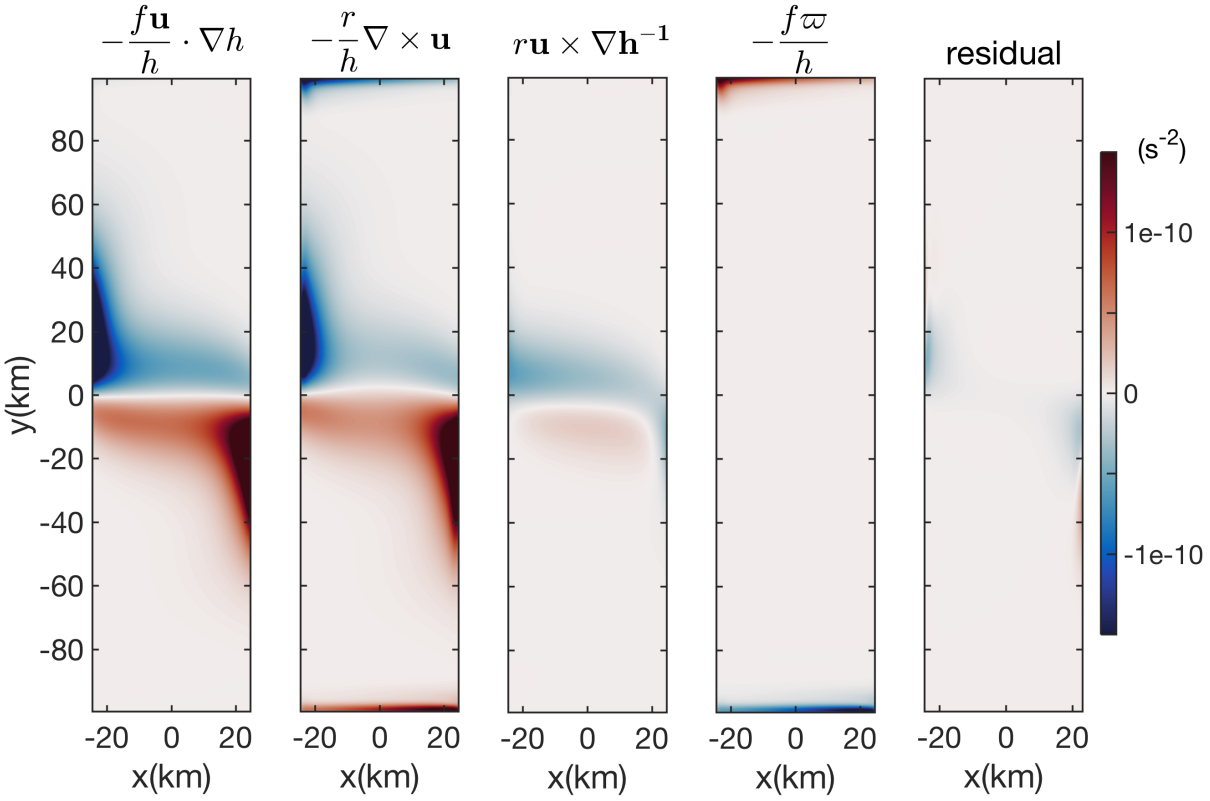

Figure 2.4: Terms in the thickness-weighted PV equation (Eq. (2.13)) for the bottom layer of the high-friction case $S_{400}r_{500}F_{100}$ shown in Fig. 2.3 at day 1000. The primary terms in the thickness-weighted PV balance are friction and Coriolis torques from traditional Stommel balance (left two panels), with the torque from interface nudging (fourth panel) balanced by friction in the nudging regions, and a small residual primarily due to viscosity. The torque term due to lateral variations of the effective friction (middle panel) provides a secondary contribution to the bottom layer vorticity budget. The boundary layer width L_{St} reaches a minimum of 4 km near $y = \pm 20$ km and grows exponentially towards the sill maximum (see Fig. 2.3).

The sill imposes a PV barrier that must be surmounted to allow water mass exchange. We use the PV budget to identify processes that facilitate transport across the PV gradient over bathymetry. The shallow water absolute vorticity equation (or equivalently, the thickness-weighted PV equation for steady flow) for a homogeneous fluid layer with friction, but neglecting viscosity, is

$$\frac{\partial h_n q_n}{\partial t} + \nabla \cdot (h_n q_n \mathbf{u}_n) = -\nabla \times \left(\frac{r \mathbf{u}_n}{h_n} \right) . \tag{2.12}$$

For further discussion of the thickness-weighted PV equation, see Appendix C. In the high-friction limit, we can assume a steady state, small Rossby number approximation (where Ro $= \zeta/f$), $q_n \approx f/h_n$, to the thickness-weighted PV equation. Along with the definition in Eq. (2.3), we can simplify Eq. (2.12) as the layerwise vorticity balance

$$-\frac{f \mathbf{u}_n}{h_n} \cdot \nabla h_n = -\frac{r}{h_n}(\nabla \times \mathbf{u}_n) + r \mathbf{u}_n \times \nabla h_n^{-1} - \frac{f \varpi_n}{h_n} . \tag{2.13}$$

The first two terms represent the traditional Stommel boundary layer balance (Stommel, 1948), but with the topographic β_{topo} in place of the planetary β. The third term is the torque due to lateral variations in the effective friction associated with variations in the layer thickness. The last term represents the torque imposed by diabatic stretching in the nudging regions. We show the term-by-term vorticity balance in Fig. 2.4 for the case $S_{400} r_{500} F_{100}$ (same case as Fig. 2.3), which illustrates the magnitude of each of the terms in Eq. (2.13). The first two terms are the dominant ones in the HF regime, the third term provides a small contribution to the bottom layer vorticity budget near the sill maximum, and the last term represents the torque imposed by diabatic stretching and is only important in the nudging regions.

2.4.2 Stommel Boundary Layer

We now extend Stommel's theory to make an explicit prediction for the structure of the boundary layer, and derive a suitable nondimensionalization for the friction coefficient based

on boundary layer modification of PV. We make a QG approximation to Eq. (2.13) in the bottom layer (n=2) using the assumption of small thickness perturbations $\Delta h_n/H_n \sim \mathcal{O}(Ro)$, which allows the leading order balance to be written as

$$\beta_{\text{topo}} v_2 + \frac{f}{H_2^M}\varpi_2 = -\frac{r}{H_2^M}\zeta_2 \,. \tag{2.14}$$

This also implicitly assumes that the variations in the bottom layer thickness are due solely to bathymetry instead of the interface elevation, which is justified when the bottom slope dominates the isopycnal thickness gradient. We assume that the flow is spatially slowly-varying in the along-channel direction, $\partial_x v_2 \gg \partial_y u_2$, and make the QG approximation, $v_2 = (1/H_2^M)\partial_x \psi_2$. Thus, Eq. (2.14) leads to the approximation

$$\beta_{\text{topo}} \partial_x \psi_2 \approx -\frac{r}{H_2^M}\partial_x^2 \psi_2 \,, \tag{2.15}$$

the solution of which is

$$v_2 = v_0 \exp\left(-\frac{\beta_{\text{topo}} H_2^M}{r} x\right) = v_0 \exp\left(-\frac{x}{L_{\text{St}}}\right) \,, \tag{2.16}$$

where L_{St} is a length scale described in further detail below. We can determine the constant v_0 using y-invariance of the transport set by the nudging zone

$$\iint_{A_N} \varpi_2 \, \mathrm{d}A = H_2^M \int v_2 \, \mathrm{d}x \approx v_0 H_2^M L_{\text{St}} \,, \tag{2.17}$$

where A_N is area of the northern nudging region. This assumes all of the along-channel transport occurs in the boundary layer.

The velocity profile in Eq. (2.16) establishes a Stommel boundary width scale

$$L_{\text{St}} = r/(\beta_{\text{topo}} h_2) \,, \tag{2.18}$$

which approximately matches the boundary structure in Fig. 2.4 and is shown in the bottom layer streamfunction panel in Fig. 2.3 as a dotted red line. This demonstrates the agreement of boundary layer width in the numerical results with this simple theory. In our runs, the minimum L_{St} varies significantly from 20 m to 30 km from case $S_{400}r_1F_{100}$ (LFHS) to $S_{100}r_{500}F_{100}$ (HF).

2.4.3 Scaling for the Importance of Bottom Friction

The transition from high-friction to low-friction cases is determined by friction being $\mathcal{O}(1)$ in the vorticity budget in Eq. (2.12); when friction becomes sufficiently weak, the flow must surmount the sill's PV gradient via advective mechanisms instead. Our solutions (further discussed in Sect. 2.6) and previous literature (Pratt and Whitehead, 2007) indicate that frictionless boundary currents have widths of approximately L_d, so the transition may be expected to occur when L_{St} becomes smaller than the deformation radius L_d. However, this criterion is ambiguous because L_{St} typically varies by an order of magnitude along the length of the channel (see Fig. 2.3), while L_d varies much less (from L_d^N to about $L_d^N/2$ at the sill maximum for the tallest sills). We therefore define an integral Stommel boundary width L_{St}^*, which estimates the meridionally-integrated influence of friction and motivates the nondimensionalization of $\hat{r}$ in Eq. (2.10a). Our integral Stommel width also relaxes the assumption of QG flow used to derive L_{St}.

To find the friction-induced change in PV within the boundary layer of width L_d from the northern boundary to the sill maximum is $\mathcal{O}(1)$, we start with an integral of Eq. (2.12) over a friction-dominated boundary layer

$$\int_0^{L/2}\int_{-W/2}^{-W/2+L_d} \left[\partial_y(hqv)+\partial_x(hqu)\right]\,\mathrm{d}x'\mathrm{d}y' = \int_0^{L/2}\int_{-W/2}^{-W/2+L_d} r(\partial_y u/h-\partial_x v/h)\,\mathrm{d}x'\mathrm{d}y'\,. \tag{2.19}$$

For a steady-state semigeostrophic flow $v \gg u$ for $L \gg W$ (later discussed in Sect. 6a), with no cross-channel flow across the boundary layer, $u(-W/2) = u(-W/2+L_d) = 0$, this yields

$$\int_0^{L/2}\int_{-W/2}^{-W/2+L_d} \partial_y(hqv)\,\mathrm{d}x'\mathrm{d}y' = -\int_0^{L/2}\int_{-W/2}^{-W/2+L_d} r\partial_x v/h\,\mathrm{d}x'\mathrm{d}y'\,. \tag{2.20}$$

For a boundary layer of width L_d, the terms scale according to the dimensional estimates $\partial_x \sim 1/L_d$, $\partial_y \sim 1/L_{\mathrm{Sill}}$, $v \sim Q/(L_d h)$ (since the meridional transport $Q \sim vL_d h$), and

$\partial_x v \sim Q/(L_d^2 h)$. Thus, Eq. (2.20) yields the scaling relationship

$$Q\Delta q \sim rQL_{\text{Sill}}/(L_d H_0^2)\,, \tag{2.21}$$

so that the meridional PV difference due to friction scales as $\Delta q = rL_{\text{Sill}}/(L_d H_0^2)$. To find how much friction accounts for in the total PV change from the northern boundary to the sill maximum, we find the ratio $\Delta q/(q_N - q_0)$, which is $\mathcal{O}(1)$ when friction is dominant, where $q_N = f/H_2^N$ is the upstream PV, $q_0 = f/H_0$ is the bottom layer PV, and H_0 is the layer thickness at the sill maximum $y = 0$. This allows us to define the integral Stommel width via

$$\frac{\Delta q}{q_N - q_0} = \frac{rL_{\text{Sill}}H_2^N}{|f|L_d H_0(H_2^N - H_0)} \equiv \frac{L^*_{\text{St}}}{L_d}\,. \tag{2.22}$$

We define $H_0 = H_2^M - H_{\text{Sill}}$ as the bottom layer thickness at the sill maximum based on a simple average of the North and South interface heights.

Therefore, the integral Stommel boundary width is

$$L^*_{\text{St}} = \frac{rL_{\text{Sill}}H_2^N}{|f|H_0(H_2^N - H_0)}\,, \tag{2.23}$$

and is an estimate for the bulk frictional boundary layer width. For our runs, L^*_{St} ranges from 20 m to 120 km from the LFLS to HF cases. Using L^*_{St}, we can equivalently express our nondimensionalized friction parameter from Eq. 2.10a as the ratio of the integral Stommel boundary layer width to the deformation radius width

$$\hat{r} = L^*_{\text{St}}/L_d \approx L^*_{\text{St}}/L_d^N\,. \tag{2.24}$$

The simplifying approximation $L_d \approx L_d^N$ is made since this allows $\hat{r}$ to be defined as a fixed value for each run and is a reasonable bulk estimate of the domain. However, it should be noted that $L_d \approx L_d^N/2$ at the sill maximum of the tallest sills in our runs. We will use this definition of $\hat{r}$ to define the boundary between low-friction and high-friction regimes and quantify the success of this classification in Sect. 2.7.

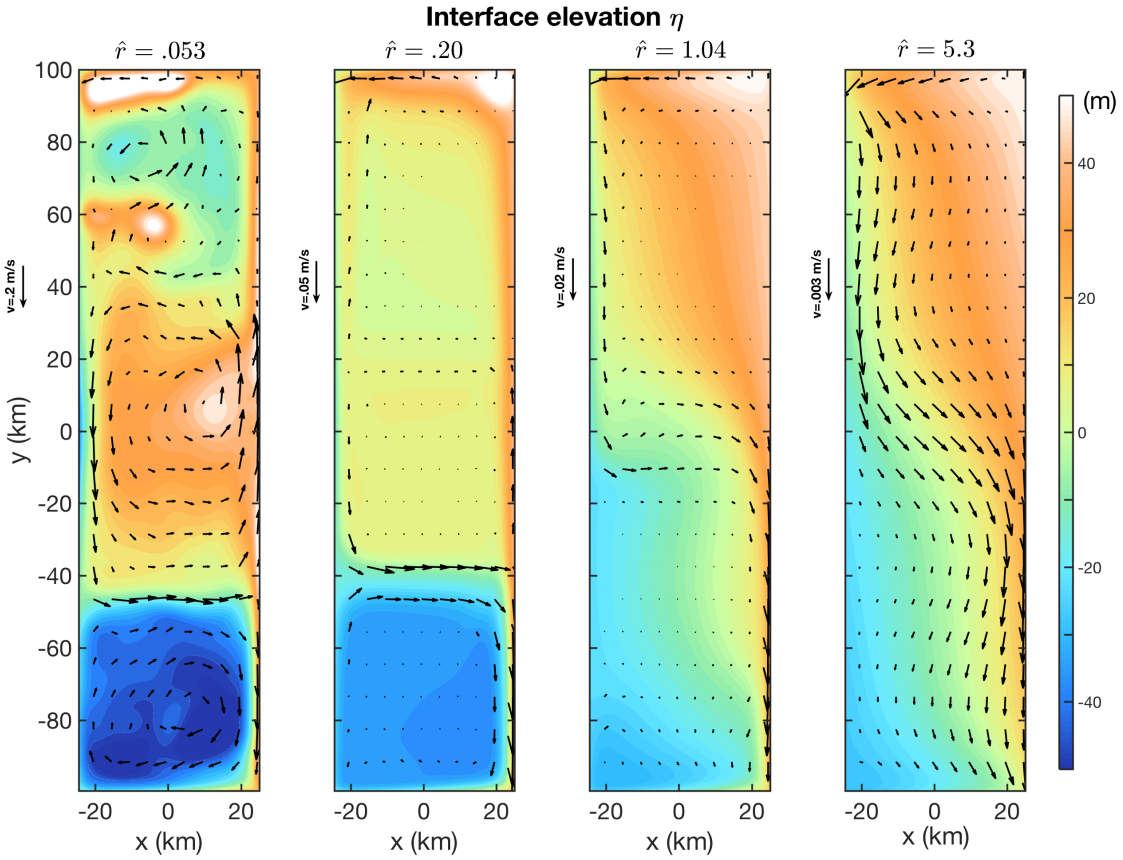

Figure 2.5: Snapshot of interface elevation η at day 1000 for varying friction (low-friction, low-sill to high-friction) cases ($S_{200}r_5F_{100}$, $S_{200}r_{20}F_{100}$, $S_{200}r_{100}F_{100}$, $S_{200}r_{500}F_{100}$) i.e. $\hat{r}$= [.053, .20, 1.04, 5.3] for $\widehat{H}_{\text{Sill}} = .36$, $\Delta\widehat{H}_2 = .18$. Eddies emerge as the friction is reduced, in addition to a gyre-like circulation around the sill. For higher friction, the solution is well-described by the Stommel boundary layer theory (see Sect. 2.4.2). The thickness-weighted velocity vectors are shown in black for each case.

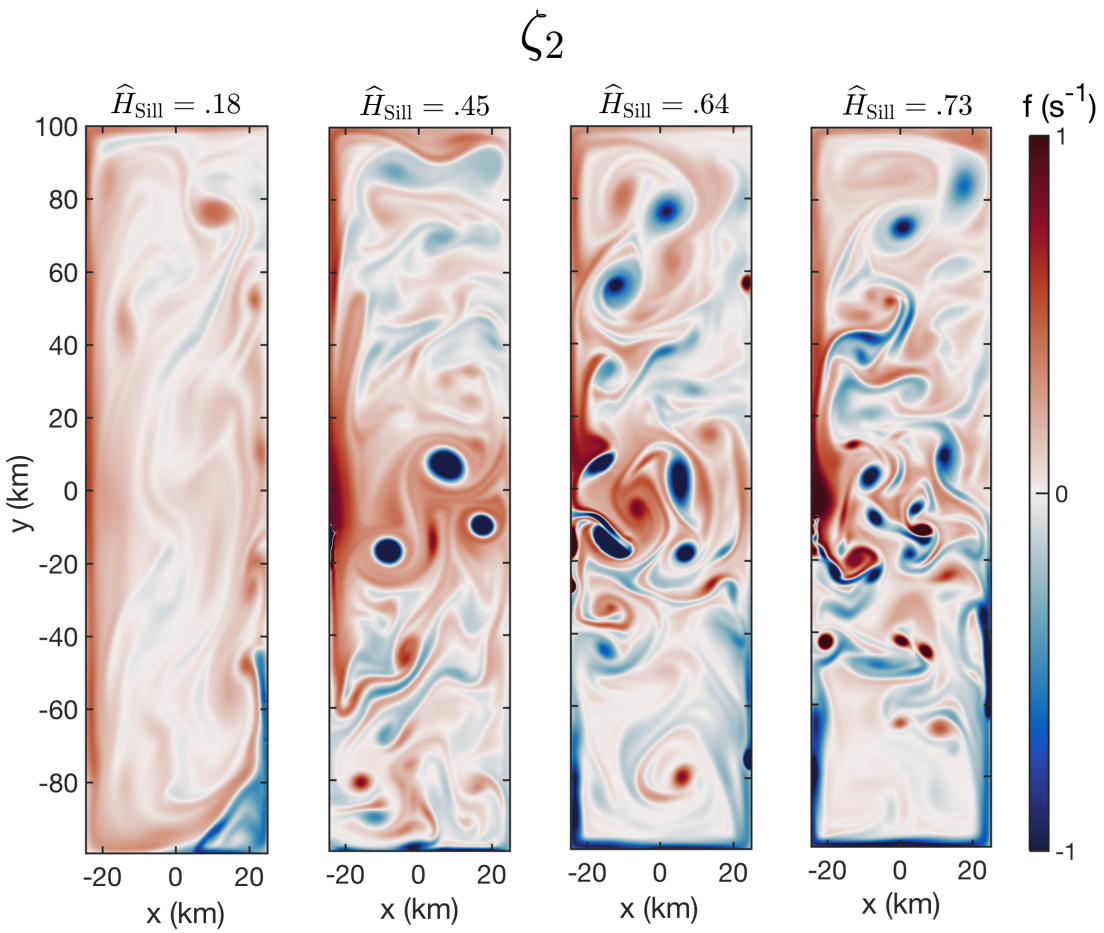

Figure 2.6: Snapshot of bottom layer vorticity ζ_2 for varying sill height and (approximately) fixed $\hat{r} \ll 1$ ($S_{100}r_1F_{100}$, $S_{250}r_1F_{100}$, $S_{350}r_1F_{100}$, $S_{400}r_1F_{100}$) i.e. $\widehat{H}_{\text{Sill}} = [.18, .45, .64, .73]$ and $\hat{r}$= [.013, .011, .013, .017] at day 1000. The solution develops an unimpeded domain-filling circulation for low sill heights, an intensification of the western boundary current and eddies for intermediate sill heights, and the emergence of shocks and more abundant, smaller eddies for greater sill heights. The decrease in the radii of the eddies with increasing sill height is due to the decrease in the deformation radius L_d over the sill as the bottom layer thickness is reduced. The vorticity color scale range is normalized by the Coriolis parameter $f = -1.41 \times 10^{-4}\, s^{-1}$.

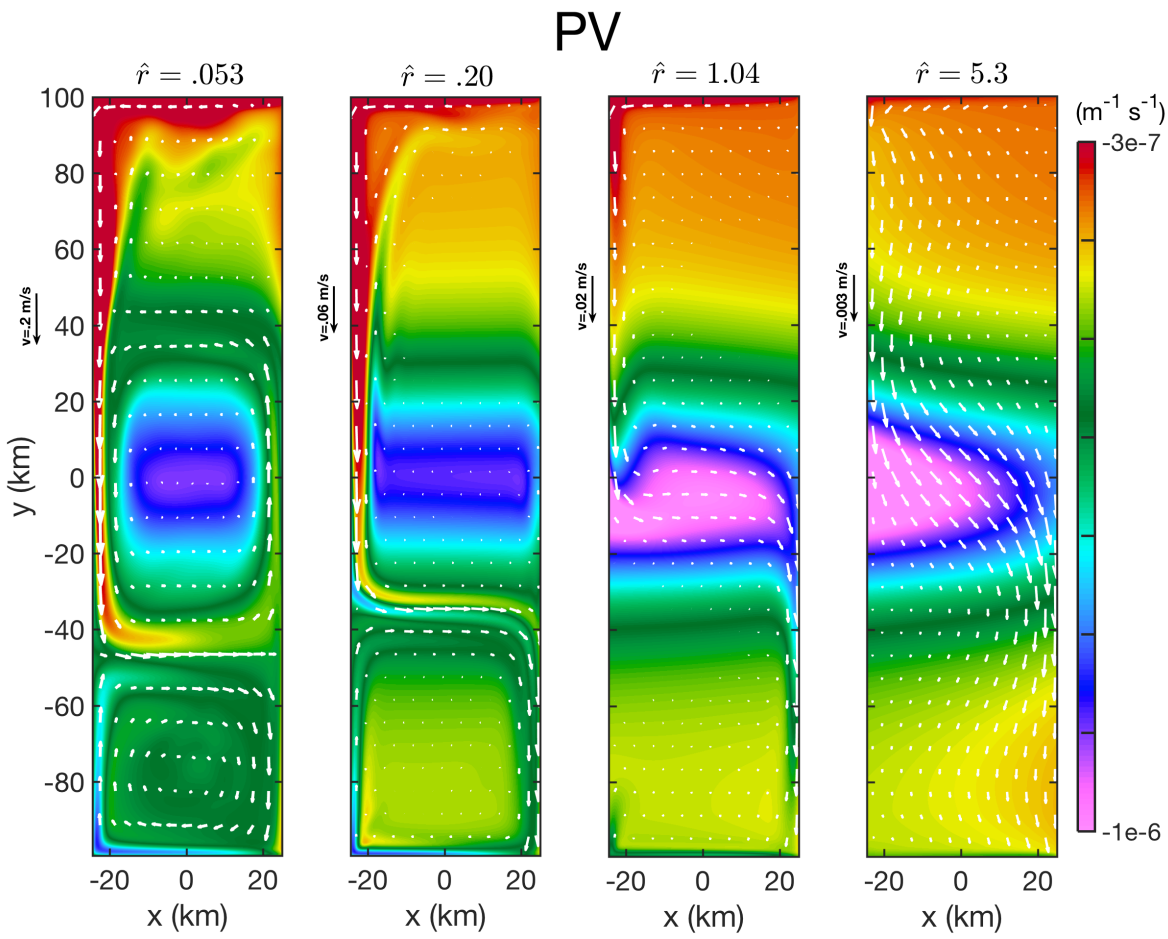

Figure 2.7: Bottom layer potential vorticity (defined in Eq. (2.11b)) for the same cases shown in Fig. 2.5 ($\hat{r}$= [0.053, 0.20, 1.04, 5.3] for $\widehat{H}_{\text{Sill}} = 0.36$, $\Delta\widehat{H}_2 = 0.18$, corresponding to $S_{200}r_5F_{100}$, $S_{200}r_{20}F_{100}$, $S_{200}r_{100}F_{100}$, $S_{200}r_{500}F_{100}$) averaged over days 900-1000. The PV is approximately conserved in the boundary layer until it approaches the sill for the LFLS cases (small $\hat{r}$), while the wide frictional boundary layer permits flow across mean PV contours throughout the domain in the HF cases (high $\hat{r}$). The thickness-weighted average velocity vectors are shown in white for each case.

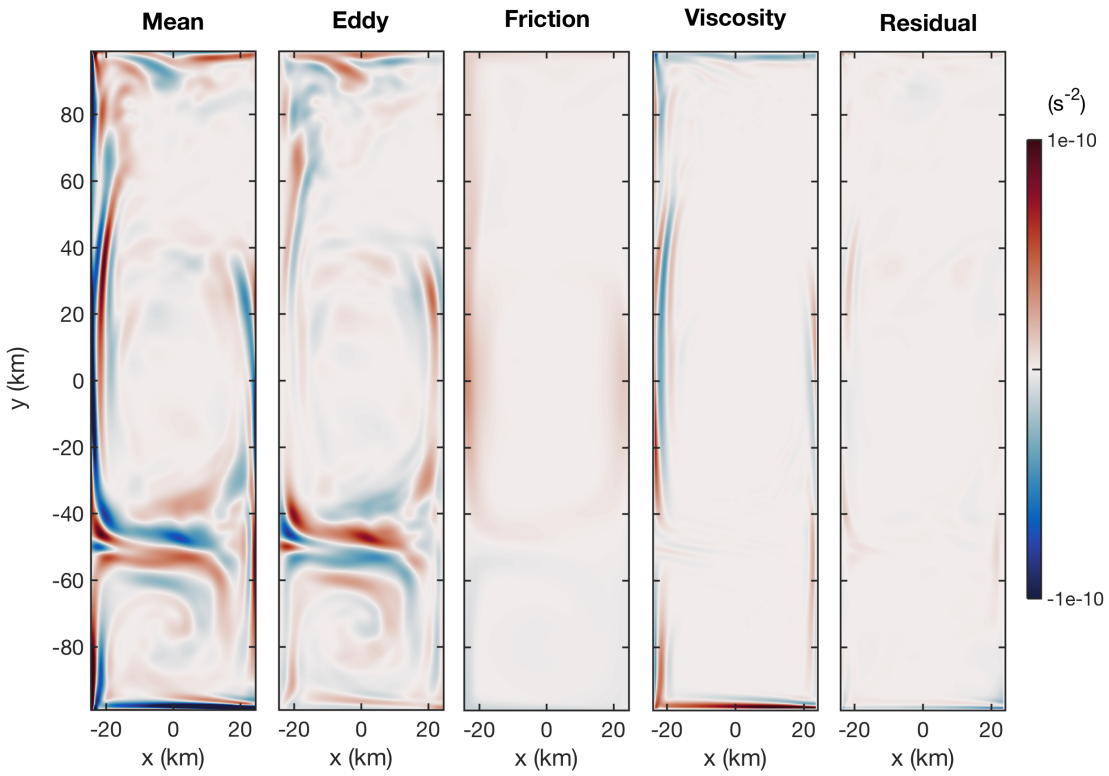

Figure 2.8: Terms in the thickness-weighted PV balance in Eq. (2.25) for LFLS case $\hat{r} = .053$, $\widehat{H}_{\text{Sill}} = 0.36$, $\Delta\widehat{H}_2 = 0.18$ corresponding to $S_{200}r_5F_{100}$, averaged over days 900-1000. The residual is due to a small tendency in the solution. Note the difference in color scale from Fig. 2.4. See the discussion in Sect. 2.5.1.

2.5 Low-Friction, Low-Sill (LFLS) Regime

$(\hat{r} \ll 1,\ \widehat{H}_{\mathbf{Sill}} \ll 1)$

2.5.1 Transition to Low-Friction: Gyres and Eddies

In the HF cases, the numerical and analytical solutions predict a meridional anti-symmetry about the domain center (due to a symmetric sill with equal magnitude and opposite sign in β_{topo}). As we decrease friction, the flow develops meridional asymmetry about the sill and intensification of the western boundary current. These features are visible in Fig. 2.5, which shows snapshots of the interface elevation η for various values of the dimensionless friction velocity $\hat{r}$. For weak friction, the boundary layer does not widen and weaken over the sill maximum, as it does in the HF cases. The flows in this regime also exhibit significant variability in time, and generate eddies that intensify as friction is reduced.

Fig. 2.6 shows the bottom layer relative vorticity ζ_2 for several sill heights $\widehat{H}_{\text{Sill}}$. These snapshots demonstrate the effect of decreased friction and increased sill heights on the flow variability, most notably in the boundary layer. Not shown is the instantaneous vorticity over a range of $\hat{r}$, and the interface elevation and velocities over a range of H_{Sill}. The vorticity for decreasing friction velocity is consistent with the narrowing and strengthening of the western boundary current and cross-sill separation location (also seen in Fig. 2.5), as well as the emergence of eddies primarily shed from the boundary current. For greater sill heights, there are greater velocity magnitudes near the sill maximum along with larger isopycnal tilts. The evidence for the sill-impedance of the flow is in the lower calculated transports for greater sill heights, as shown in Fig. 2.2. Qualitatively, the cross-sill separation region occurs progressively closer to the sill maximum (partly observed in the boundary current separation location in Fig. 2.6).

We show the time-averaged bottom layer PV for various values of $\hat{r}$ in Fig. 2.7, which filters out the transport variability associated with eddy formation. This figure illustrates

the steady-state narrowing and intensification of the western boundary current, a gyre-like circulation around the sill, and the along-channel asymmetry that develop as the friction is reduced. In the LFLS cases, the PV in the boundary current is observably less modified as the flow crosses the sill compared to the HF cases. Upstream of the sill, PV is particularly well-conserved within the boundary current, which suggests that flow across mean PV contours primarily occurs in the eddying region downstream of the sill.

To quantify the role of eddies in facilitating cross-sill exchange, we use the time-averaged thickness-weighted PV balance

$$\underbrace{\overline{h}_n \frac{\partial \langle q_n \rangle}{\partial t}}_{\text{tendency}} + \underbrace{\overline{h}_n \langle \mathbf{u}_n \rangle \cdot \nabla \langle q_n \rangle}_{\text{mean advection}} + \underbrace{\nabla \cdot [\overline{h}_n \langle \mathbf{u}_n^\dagger q_n^\dagger \rangle]}_{\text{eddy advection}}$$
$$= \underbrace{-\nabla \times \overline{\left(\frac{r \mathbf{u}_n}{h_n} \right)}}_{\text{friction}} + \underbrace{\overline{h \nabla \times (\upsilon S_n)}}_{\text{viscosity}} - \underbrace{\varpi_n \langle q_n \rangle}_{\text{nudging}} . \tag{2.25}$$

Here, we define the thickness-weighted average and deviations from that average via

$$\langle \cdot \rangle \equiv \frac{\overline{h_n \, \cdot}}{\overline{h}_n} , \tag{2.26a}$$

$$\cdot^\dagger \equiv \cdot - \langle \cdot \rangle , \tag{2.26b}$$

as discussed in Appendix C. The mean and eddy components are separated on timescales of $\mathcal{O}(100$ days), which is about a residence timescale, as previously stated. The terms on the left-hand side of Eq. (2.25) together represent the PV advection decomposed into the tendency, mean, and eddy contributions. This is balanced by the vorticity forcing due to friction, viscosity, and vortex stretching due to nudging at the boundaries.

We plot the terms of the PV balance in Fig. 2.8 for the LFLS case $S_{200} r_5 F_{100}$. The dominant balance is between mean and eddy advection, particularly south of the sill where the boundary current separates from the western wall (see leftmost panel in Fig. 2.7), with non-negligible viscosity and friction contributions along the western boundary. Despite the prominent eddy PV fluxes, the eddy component of the transport is consistently much smaller

than the transport by the time-mean flow (the mean flow has velocities of $\mathcal{O}(1$ m/s) while the eddying velocity is $\mathcal{O}(0.1$ m/s)); it contributes up to 15% of the transport in the lowest friction cases, as seen in Fig. 2.2. Even though the eddies do not directly influence the cross-sill transport (whose controls are discussed in Sect. 2.7), the eddies mix and homogenize PV, and the resulting eddy PV flux convergence allows the flow to cross mean PV contours in the absence of friction. There is also a non-negligible modification of the PV by viscosity as the flow crosses the sill.

2.5.2 Eddy Energetics

To understand the mechanisms of eddy generation and their locations, we now examine the energy budget. Here, we consider kinetic energy (KE) and available potential energy (APE) reservoirs separately and split them into mean and eddy components using thickness-weighted averaging according to the following isopycnal eddy-mean decomposition,

$$MKE_n = \overline{h}_n |\langle \mathbf{u}_n \rangle|^2/2\,, \tag{2.27a}$$

$$EKE_n = \overline{h_n |\mathbf{u}_n^\dagger|^2}/2\,, \tag{2.27b}$$

$$MAPE = g'(H_1^M - \overline{h}_1)^2/2\,, \tag{2.27c}$$

$$EAPE = g'\overline{h_1'^2}/2\,. \tag{2.27d}$$

We partition the time derivatives of these four quantities into transport and conversion terms following Aiki et al. (2016).

The barotropic and baroclinic mean-to-eddy conversion terms in isopycnal coordinates are

$$C_{\mathrm{BT}} = \langle \mathbf{u}_n \rangle \cdot (\nabla \cdot (\overline{h}_n \langle \mathbf{u}_n^\dagger \mathbf{u}_n^\dagger \rangle))\,, \tag{2.28a}$$

$$C_{\mathrm{BC}} = \langle \mathbf{u}_n \rangle \cdot \overline{h_n' \nabla \phi_n'}\,, \tag{2.28b}$$

and correspond to the forces exerted on the mean flow by Reynolds stress convergence and isopycnal form drag convergence. These terms decelerate the mean flow by converting the

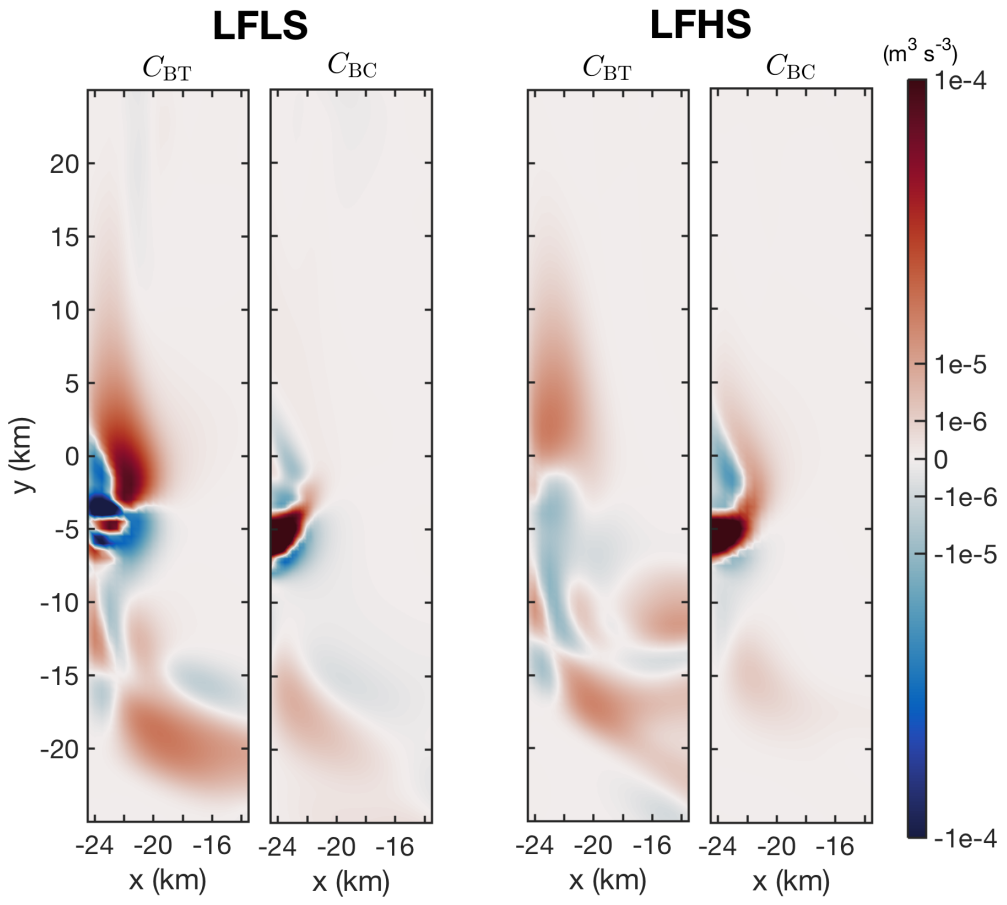

Figure 2.9: Zoom of conversion terms in the eddy generation region comparing low-friction, low-sill and low-friction, high-sill cases $S_{200}r_{1.7}F_{100}$ and $S_{400}r_1F_{100}$ for a fixed nondimensionalized friction $\hat{r} = 0.017$ and sill heights $\widehat{H}_{\mathrm{Sill}} = 0.37,\ 0.73$, averaged over days 900-1000. The terms are calculated from Eq. (2.28a) and show a relatively constant partition between barotropic and baroclinic mean-to-eddy conversion terms. For LFLS, the conversions integrated over the central area A_C shown above (localized to the shock region) is $\int C_{\mathrm{BT}}\, dA = 0.0053\,\mathrm{m^5 s^{-3}}$ and $\int C_{\mathrm{BC}}\, dA = 0.0083\,\mathrm{m^5 s^{-3}}$, while for LFHS, $\int C_{\mathrm{BT}}\, dA = 0.0042\,\mathrm{m^5 s^{-3}}$ and $\int C_{\mathrm{BC}}\, dA = 0.0067\,\mathrm{m^5 s^{-3}}$.

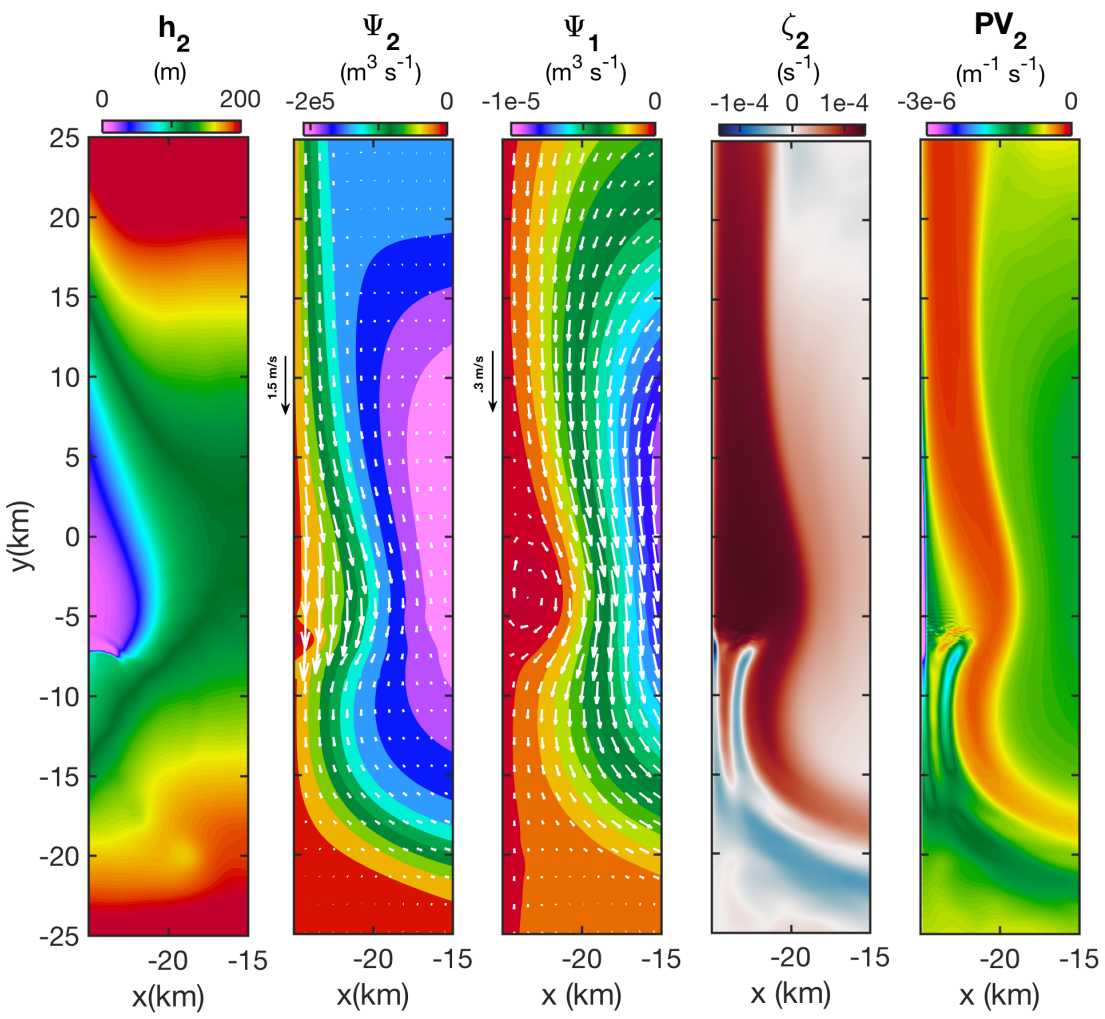

Figure 2.10: Zoom view of $h_2, \psi_2, \psi_1, \zeta_2, \mathrm{PV}_2$ for a LFHS case $S_{400}r_5F_{100}$ with $\hat{r} = 0.087$ and $\widehat{H}_{\mathrm{Sill}} = 0.73$, which exhibits shock and layer-grounding, averaged over 100 days. The highest velocities occur in the bottom western boundary layer; the thickness-weighted average velocity vectors are shown in white for each layer. This highlights a LFHS case exhibiting a hydraulic shock and layer-grounding region due to a high sill and an inertial boundary current due to low-friction, demonstrating a strong contrast with the HF case shown in Fig. 2.3. For further discussion, see Sect. 2.6.2.

mean kinetic energy to eddy kinetic energy for positive values and extract energy from the eddy kinetic energy to accelerate the mean flow for negative conversion values. These terms approach the barotropic and baroclinic analogues in the QG limit of Lorenz (1955), and quantify the degree of local horizontal shear and baroclinic instability processes that generate eddies in our model. We show these terms in Fig. 2.9 for the LFLS case $S_{200}r_{1.7}F_{100}$ and the LFHS case $S_{400}r_1F_{100}$, with a fixed friction $\hat{r} = 0.17$, so the effects of friction are controlled for a fair comparison between two different sill heights. Note the axes of this and the next two figures (Figs. 2.9–2.11), which we show in a zoom view of the domain.

The LFLS panels in Fig. 2.9 show that both the barotropic and baroclinic eddy energy sources are concentrated close to the western boundary sill maximum. The horizontally-integrated energy production is approximately 40% barotropic and 60% baroclinic, with a small region of intense negative barotropic conversion just before a localized peak in baroclinic conversion. Due to the sill, the bottom layer domain-integrated dissipation (calculated from the non-conservative terms in the thickness-weighted momentum equations from Aiki et al. 2016) accounts for 2/3 of the total energy dissipated, while the top layer accounts for the remaining 1/3, since the bottom layer is more strongly eddying and the EKE dissipation by friction is roughly proportional to the EKE itself.

2.6 Low-Friction, High-Sill (LFHS) Regime ($\hat{r} \ll 1$, $\widehat{H}_{\mathbf{Sill}} = \mathcal{O}(1)$)

2.6.1 Varying Sill Height

Increasing the sill height causes the boundary current velocities to increase, which strengthens the eddy intensity, as shown in Fig. 2.6. However, the bottom layer thickness decreases, so the vertically integrated transport and energy conversions generally decrease. The dynamics of the separation region of the western boundary current near the sill maximum change

in structure and as seen in Fig. 2.2, the transport variability increases for intermediate sill height, and then decreases for the tallest sills. Fig. 2.6 shows the bottom layer relative vorticity ζ_2 snapshots for varying sill height. Although it is not clearly observed in Fig. 2.6 why transport variability first increases, then decreases as a function of increasing sill height, the western boundary current reaches the furthest extent (south) past the sill maximum in the $\widehat{H}_{\text{Sill}} = .45$ case and exhibits the greatest magnitude oscillations in the boundary current separation location. The tallest sill cases exhibit similar vorticity peaks (with eddies that scale with L_d), but compared with intermediate sill heights, the eddy energy generation is reduced. In the rightmost two panels of Fig. 2.9, both the barotropic and baroclinic eddy energy production rates decrease by about 20% as the sill height increases from 200 m to 400 m. The conversion partition between C_{BT} and C_{BC} stays relatively constant over this range of sill heights, but C_{BT} is more dominant for sill heights below 150 m.

Increasing the sill height also decreases the water column thicknesses at the sill maximum substantially, and most of this decrease occurs in the bottom layer. Therefore, the minimum width of boundary currents, which scales as L_d at the sill maximum, decreases from approximately 4 km (low sills) to 2 km (tall sills). In order to achieve the same amount of geostrophic transport, velocities in the boundary current must increase. This acceleration of the boundary current proceeds as we increase the sill height (decrease the bottom layer thickness) until shocks form.

2.6.2 Shock Formation

Shocks (or hydraulic jumps) are sharp interface gradients that arise when wave steepening due to nonlinear propagation occurs faster than any counteracting wave dispersion or dissipative processes (Helfrich et al., 1999). We observe the existence of standing shocks in our LFHS cases (defined here as the isopycnal steepness in a localized region of width L_d exceeding the average isopycnal tilt by an order of magnitude). These conditions occur for $\widehat{H}_{\text{Sill}} \geq 0.45$, which coincides with velocities that exceed the baroclinic gravity wave speed

$\sim \sqrt{g'h_2}$ and lead to a reduction in transport (discussed in Sect. 2.7).

For the highest sills $\widehat{H}_{\text{Sill}} \geq .73$, the amplitude of the standing shocks can be on the same order as the bottom layer water column thickness, leading to grounding of the interface between the two density layers. In the model this manifests as a Salmon layer with thickness $h \sim \mathcal{O}(h_{\text{sal}})$. The layer-grounded region is generally localized and occurs along the bottom layer western boundary current just downstream (or upstream for high enough sills) of the sill maximum in the highest sill cases. We show an example of this in Fig. 2.10.

Shocks and as a subset, layer-grounding, occur when the flow is critical at the sill maximum. We define criticality using the composite Froude number G (Pratt and Whitehead, 2007) as

$$G^2 = Fr_1^2 + Fr_2^2\,, \tag{2.29a}$$

$$\text{where } Fr_n = |\mathbf{u}_n|/\sqrt{g'h_n}\,. \tag{2.29b}$$

There are additional criteria for the criticality of flows with generalized PV (Stern 1974, Pratt and Whitehead 2007), which have an associated necessary, but not sufficient condition that G must be unity for some value in the range $-W/2 < x < W/2$. However, this condition is incomplete since this indicates at least one, and not necessarily all, of the wavemodes are arrested. Since the dynamics in the wide channel case are primarily localized to a boundary layer of width $L_d \ll W$, the integral relation to determine the critical condition should be calculated within this boundary layer. Furthermore, since the relevant waves here are Kelvin waves, which are entirely arrested at criticality within this boundary layer (with a dominant contribution from the bottom layer), an appropriate measure in our case for criticality is the maximum value of G since the transport, waves, and shocks are localized to the boundary layer where the velocity reaches a maximum. For grounded layers, the internal wave speed changes due to the modification of the potential energy by the Salmon layer term (Salmon, 2002). However, this is still a reasonable approximation for the criticality of the boundary current flowing around the grounded region.

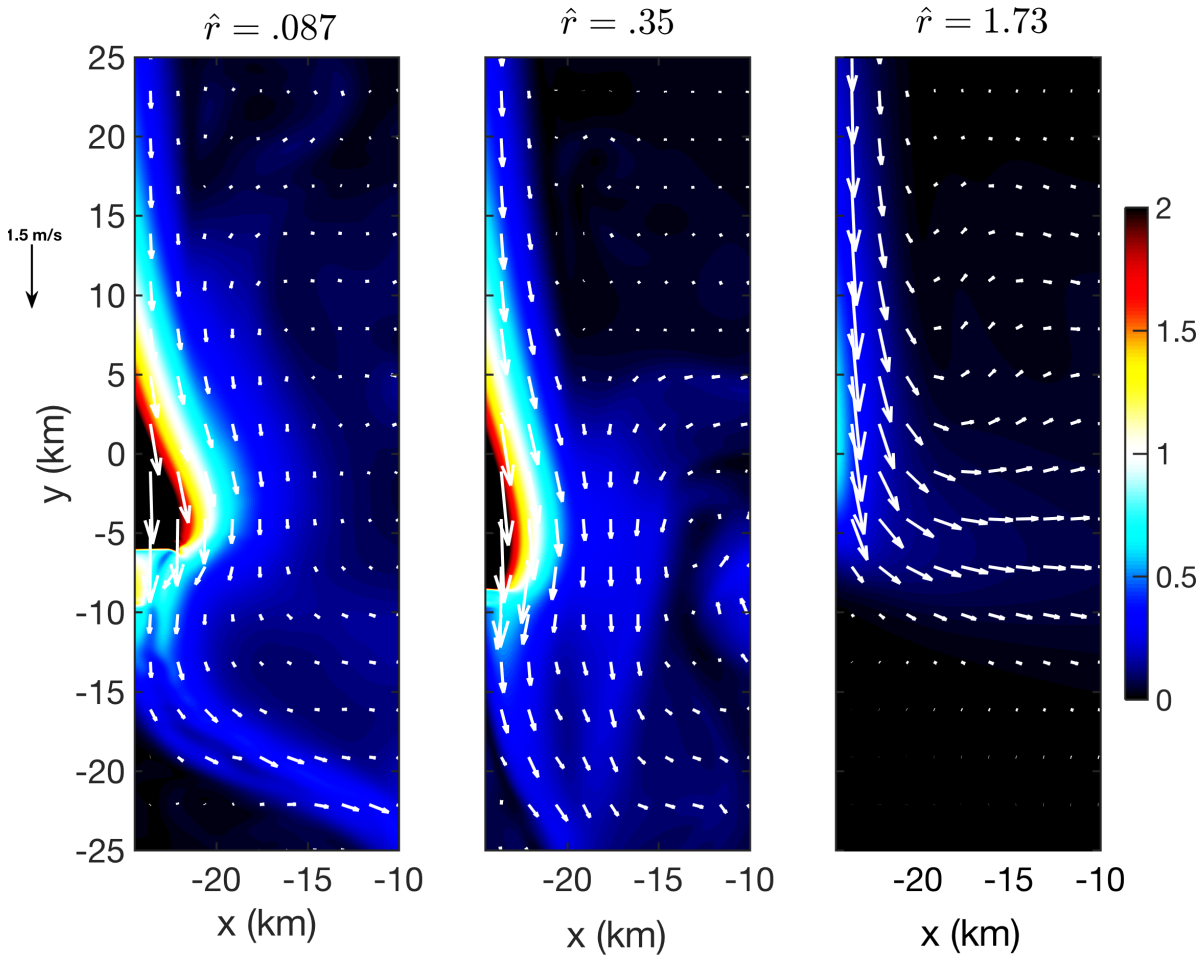

Figure 2.11: Zoom view of composite Froude number G for varying friction and fixed sill height $\widehat{H}_{\text{Sill}} = 0.73$ for cases $S_{400}r_5F_{100}$, $S_{400}r_{20}F_{100}$, and $S_{400}r_{100}F_{100}$, averaged over 100 days. This shows that shocks form as we move towards the LFHS regime. The transport is unaffected by decreasing friction, as previously shown in Fig. 2.2, but the flow profiles change significantly, especially near the separation region. The thickness-weighted average velocity vectors are shown in white for each case.

In Fig. 2.11, we plot G in the vicinity of the sill maximum for three different values of $\hat{r}$. In these runs, the standing shocks appear along the western boundary and have widths of order L_d with background currents with velocities similar to internal gravity wave propagation $\sim$ 1 m/s, as shown in Fig. 2.10. This suggests they are Kelvin wave shocks i.e. shocks that are formed from Kelvin waves that are arrested and reach criticality within the boundary layer (Federov and Melville 1996, Hogg et al. 2011). Kelvin wave shocks have been observed in previous numerical simulations (Pratt et al., 2000) and attempts to produce them in laboratory conditions have been made (Pratt, 1987).

In our LFHS cases, we find that the meridional velocities are much larger than the zonal velocities near the shock region, similar to the dynamics in the western boundary layer before reaching the shock. The velocity field near the shock is approximately semigeostrophic (not shown), i.e. meridional velocities across the shock are in near geostrophic balance (with small frictional and Salmon layer contributions), while the zonal momentum balance has a leading-order advective contribution.

Even though the boundary current mainly flows around the separated region for these wide channel cases, we find that the bathymetric form drag of the shock acts to reduce the overall transport. The influence of form drag on the transport is further discussed in Sect. 2.7.1.

The small transport contribution within the grounded region is due to the Salmon layer, discussed in Sect. 2.2.2. The Salmon layer term in the region where the bottom layer $h_2 \sim \mathcal{O}(h_{\text{sal}})$ is important, otherwise the bottom layer would be grounded. The role of the modified potential energy of the Salmon layer can be estimated from the momentum budget using geostrophic balance (accounting for bottom friction). The Salmon layer term is largest for the region of separation seen in Fig. 2.11. Also, the integrated effect of viscosity on energy is insignificant, but can be important locally in small regions near layer-grounding, shocks, and western boundary currents for the lowest friction cases. However, the velocity fields remain smooth across the shocks and the transport within the Salmon layer is not significant.

The positive vorticity region south of the sill coincides with the location of separation of the western boundary current and elevated barotropic conversion shown in Fig. 2.9. The location of the shock oscillates meridionally along the western boundary with period of days and distance $\sim L_d$ (not shown) accompanied by an increase in amplitude for shocks that are further south of the sill. The amplitude of the shock and its meridional oscillation distance both increase as friction decreases. The strength of the oscillatory motion decreases for sills higher and lower than $\widehat{H}_{\text{Sill}} \approx .45$, which is consistent with the peak in RMSD transport shown in Fig. 2.2 and combined EKE generation in Sect. 2.5.2 for intermediate sills.

Since a steady-state viewpoint of the existence of Kelvin wave shocks appearing under critical conditions necessarily involves hydraulic control, we discuss the theory involved and how this influences the cross-sill exchange in the next section.

2.7 Constraining Cross-Sill Exchange

In Fig. 2.2, transport is shown to be insensitive to friction, while sill height significantly reduces transport for $\widehat{H}_{\text{Sill}} > .45$. The quasi-geostrophic transport in Eq. (2.9) accurately predicts the transport for the LFLS and to a lesser extent, the HF cases. The small difference between our observed results and the geostrophic prediction is primarily due to the observed pressure head $H_2^N - H_2^S$ deviating slightly from the prescribed forcing $\Delta H_2 = 100$, which is affected by the choice of nudging timescale τ_h.

Additionally, the central gyre-like recirculation strength (which varies proportionally with the western boundary current) increases for low-friction cases, whose strength reaches 3 times the total transport for the lowest friction case (shown in Fig. 2.7). There are also weaker gyre-like recirculations that develop in the northern and southern regions of the domain in response to the central gyre and connect it to the nudged regions in Fig. 2.7. The existence and strength of the gyre depends on a cross-isobath PV flux (unknown a priori), which is balanced by frictional vorticity destruction. However, the overall transport is approximately

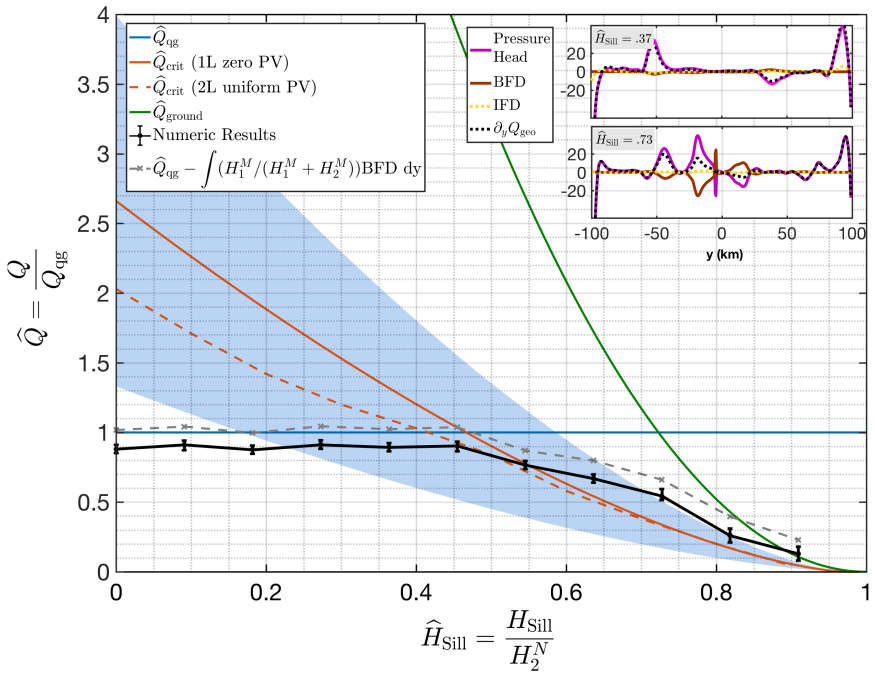

Figure 2.12: Theoretically-predicted transport based on quasi-geostrophic (Eq. (2.9)), critical, and grounded conditions, compared with time-averaged transport from our numerical simulations (with a gray, dotted line including only the BFD term in Eq. (2.6)) with weakest friction $r = 1 \times 10^{-5}$ m/s, which corresponds to $\hat{r} \approx .01$. The insets show the zonally-averaged terms in Eq. (2.6) for a LFLS and LFHS case. The weakest friction cases are used since the theory is based on the limit of zero friction. Here, the critical condition refers to the maximum exchange flow according to hydraulic control theory using rotating 1-layer zero PV theory (see Eq. (2.31)), and rotating 2-layer uniform PV theory discussed in Appendix D. The blue wedge indicates the uncertainty due to the width of the current calculated using a spread of $w = L_d \pm L_d/2$ for the rotating 1-layer zero PV theory, as it does not describe the cross-channel structure of the boundary layer. The grounded condition Q_{ground} approximates the maximum boundary layer transport before grounding occurs at the western wall and is derived in Appendix E. The transport adheres to the quasi-geostrophic constraint for lower sills and the critical constraint for high sills, with a transition where the predictions intersect.

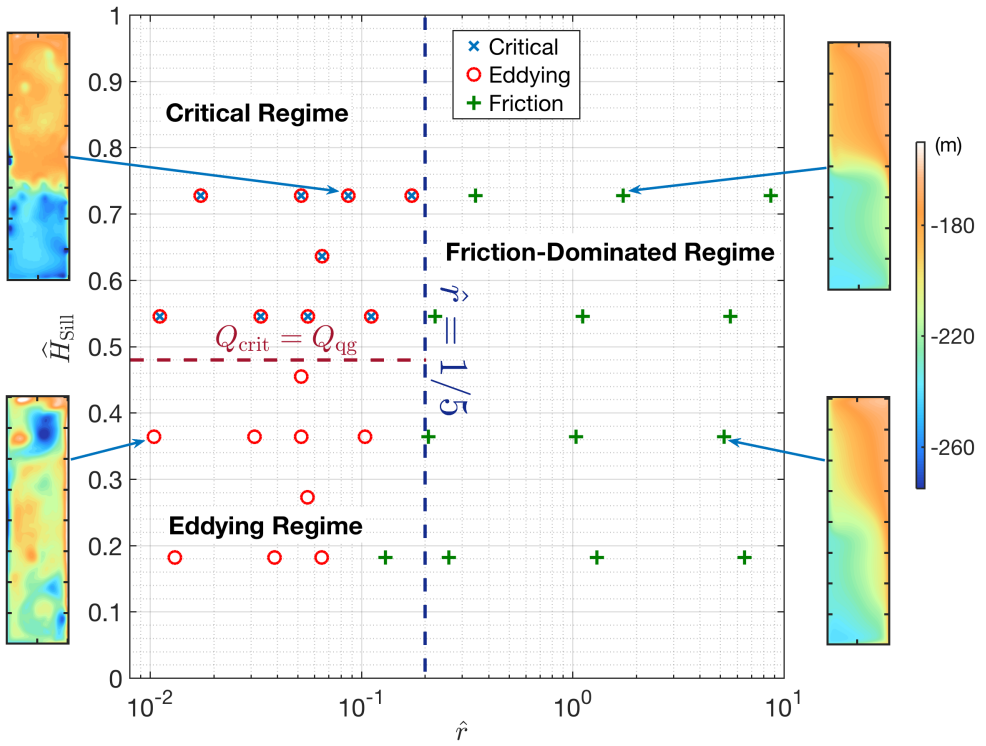

Figure 2.13: Diagram of the three regimes discussed in Sects. 2.4 – 2.6 over nondimensionalized friction and sill height with insets showing illustrative snapshots of the interface elevation η. The numerical runs were categorized into these three regimes with different markers, as shown in the legend. The critical regime is classified as having a maximum composite Froude number $G^2 > 1$ in the domain, while the eddying and friction-dominated (subcritical) regimes are distinguished by the domain-integrated thickness-weighted PV balance being dominated by eddy PV fluxes and frictional torques, respectively in Eq. (2.25). An analytical prediction is also shown for the critical boundary (red line) $Q_{\rm crit} = Q_{\rm qg}$ (based on Eq. (2.31)) and the eddy-friction boundary (blue line) where $\hat{r} = 1/5$, chosen empirically. The insets show that eddies and sill heights have substantial effects on the interface depth, which are plotted in the usual xy domain as in Figs. 2.3-2.8.

determined by only the forcing strength and the sill height, which leads to the difference in recirculation and overall transport.

The timescale needed to establish the total transport is on the order of tens of days (a few recirculation timescales, which is defined by the approximate time the current takes to cross from the northern to the southern boundary), while the western boundary current/recirculation strength takes hundreds of days to achieve equilibrium (a few residence timescales, not shown). In ice shelf cavities, the boundary layer transport influences the gyre-like recirculation strength, while the overall transport exerts a more direct control on the heat flux brought to the ice sheet (ignoring mixing processes, which may be important).

2.7.1 Hydraulic Control Theory

In this section, we test 3 different theoretical constraints for the cross-sill transport against the numerically diagnosed transports. These theoretical predictions rely on a steady-state analysis in the limit of no friction, often used for hydraulically-controlled flows. Our aim is to predict the LFHS cross-sill exchange, which is important since the net cross-sill exchange most directly relates to basal melt.

The theory of hydraulically-controlled oceanic flows was established on the grounds of comparing oceanic abyssal flows between deep basins separated by bathymetric ridges to similarly controlled flow states in dams and reservoirs (Whitehead et al., 1974). A key characteristic of hydraulically-controlled exchange flows is that the flow dynamics can be expressed in terms of one controlling parameter, e.g. bathymetry, using appropriate approximations to derive an analytical solution for the steady-state flow. Here we use classical rotating hydraulic control theory under simplifying assumptions i.e. 1-layer zero PV and 2-layer uniform PV (Whitehead et al. 1974, Gill 1977, Pratt and Armi 1990), to understand the dynamics of idealized glacial cavity circulation. For the simplest case of one-layer flow with a free surface, assuming slow variations of the flow in the along-channel direction (Pratt and Whitehead, 2007) leads to a system of three equations (geostrophy in the cross-channel

direction i.e. semigeostrophy, uniform PV, and Bernoulli equations),

$$v = \frac{g'}{f} h_x \,, \tag{2.30a}$$

$$\frac{f + v_x}{h} = \frac{f}{H_\infty} \,, \tag{2.30b}$$

$$g'(h + h_B) + \frac{v^2}{2} = \frac{f\psi}{H_\infty} + g' H_\infty \,. \tag{2.30c}$$

The three unknowns are (v, h, ψ), and H_∞ is the layer thickness infinitely far upstream (assumed to be infinite for zero PV). The Bernoulli equation is derived from the Bernoulli function being conserved along streamlines (ψ =constant) for a steady flow.

Assuming most of the flow is contained within the boundary layer current, we estimate the cross-sill exchange based on a boundary layer of fixed width $L_d \approx L_d^N$. We find the prescribed transport that leads to the flow reaching criticality at the sill maximum, which may be used as an estimate for the transport necessary to establish control as a function of H_{Sill}. The analytically predicted critical transport according to 1-layer zero PV, rotating hydraulic control theory (Pratt and Whitehead 2007) is

$$Q_{\text{crit}} = w\sqrt{g'} \left(\frac{2}{3} \left[H^N - H_{\text{Sill}} - \frac{f^2 w^2}{8g'} \right] \right)^{3/2} \,, \tag{2.31}$$

where w is the width of the flow, yielding a simple expression that captures the first-order dynamics of critical flow.

We also derive a more comprehensive critical transport estimate for a rotating 2-layer uniform PV assumption within a fixed width $w = \mathcal{O}(L_d^N)$ boundary layer and transport that occurs entirely within the lateral boundary regions. We present a derivation of the rotating 2-layer uniform PV solution in Appendix D.

For the highest sills, we can also predict the transport required for layer-grounding to occur, by considering a 1-layer uniform-PV boundary layer of dynamic width $w_{\text{BC}}(y)$. This provides an analytical solution for the boundary layer width as a function of bathymetric height $w_{\text{BC}}(h_B)$, and is discussed further in Appendix E. For the high-sill cases, this predicts the transport required for layer-grounding.

We compare the geostrophic, rotating 1-layer zero PV, rotating 2-layer uniform PV, and dynamic width transport estimates to the numerical results in Fig. 2.12. This shows that even the rotating 1-layer zero PV version of the theory is reasonably accurate, particularly in the LFHS regime, since the Froude number in the bottom layer is generally much larger than the top layer Froude number for higher sills $Fr_1 \ll Fr_2$. Both the rotating 2-layer uniform PV and the rotating 1-layer zero PV transport estimates assume no friction, so they are well suited to the LFHS regime.

For low sills, the transport matches the quasi-geostrophic scaling (Eq. (2.9)) and decreases when critical conditions are reached. The quasi-geostrophic scaling regime applies when the sill does not strongly affect the circulation strength and is also an upper bound that slightly overestimates the transport. One factor that accounts for this overestimation is the boundary nudging, which establishes a North-South interface gradient slightly smaller than the prescribed $\Delta H_2 = H_2^N - H_2^S$. Even though the flow profiles in low-sill cases may be somewhat modified by the sill, the sills do not control the transport imposed by the boundary conditions.

For intermediate sill heights where $\widehat{H}_{\text{Sill}} > .45$, the observed transport decreases with the trends predicted by 1-layer and 2-layer theories. We use a spread of $L_d^N/2$ in the boundary layer width used to calculate the solution to the 1-layer zero PV case, since the width of the boundary layer changes by a factor of ~ 2 with varying sill height. Given that the actual flow is unsteady and a uniform PV assumption is made, we do not expect these solutions to match the predictions perfectly. However, the predicted sill height necessary for critical flow (as defined in Sect. 6b) is $\widehat{H}_{\text{Sill}} > 0.48$ for the 1-layer zero PV theory, $\widehat{H}_{\text{Sill}} > 0.41$ for the 2-layer uniform PV theory, which is consistent with the numerical result showing $\widehat{H}_{\text{Sill}} > 0.45$. The theoretical prediction for the transition between critical and eddying regimes is defined as the sill height H_{Sill} for which the geostrophic transport is predicted to become critical $Q_{\text{qg}} = Q_{\text{crit}}$ from Eq. (2.31). While the theory captures the overall drop-off in transport beyond $H_{\text{Sill}} = 0.45$, there are still substantial differences, e.g. up to a factor of 2 difference

between theory and simulation, and different functional dependencies on H_{Sill}.

An alternative way of understanding the transport reduction is that for LFHS cases, the flow becomes asymmetric across the sill and produces appreciable form drag terms, that were previously assumed to be small in Eq. (2.6). The bathymetric and interfacial form drags contribute to the balance of the along-channel pressure force due to the imposed horizontal stratification, and thereby reduce the zonal (cross-sill) transport. The interface has approximate rotational symmetry in the HF cases, but does not in the LFLS cases. In both these cases, the interface does not exhibit large vertical excursions unless a shock forms, which is necessary for an appreciable form drag.

We calculate the relative contribution of transport reduction by IFD and BFD. The gray, dotted line in Fig. 2.12 shows $\widehat{Q}_{\mathrm{qg}} - \int (H_1^M/(H_1^M + H_2^M))\mathrm{BFD}\ \mathrm{d}y$, for Q_{qg} and BFD defined in Eq. (2.6), which demonstrates that the pressure head transport term is primarily balanced by the transport reduction due to BFD for the LFHS cases, while IFD and other non-conservative terms reduce transport by approximately 15% for all cases. A zonally-averaged breakdown of the terms in Eq. (2.6) is also provided in Fig. 2.12 for a LFLS and LFHS case and shows that the pressure head transport is the dominant term for lower sill heights and both pressure head transport and BFD terms are dominant, partially-canceling terms for taller sills.

2.7.2 A Regime Diagram for Cross-Sill Circulation

Based on the dynamical regimes discussed in the preceding sections, we now characterize the regimes of cross-sill flow over the entire parameter space of nondimensionalized friction and sill height parameter space in Fig. 2.13, which includes representative snapshots of the instantaneous bottom layer thickness. This diagram summarizes the three regimes that have been discussed in Sects. 4 – 6 and the analytical predictions and numerical results that define the regime boundaries.

We empirically classify each individual simulation, which is represented as a point on the regime diagram, as critical if the maximum composite Froude number satisfies $\max(G^2) = \max(Fr_1^2 + Fr_2^2) \geq 1$. We choose this boundary based on the success of hydraulic control theory in predicting the transition between geostrophically-constrained and hydraulically-controlled transport in Sect. 2.7.1. The analytical boundary between critical and eddying regimes (red dotted line in Fig. 2.13) is defined based on the theory in Sect. 2.7.1, which is consistent with the numerical classification based on the maximum composite Froude number.

Similarly, we classify individual simulations as eddying or friction-dominated based on the thickness-weighted PV equation (2.25). When the ratio of the friction to eddy terms spatially-integrated and time-averaged over the last 100 days of the run exceeds 1 ($-\iint \nabla \times \overline{(r\mathbf{u}_n/h_n)}\, dA / \iint \nabla \cdot [\overline{h}_n \langle \mathbf{u}_n^\dagger q_n^\dagger \rangle]\, dA \geq 1$), we classify the point as friction-dominated based on our findings in Sect. 2.4. We define the theoretical boundary between friction and eddying regimes as $\hat{r} = L_{\mathrm{St}}^*/L_d^N = 1/5$ (blue dotted line), which we choose empirically. The theoretical and numerical classifications for the friction and eddying regimes agree approximately, but exhibits some disagreement at lower sill heights. This is due to limitations of Stommel theory for intermediate friction, which is plausible since the theory in Sect. 2.4 primarily applies for asymptotically large $\hat{r}$. The constant value of 1/5 validates the assumptions made in deriving the scaling argument in Eq. (2.23) since $\hat{r}$ is constant over varying sill height and $\mathcal{O}(1)$.

We note that there is no explicit prediction for the boundary between the critical regime and the friction-dominated regime since friction does not have a strong effect on the transport, as discussed in Sect. 2.3. However, we have extended the $\hat{r} = 1/5$ boundary line between the critical and friction-dominated regimes based on experimental evidence and the definition for $\hat{r}$, which takes into account the varying sill height.

2.8 Summary and Discussion

In this chapter, we model the dynamics of ocean circulation in sill-impeded sub-shelf cavities, motivated by the fast-melting PIG (Jenkins et al. 2010, Dutrieux et al. 2014). To investigate the dynamics, we simplified the problem to a 2-layer diabatically-forced circulation with a simple channel geometry overlying a bathymetric sill. Our numerical solutions exhibit a variety of phenomena, including Stommel boundary layers, gyre-like circulations, eddies, hydraulic shocks, and layer-grounding.

This chapter demonstrates that friction and sill height have important controlling effects on the flow structure and variability of the flow in a simple buoyancy-forced flow. Increasing the friction does not strongly influence the transport, but decreases the variability. The transport under ice shelves is approximately geostrophic and generally controlled by pressure head and local water mass transformations due to the interaction with the ice base, except when the sill height begins to impede the flow. In the case of the PIG, this occurs for pycnocline depths $H_2^N \sim 550$ m and pressure head $\Delta H = 100$ m, which are comparable to values observed in the PIG ($H_2^N = 500$ to 600 m, $\Delta H = 100$ to 200 m, based on Dutrieux et al. 2014). The transport and variability as a function of friction, sill height, and pressure head suggests a division of the parameter space into 3 separate regimes: HF, LFLS, and LFHS.

The theory for the HF regime provides an analytical solution for the flow profile and western boundary current over the sill, which narrows with larger β_{topo}, and exhibits sill crossing at the sill maximum due to a sign change in β_{topo}.

In the LFLS regime, barotropic/baroclinic eddies are abundant in the cavity, and reshape the flow into gyre-like circulations with strong inertial western boundary currents. We showed in Sect. 2.5.1 that the inertial boundary layer and eddy PV fluxes, rather than friction, facilitate flow across the sill-imposed PV gradient. The central gyre-like recirculation does not reach the northern and southern nudged boundaries, but may still be important

for diabatic mixing processes in the interior especially over the sill maximum (which may indirectly contribute to the heat transfer into and out of the domain and locally increase the heat exchange at the ice base).

In the LFHS regime discussed in Sect. 2.6, standing shocks emerge in the numerical solutions when the flow reaches criticality, and either an increase in sill height or a shock amplitude increase due to low friction can lead to layer-grounding. The composite Froude number provides justification of the shock the shock as an arrested Kelvin wave for the lowest friction cases.

The HF and LFLS cases generally exhibit a constant transport predicted by QG, while in the LFHS regime, the transport is sill-constrained and is reduced in accordance with hydraulic control theory. A regime diagram (Fig. 2.13) summarizes the HF, LFLS, and LFHS regimes. The dynamics of various glaciers in Antarctica and Greenland may be studied with their position in the regime diagram in mind. Specifically, the latest measurements in the PIG suggest that the sill-controlled circulation is in the LFHS critical regime, based on microstructure estimates that suggest $\hat{r} \sim \mathcal{O}(0.1)$, as briefly discussed in Sect. 3 (Kimura et al. 2016). The results from the bottom circulation in a high-resolution model of the PIG cavity (Dutrieux et al., 2014) and a process model with additional dynamics (De Rydt et al., 2014) are also qualitatively similar to our results from low-to-intermediate friction $0.1 < \hat{r} < 1$ and those with quadratic friction (Appendix A). All of these show an inflow that crosses the sill from West to East close to the sill maximum and exhibit similar gyre recirculations.

For ice shelf cavities, an additional way for flow to cross mean PV contours in the absence of eddies and bottom friction is lateral friction against the side-walls (e.g. Little et al. 2008), but typically the depth tapers to zero at lateral boundaries in an ice shelf cavity (Kimura et al., 2016) and the top/bottom friction becomes dominant instead. The importance of lateral friction for each scenario can be formally calculated by finding its associated boundary length scale and comparing with L_d and L^*_{St}, as discussed in Sect. 2.4.3. Also, the evolution

of glaciers as they melt may generally allow the behavior of ocean circulation to change across different regimes. For hydraulically-controlled circulations, the ice shelf cavity potentially evolves in a way to favor the development of controlled states. These states may be preferred since they provide the greatest exchange of warm water masses carrying heat to the ice shelf for a specified geometry. The existence of bathymetry acts to reduce the transport, so it is generally less than the geostrophic transport.

Given the transport and L_d^N, this also has implications for the ice-ocean heat flux if the transport is geostrophic. Based on this fixed transport, the total water mass transformation in the interior and ice-ocean heat flux may be calculated using the water mass properties of the exiting shelf water. Using the geostrophic transport as an estimate of ocean circulation in ice shelf cavities, we can calculate the residence time of the water masses as a function of the pressure head corresponding to $\tau_{\text{res}} = W \cdot L \cdot H/Q_{\text{qg}} \approx 3$ months for the PIG, based on $Q_{\text{qg}} \approx 0.4$ Sv from Jenkins et al. (2010). If the time-averaged stratification H_2^N at the ice shelf cavity entrance is small enough to allow the sill to constrain the transport, our hydraulic control estimate predicts a transport of ≈ 0.24 Sv for the choice of forcing $H_2^N = 550$ m used in this chapter (based on Jacobs et al. 2011), which yields $\tau_{\text{res}} = 5$ months. These estimates do not take recirculations into account (see Borenas and Whitehead 1998), which may be significant for low-friction cases. It is also likely that in the presence of large external variability, the total transport is more likely to be able to respond to external variability. See Holland (2017) for a discussion of the importance of circulation residence times on glacial melt rates.

Although this chapter is primarily motivated by the hydraulically-controlled sill under an ice shelf cavity in the PIG, the regimes observed in Fig. 2.13 can also be generalized to many more sill-influenced exchange flows. Specifically, the top layer friction does not strongly influence the regime diagram, since this layer is weakly modified by the sill and exhibits much weaker velocities (the composite Froude number is dominated by the bottom layer unless the top layer is much shallower). Therefore, these results can be directly applicable to scenarios

with a free surface in open-ocean, wide sill overflows with similar stratifications such as the Denmark Strait and the Faroe-Bank Channel (Pratt and Whitehead, 2007), among many others.

Given the highly idealized nature of the chapter, there are numerous caveats associated with our results. In addition to geometric simplifications and quadratic friction (discussed in Appendix A), there is no direct representation of ice-ocean thermodynamic interactions, no tidal flows, and no tidal mixing in the cavity. Also, the numerical model implements an advection and spatial discretization scheme that is not optimized for the study of shocks. However, with high horizontal and temporal resolution, and an observed steadiness in shock location, we are able to resolve these features with improved accuracy. Layer-grounding is treated in a special way in our simulations using Salmon layers, which prevent instabilities involving layer-grounding.

2.9 Conclusions

Our results corroborate well with previous modeling studies with idealized geometry (De Rydt et al. 2014, De Rydt and Gudmundsson 2016), and our idealized posing and high-resolution sweep over the key dimensionless parameters, allowing an exhaustive exploration of the dynamics. Based on this chapter, there are direct implications for future observations under ice shelves. These predictions may be used to guide measurements of the flow properties in ice shelf cavities and look for western boundary currents and shocks that may cause large diabatic fluxes, observable in western boundary currents downstream of the sill maximum. Such a region is likely to be a location of elevated mixing due to the sharp isopycnal tilt that forms when the bottom layer thins as it flows over the sill. The thinness of this layer and measured transport should have an influence on the magnitude of the shock amplitude and therefore, the turbulent mixing of subglacial water masses. Enhanced mixing near the sill is also likely to cause dynamical feedbacks, i.e. when an initial pressure head inducing a

circulation bringing heat towards the ice shelf causes increased water mass transformation, this further increases the pressure head. Measurements indicate that melting is concentrated close to the grounding lines (Dutrieux et al., 2014), but that it is non-negligible elsewhere and the influence of that melt on the circulations we have explored remains to be investigated. Also, the importance of the missing surface forcing is important in nudging the stratification in otherwise more weakly stratified cases, but has not been considered in this chapter.

CHAPTER 3

Circulation in Idealized Glacial Fjords

3.1 Introduction

The melting at the margins of the Greenland Ice Sheet (GrIS) and Antarctic Ice Sheet (AIS) has accelerated in recent years. Near many marine-terminating glaciers in Greenland, the submarine melt rate outweighs the contribution from surface runoff (Straneo and Heimbach, 2013). The postulated main cause of the recent accelerated melting of the GrIS is the warming of the East and West Greenland currents that influence the water mass properties at the termini of tidewater glaciers (Wood et al., 2018). Similar accelerated melting of the AIS is likely due to greater heat fluxes supplied to the ice shelf cavities by the Circumpolar Deep Water currents (Rignot et al., 2013; Cook et al., 2016).

In recent decades, the melting of the GrIS contributed 1 mm/yr in global sea level rise on average and this contribution is accelerating and has the potential to contribute over 7 m total (Pörtner et al., 2019). The West Antarctic Peninsula, which is a small sector of the AIS with glaciers that terminate in fjords, contributes approximately 0.2 mm/yr in global sea level rise (Pritchard and Vaughan, 2007). A major implication of the accelerated ocean-driven melting of marine-terminating glaciers in these two regions is the retreat of ice sheets, which along with calving and other ice sheet processes may lead to thinning of the outward-flowing GrIS and AIS (Seroussi et al., 2011).

Fjords abutting marine terminating glaciers have also been studied in regions other than the GrIS and West Antarctic Peninsula: the Canadian Arctic Archipelago, which is occa-

sionally grouped with the GrIS and accounts for 9% of the freshwater flux anomaly in Baffin Bay (Bamber et al., 2018); the Patagonia Ice Field (Moffat, 2014); Alaska (Sutherland et al., 2019); and Svalbard (Jakacki et al., 2017). In these regions, the fjord circulation has implications for physical and biogeochemical ocean properties and potentially regional ice sheet cover and albedo, but are not important contributors to sea level rise due to the smaller ice sheet volumes.

The oceanic exchange flows between fjords and the continental shelf constrains the ocean-driven melting of the GrIS and West Antarctic Peninsula glaciers. Although progress has been made in understanding the overall sensitivity of ice sheet melt to atmospheric and oceanic forcing (see Straneo and Cenedese 2015 and references therein), the translation of open ocean and fjord conditions to glacial melt rates is not well understood.

To better understand how fjords connect the open ocean to marine-terminating glaciers, recent idealized and regional modeling investigations have explored the constraints of the fjord-to-shelf circulation. Previous studies either use 2D simulations and do not account for rotational effects (e.g., Gladish et al. 2015, Sciascia et al. 2013, and Xu et al. 2012), or use 3D simulations but focus on specific processes such as winds (Spall et al., 2017), coastally-trapped waves (Fraser et al., 2018), and the wave-influenced fjord response to shelf forcing (Jackson et al., 2018). The effect of varying multiple parameters in a 3D fjord setup, e.g., sill height, tides, and wind forcing, was examined in Carroll et al. (2017). This study concluded that sill depth compared to the grounding line depth is a primary control on fjord overturning and renewal, which is amplified by both winds and tides. Carroll et al. (2017) also finds that horizontal recirculation is stronger for wider fjords, which influences the fjord stratification. However, in general, there remains a lack of theoretical constraints to predict the leading-order dynamics of fjord circulation: the fjord-to-shelf overturning circulation and the horizontal recirculation. Many of these previous numerical studies examine the sensitivity of the overturning circulation to various fjord parameters, but horizontal recirculation is rarely discussed and there are no existing theories to predict its strength.

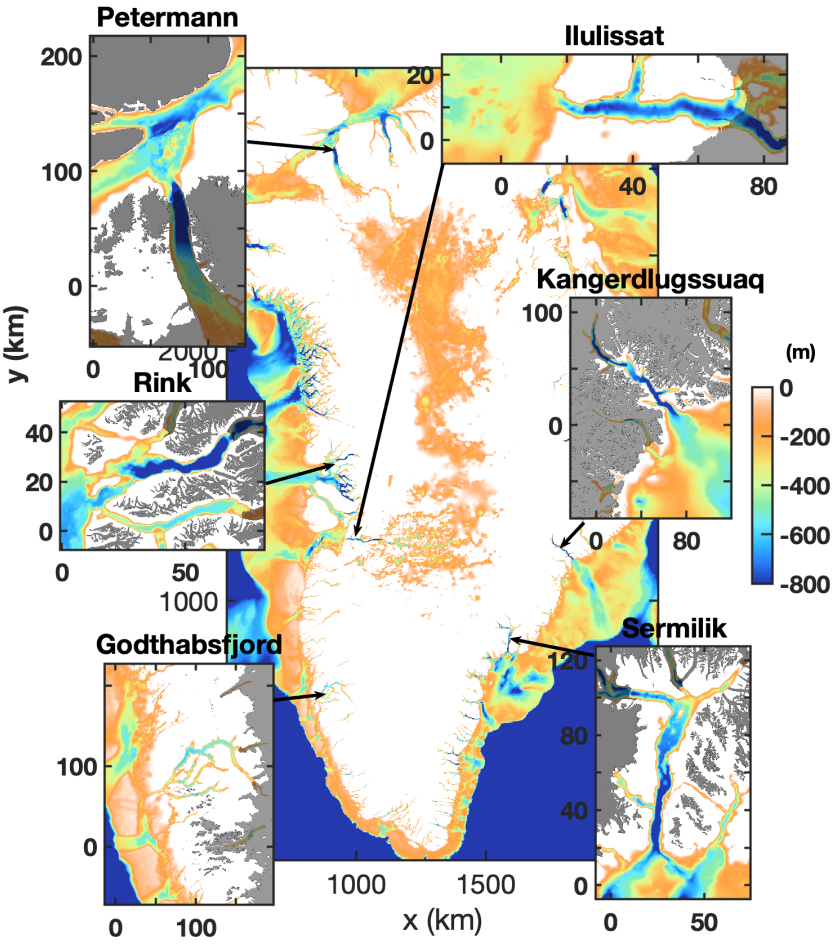

Figure 3.1: Bathymetry around Greenland and zoomed-in panels of six major Greenlandic fjords with ice sheet extent (shown in gray). The data shown is from Bedmachine V3 (Morlighem et al., 2017).

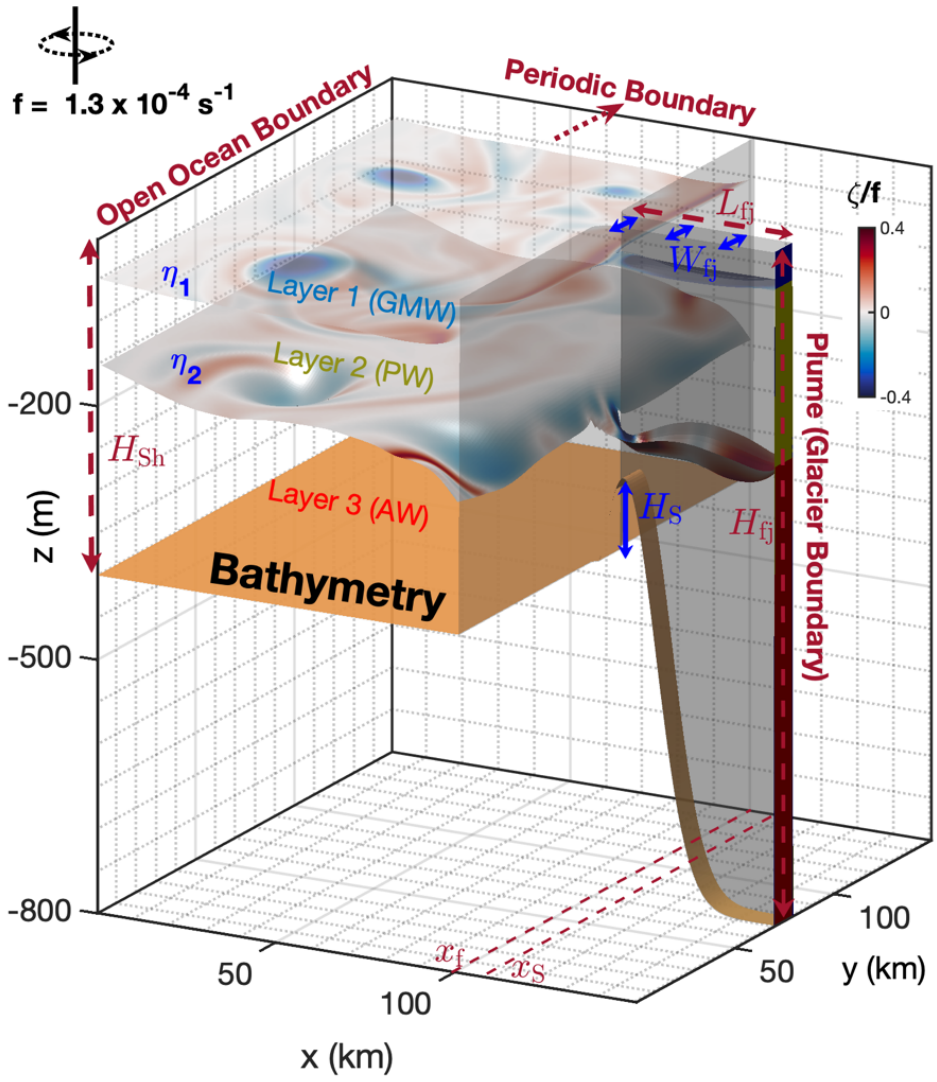

Figure 3.2: Configuration and geometry of our fjord-to-shelf isopycnal model. Snapshots of middle and bottom layer vorticity are displayed on surfaces of interface depth (η_1, η_2) for the reference case with $H_S = 100$ m and $W_{fj} = 8$ km above a surface of bathymetry. The parameters in blue vary between simulations while the parameters in red are fixed. The eastern glacial boundary is coupled to a dynamic plume model which transforms water masses from denser (ρ_3 = red, Atlantic Water) to lighter water masses (ρ_2 = yellow, Polar Water, and ρ_1 = blue, Surface Water) of discrete densities.

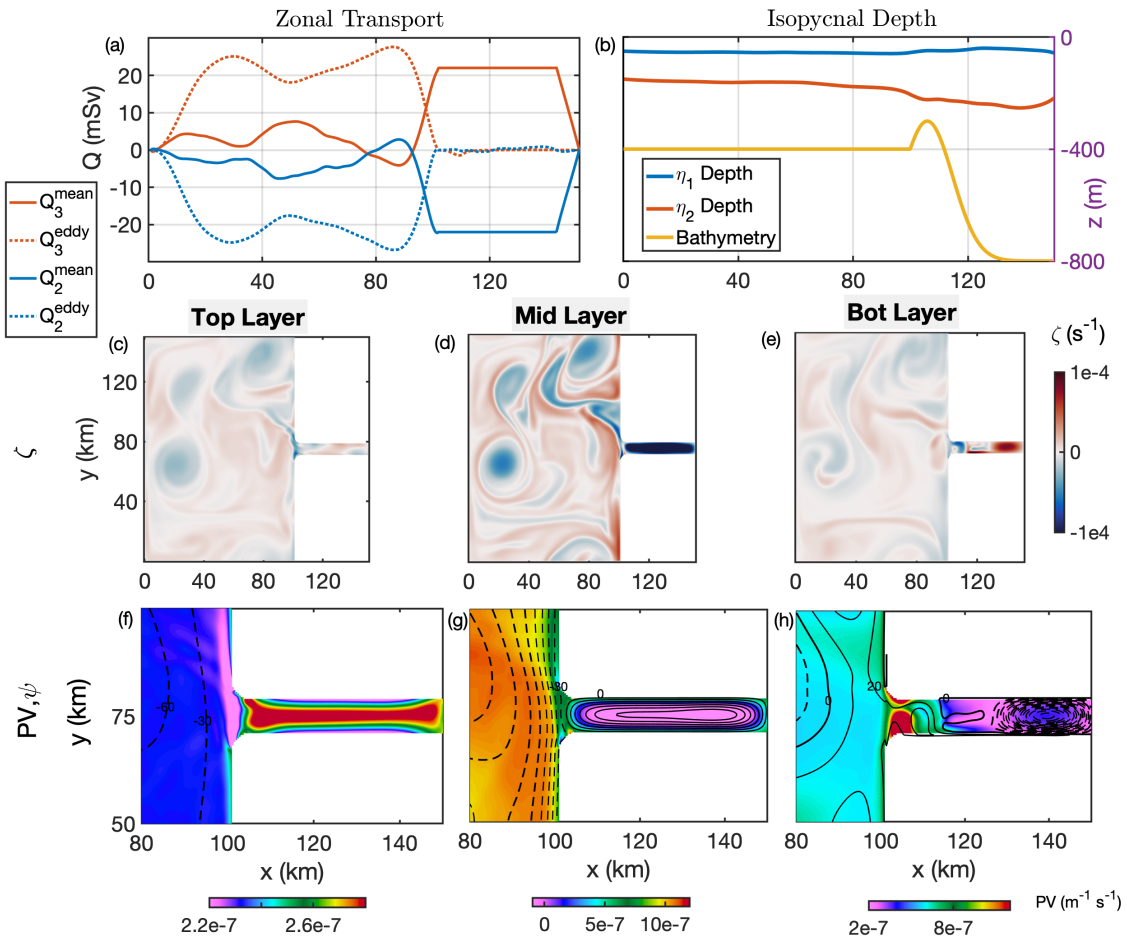

Figure 3.3: Reference case simulation with $H_S = 100$ m and $W_{fj} = 8$ km. (a) Zonal transport decomposed into mean and eddy components based on Eq. (3.7) for the bottom and middle layer (top layer zonal transport is negligible and is therefore not shown). (b) Isopycnal interface depths η_1, η_2 and bathymetry along the midline, y = 75 km. (c)-(e) Snapshots of vorticity for each layer (at day 1600). (f)-(h) Zoomed-in PV (in color) and transport streamfunction for each layer with 30 mSv contours in top and middle layers and 20 mSv contours in bottom layer (dotted line contours are negative values). The fields in the top and bottom rows are time-averaged over days 1300 - 1600.

To fill this gap, in this study we present numerical solutions of an idealized model, supported by dynamical theories of fjord-to-shelf overturning circulation and the horizontal recirculation in the fjord interior. The main difference between this study and its closest predecessor (Carroll et al., 2017) are that it allows the development of a freely-evolving shelf circulation and coastal current which interact with the fjord circulation. Including this requires our model experiments to be run for 5 years to fully equilibrate the shelf circulation and coastal current adjacent to the fjord. We also test additional parameters in the sensitivity experiments to include more parameters of leading-order importance to the fjord overturning and recirculation. This expanded exploration of parameter space allows us to develop and test simple, but comprehensive dynamical theories for the overall fjord-to-shelf overturning circulation and the horizontal recirculation in the fjord interior.

In Sect. 3.2, we present the model configuration and describe the setup and phenomenology of a reference simulation. In Sect. 3.3, we explore the dependencies of the overturning circulation and horizontal recirculation on six key geometric fjord and forcing parameters. In Sect. 3.4, we develop theoretical constraints for the overturning circulation/warm-water inflow in three regions of the shelf-to-glacier-face domain: the continental shelf, the fjord mouth sill, and the fjord head. Piecing together the theories of these three regions yields an overall overturning prediction in terms of the parameters explored in Sect. 3.3, which is supported by the simulation results. In Sect. 3.5, we present a theory for the recirculation strength within the fjord using the vorticity budget, which is also supported by simulations diagnostics. In Sect. 3.6, we discuss additional fjord phenomena observed in our simulations: the onset and effect of hydraulic control at the sill and fjord mouth, low-frequency variability manifesting as periodic fjord flushing, and high-frequency submesoscale variability in the fjord and coastal current. In Sect. 3.7, we discuss the major implications of including the fjord circulation in glacial melt rate estimates, summarize our findings, and provide concluding remarks.

3.2 Idealized Fjord-to-Shelf Model

The design of our model setup is primarily motivated by Greenland's fjords and continental shelf, but the results from the simulations are likely useful towards understanding fjord circulation in the West Antarctic Peninsula and other regions. Fig. 3.1 shows the bathymetry around Greenland with zoomed-in panels of bathymetry and ice-sheet extent near six major Greenlandic fjords that are amongst the most observed (Morlighem et al., 2017).

We aim to capture only a few salient geometric features in our idealized model configuration. They are often long, narrow, deep submerged glacial valleys that connect to continental shelves hundreds of meters shallower. Some fjords have a shallow sill either near the mouth of the fjord or between the fjord interior and the open ocean (Ilulissat, Godthabsfjord, and Petermann are notable examples) and fjord width is typically between 2 and 20 kilometers. The coastal winds vary significantly during the year from katabatic to alongshore winds between 0 to 14 m/s (monthly averages) and 0 to 9 m/s (annual averages), which correspond to monthly-averaged wind stresses up to 0.25 N/m^2 and annual-averaged wind stress up to approximately 0.1 N/m^2 (Lee et al., 2013). Subglacial discharge exits at the base of the glacier and is generally 100s of m^3/s in the summer and nearly zero in winter (Straneo and Cenedese, 2015; Chu, 2014). Areas of elevated mixing within the fjord-to-shelf region are primarily forced by subglacial and ambient melt plumes as they are a dominant mode of mixing for the majority of Greenland's fjords (Carroll et al., 2017; Gladish et al., 2015; Magorrian and Wells, 2016). However, wind-driven mixing in the surface mixed layer (often shallow enough to be ignored for the interior fjord dynamics) and tidal/gravity-overflow mixing near shallow sills (which is outside the scope of this study) are also potentially important contributors.

We note that this simplified fjord-shelf configuration is not intended to fully represent the geometric complexity of Greenland's fjords, but rather to capture a few geometric features that are representative of a number of these fjords. The lack of floating ice shelves, sea ice,

melange, icebergs, canyons, enclosed bays, narrow straits, remotely-generated coastal currents, etc., likely play important roles in individual fjord-shelf systems but are not captured in our simple model configuration. We do not anticipate these factors to qualitatively change our findings although they may be separately important as drivers or controls on fjord-shelf exchange (see Sect. 3.7 for further discussion).

3.2.1 Model Configuration

To capture key aspects of the fjord-to-shelf dynamics, we implement a 3-layer isopycnal model. With this simple model, we aim to include important elements of fjord-shelf dynamics with minimal complexity and computational cost, allowing us to conduct fully-equilibrated (5-year) simulations over a wide parameter space. The model uses 3 density layers for simplicity to represent the Atlantic layer, polar layer, and surface waters that are observed in many Greenlandic fjords (e.g. Gladish et al., 2015; Bartholomaus et al., 2016) and a 3-layer isopycnal model describes the barotropic and first two baroclinic modes while prohibiting spurious diabatic mixing. By comparison, it has been shown that 75 well-positioned vertical layers are typically necessary to adequately resolve the first two baroclinic modes in z-coordinates (Stewart et al., 2017). Observed temperature and salinity profiles within fjords often shown three relatively unstratified layers (compared to the shelf waters), which is captured in the thicknesses of our 3 layers in a discretized and simplified way (Carroll et al., 2016).

In our model configuration, the three layers represent Atlantic Water (AW), which is warmer, saltier, and denser; Polar Water, which is colder, fresher, and lighter; and Surface Water, which is the coldest, freshest, and lightest (see Fig. 3.2). The fjord overturning circulation is modeled as bottom layer AW entering the fjord, which is then converted into either the middle layer Polar Water or the Surface Water layer.

We develop an idealized geometric representation of the region (see Fig. 3.2) from the glacier face to the open ocean (100 km offshore), which captures a few geometric features that

apply to some of the Greenland fjords shown in Fig. 3.1. The The model domain dimensions are $W \times L \times H = 150$ km $\times$ 150 km $\times$ 800 m. The simple model geometry consists of a flat shelf connected to a deep fjord with a Gaussian sill in the x-direction with the maximum at $x_S = 107.5$ km, which is near the fjord mouth located at $x_f = 100$ km. The bathymetric depth is

$$z_B(x) = \begin{cases} \max\{-H_{\rm Sh}, z_S(x)\}\,, & \text{if } 0 < x < x_S \,(\text{shelf region})\,, \\ z_S(x)\,, \text{ if } x_S < x < 150 \text{ km } (\text{fjord region})\,, \end{cases}$$
$$\text{where } z_S(x) = -H_{\rm fj} + [H_{\rm S} + (H_{\rm fj} - H_{\rm Sh})] \exp(-(x - x_S)^2/L_{\rm S}^2) \tag{3.1}$$

The sill has a width scale $L_{\rm S} = 12.5$ km and sill height $H_{\rm S}$ (the amplitude of the sill above the shelf). The shelf has a depth of $H_{\rm Sh} = 400$ m, and is connected to a fjord of depth $H_{\rm fj} = 800$ m, length $L_{\rm fj} = 50$ km, and width $W_{\rm fj}$. Note that $H_{\rm S}$ and $W_{\rm fj}$ are the only geometric parameters varied between our experiments with ranges shown in Table 3.1 (see parameter sensitivity discussion in Sect. 3.3). The shelf is 100 km wide in the across-shelf direction (x) and 150 km long in the along-shelf direction (y) and is periodic in y. The across and along-shelf length scales are fixed and chosen to represent the width of a continental shelf and the choice of a periodic domain represents an average inter-fjord separation distance (approximately 100 to 150 km between one fjord to the next in Fig. 3.1).

The lateral side boundaries of the fjord and coastline are represented as vertical walls due to the horizontal resolution limiting realistic coastal slopes to span only 2-3 horizontal grid-points (1 km), i.e. a bathymetric steepness of 1/2 near the six fjords in Fig. 3.1 (Morlighem et al., 2017). At coarse resolution, such under-resolved coastal slopes would produce spurious results in the boundary currents that emerge. A high-resolution near-fjord configuration with a smaller shelf was tested with both vertical walls and varying side slope steepness (1/4 to 1, not shown) without significant variation in boundary current transport. Using 90$^{\rm o}$ corners at the fjord mouth led to large, spurious sources of vorticity, so we replaced them with quarter-circular rounded corners with radii of 3 km. We also experimented with a

continental shelf slope of width 5 km and steepness 1/10 positioned at $x = 0$ (i.e., extending the Fig. 3.2 domain 20 km offshore to include a shelf and flat deep bathymetry), but found that this did not significantly alter our results.

3.2.2 Model Equations

We use the Back of Envelope Ocean Model (BEOM), which is a publicly available code (St-Laurent, 2018). BEOM is a hydrostatic shallow-water isopycnal model with a nonlinear free surface that simulates rotating basins and allows for layer-outcropping.

We pose our problem as a 3-layer exchange flow over bathymetry on an f-plane using shallow-water momentum and continuity equations

$$\frac{\partial \mathbf{u}_n}{\partial t} + (\mathbf{u}_n \cdot \nabla)\mathbf{u}_n + f\hat{\mathbf{z}} \times \mathbf{u}_n = -\nabla \phi_n + \boldsymbol{F}_{\text{wind},n} - \boldsymbol{F}_{\text{fric},n} + \upsilon \mathbf{S}_n \,, \tag{3.2a}$$

$$\frac{\partial h_n}{\partial t} + \nabla \cdot (h_n \mathbf{u}_n) = \varpi_n \,, \tag{3.2b}$$

for layers $n = 1, 2, 3$. Here, u is the zonal velocity (in the x-direction), v is the meridional velocity (in the y-direction), and the top, middle, and bottom layer thicknesses are h_1, h_2, and h_3. We parameterize the water mass transformation as ϖ, surface and bottom boundary stresses as $\boldsymbol{F}_{\text{wind}}$ and $\boldsymbol{F}_{\text{fric}}$, and eddy viscosity as $\upsilon \mathbf{S}$. We use an f-plane approximation with a representative Coriolis parameter of $f = 1.31 \times 10^{-4}\, s^{-1}$ corresponding to latitudes in central Greenland.

The water mass transformation between the layers occurs at the western (open-ocean) and eastern (plume parameterization) boundaries and is defined as

$$\varpi_n = \begin{cases} -\tau_h^{-1}(h_n - H_n^W), & \text{for } \mathbf{x} \in A_W, \\ \varpi_{n,\text{p}}, & \text{for } \mathbf{x} \in A_E, \\ 0, & \text{otherwise.} \end{cases} \tag{3.3}$$

In the 10 km-wide nudging region at the western boundary, A_W, each layer n is restored to

H_n^W with a nudging strength $\propto \tau_h^{-1}$ for a timescale $\tau_h = 1$ day that decreases linearly to zero in the interior edge of the nudging zone. At the eastern boundary, we parameterize the time-evolving plume-driven water mass transformation as $\varpi_{n,\mathrm{p}}$ using a point plume model (Turner, 1979) applied to the 3-layer density stratification (see Appendix F for the details). We also implemented a line plume parameterization of variable width in our model, which exhibits negligible differences in the water mass transformation for small plume source widths (further discussed in Appendix F). We assume in our model setup that all of the diabatic forcing occurs at the western and eastern boundary and exclude mixing within the domain due to tides and sill overflows.

A wind stress of $\boldsymbol{F}_{\mathrm{wind},n} = \boldsymbol{\tau}/(\rho_n h_n)$ is imposed in the highest layer n with non-negligible thickness ($h_n > 0.5$ m) with $\boldsymbol{\tau} = (\tau_x, \tau_y)$. Bottom friction is parameterized by a quadratic drag $\boldsymbol{F}_{\mathrm{fric},n} = C_d {h_n}^{-1} |\mathbf{u}_n| \mathbf{u}_n$ with $C_d = 2.5 \times 10^{-3}$ and only acts in the lowest layer n with non-negligible thickness ($h_n > 0.5$ m). In numerical calculations, we control grid-scale energy and enstrophy using a thickness-weighted biharmonic eddy viscosity term $\upsilon \mathbf{S}_n$, for which $S_n^x = h^{-1}[\partial_x(hF^x) + \partial_y(hF^y)]$, $S_n^y = h^{-1}[\partial_x(hF^y) - \partial_y(hF^x)]$, where $F_n^x = \partial_x \nabla^2 u_n - \partial_y \nabla^2 v_n$, $F_n^y = \partial_x \nabla^2 v_n + \partial_y \nabla^2 u_n$ (Griffies and Hallberg, 2000). The Montgomery potential is defined as

$$\phi_1 = g\eta_0 \,, \tag{3.4a}$$

$$\phi_2 = g\eta_0 + g'_{3/2}\eta_1 \,, \tag{3.4b}$$

$$\phi_3 = g\eta_0 + g'_{3/2}\eta_1 + g'_{5/2}\eta_2 \,, \tag{3.4c}$$

where η_0 is the free surface elevation. The reduced gravity at the two interfaces η_1 and η_2 are

$$g'_{3/2} = g(\rho_2 - \rho_1)/\overline{\rho} \,, \tag{3.5a}$$

$$g'_{5/2} = g(\rho_3 - \rho_2)/\overline{\rho} \,, \tag{3.5b}$$

as defined by the layer interface depths $\eta_1 = \eta_0 - h_1$ and $\eta_2 = \eta_0 - h_1 - h_2$. The reference densities (chosen based on Ilulissat conditions from Gladish et al. 2015) for the three layers

are $(\rho_1, \rho_2, \rho_3) = (1025.5, 1026.5, 1027.0)$ kg/m^3, but varying stratification is also explored in Sect. 3.3. This choice of stratification corresponds to a reduced gravity at the two interfaces of $g'_{3/2} = 9.6 \times 10^{-3}$ m^2/s and $g'_{5/2} = 4.8 \times 10^{-3}$ m^2/s.

Throughout this study, we use an internal baroclinic deformation radius defined as

$$L_\mathrm{d}(h_2, h_3) = \left(\frac{g'_{5/2} h_2 h_3}{f^2 (h_2 + h_3)} \right)^{1/2}, \tag{3.6}$$

which only takes into account the stratification of the bottom two layers because the uppermost layer is typically negligibly thin in most of our simulations. To adequately resolve the transport of a L_d-wide boundary current, we use a horizontal resolution of dl = 400 m all of the runs discussed (except for the dl = 68 m experiment discussed in Sect. 3.6). We find that L_d based on h_2 and h_3 evaluated at the sill maximum (x = 107.5 km) is a useful approximation for the boundary current width due to the sill's role in establishing the boundary current width. We use a time step of 100 s and simulations are run for 1600 days to reach a statistically steady state, which is measured by the domain-integrated available potential energy. This duration is required to fully spin up the shelf circulation and coastal current, which influences the dynamics within the fjord.

The 3-layer setup is more advantageous than a 2-layer setup primarily because the plume parameterization in three layers allows a partition of the exiting water masses between the top two layers, which serves as a proxy for exiting plume depth. By comparison, the 2-layer setup has no way of specifying the exiting plume depth since all of the bottom layer inflow must exit as outflow in the top layer. Moreover, this degree of freedom provided by a 3-layer setup is critical for the implementation of the plume parameterization since the overturning circulation in a 2-layer setup can be determined entirely by the density of the two layers and the rate of subglacial discharge via the Knudsen relations. However, a 3-layer setup must take into account the plume density and its level of neutral buoyancy, which provides a more physical control of the plume on the overturning circulation (see Appendix F for further discussion). Another implication for using three layers is that the overturning between the

bottom two layers is allowed to realistically transition to an overturning between the top two layers, which results in a substantially decreased heat transport since the middle layer has significantly less available heat content than the bottom layer. Although our isopycnal model does not carry a temperature variable, onshore heat transport inferences can be made by assigning realistic potential temperatures to each of the three density classes. In Greenland's fjords, the lower layer has typical potential temperatures of 2 to 4 °C, while the middle and top layers are within the range of -1 to 1 °C, which is why the bottom layer inflow is particularly important.

The goal of our choice to specify the boundary conditions (wind stresses, subglacial discharge rate, and open-ocean stratification) to be constant with time is to better understand the fully-equilibrated shelf-to-fjord mean circulation. While it is true that this constant forcing does not represent the full reality of Greenland's fjords, we believe it to be a necessary step before considering the superimposed effects of variability on the system, which is further discussed in Sect. 3.6.

3.2.3 A Reference Case

Diagnostics from a reference case simulation with sill height $H_{\mathrm{S}} = 100$ m and fjord width $W_{\mathrm{fj}} = 8$ km are shown in Fig. 3.2. Snapshots of the middle and bottom layer vorticities are mapped onto the isopycnal interface depths η_1 and η_2. The reference case parameters are selected based on conditions in Ilullisat Icefjord in West Greenland (Gladish et al., 2015) and are intermediate values for the parameter space explored in the sensitivity experiments in Sect. 3.

In Fig. 3.3, we present a series of diagnostic fields that capture the dynamics of this reference case including the time-mean zonal transport and isopcynal gradients, instantaneous vorticity fields showing mesoscale eddies on the shelf, and the fjord-focused circulation using time-averaged potential vorticity (PV) and transport streamfunction. Nearly all of the features in this reference case are observed in the series of parameter sensitivity simulations

discussed in Sect. 3.3.

In Fig. 3.3a, we show the meridionally-integrated zonal transport decomposed into mean and eddy components, defined as

$$Q_n = \int \overline{h_n u_n}\,\mathrm{d}y = \underbrace{\int \overline{h}_n \overline{u}_n\,\mathrm{d}y}_{Q_n^{\mathrm{mean}}} + \underbrace{\int \overline{h'_n u'_n}\,\mathrm{d}y}_{Q_n^{\mathrm{eddy}}}\,. \tag{3.7}$$

The total transport is inflowing (towards the fjord) in the bottom layer and outflowing (away from the fjord) in the middle layer. The zonal transport is dominated by eddies on the shelf with a small contribution of mean transport due to eddy momentum flux convergence (not shown) and dominated by mean flow primarily via boundary currents in the fjord interior. The midline ($y = 75$ km) isopycnal interface depths highlight the across-shelf pressure gradient in the middle and bottom layer (particularly those near the fjord mouth), which drives a baroclinic coastal current that is weaker/southward in the bottom layer and stronger/northward in the middle layer.

The vorticity snapshots for each layer in Fig. 3.3c-e show eddies shedding from the fjord mouth and coastal current primarily via baroclinic instability, which depends on the zonal isopycnal/pressure gradient. This is diagnosed using the same analysis as Zhao et al. 2019, which in this case shows the eddy energy production is dominated by conversion from potential energy rather than kinetic energy (not shown). These eddies are the dominant mode of transport across the y-periodic shelf. However, the peak in vorticity is located in the middle and bottom layer steady recirculation within the fjord and is connected to the overturning circulation via the bottom layer boundary current and middle layer coastal current.

Fig. 3.3f-h shows a zoomed-in view of the fjord interior transport streamfunction and PV for each layer, which are defined as

$$\overline{h_n \mathbf{u}_n} = (-\partial_y \psi_n, \partial_x \psi_n)\,, \tag{3.8a}$$

$$q_n = (f + \zeta_n)/h_n\,. \tag{3.8b}$$

Note that the streamfunction is not well-defined in the eastern and western diabatic boundaries due to the divergence of the time-mean mass flux in each layer, so we set $\psi = 0$ at the northern fjord wall and integrate meridionally across the fjord to determine ψ throughout the fjord, and then integrate zonally across the shelf (i.e., using a path of integration that avoids diabatic regions for the non-diabatic interior).

In the bottom layer streamfunction, the southward coastal current enters the fjord via a boundary current, which initially flows retrograde (with the boundary to the left of the flow) along the northern boundary of the fjord. The flow crosses the channel on the eastern side of the sill maximum since topographic beta, $\beta_{\text{topo}} = -f\partial_y(z_B)/h_3$, changes sign due to a reversal of the bathymetric slope. In this case, the flow crossing occurs at $x = 114$ km, which is diagnosed using the 20 mSv contour in Fig. 3.3h. The sill establishes a PV barrier in the bottom layer, which appears as a red patch in the PV field. The 20 mSv transport streamfunction illustrates the transport pathway approximately following PV-isolines, which serve as barriers that guide the flow. The boundary current then feeds the gyre-like recirculation in the deeper fjord interior, where it is converted into the middle layer water mass by the diabatic plume-driven water mass transformation. The flow in the middle layer recirculates with a small fraction flowing back out towards the open ocean via eddy transport across the shelf.

The recirculation in the middle layer is slightly weaker than the bottom layer and extends the length of the fjord since it is effectively unconstrained by bathymetry. Compared to the bottom layer, the bathymetry exhibits a much weaker influence on the top and middle layers. We quantify the recirculation using the streamfunction extrema within the fjord as

$$\psi_r = \max_{100<x<150 \text{ km}} (|\psi_n|)\,, \tag{3.9a}$$

which is ∼200 mSv in the middle layer and ∼300 mSv in the bottom layer — an order of magnitude larger than the overturning circulation.

3.3 Parameter Dependencies

The reference case motivates us to seek an understanding for the parameter dependencies of the two bulk fjord circulation properties: the overturning circulation and horizontal recirculation. The overturning and recirculation control parameters can be classified into geometric, forcing-related, and stratification, and our goal is to test the sensitivity of a few simple parameters that to first order capture the parameter variations amongst Greenland's fjords.

Although various complex geometric controls can exist (bends in the fjord, non-uniform fjord width, shelf troughs, multiple sills, etc.), we anticipate that the features of first-order importance to the overturning are sill height, H_{S}, and fjord width, W_{fj}, which act to horizontally and vertically constrict the exchange flow at the fjord mouth. Forcing parameters that are of first-order importance to the fjord-shelf exchange are wind direction and strength, subglacial discharge strength, and open ocean boundary conditions, which we quantify as AW depth, η_2^{W}. Some of these parameters have been tested previously in modeling results (Carroll et al., 2017; Gladish et al., 2015), and are known to influence the dynamics of the continental shelf, the fjord mouth sill, and the fjord head regions (Straneo and Cenedese, 2015).

Therefore, we choose to vary the following six parameters: sill height, fjord width, wind direction/strength, subglacial discharge strength, AW depth, and stratification. The key parameters and test cases are listed in Table 3.1, with parameter variations selected to span the range of existing glacial fjord measurements.

3.3.1 Summary of Dependencies

Fig. 3.4a-f shows the sensitivity of the overturning circulation and its root-mean-square deviation (RMSD) to each of the six parameters. Relative to the reference case, the overturning circulation varies most significantly with sill height, AW depth, winds, and subglacial discharge over realistic parameter variations.

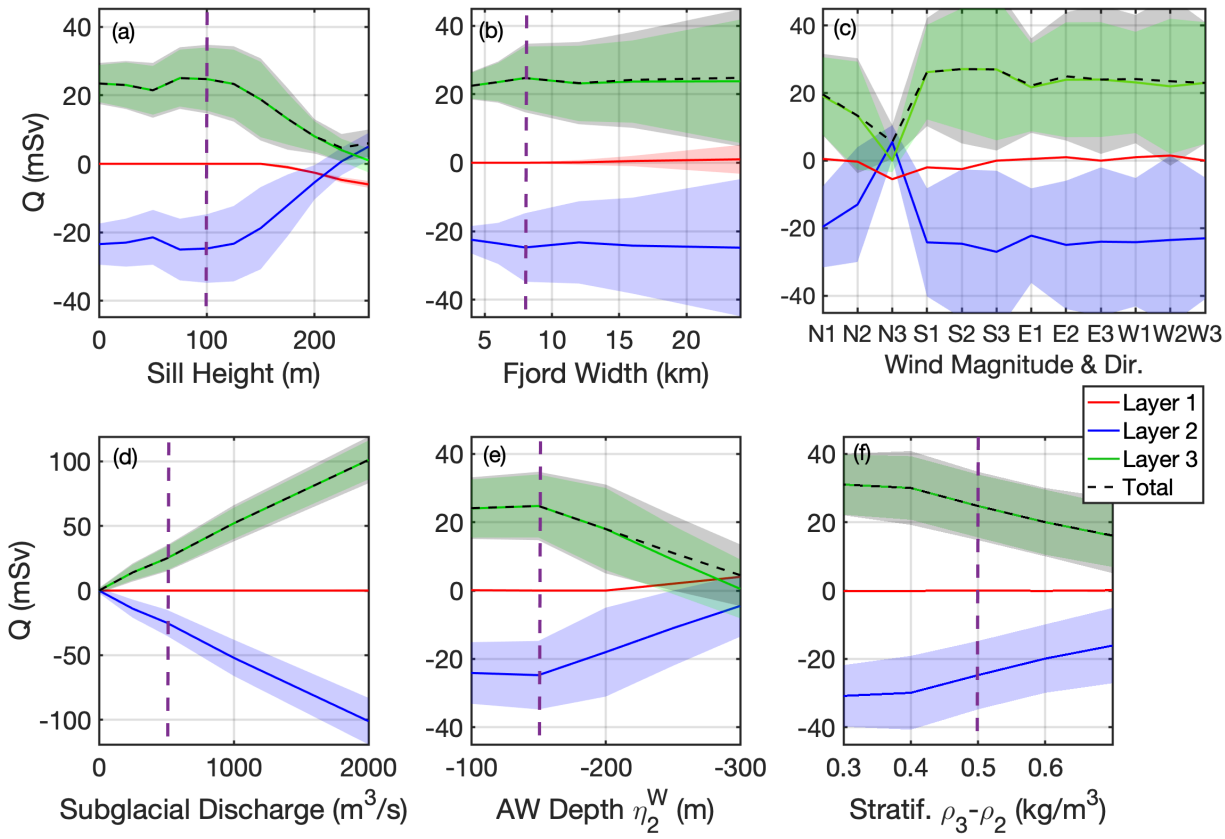

Figure 3.4: (a)-(f) Time-averaged (days 1300-1600) mean transport for each layer n based on Eq. (3.7) diagnosed at the sill maximum ($x = 107.5$ km) and its root-mean-square deviation (color shading denotes positive and negative values calculated from the timeseries for each respective case). Transports are positive toward the glacier. The purple dotted line shows the parameter choice of the reference case (from Figs. 3.2 and 3.3). The wind magnitude is [N1, N2, N3] = [0.015, 0.03, 0.1] N/m^2 and similarly for the other wind directions in panel (c).

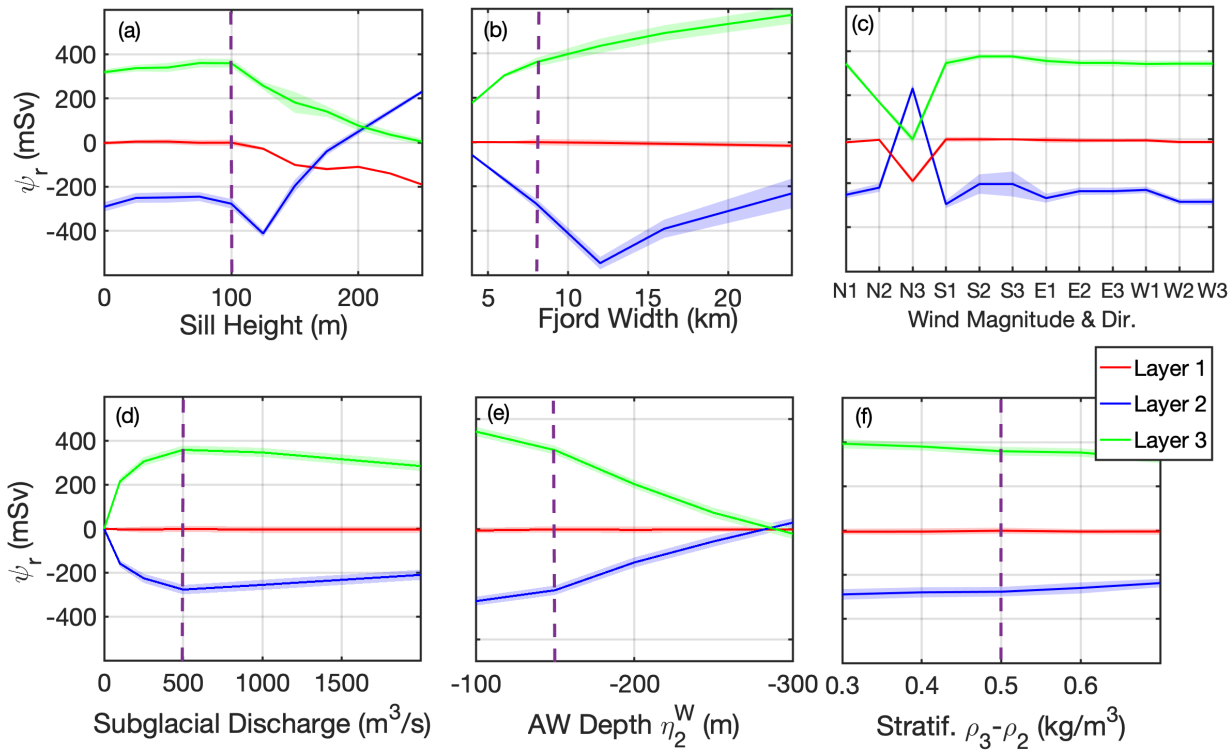

Figure 3.5: (a)-(f) Time-averaged (days 1300-1600) recirculation strength ψ_r (diagnosed as the streamfunction extremum using Eq. (3.9a)) within the fjord in each layer, where positive values correspond to cyclonic circulation. Recirculation root-mean-square deviation is shown with color shading (calculated from the timeseries for each respective case). The purple dotted line shows the parameter choice of the reference case (from Figs. 3.2 and 3.3). The wind magnitude is [N1, N2, N3] = [0.015, 0.03, 0.1] N/m^2 and similarly for the other wind directions in panel (c).

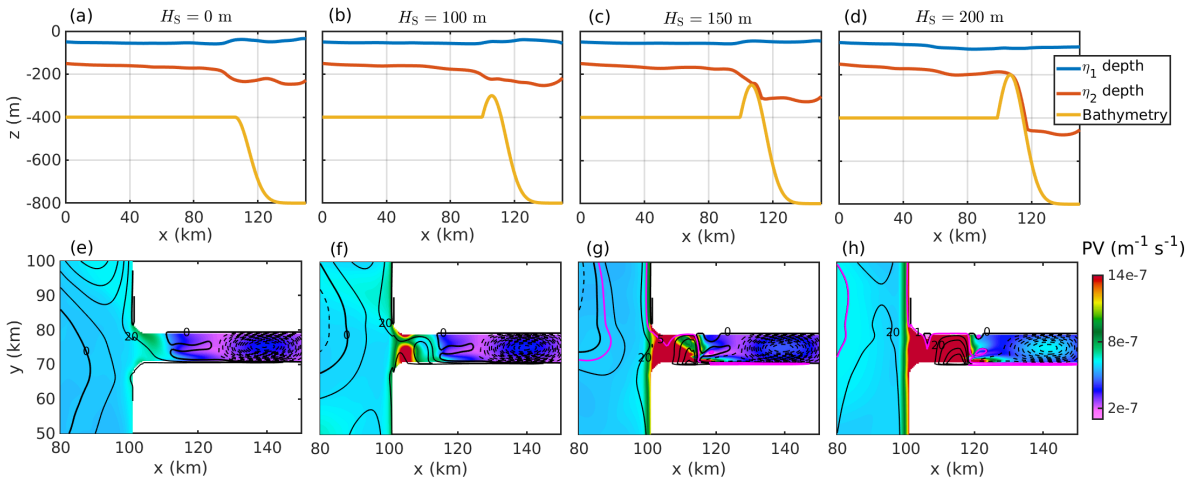

Figure 3.6: (a)-(d) Side profile depths of η_1, η_2, and bathymetry along midline (y = 75 km); and (e)-(h) zoomed-in bottom layer PV (in color) and transport streamfunction using 20 mSv contours for four cases of varying sill height. The dotted line contours show negative values and additional pink contours in panels g and h highlight the fjord-shelf connectivity. All fields are time-averaged over days 1300 - 1600.

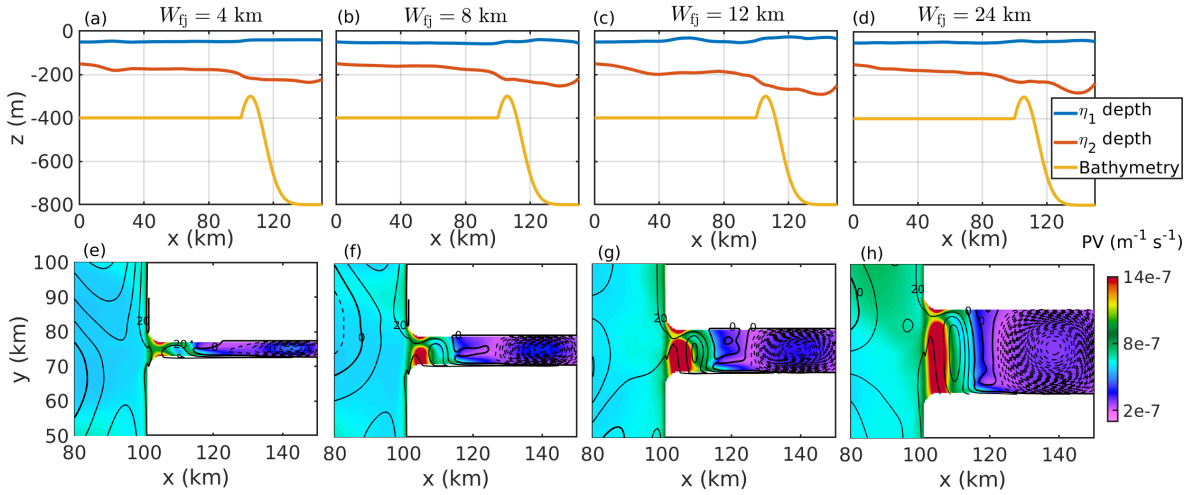

Figure 3.7: Same as Fig. 3.6 for four cases of varying fjord width.

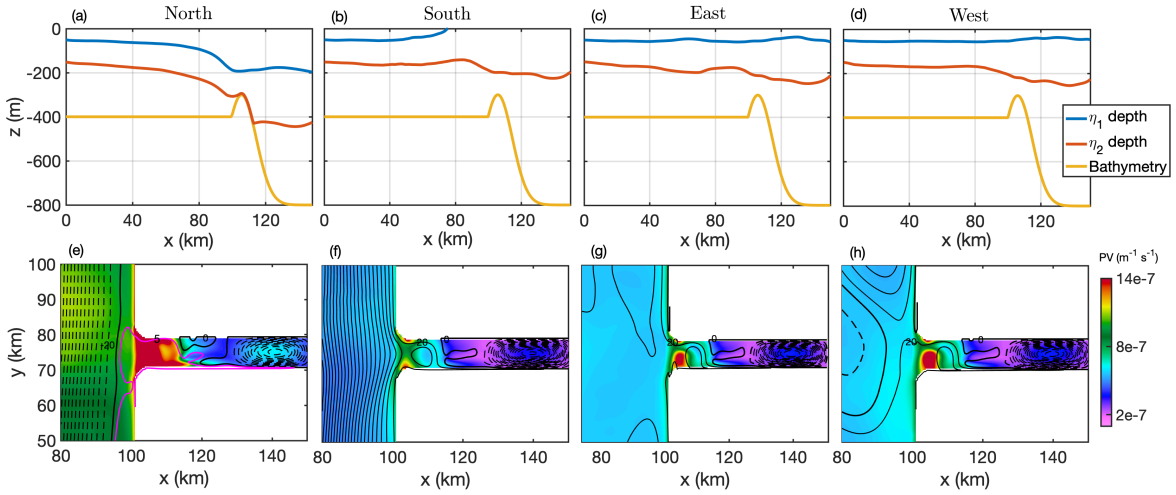

Figure 3.8: Same as Fig. 3.6 for four cases of varying wind direction with constant magnitude 0.03 N/m^2. An additional pink contour in panel e highlights the fjord-shelf connectivity for the northward wind case.

For tall enough sills (H_S above 150 m), deeper AW ($\eta_2^\mathrm{W} + H_\mathrm{Sh} \approx H_\mathrm{S}$), and strong northward winds, the outflow transitions from the middle to the top layer (red line in Fig. 3.4a,e). In such cases, the plume density is light enough to rise past the middle layer and exit via the top layer due to a thin bottom layer water mass that is only weakly entrained by the plume. Here, the AW depth at the western boundary η_2^W increases as the bottom layer thickness $H_3^\mathrm{W} = H_\mathrm{Sh} + \eta_2^\mathrm{W}$ decreases. This transition of the overturning circulation between the bottom two layers to the top two layers for high sill cases as well as greater AW depth or stronger downwelling-favorable winds is seen in Fig. 3.4a,c,f and is further discussed in Appendix F. Although large H_S, deeper AW, and small Q_0 can each lead to the complete shutoff of warm AW (bottom layer) transport toward the fjord, denoted as Q_3, it is also plausible that a weak enough stratification between the bottom and middle layers ($\sim$0.1 kg/m^3 or less) or a small enough fjord width (1 km or less) may also lead to weakened heat transport into the fjord.

Similarly to Fig. 3.4 for overturning sensitivity, Fig. 3.5a-f shows the dependency of

Name	*Parameter*	*Test Cases*	*Ilulissat estimate*	*Units*
Sill Height	H_{S}	[0:25:250]	100	m
Fjord Width	W_{fj}	[4,6,8,12,16,24]	8	km
Fjord Length and Depth (constant)	$L_{\mathrm{fj}} \times H_{\mathrm{fj}}$	50×0.8	47×0.75	km
Wind Magnitude and Direction	τ_x, τ_y	[0, 0.015, 0.03, 0.1] × [N,S,E,W]	∼0.03 × [N,S,E,W]	$\mathrm{N/m^2}$
Subglacial Discharge	Q_0	[0, 100, 250, 500, 1000, 2000]	∼1700	$\mathrm{m^3/s}$
Atlantic Water Depth	η_2^{W}	[-100, -150, -200, -250, -300]	∼-150 ± 50	m
Stratification	$\rho_3 - \rho_2$	[0.3, 0.4, 0.5, 0.6, 0.7]	∼0.5	$\mathrm{kg/m^3}$

Table 3.1: Summary of key fjord parameters and test cases for the numerical simulations and their corresponding estimates for Ilulissat Icefjord in West Greenland. All variables are independently varied relative to the reference case in Sect. 3.3.3 except fjord length and depth. The estimates of Ilulissat fjord properties are based on data from Gladish et al. (2015) and Beaird et al. (2017).

horizontal recirculation on the same six parameters. The recirculation in the bottom/AW layer, which is the most important due to its lateral heat transport to the glacier face, varies primarily with sill height, fjord width, subglacial discharge, and AW depth. If we compare the recirculation sensitivity in each layer with the overturning circulation sensitivity in Fig. 3.4, we see approximately the same trends for sill height, winds, η_2^{W}, and stratification. However, the sensitivity of recirculation to fjord width in Fig. 3.5b is visibly higher than for overturning in Fig. 3.4b. For discharge strength shown in Fig. 3.5d, the recirculation saturates near $Q_0 = 500$ $\mathrm{m^3/s}$ while the overturning continues to linearly increase in Fig. 3.4d. The middle layer recirculation approximately opposes the recirculation in the bottom layer, except for cases of wide fjords or nonzero top layer recirculation (especially in tall sill cases).

We now discuss the parameter sensitivity of the fjord dynamics in greater detail and

describe the flow behavior in response to these key parameter variations.

3.3.2 Sill Height and Fjord Width

Fig. 3.6a-d shows the time-averaged isopycnal depth variations along the y-midline and panels e-h shows the bottom layer PV and transport streamfunction for four cases of varying sill height. As discussed in the reference case (Fig. 3.3), a common feature is the coastal current, which flows southward in the bottom layer and enters the fjord as a narrow L_{d}-wide boundary current. The boundary current flows along and across the fjord and subsequently feeds a cyclonic recirculation gyre in the fjord interior.

The interface depth in Fig. 3.6a-d shows a transition from a 100 m zonal η_2 difference ($\eta_2^{\mathrm{W}} - \eta_2^{\mathrm{E}}$) in the no-sill case (Fig. 3.6a) to a significantly larger 300 m difference for the $H_{\mathrm{S}} = 200$ m case in Fig. 3.6d, with the bottom layer nearly grounded on the sill bathymetry. The bottom layer thickness inside the fjord decreases by approximately a factor of 2 between the $H_{\mathrm{S}} = 0$ and the $H_{\mathrm{S}} = 200$ m cases.

In Fig. 3.6e-h, the time-averaged PV and transport streamfunction also show a noticeable change in the fjord-shelf connectivity via the coastal and boundary current for taller sills. The sill establishes a PV barrier in the bottom layer, which appears as a red patch in the PV for cases with sills. In the $H_{\mathrm{S}} = 0$ case, the PV barrier is weak and the streamfunction shows that the flow from the coastal current crosses the fjord gradually to join the boundary current and recirculation gyre. For taller sills, the boundary current enters as a narrower boundary current with weaker transport (outlined in a pink contour in panels g and h). In these cases, the isopycnal structure is suggestive of a hydraulically-controlled exchange flow (Pratt and Whitehead, 2007), discussed further in Sect. 3.4. An anticylonic recirculation develops on the downstream side of tall sills and the bottom layer recirculation weakens for the tallest sills due to decreased overturning strength and the bottom friction acting on a decreased bottom layer thickness (further discussed in Sect. 3.5).

Fig. 3.7a-h shows plots of isopycnal depth, bottom layer PV, and transport streamfunction for varying fjord width. In Fig. 3.7a-d, interfacial depths of η_2 along the y-midline show a $\sim$10% increase in zonal η_2 differences between $W_{\rm fj} = 4$ to 24 km, which is consistent with the minimal increase in overturning circulation for wider fjords shown in Fig. 3.4b. However, the bottom layer recirculation strengthens by $\sim$80% between the 4 km and 8 km case and $\sim$60% between the 8 km and 24 km cases. Depressions in the isopycnal depths due to the strength of the opposing gyre recirculation in the bottom and middle layers are more clearly observed for the wider fjords, e.g. Fig. 3.7c,d. In these cases, a weak recirculation of $\sim$20 - 40 mSv also develops over the sill. Regardless of fjord width, we see the flow consistently entering the fjord through an $L_{\rm d}$-wide current in the northern boundary, which appears visually in the PV field as a small trough in the near-sill PV barrier in Fig. 3.7e-h. Although the narrow fjord widths cases are limited by horizontal resolution, fjord-only test cases (not shown) suggest a reduction in overturning and larger zonal isopycnal gradients for fjords narrower than $L_{\rm d}$.

3.3.3 Wind Strength and Direction

Wind stress magnitudes of τ = [0.015, 0.03, 0.1] N/m^2 were tested (corresponding approximately to a range of 3.5 to 9 m/s wind velocities), which are fairly representative of the annual average winds along the Greenland coast and not of shorter-term extremes (Lee et al., 2013). The resulting y-midline depths of η_1 and η_2 are shown in Fig. 3.8a-d and time-averaged bottom layer PV and transport streamfunction in panels e-h for four cases of varying wind direction and wind stress magnitude $\tau = 0.03$ N/m^2.

The eastward and westward wind cases did not change the mean state appreciably, but the northward and southward cases visibly tilt both isopycnals (through Ekman transport) in Fig. 3.8a,b leading to a zonal isopycnal depth change of $\Delta\eta_2 = -190$ m and $\Delta\eta_1 = -150$ m for northward winds, and $\Delta\eta_2 = 50$ m and $\Delta\eta_1 = 50$ m for southward winds. For the northward wind case shown, 80% of the zonal gradient in η_2 occurs on the shelf and the

bottom layer is ∼200 m thinner in the fjord interior than the eastward/westward wind cases.

The streamfunctions in Fig. 3.8e,f show an inflow that is significantly weaker in the northward wind case and slightly stronger in the southward wind case compared to the eastward and westward wind cases (Fig. 3.8g,h). This is influenced by the bottom layer coastal current supplying the fjord overturning, which changes from a weak southward transport of ∼40 mSv in the reference case (in Fig. 3.3) to a ∼200 mSv northward transport for northward winds, ∼500 mSv southward transport for the southward wind case, ∼40 mSv (no change) for the eastward wind case, and ∼20 mSv northward transport for the westward wind case. Due to the thin bottom layer thickness above the sill for the northward wind case, there is a strong PV barrier (similar to the tall sill cases) for the northward wind case and a reduced barrier for the southward winds.

The sensitivity of the fjord dynamics to northward winds via differences in the isopycnal depths, coastal current strength, and meridional profile of the inflow lead to a 45% reduction in overturning and 40% reduction in recirculation for the intermediate wind case (0.03 N/m^2) and a complete shutoff of both the overturning and recirculation for the highest northward wind case (0.1 N/m^2). These results show northward winds are the most important in reducing the overturning and recirculation and is likely to be even more significant for fjords with weaker plume-driven overturning where the Ekman transport contribution is comparatively larger.

Our wind tests use time-constant winds that are uniform over the whole domain and are intended to capture the influence of steady winds on shelf circulation (upwelling and downwelling) and its influence on mean fjord circulation. We use annual-mean winds since the shelf circulation and across-shelf transport requires years to spin up, while seasonal winds may likely lead to strong, but transient controls on fjord-shelf exchange. In this setup, a strong northward wind (0.1 N/m^2) was sufficient to completely shut off the warm AW transport due to a vanishing bottom layer near the fjord mouth with strong eddies dominating the shelf, which in practice may be dampened by bathymetric features on the

shelf.

Although it is likely that time-varying winds are equally or more important than the annual-mean winds, we have only included the annual-mean wind effects as a starting point for assessing the role of winds on fjord-shelf exchange in this study. A more realistic time-varying wind forcing including shorter timescale extreme events are likely to excite coastally-trapped waves and other modes of variability as well as non-equilibrium rapid flushing events (e.g., Spall et al., 2017), which are not considered in this study and require further exploration.

3.3.4 Subglacial Discharge, AW Depth, and Stratification

Of the parameters tested, subglacial discharge has the most predictable effect on overturning strength (as shown in Fig. 3.4d), which increases linearly with discharge along with a moderate increase in transport RMSD. This is unsurprising given the theory of diabatic plume forcing in Appendix F implemented in the eastern boundary condition. Increasing the overturning circulation via subglacial discharge from 0 to 100 mSv strengthens the boundary current from ∼0 to 100 mSv, coastal current from ∼0 to 300 mSv, and recirculation in the middle and bottom layers from ∼0 to 300 mSv (which saturates near $Q_0 = 500$ m^3/s). The strength of the recirculation and overturning is likely dependent on the grounding line depth (level of subglacial discharge), which is a parameter we do not vary.

Varying the AW depth at the western boundary η_2^{W} is found to have nearly the same effect as varying the sill heights, i.e. decreasing η_2^{W} from -100 m to -300 m had approximately the same effect as increasing H_{S} from 0 m to 250 m (see Fig. 3.4a,e). This is unsurprising since the nondimensionalized sill height, $H_{\mathrm{S}}/H_3^{\mathrm{W}}$, varies inversely with $H_3^{\mathrm{W}} = H_{\mathrm{Sh}} + \eta_2^{\mathrm{W}}$ and represents the importance of sill height in constraining the overturning circulation. Additionally, in Fig. 3.5e, the recirculation within each layer is proportional to the overturning and follows the same trend.

Increasing stratification (i.e., increasing $\rho_3 - \rho_2$ from 0.3 to 0.7 kg/m^3) has the effect of decreasing the overturning circulation from 30 mSv to 17 mSv (shown in Fig. 3.4f), which, similarly to the other parameters, led to increases in the recirculation and coastal current albeit with much weaker trends (10% increase over the range of stratification). The effect of stratification on fjord dynamics in the context of plume theory is further discussed in Appendix F.

3.4 Overturning Circulation

Following the results from the sensitivity studies, we develop theories to predict the overturning circulation as a function of the parameters explored in Sect. 3.3. For simplicity, we focus on the AW inflow in the bottom layer, Q_3, since it is nearly proportional to the heat flux towards the glacial face and the most important transport for melt rate estimates (e.g., Inall et al., 2014).

We present and assess theories for the transport across each of the three regions: the continental shelf, the fjord mouth sill, and the fjord head. We first discuss the continental shelf region with an across-shelf transport, Q_{shelf}, primarily driven by eddies and Ekman transport. We then discuss the fjord mouth sill region with a sill-overflow transport, Q_{fjord}, which admits both geostrophic and hydraulically-controlled transport predictions (based on the theory from Zhao et al. 2019). Following this, we discuss the fjord head region with a diabatic water mass transformation, Q_{plume}, driven by plume entrainment at the glacier face. This diabatic water mass transformation in the steady state is balanced by the diabatic transport at the western boundary and due to the restoring, this transport must match the other transports and is not included in the theory.

In the following subsections, we use diagnosed bottom layer thicknesses at the fjord mouth H_3^{f} and at the glacier boundary H_3^{E}) to test the theoretical transport estimates, and then combine these estimates to develop a prediction for the isopycnal depths in each region and

the overall transport. A schematic showing the zonal overturning circulation and relevant definitions is shown in Fig. 3.9a.

3.4.1 Across-Shelf Transport

The bottom layer across-shelf transport Q_{shelf} is the sum of both eddy and mean contributions. We first discuss the eddy transport in the absence of winds and then discuss the mean Ekman transport.

In Fig. 3.3, the zonal transport for the reference case (with no winds) shows that the across-shelf eddy thickness fluxes driven by the zonal isopycnal difference dominate the total transport. We can use the conventional downgradient assumption applied to eddy thickness fluxes to derive the across-shelf eddy transport (e.g., Gent and McWilliams, 1990). The eddy transport from the open ocean to the fjord mouth is described by

$$Q_{\text{eddy}} = \kappa W (H_3^{\text{W}} - H_3^{\text{f}})/L_{\text{Sh}}\,, \tag{3.10}$$

where $W = 150$ km is the meridional domain size, $L_{\text{Sh}} = 100$ km is the zonal shelf length. There are many ways of specifying the eddy diffusivity κ (e.g., Gent and McWilliams, 1990; Visbeck et al., 1997; Gent, 2011). In the interest of simplicity, we use an empirically-selected constant $\kappa = 234$ m^2/s since this yields a good agreement with the across-shelf transport.

In addition to the eddy transport, there is a mean across-shelf transport that is maintained by the winds. Although the mean transport is not entirely wind driven, the Ekman transport far outweighs the contribution due to eddy momentum flux convergence (seen in Fig. 3.3a). To see this, we time-average and integrate the meridional momentum equation in Eq. (3.2a) vertically over all layers

$$C_d \overline{v}_3^2 \approx \frac{\tau_y}{\rho_1}\,, \tag{3.11}$$

i.e., that momentum input from the winds must be balanced in steady state by the momentum sink due to bottom friction. We combine Eq. (3.11) with the vertically-integrated

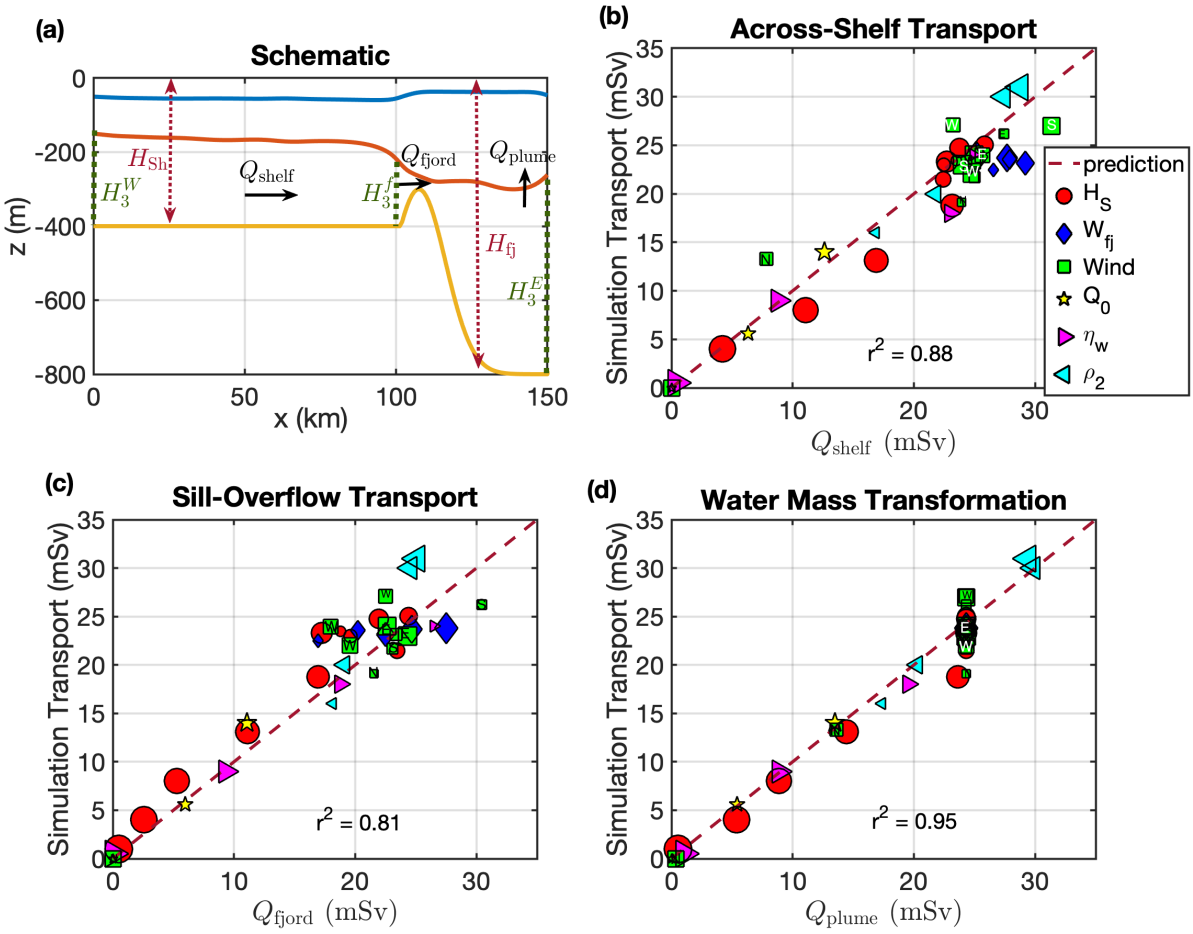

Figure 3.9: (a) Schematic for the overturning circulation showing the three components of the shelf-to-glacier-face overturning. A comparison between the strength of the simulated overturning circulation diagnosed in the model and the predictions for onshore transport from: (b) Q_{shelf}, the sum of eddy and Ekman transports across the shelf given by Eqs. (3.10) and (3.13); (c) Q_{fjord}, the minimum of the geostrophic and hydraulically-controlled transports given by Eqs. (3.14),(3.15), and (3.17); and (d) Q_{plume}, the diabatic water mass transformation given by Eq. (3.18). Increasing marker sizes correspond to increasing values of each parameter with letter labels for varying wind direction.

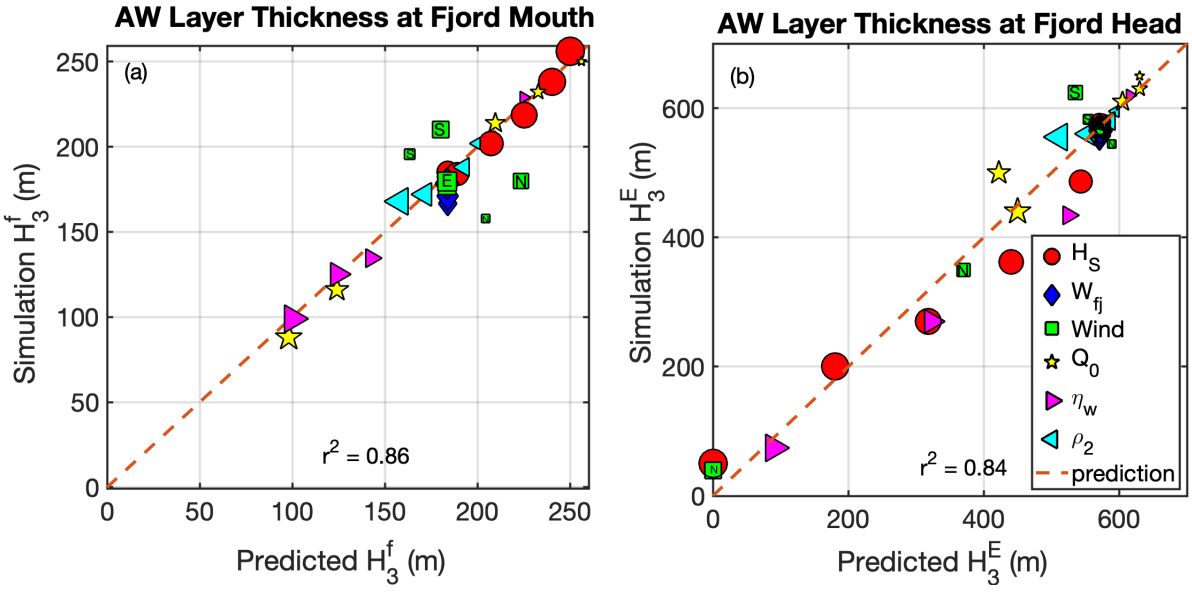

Figure 3.10: A comparison between: (a) the simulated H_3^{f} (bottom layer thickness at $x =$ 100 km, as labeled in Fig. 3.9a) and the predicted H_3^{f} from Eq. (3.22); (b) the simulated H_3^{E} (bottom layer thickness at $x = 150$ km, as labeled in Fig. 3.9a) and the predicted H_3^{E} from Eq. (3.20). Increasing marker sizes correspond to increasing values of each parameter with letter labels for varying wind direction.

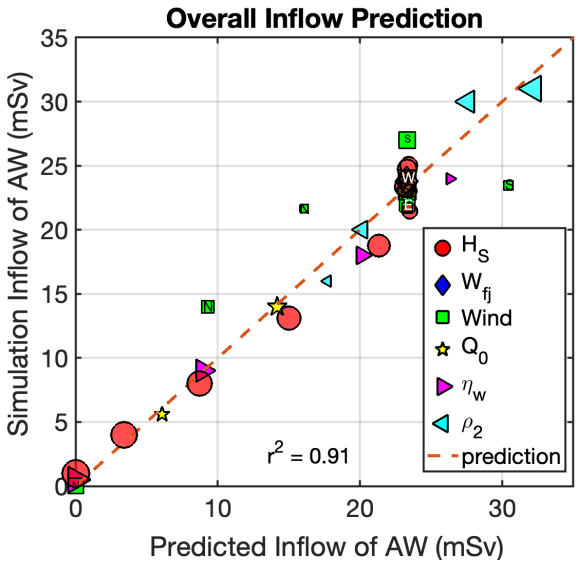

Figure 3.11: A comparison between the strength of the simulation inflow of Atlantic Water diagnosed in the model to the predicted inflow (equivalent to bottom layer overturning circulation, Q_3) calculated from Eq. (3.23). Increasing marker sizes correspond to increasing values of each parameter with letter labels for varying wind direction.

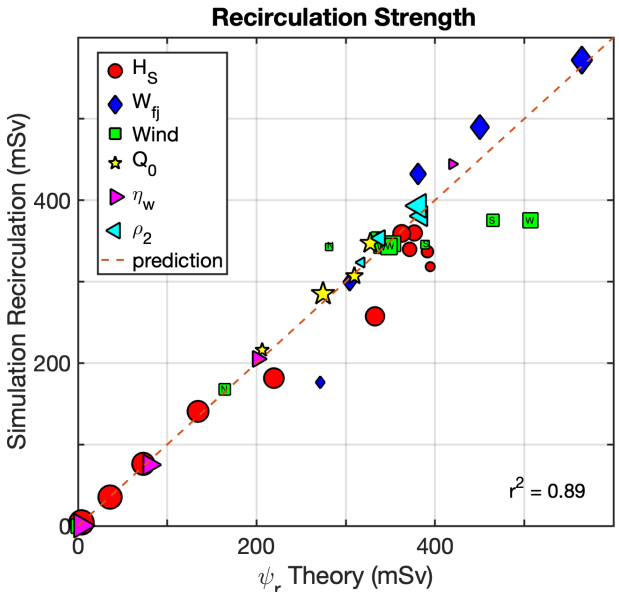

Figure 3.12: A comparison between the strength of the simulation recirculation diagnosed in the model to the prediction for recirculation based on Eq. (3.28). Increasing marker sizes correspond to increasing values of each parameter with letter labels for simulations of varying wind direction.

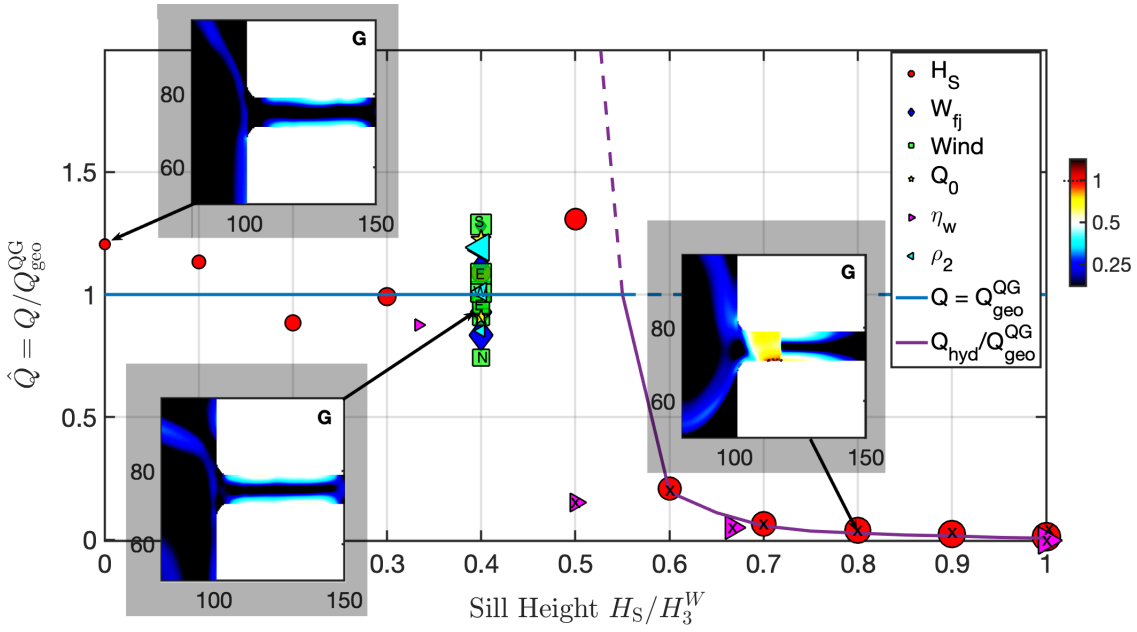

Figure 3.13: Critical transport prediction using rotating 1-layer theory from Eq. (3.17) and simulation results both nondimensionalized by the geostrophic transport for varying nondimensionalized sill height. The solid lines show where the geostrophic and hydraulic-control theories set the bound on transport while the dashed lines do not (in accordance with Eq. (3.14)), which shows a transition to hydraulic control theory for $H_S/H_3^W > 0.55$. Insets show the composite Froude number G over a zoomed-in domain (x and y axes in km) centered on the fjord. Increasing marker sizes correspond to increasing values of each parameter with letter labels for simulations of varying wind direction. Experiments where G exceeds 0.8 at any location within the domain are marked with an 'x'.

meridional momentum equation in the bottom layer, which is approximately a balance between bottom friction and the Coriolis force

$$C_d \overline{v}_3^2 \approx -f \overline{h}_3 \overline{u}_3 \,. \tag{3.12}$$

This implies a time-mean bottom layer return flow $\overline{h}_3\overline{u}_3$, which can be shown to be equal and opposite to the top layer Ekman transport $U_{\rm Ek} \equiv \overline{h}_1\overline{u}_1 = -\overline{h}_3\overline{u}_3$. Therefore the onshore top layer Ekman transport contribution to the mean overturning circulation is

$$Q_{\rm Ek} = LU_{\rm Ek} = L\tau_y(\rho_1 f)^{-1} \,, \tag{3.13}$$

where $L = 150$ km is the meridional domain length, and τ_y is the northward wind stress.

For the scenario where offshore Ekman return flow in the bottom layer exceeds the onshore eddy transport in the bottom layer, the bottom layer thickness vanishes at the fjord mouth, which results in a bottom layer transport, $Q_{\rm shelf} = 0$, where the Ekman return flow transitions from the bottom layer to the intermediate layer such that $U_{\rm Ek} \equiv \overline{h}_1\overline{u}_1 = -\overline{h}_2\overline{u}_2$. For the reference sill height $H_{\rm S} = 100$ m, the theoretical prediction for a shutoff of AW access is achieved by a northward wind stress $\tau_y = 0.05$ N/m^2; for the case of no sill, this is achieved by a northward wind stress $\tau_y = 0.08$ N/m^2.

In Fig. 3.9b, we plot the overturning circulation strength diagnosed from the simulations compared to our theory for the bottom layer across-shelf transport $Q_{\rm shelf} = \max(Q_{\rm eddy} - Q_{\rm Ek}, 0)$ using Eqs. (3.10) and (3.13). This theory predicts the across-shelf transport with a coefficient of determination of $r^2 = 0.88$.

3.4.2 Sill-Overflow Transport

The sill-overflow transport into the fjord is driven by the zonal isopycnal gradients in the AW depth η_2 outside the fjord relative to inside, which establishes a zonal pressure gradient along the fjord. This pressure gradient drives a (meridional) geostrophic flow within the fjord for smaller sill-overflow velocities, and becomes hydraulically-controlled for larger velocities (due to either taller sills or other parameters).

We present a prediction for both the geostrophic transport and critical transport (using hydraulic control theory) with the overall sill-overflow transport set by the minimum of the geostrophic and critical transport

$$Q_{\text{fjord}} = \min(Q_{\text{hyd}}, Q_{\text{geo}}^{\text{QG}}) \,. \tag{3.14}$$

The rationale for this is that the flow is geostrophic (subcritical) if it is not hydraulically-controlled, and if the flow is hydraulically-controlled (necessarily evolving toward a critical flow in the steady state) the transport according to hydraulic control theory is the maximum achievable transport and is smaller than the geostrophic transport (Pratt and Whitehead, 2007). This transition behavior from geostrophic to hydraulically-controlled flows is further discussed in Sect. 3.6.1.

3.4.2.1 Geostrophic Transport

The across-sill (defined here as the zonal direction) geostrophic sill-overflow transport can be estimated based on the along-sill (meridional) geostrophic transport. This is based on the assumption that boundary currents in the fjord interior establish a zonal/along-fjord pressure head that is similar to the meridional/across-fjord pressure head within the fjord (Zhao et al., 2019). This is suggested in the bottom layer streamfunction from Fig. 3.3h, which shows a boundary current entering the fjord and flowing coherently across and along the sill. The pressure head across the boundary current in the along-sill and across-sill directions are thus similar values and representative of the geostrophic transport into the fjord.

The across-sill geostrophic transport (using the along-sill geostrophic transport as a proxy) is therefore based on the along-sill isopycnal gradient $H_3^{\text{f}} - H_3^{\text{E}} + (H_{\text{fj}} - H_{\text{Sh}})$, and is

derived using the quasigeostrophic (QG) approximation as

$$Q_{\text{geo}}^{\text{QG}} = \int H_3^M u_3 \, \mathrm{d}x' \approx \int H_3^M \left(\frac{g'_{5/2} H_2^M \partial_x \eta_2}{|f|(H_2^M + H_3^M)} \right) \mathrm{d}x'$$
$$\approx |f| L_{\text{d}}^2 (H_3^{\text{f}} - H_3^{\text{E}} + (H_{\text{fj}} - H_{\text{Sh}})) \,, \tag{3.15}$$

where H_n^M is the mean reference thickness in each layer n (see Zhao et al. 2019 for further details).

3.4.2.2 Hydraulically-Controlled Transport

When the geostrophic transport in the bottom layer is large enough, the velocity of the flow becomes comparable to the internal gravity wave speed. This occurs for a critical flow with respect to the composite Froude number $G = 1$, which may be defined as (Pratt and Whitehead, 2007)

$$G^2 = \text{Fr}_1^2 + \text{Fr}_2^2 + \text{Fr}_3^2 \,, \tag{3.16a}$$
$$\text{where } \text{Fr}_n = |\mathbf{u}_n| / \sqrt{g'_{n-1/2} h_n} \,, \tag{3.16b}$$

for g' defined in Eqs. (3.5a)-(3.5b) and $g'_{1/2} \equiv g$. Alternative definitions for the critical condition (e.g., Stern, 1974) were tested, but did not lead to significant differences in our results.

This critical flow can be predicted using a variety of assumptions ranging from 1-layer rotating to multiple rotating layers. For simplicity, we use the 1-layer rotating solution for a hydraulically-controlled critical transport in the bottom layer (Whitehead et al., 1974),

$$Q_{\text{hyd}} = W_{\text{BC}} \sqrt{g'_{5/2}} \left(\frac{2}{3} \left[H_3^{\text{f}} - H_{\text{S}} - \frac{f^2 W_{\text{BC}}^2}{8 g'_{5/2}} \right] \right)^{3/2} . \tag{3.17}$$

Here, we assume the transport follows a boundary current of width $W_{\text{BC}} = \min(L_{\text{d}}, W_{\text{fj}})$, which is supported by our simulation results. We find that applying Eq. (3.17) is valid if Fr_3 dominates the Froude number in Eq. (3.16a). For tall enough sills, hydraulic control can occur in the top and middle layers (not shown), but this does not influence Q_3.

In Fig. 3.9c, we plot the overturning circulation strength diagnosed from the simulations vs. our theory for the sill-overflow transport Q_{fjord} as the minimum of the geostrophic and hydraulic transport (using Eqs. (3.14), (3.15), and (3.17)). This theory predicts the sill-overflow transport for each of the parameter variations with a coefficient of determination of $r^2 = 0.81$.

Although hydraulic control has been applied to many sill overflows in the open ocean (Pratt and Whitehead, 2007), hydrographic measurements and numerical simulations support the existence of hydraulically-controlled flow within the Pine Island Glacier ice shelf cavity (Zhao et al., 2019; De Rydt et al., 2014), and outside the 79 North Glacier ice tongue cavity (Lindeman et al., 2020; Schaffer et al., 2020).

3.4.3 Diabatic Water Mass Transformation

The overturning circulation in steady state must be balanced by the near-glacier diabatic water mass transformation at the fjord head. Within the uniform density bottom layer, the theory for the vertical volume flux for a point source plume can be derived from classic self-similarity and entrainment assumptions as (Morton et al., 1956)

$$Q_{\text{plume}} = c_\epsilon B_0^{1/3} (H_3^{\text{E}})^{5/3}\,, \tag{3.18}$$

where $c_\epsilon = (6/5)(9/5)^{1/3}\pi^{1/3}\epsilon^{4/3}$ (modified for a half-cone plume) for an experimentally-derived entrainment coefficient, $\epsilon = 0.13$ (Linden, 2000). The buoyancy flux $B = g'Q$ varies with depth, but is constant in the uniform density bottom layer $B_0 = g'_0 Q_0$, which is the buoyancy flux at the plume source (where $g'_0 = g(\rho_3 - \rho_0)/\overline{\rho}$). We can alternatively express this as a diabatic water mass transformation in terms of stratification and plume density (see Appendix F), which more clearly demonstrates how the overturning circulation may increase or decrease depending on the stratification and discharge strength due to the plume exit depth.

In Fig. 3.9d, we plot the overturning circulation strength diagnosed from the simulations

compared to our theory for Q_{plume} in Eq. (3.18). This theory predicts the diabatic water mass transformation for each of the parameter variations with a coefficient of determination of $r^2 = 0.95$.

3.4.4 Piecing Together the Overturning Circulation

The bottom layer AW inflow is set by eddy-driven and Ekman transport in the continental shelf region, the minimum of the geostrophic transport and hydraulically-controlled transport in the fjord mouth sill region, and the plume-driven diabatic water mass transformation in the fjord head region. In order to make this prediction more comprehensive, we can equate the transport in these three regions and solve the system of equations to develop an a priori prediction of Q_3 without knowledge of the zonal isopycnal gradients in the continental shelf and fjord mouth sill regions. The bottom layer transport across the shelf-to-glacier-face domain can be summarized as

$$\max(\underbrace{Q_{\text{eddy}} - Q_{\text{Ek}}}_{Q_{\text{shelf}}}, 0) = Q_{\text{plume}} = \underbrace{\min(Q_{\text{hyd}}, Q_{\text{geo}}^{\text{QG}})}_{Q_{\text{fjord}}} . \tag{3.19}$$

If we equate $Q_{\text{plume}} = Q_{\text{shelf}}$ assuming that the bottom layer transport does not vanish, we can express H_3^{E} as

$$H_3^{\text{E}} = E^{-3/5} \left(\frac{\kappa W (H_3^{\text{W}} - H_3^{\text{f}})}{L_{\text{Sh}}} - \frac{L\tau_y}{\rho_1 |f|} \right)^{3/5} . \tag{3.20}$$

If all variables are known except H_3^{f} and H_3^{E}, we can solve the system of two equations that arise from equating $Q_{\text{geo}}^{\text{QG}} = Q_{\text{shelf}}$ and $Q_{\text{hyd}} = Q_{\text{shelf}}$ separately (Eq. (3.19)),

$$\begin{aligned} |f| L_{\text{d}}^2 \left(H_3^{\text{f, geo}} - H_3^{\text{E}} \right) + \frac{\kappa W}{L_{\text{Sh}}} H_3^{\text{f, geo}} \\ = |f| L_{\text{d}}^2 (H_{\text{Sh}} - H_{\text{fj}}) + \frac{\kappa W H_3^{\text{W}}}{L_{\text{Sh}}} - \frac{L\tau_y}{\rho_1 |f|} , \end{aligned} \tag{3.21a}$$

$$\begin{aligned} W_{\text{BC}} \sqrt{g'_{5/2}} \left(\frac{2}{3} \left[H_3^{\text{f, hyd}} - H_{\text{S}} - \frac{f^2 W_{\text{BC}}^2}{8 g'_{5/2}} \right] \right)^{3/2} \\ + \frac{\kappa W}{L_{\text{Sh}}} H_3^{\text{f, hyd}} = \frac{\kappa W H_3^{\text{W}}}{L_{\text{Sh}}} - \frac{L\tau_y}{\rho_1 |f|} , \end{aligned} \tag{3.21b}$$

for $E \equiv c_\epsilon (g_0' Q_0)^{1/3}$. These two solutions ($H_3^{\mathrm{f,\,geo}}$ and $H_3^{\mathrm{f,\,hyd}}$) correspond to the water column thicknesses at the fjord mouth for the geostrophic ($Q_{\mathrm{geo}}^{\mathrm{QG}}$) and hydraulic-control (Q_{hyd}) overturning. Unfortunately, these relationships do not lend themselves easily to closed form solutions.

It can be shown that Q_{fjord} corresponds to the maximum H_3^{f}, defined as

$$H_3^{\mathrm{f}} = \max(H_3^{\mathrm{f,\,geo}}, H_3^{\mathrm{f,\,hyd}})\,, \tag{3.22}$$

due to Q_{eddy}, and thus Q_{shelf}, monotonically decreasing with increasing H_3^{f}. We can then solve for H_3^{E} using Eq. (3.20). In Fig. 3.10a, the simulation-diagnosed H_3^{f} is shown vs. the solution to Eq. (3.22), which predicts the simulation values with a coefficient of determination of $r^2 = 0.86$. In Fig. 3.10b, the simulation-diagnosed H_3^{E} is shown vs. the solution to Eq. (3.20), which predicts the simulation values with a coefficient of determination of $r^2 = 0.84$.

Thus, substituting H_3^{E} in Eq. (3.18) for Q_{plume} predicts the warm AW inflow as an explicit function of the input parameters in Sect. 3,

$$Q_3(H_3^{\mathrm{f}}, H_3^{\mathrm{E}}) = Q_3(H_{\mathrm{S}}, W_{\mathrm{BC}}, \tau_y, Q_0, H_3^{\mathrm{W}}, \rho_n)\,. \tag{3.23}$$

This can also be evaluated using any of the formulas for the individual regions in Sects. 3.4.1-3.4.3 as a result of Eq. (3.19).

In Fig. 3.11, the simulation-diagnosed AW inflow is shown vs. the solution to Eq. (3.23). Even though predictions in each of the three individual regions are accurate separately (as shown in Fig. 3.9b-d), this comparison demonstrates that the overall prediction for the entire shelf-to-glacier-face theory predicts the AW inflow transport with a coefficient of determination $r^2 = 0.89$ and may be calculated a priori without knowledge of H_3^{f} and H_3^{E}. The theory provides a way to prognostically understand the role of each of the six parameters in the three regions (the continental shelf, the fjord mouth sill, and the fjord head) in setting the isopycnal gradients from the shelf to the glacier. This also provides a simple tool for guiding the interpretation of observations or estimation of parameters in Eq. (3.23) that may be difficult to observe.

3.5 Recirculation and Vorticity Balance

Although the overturning circulation is a critical component of the renewal of fjords and has received more attention in existing literature, the horizontal recirculation may play an equally important role in fjord dynamics and glacial melt rates. Specifically, recent work suggests that the near-glacier horizontal velocity, which owes its magnitude to the horizontal recirculation within the fjord, plays an important role in driving ambient front-wide glacial melt and may be comparable to the subglacial discharge-driven melt (Slater et al. 2018, Jackson et al. 2019). The importance of this contribution to melt rate is further discussed in Appendix G.

We approach the theory of horizontal recirculation strength using a recirculation region-integrated vorticity budget. We start with Eq. (3.2a) and multiply by thickness, h, and take the curl of the result to express the vorticity budget within each layer as

$$\underbrace{\partial_t \overline{\nabla \times h\mathbf{u}}}_{\text{tendency}} + \underbrace{\nabla \times (\nabla \cdot (\overline{h\mathbf{u}\mathbf{u}}))}_{\text{vort. advection}} - \underbrace{f\overline{\varpi}}_{\text{vort. generation}} - \underbrace{\nabla \times (\overline{\mathbf{u}\varpi})}_{\text{diapycnal advection}} = - \underbrace{\nabla \times \overline{h\nabla\phi}}_{\text{form stress curl}} - \underbrace{C_d \nabla \times \overline{|\mathbf{u}|\mathbf{u}}}_{\text{friction}} . \tag{3.24}$$

In the bottom layer, we find the dominant terms to be the diabatic vorticity generation, vorticity advection, and the bottom friction. Integrating Eq. (3.24) over the recirculation region, we find that the vorticity advection and diapycnal advection are each up to 15% of the magnitude of the other two terms and form stress curl and tendency are negligibly small (not shown). Therefore, our steady state balance may be roughly approximated by the diabatic vorticity generation, which spins up the bottom layer recirculation, and the bottom friction, which spins it down. This can be expressed as

$$\iint f\overline{\varpi}\,\mathrm{d}A \approx \iint C_d \nabla \times \overline{|\mathbf{u}|\mathbf{u}}\,\mathrm{d}A\,. \tag{3.25}$$

We can simplify this relationship with a scaling argument for Eq. (3.25) in terms of the recirculation strength ψ_r and bottom layer transport Q_3. The time-average of Eq. (3.2b)

implies that $\overline{\varpi} = \nabla \cdot \overline{h\mathbf{u}}$ and by continuity, Q_3 equals the area integral of $\nabla \cdot \overline{h\mathbf{u}}$ in the diabatic region (a subregion of the bottom layer recirculation), so the left hand side of Eq. (3.25) is equal to fQ_3.

The right hand side of Eq. (3.25) (using Stokes' theorem) scales as

$$\iint C_d \nabla \times \overline{|\mathbf{u}|\mathbf{u}}\, \mathrm{d}A = \oint_{\partial A} C_d \overline{|\mathbf{u}|\mathbf{u}} \cdot \hat{\tau}\, \mathrm{d}s \sim C_A C_d (\psi_r/(L_r H^E))^2\,, \tag{3.26}$$

where $\hat{\tau}$ is a unit vector tangent to the boundary contour ∂A and s is the corresponding along-contour coordinate over the gyre recirculation region A, and C_A is the circumference of the region A. Here, the mean velocity acted on by bottom friction scales as $\psi_r/(L_r H^E)$ for bottom friction concentrated in a boundary layer width L_r and near-glacier bottom layer thickness, H^E.

Thus, based on Eq. (3.25), we can make the following scaling argument

$$Q_3 f \sim C_A C_d \psi_r^2/(L_r H^E)^2\,. \tag{3.27}$$

Based on our simulation results, L_r falls empirically between the boundary current width and the fjord half-width, $L_r \sim (L_\mathrm{d} + W_\mathrm{fj}/2)/2$. For narrow fjords $W_\mathrm{fj} < L_\mathrm{d}$, this empirical relationship fails and the recirculation boundary width likely fills the entire fjord half-width, $L_r \sim W_\mathrm{fj}/2$, which is untested due to resolution limitations. Therefore, for fjords of width L_d or larger, the scaling for recirculation strength is

$$\psi_r = \left(f(L_r H^E)^2 Q_3/(C_A C_d)\right)^{1/2}\,. \tag{3.28}$$

In Fig. 3.12, we compare the simulation recirculation strength to Eq. 3.28, which shows the theory predicts the bottom layer recirculation strength over varying parameters with a coefficient of determination of $r^2 = 0.87$. Additionally, if we assume a constant vorticity in the recirculation gyre, the maximum velocity v_max is approximately

$$v_\mathrm{max} \sim 2\psi_r/(L_r H^E)\,, \tag{3.29}$$

which is a useful parameter for the melt rate estimate further discussed in Sect. 3.7 and Appendix G.

3.6 Roles of Fjord Geometry and Variability

The simulation results in Sect. 3.3 and overturning and recirculation theory in Sects. 3.4 and 3.5 aim to capture many factors controlling fjord circulation. However, there are additional fjord circulation characteristics and phenomena that are potentially also important and deserve further investigation. First, we present an expanded discussion on the role of vertical and horizontal hydraulic control in fjord circulation and as a driver of intra-fjord variability. Following this, we diagnose the existence and role of low-frequency variability within the fjord and coastal currents in our simulations and subsequently, its high-frequency counterpart including submesoscale variability.

3.6.1 Transition to Hydraulic Control

In Sect. 3.4.2, we applied simple theories for the transport in geostrophic and hydraulically-controlled flows. Although these simple theories fit our simulation results, the onset of hydraulic control in a complex fjord-to-shelf geometry (with both horizontal and vertical constrictions) in the presence of variability is not adequately addressed in the hydraulic-control theory literature and requires further discussion.

In Fig. 3.13, we highlight the transition from the geostrophic to the hydraulically-controlled regimes in our simulation results. We compare the diagnosed nondimensionalized transport ($\hat{Q} \equiv Q/Q_{\text{geo}}^{\text{QG}}$) to the geostrophic and hydraulic control theory predictions (Eqs. (3.15) and (3.17)), calculated as a function of nondimensionalized sill height ($H_{\text{S}}/H_3^{\text{W}}$). The subpanels show xy-plane maps of the composite Froude number G for three cases of varying sill height, with the hydraulically-controlled case exhibiting critical values of $G \approx 1$.

In the sensitivity experiments (Sect. 3.3), we varied each parameter individually relative to the reference case, but further regimes are possible when we co-vary parameters. Fig. 3.14 shows the nondimensionalized mean bottom layer transport ($\hat{Q} = Q/Q_{\text{geo}}$) and its root-mean-square deviation as a function of nondimensionalized sill height (H_S/H_3^{W}) and fjord width

($W_{\mathrm{fj}}/L_{\mathrm{d}}$)for one such combination of parameters: co-varying sill height and fjord width. In this figure, for nondimensionalized sill heights above 0.5, the overturning circulation weakens, but for higher fjord widths, this critical sill height threshold increases to 0.9. Although the fjord widths tested in Sect. 3.3 are not narrow enough to permit hydraulically-controlled solutions, fjord width does lead to hydraulic control for taller sills, which is only apparent after co-varying sill height and fjord width.

The hydraulic control theory quantitatively captures the transport reduction in Fig. 3.14 for tall sills $H_{\mathrm{S}}/H_3^{\mathrm{W}} > 0.5$ and narrow fjords $W_{\mathrm{fj}}/L_{\mathrm{d}} < 1$. This also suggests the possibility that fjord width may lead to hydraulic control for sill heights $H_{\mathrm{S}}/H_3^{\mathrm{W}} < 0.5$, but requires narrower fjord widths. This is supported by the limitation of boundary current hydraulic control transport (Eq. (3.17)) on fjord width if it is narrower than the deformation radius. The transition to hydraulic control is also likely to vary for the covariation of other parameters, although this is untested.

The right panel in Fig. 3.14 shows that RMSD is greater for wider fjords, where shelf eddies can more easily penetrate into the fjord, and cases near hydraulic control, which reflects the observation that the regions of critical flow ($G \approx 1$) are also important sources of variability. This is due to the formation of isopycnal jumps/shocks with the same properties observed in Zhao et al. (2019), which have been shown to convert mean baroclinic and barotropic energy into eddy kinetic energy, and may be characterized as Kelvin-wave hydraulic shocks (Hogg et al., 2011).

3.6.2 Long-Term Variability and Periodic Flushing Events

In addition to variability on the shelf maintained by baroclinic instability (which leads to the across-shelf exchange, Q_{eddy}) and the variability generated at hydraulic shocks near vertical/horizontal constrictions, we observe additional modes of variability.

Longer-term variability of the overturning circulation exists in our simulations and occurs

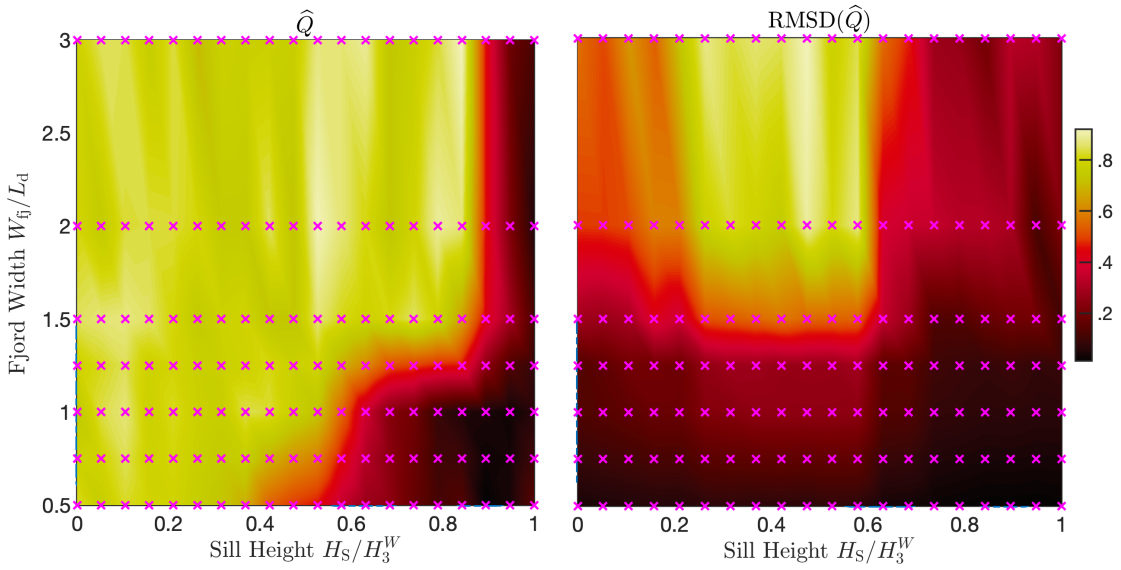

Figure 3.14: Time-averaged (days 1300-1600) nondimensionalized bottom layer transport ($\hat{Q} = Q/Q_{\mathrm{geo}}$) and its root-mean-square deviation as a function of nondimensionalized sill height ($H_{\mathrm{S}}/H_3^{\mathrm{W}}$) and fjord width ($W_{\mathrm{fj}}/L_{\mathrm{d}}$). All other parameters are fixed to the reference case. Pink markers represent the geometric parameter combinations tested.

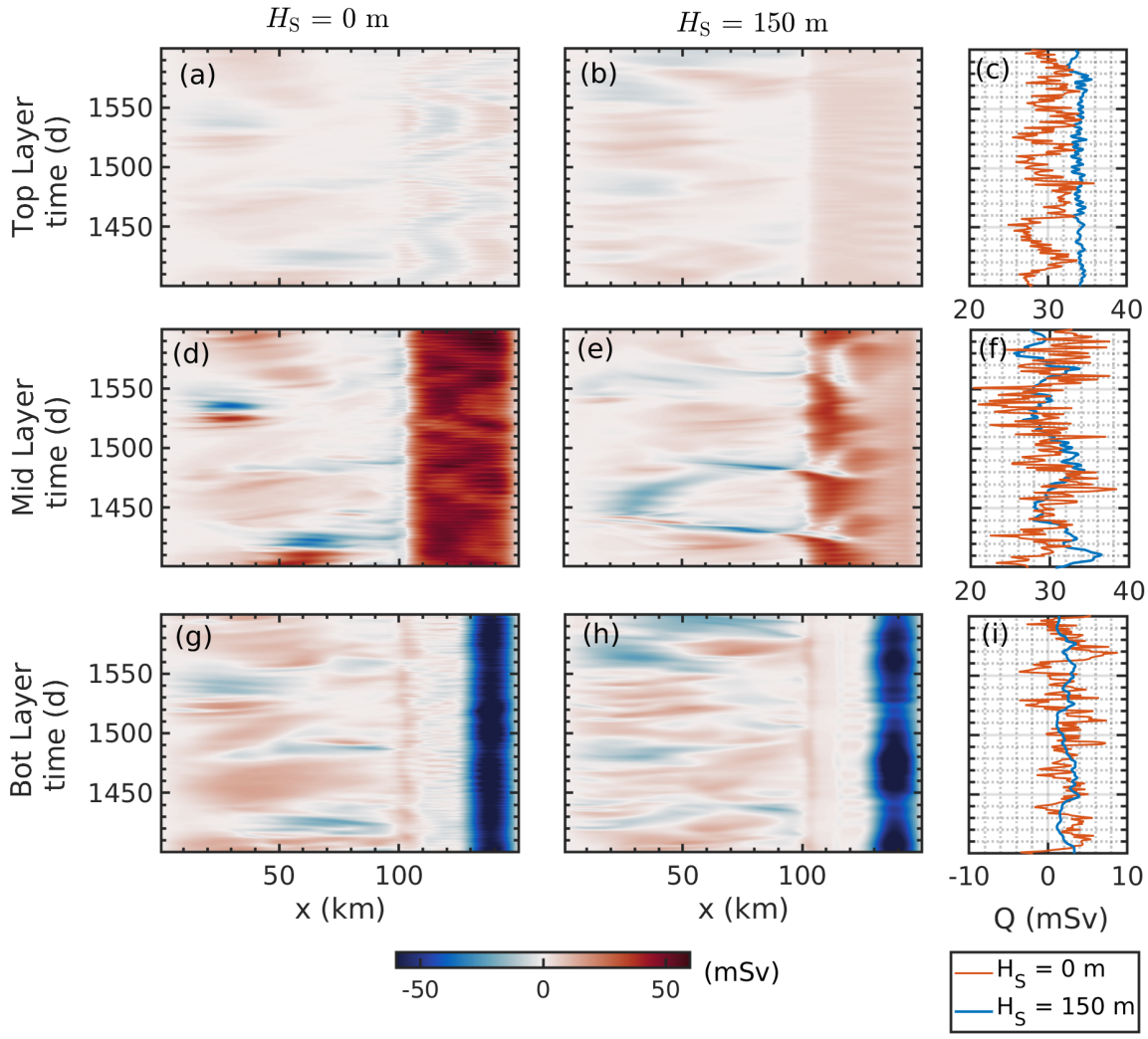

Figure 3.15: (a)-(c) Top, (d)-(f) middle, and (g)-(i) bottom layer zonal transport Q calculated by integrating from y = 75 km (midline) to y = 79 km (northern fjord boundary). This is shown as a function of x for two cases of sill height: $H_S = 0$ m (left column) and $H_S = 150$ m (middle column) for the same fjord width $W_{fj} = 8$ km. The right column shows the timeseries of this half-fjord transport at $x = 107.5$ km (sill maximum). Periodic flushing events on timescales of 60 days (long-term variability) are more apparent for the $H_S = 150$ m case in the middle and bottom layers, while high frequency variability on timescales of 1-2 days is more apparent in the $H_S = 0$ m case, but also exists in the $H_S = 150$ m case.

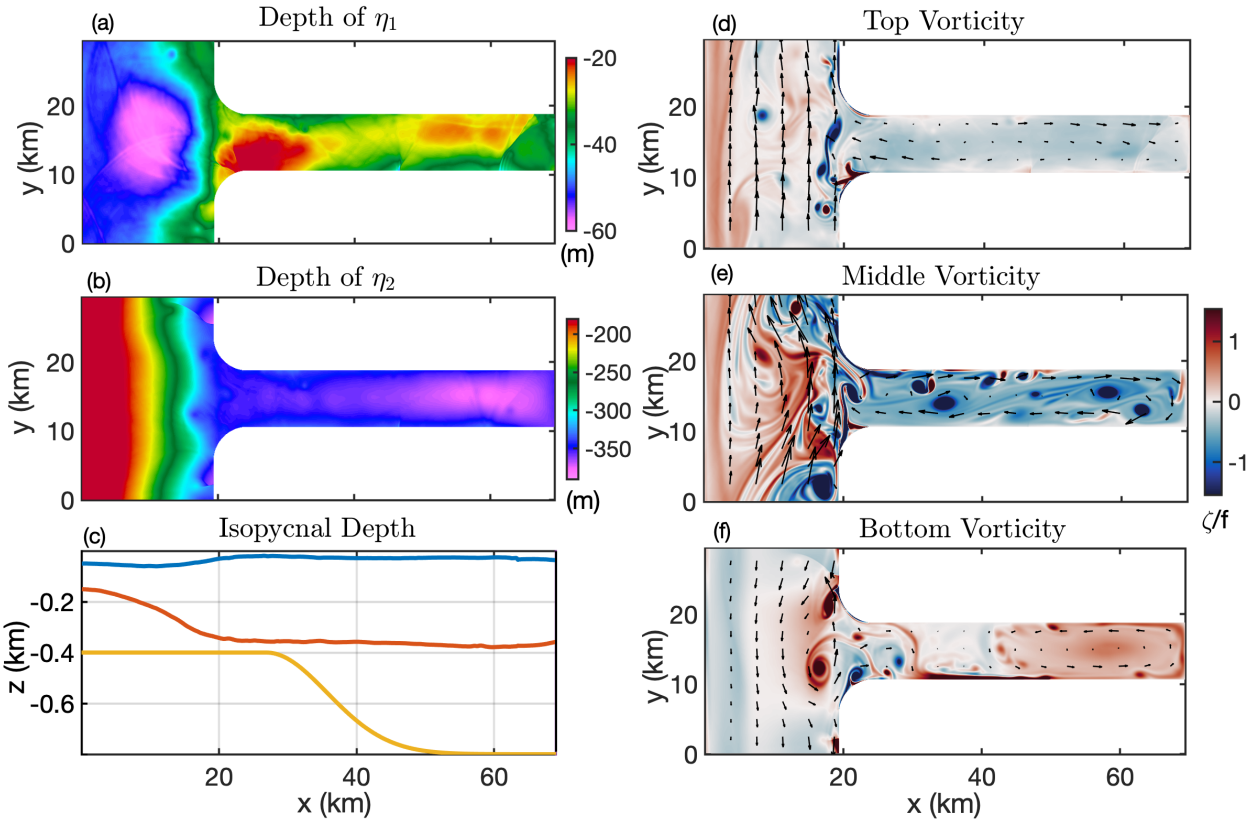

Figure 3.16: High-resolution (dl = 68 m) simulation of a case with no sill and $W_{\text{fj}} = 8$ km with snapshots of (a),(b) surfaces of interface depth η_1 and η_2 and (c) their along-midline depth ($y = 75$ km). (d)-(f) Snapshot of vorticity with velocity quivers for each layer (at day 200). The maximum velocities are 0.42, 0.66, 0.37 m/s in the top, middle, and bottom layers, respectively.

simultaneously with perturbations in horizontal recirculation strength. To illustrate this, we show a time series of zonal transport using a Hovmöller plot for a $H_S = 0$ m case in Fig. 3.15a,d,g in comparison with a $H_S = 100$ m case in Fig. 3.15b,e,h (with columns corresponding to layer). In these Hovmöller plots, the transport is integrated from $y = 75$ km to 79 km (inflow into northern half of the fjord) as a function of x and time, since it visually highlights the variability of recirculation and exchange near the fjord mouth. The right column (Fig. 3.15c,f,i) shows this northern half zonal transport profiled at the sill maximum ($x = 107.5$ km).

In the middle layer (Fig. 3.15d,e,f), we observe three cycles of a periodic flushing event on timescales of 60 days, which is approximately the residence timescale of the fjord, $\tau_r = W \times L \times H/Q$. This is particularly clear in the $H_S = 150$ m case, where the sill is tall enough to influence the middle layer. In Fig. 3.15e, this periodic flushing appears as blue streaks representing westward outflow, which originate in the middle layer fjord interior as a disruption to the anticylonic recirculation and propagate across the shelf over a period of 20 days. The trend of the half-fjord transport at the sill-overflow in Fig. 3.15f also clearly shows a periodic signal on 60 day cycles for the $H_S = 150$ m case (blue line). The bottom layer exhibits the same periodic signal, but is approximately 3 times weaker due to weak recirculation near the sill maximum since the main region of recirculation extends from $x =$ 130 km to 150 km (whose magnitude also observably varies over a 60 day cycle in Fig. 3.15h). Fig. 3.15c,f,i shows that in general, the $H_S = 0$ m case has more short-term variability and the $H_S = 150$ m exhibits greater long-term variability.

The long-term variability (compared to the short-term) has a smaller contribution to the overall RMSD of the overturning circulation in the $H_S = 0$ case, but becomes increasingly important to consider for fjords with limited overturning and renewal.

The short-term variability accounts for most of the RMSD in Fig. 3.4 except for a few cases of weak overturning. This variability is apparent in Fig. 3.15 as the 1-2 day fluctuations in transport, although it is diagnosed differently. Within the fjord, this variability is

dominated by coastally-trapped waves, which are generated either at the fjord mouth/sill maximum (due to the horizontal and vertical constriction) or the coastal current. The amplitude of the observed waves is larger for wider fjords, intermediate sill heights, stronger winds, stronger subglacial discharge, and larger zonal pressure gradients. The daily and monthly timescales of short-term and long-term variability, respectively, coexist in Fig. 3.15c,f,i.

3.6.3 Submesoscale Fjord Dynamics

The simulations presented so far span the non-eddying to weakly-eddying regime within the fjord. Although the eddy kinetic energy within the fjord is weak due to our choice of resolution, it does increase substantially for high-resolution simulations of fjord-only domains. We find that although the total overturning strength and recirculation strength do not depend strongly on resolution ($\sim$20% increase for both from dl = 1000 m to dl = 68 m), submesoscale eddies do appear within fjords and the eddy contribution accounts for a significant proportion of the overturning circulation (up to 40% in the highest resolution cases).

In Fig. 3.16, a reference run at high resolution (dl = 68 m) with $H_{\mathrm{S}} = 0$ m and $W_{\mathrm{fj}} = 8$ km shows evidence of submesoscale activity. The submesoscale eddies in Fig. 3.16d-f have a peak vorticity of $\zeta/f \approx 4$ and diameters on the order of 1 km, which are small compared to the deformation radius. They are found to be primarily generated near the curved sidewall regions near the mouth of the fjord. These eddies influence both the mean along-fjord and across-fjord isopycnal gradients, as can be seen in Fig. 3.16a-c in comparison with the corresponding low-resolution case in Fig. 3.6a.

In the surfaces of interface depth (Fig. 3.16a-b), coastally-trapped waves (as previously discussed) appear to form isopycnal shocks within the fjord and near the coastal current. These waves and shocks propagate in the prograde direction and have shock amplitudes that decay from the coast with a width L_{d} and are similar in behavior to the Kelvin wave hydraulic shocks discussed in Hogg et al. (2011). Interestingly, the bottom layer coastal eddies in Fig. 3.16f propagate in the same direction as the waves and shocks (northward/prograde), while

the background coastal mean flow in this layer is southward. In both reality and models that permit such effects, these sources of variability may lead to elevated mixing in the fjord interior and variability of the recirculation and boundary current transport, which may be explored in a future study.

3.7 Discussion and Conclusions

3.7.1 Summary

In glacial fjords, there is a complex interaction of dynamics in the shelf, fjord, and discharge/melt plumes, with multiple controls of the overturning circulation and horizontal recirculation (Straneo and Cenedese, 2015; Carroll et al., 2017; Jackson et al., 2018). In this chapter, we examine the influence of key geometric controls (sill height, external stratification, and fjord width) on overturning in the shelf-to-glacial face system and horizontal recirculation in the fjord interior.

In Sect. 3.2, we discuss the idealized 3-layer numerical model setup to simulate the full shelf-to-glacial-face system. We examine the sensitivity of overturning and recirculation to six important parameters in Sect. 3.3 that capture variations in geometry (fjord width and sill height), boundary forcing (AW depth, winds, and subglacial discharge), and stratification. We find that the overturning and recirculation increase more significantly with decreasing sill height, deeper AW, and increasing subglacial discharge (shown in Figs. 3.4 and 3.5). Additionally, the horizontal recirculation significantly increases with fjord width.

We develop and test comprehensive theories that provide clarity on the role of each control in Sect. 3.4. The theory for the overturning circulation is pieced together using theories for the continental shelf, the fjord mouth sill, and the fjord head regions. The theory accurately predicts the simulated overturning over realistic ranges of each control parameter for each of the three regions and provides predictions for the AW layer thickness at the fjord mouth and fjord head (Fig. 3.10), which can be used to predict the overall AW transport (Fig. 3.11).

In Sect. 3.5, we develop a theory for the bottom-layer horizontal recirculation based on a vorticity balance between bottom friction and the diabatic vorticity generation of the water mass transformation, which accurately predicts the recirculation over realistic ranges of each control parameter (Fig. 3.12).

In Sect. 3.6 we discuss the modes of external and internal variability of the system. We further discuss hydraulic control at the fjord mouth and the role of both low-frequency and high-frequency variability on the shelf and within the fjord. The sill overflow can transition from geostrophic to hydraulically-controlled regimes with varying sill height, AW depth, and fjord width, and can explain the reduction in warm water inflow over realistic fjord parameters similarly to results from Zhao et al. (2019). Submesoscale variability was also observed in a configuration with a fjord attached to a smaller coastal shelf region shown in Fig. 3.16, and potentially plays an important role in the overturning and recirculation.

3.7.2 Glacial Melt Rate Implications

Using the theories we presented in Sects. 3.4 and 3.5 supported by the numerical simulations presented in Sect. 3.3, we can estimate glacial melt rates taking into account fjord circulation. The melt rate is predominantly dependent on two parameters: the vertical velocity of the discharge plume, which depends on discharge strength and the stratification set by open ocean and the overturning circulation, and the near-glacier horizontal velocity (the main driver of ambient melt), which depends on the strength of the horizontal recirculation.

Although we do not expect accurate estimates given the possible range of the empirical coefficients C_d and γ_T, it is still useful to provide melt rate estimates based on Eqs. (G.1a) - (G.2b) with horizontal and vertical velocities from our simulation results and theory, which we hope will guide future circulation-aware glacial melt rate parameterizations (further discussed in Appendix G). Our predicted maximum discharge plume-driven melt rate (or rate of undercutting) for Jakobshavn parameters is 8.7 m/day and the predicted ambient melt rate over the rest of the terminus in contact with the bottom layer AW is 1.1 m/day. However,

due to its much larger area, the ambient melt accounts for 80% of the total volume melt and is $\sim$1.0 km^3/year based on a bottom layer thickness of 400 m and fjord width of 8 km (see Appendix G for further details). However, the freshwater input is still dominated by the discharge plume rather than meltwater, which supports our model assumptions of excluding the meltwater contribution to the buoyancy forcing in the fjord and supports recent findings that ambient melt driven by horizontal recirculation may be as important or more than the subglacial discharge-driven melt (Slater et al., 2018; Jackson et al., 2019).

The connection between overturning circulation, horizontal recirculation, and melt rates raises the possibility of a dynamical feedback, which is not simulated in our model and can be described as follows: stronger horizontal recirculation leads to stronger ice front velocities, which leads to higher melt rates by increasing turbulent transfer of heat to the ice face, which leads to stronger buoyancy forcing and thus, water mass transformation and overturning, which induces stronger horizontal recirculation to balance the vorticity budget. However, additional modeling and observations are needed to assess the importance of the melt-circulation feedback.

3.7.3 Caveats

Due to the limitations of a simplified model configuration, there are a number of caveats. These include the simplicity of geometry on the shelf, the lack of sea ice/melange/icebergs and surface buoyancy forcing in the fjord, the low-order representation of vertical structure in the ocean, and a lack of time-dependent buoyancy forcing (both the plume and open-ocean conditions). In general, the across-shelf transport is likely to be much more complicated than presented in this study, with canyons and remotely-generated coastal currents playing important roles (e.g., St-Laurent et al., 2013; Moffat et al., 2009), such that a more realistic across-shelf transport component of the theory is likely more complex. Also, tests of the inter-fjord separation distance (not shown) suggest that the strength of the coastal current is influenced by this parameter. Furthermore, since we only consider mixing due to the

entrainment of the ambient and discharge plume, our theories assume that tides and sill overflows/bottom boundary layer processes are small contributions to the overall mixing. To account for this, the theory from Sect. 3.4 can be modified to include such contributions by replacing Q_{plume} with a total diabatic mixing term, $Q_{\text{diab}} = Q_{\text{plume}} + Q_{\text{tide}} + Q_{\text{BBL}}$. The overall overturning prediction in Eq. (3.23) can therefore by modified to include realistic parameterizations of Q_{tide} and Q_{BBL}. However, the potential importance of vertical mixing throughout the fjord to the overall overturning circulation remains an open question.

CHAPTER 4

Melt-Circulation Feedbacks

4.1 Introduction

Outflowing of marine-terminating glaciers at the margins of the Greenland Ice Sheet and Antarctic Ice Sheet has accelerated in recent years (van den Broeke et al., 2016). For the Greenland Ice Sheet, a major cause of the accelerated melting is postulated to be the warming of deep ocean currents that come into contact with the termini of tidewater glaciers (Wood et al., 2018; Cowton et al., 2018; Holland et al., 2008; Straneo and Heimbach, 2013).

Submarine melt at marine-terminating glaciers drives glacial retreat and also amplifies iceberg calving depending on the properties of the glacier and fjord (Slater et al., 2021; Wood et al., 2021; Morlighem et al., 2016; Chauché et al., 2014; Fried et al., 2018; Rignot et al., 2015; Wagner et al., 2016). The submarine melt rate consists of ambient face-wide melt and discharge plume-driven melt (Straneo and Cenedese, 2015; Jackson et al., 2019). Although subglacial discharge plumes have the potential to drive a melt rate of more than a meter per day in the glacial area near the plume (equivalent to a volumetric melt of $\mathcal{O}(10^4)$ to $\mathcal{O}(10^5)$ m^3/day, assuming a fjord width of 5 km), it only occupies a small fraction of the glacial face (Cowton et al., 2015; Slater et al., 2018). By comparison, face-wide melting occurs along the entire glacial face as a result of either convection (Magorrian and Wells, 2016) or fjord circulation (Bartholomaus et al., 2013). Estimates of face-wide melt rates range widely, but are generally below 1 meter per day (and may be up to $\mathcal{O}(10^6)$ m^3/day of volumetric melt, based on an average glacial face area). Yet, only recently have studies

considered the possibility that existing parameterizations of the ice-ocean boundary layer may be underestimating the contribution of face-wide melt (Jackson et al., 2019; Slater et al., 2018).

Fjord circulation has primarily been studied in the context of an estuary-like overturning circulation where warm and salty open-ocean water masses flow into the fjords at depth, and colder and fresher water masses flow out of the fjord at shallower depths (Stigebrandt, 1981; Farmer and Freeland, 2021; Inall and Gillibrand, 2010; Cottier et al., 2010). However, compared to most estuaries (Geyer and MacCready, 2014), deep glacial fjords in Greenland have relatively weak tidal influence and most of the vertical mixing is posited to occur near the glacial face (Straneo and Cenedese, 2015). The focus of previous 2D and 3D simulations of the shelf-to-fjord system has been to understand the sensitivity of glacial melt and the overturning circulation/fjord renewal to various fjord characteristics and atmospheric/oceanic drivers (e.g., Gladish et al. 2015, Sciascia et al. 2013, Xu et al. 2012, and Jackson et al. 2018).

So far there are very few process-oriented models or theoretical efforts to quantify the interaction between fjord circulation and glacial melt rate within fjords. Along with the relative scarcity of ocean observations near marine-terminating glaciers, only recently has the horizontal recirculation within fjords and their sensitivity to fjord and forcing parameters received attention in models (Zhao et al., 2019, 2021a), which has been suggested to have an influence on the face-wide melt rates (Slater et al., 2018; Jackson et al., 2019; Zhao et al., 2021a; Carroll et al., 2017). Existing melt parameterizations either do not take into account horizontal near-glacier velocities (e.g., Sciascia et al. 2013, Xu et al. 2012) or do not resolve the horizontal flows necessary for accurate melt rate predictions (e.g., Cowton et al. 2015, Carroll et al. 2017). To remedy this, bulk glacial melt parameterizations should ideally use either near-glacier horizontal velocities based on resolved circulations or use predictions of near-glacier horizontal velocities in terms of the fjord forcing, geometry, and stratification.

To better understand these processes, we conduct a process-oriented exploration of fjord

parameter space using simulations that can finely resolve the near-glacier horizontal circulation. We support these simulations with simple dynamical theories of overturning circulation, horizontal recirculation in the fjord interior, and glacial melt rate. Using these results, we address a gap in understanding of how fjord circulation and glacial melt co-interact, which has important implications for glacial retreat at the oceanic margins of ice sheets.

4.2 Fjord Model Setup

4.2.1 Model Configuration

To examine the interaction of fjord circulation and glacial melt, we use the Massachusetts Institute of Technology general circulation model (MITgcm, Marshall et al. 1997) in a series of idealized high-resolution simulations. Our model uses an idealized geometric representation of a simple bathtub-like fjord-only domain with sloping side walls, a glacier face along its western boundary, and a Gaussian zonal sill centered at $x_S = 20$ km (see Fig. 4.1a). The model domain dimensions are $L \times W \times H = 25$ km $\times$ 6 km $\times$ 800 m. There is quadratic bottom drag with a coefficient of 2×10^{-3} and no surface forcing. The eastern boundary region is nudged to a prescribed open ocean stratification in our reference experiment, based on near-fjord mouth observations from Ilulissat Icefjord (Gladish et al., 2015; Straneo and Cenedese, 2015), and includes a barotropic tidal velocity boundary condition in two of our perturbation experiments. See Appendix H for further information on the model setup.

On the western boundary, the model is forced by a subglacial discharge plume parameterization at the fjord midpoint ($x = 0$, $y = W/2$) and a face-wide melt plume parameterization across the glacial face. Both plume parametrizations are based on buoyant plume theory, as described in Cowton et al. 2015. The plume parameterization solves 1D equations for mass and momentum conservation vertically along the plume, while heat and salt evolve in response to advection, entrainment of ambient waters, and the turbulent transfer to the ice face (Hellmer and Olbers, 1989). The plume is coupled to the circulation and stratifi-

cation, allowing us to study feedbacks between plume dynamics and the fjord circulation. See Appendix H for further discussion of both plume parameterizations and the details of the coupling between the plumes to the model domain (slightly modified from Cowton et al. 2015).

The model horizontal resolution is 38 m and the vertical resolution is 8 m. We use a Smagorinsky biharmonic horizontal viscosity and the K-Profile Parameterization (KPP) of the vertical viscosity and diffusivity (Smagorinsky, 1963; Large et al., 1994), in addition to a background vertical diffusivity of 10^{-6} m^2 s^{-1}. We use an f-plane approximation with a representative Coriolis parameter of $f = 1.31 \times 10^{-4}$ s^{-1}, corresponding to latitudes in central Greenland. The model experiments are run for 1 year because the fjord recirculation adjusts slowly and requires multiple months of spinup for some of the test cases, and all results shown (unless otherwise specified) are time-averaged over the last month.

4.2.2 A Reference Case

Fig. 4.1 illustrates the setup and circulation of our reference simulation. We impose a subglacial discharge plume of $Q_0 = 100$ m^3/s, as well as a face-wide melt plume. For reference, most subglacial discharge plumes around Greenland range from 0 to 1000 m^3/s with most fjords at the weaker end of this range (Mankoff et al., 2020). The reference case fjord dimensions are specified in Sect. 2.1 with a sill maximum at $z = -250$ m depth and a stratification similar to Ilulissat fjord (e.g., Gladish et al., 2015; Straneo and Cenedese, 2015) with no tidal forcing. The reference case parameters are shown in the table in Appendix J.

The vorticity snapshots at $z = -100$ m and $z = -600$ m in Fig. 4.1b, c suggest intense submesoscale variability based on the vorticity magnitude and structures generated near the sill overflow, boundary current, and plume outflow. At depth, the sill-crossing overflow (located at $x = 18.5$ km) drives energetic small-scale variability and vorticity. The overflow also feeds a cyclonic boundary current, which periodically becomes unstable and sheds eddies into the interior (see Fig. J.1 in Appendix J). At shallower depths, the plume outflow is

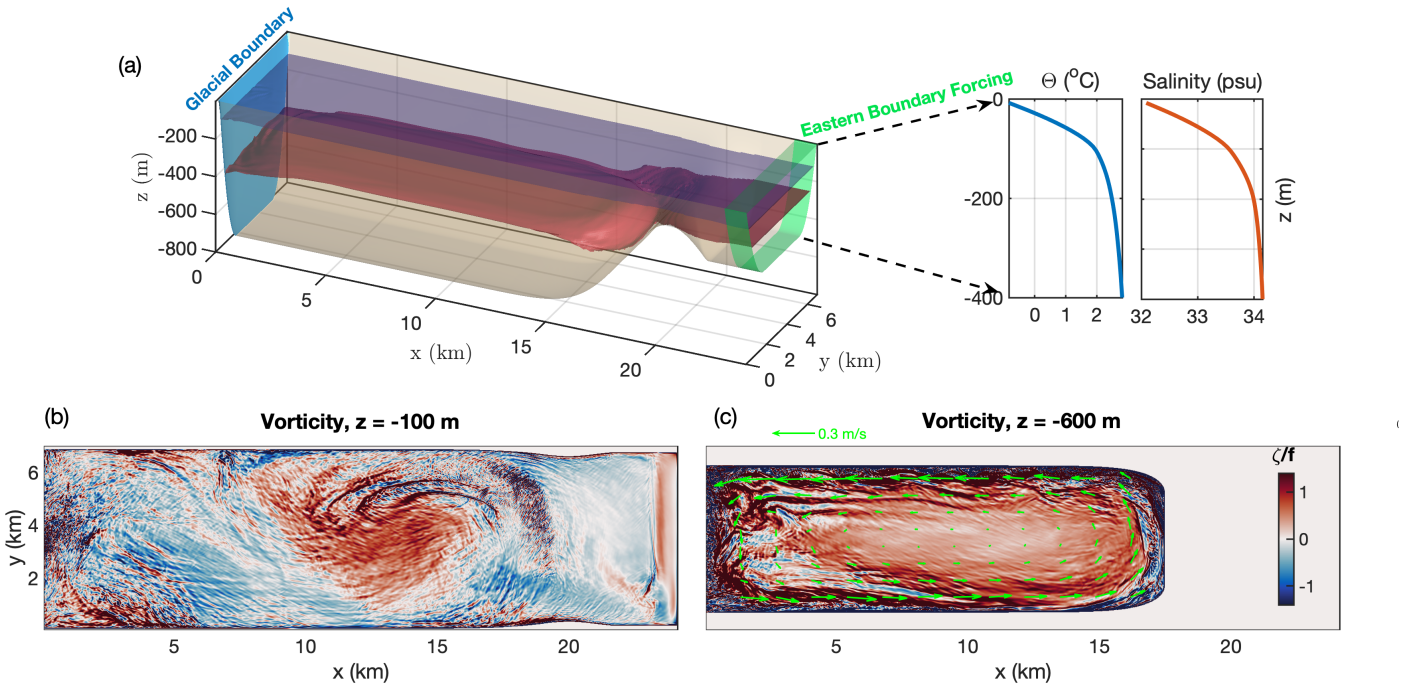

Figure 4.1: Reference simulation as specified in Sect. 4.2.2 showing (a) fjord geometry with two density interfaces $\sigma = 27.2$ (dark blue), 27.6 (red) kg/m^3 and the eastern boundary temperature and salinity forcing; and (b),(c) contemporaneous snapshots of normalized vorticity at $z = -100$ m and $z = -600$ m, respectively. Velocity quivers are included in panel (c).

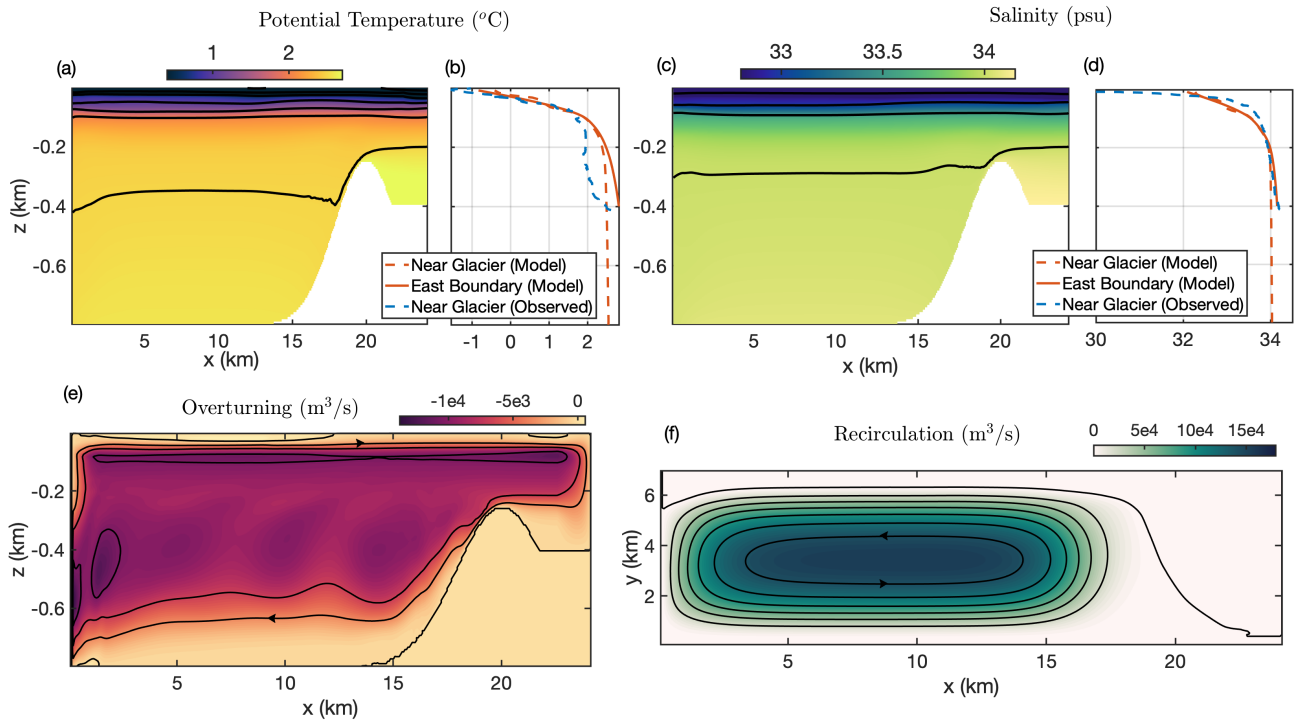

Figure 4.2: Time-averaged profiles of (a) meridionally-averaged temperature, (c) meridionally-averaged salinity with (b, d) model/observation comparisons using Ilulissat Icefjord data (Gladish et al., 2015; Straneo and Cenedese, 2015), and (e) meridionally-integrated overturning streamfunction, and (f) vertically-integrated recirculation strength over the bottom 600 m. The contour spacings are 0.5 °C, 0.5 psu, 3×10^3 m^3/s, and 2×10^4 m^3/s, in panels (a, c, e, f) respectively.

the dominant source of variability and is greatest at the neutral buoyancy depth (near $z = -100$ m). The intrafjord submesoscale variability likely plays an important role in fjord stratification and mixing, circulation, and melt rates, but a more complete exploration will be deferred to a future study.

To illustrate the simulated fjord state, in Fig. 4.2 we plot profiles of time- and meridionally-averaged potential temperature and salinity, and compare them with observations from Illulisat Icefjord (Gladish et al., 2015; Straneo and Cenedese, 2015). The profiles of potential temperature and salinity at the ice face vs. the mouth of the fjord (panels (b) and (d)) show the effect of the water mass transformation driven by the near-glacier plumes. The modification of the inflowing water properties is more pronounced in the observations (Beaird et al., 2017) because we use a smaller discharge in our reference simulations than is observed in Illulisat Icefjord.

We quantify the fjord overturning circulation via the overturning streamfunction (Fig. 4.2e), which is calculated via

$$\psi(x,z) = \int_0^W \int_{z_B(x,y)}^z \overline{u}\ \mathrm{d}z'\,\mathrm{d}y'\,. \tag{4.1}$$

Here, $\overline{u}$ is the time-averaged velocity in the x-direction (and defined to be 0 outside the bowl-shaped domain) and $z_B(x,y)$ is the bathymetric elevation. To quantify the horizontal recirculation, we first calculate the horizontal quasi-streamfunction

$$\Psi(x,y,z) = \int_0^y \overline{u}\,\mathrm{d}y'\,, \tag{4.2}$$

which is an approximation to the 3D streamfunction and is further discussed in Appendix I. We quantify the strength of the horizontal recirculation via the maximum value of the horizontal quasi-streamfunction in the region between the glacier face and the sill maximum:

$$R(z) = \max_{0<x<20\,\mathrm{km}} \{\Psi(x,y,z)\}\,. \tag{4.3}$$

The vertically-integrated recirculation strength (over the bottom 600 m) is shown in Fig. 4.2f. The overturning and recirculation observed in our model results are idealized versions of the

complex circulation observed in fjords with real geometries, but magnitudes are similar to those observed in nature (see Slater et al. 2018, Straneo and Cenedese 2015, and references therein).

4.3 Controls on Fjord Circulation and Glacial Melt

In order to understand the interaction of fjord circulation and glacial melt rate, we conduct a suite of experiments to test the effects of varying the glacial boundary layer parameterizations, discharge plume strength, geometric constraints, stratification, and tides. A complete list of the parameter ranges is shown in the table in Appendix J.

To understand the effect of the glacial face plumes on the fjord circulation and its feedback on melt rates, we compare four cases: the reference case and three different melt parameterizations, as listed in the table in Appendix J. The reference case ($\mathrm{Q_{100}M_P}$) includes a subglacial discharge plume with $Q_0 = 100$ m^3/s and a melt plume representing the face-wide melt (which for comparison, contributes a freshwater flux of approximately 40 m^3/s). We additionally test three cases: (1) only the melt plume and no discharge ($\mathrm{Q_0M_P}$), (2) a boundary layer melt parameterization and no discharge ($\mathrm{Q_0M_{BL}}$, using the 3-equation thermodynamics with no melt plume, based on Hellmer and Olbers 1989), and (3) a discharge plume only ($\mathrm{Q_{100}}$).

Fig. 4.3 shows how the near-glacier meridionally-integrated overturning streamfunction (using ψ from Eq. (4.1) and zonally-averaging over the near-glacier region, $0 < x < 5$ km), recirculation strength (R, using Eq. (4.2)), and meridionally-averaged melt rate (M) vary for each of these four cases. The overturning, recirculation, and melt rate are comparatively negligible for the boundary layer-only case $\mathrm{Q_0M_{BL}}$ because it does not include entrainment into the melt plume, which drives most of the overturning in the $\mathrm{Q_0M_P}$ case. The overturning circulation of the $\mathrm{Q_0M_P}$ case peaks at a depth of -500 m, while the $\mathrm{Q_{100}}$ case peaks at the discharge plume neutral buoyancy depth of -100 m. The two plumes are approximately

additive, i.e., the melt plume-only and discharge plume-only experiments can be added together to approximately obtain the overturning circulation in the reference case, which utilizes both plumes.

Fig. 4.3 suggests that there is an approximate correlation between overturning, recirculation, and melt rate with depth, which we will discuss further in Sect. 4.4. Contrary to expectations that discharge plumes (when active) drive a majority of the melt (Straneo and Cenedese, 2015), the melt plume case shows a total melt rate that is approximately 70% of the reference case melt rate. However, the rate of undercutting (defined here as the average melt rate over the bottom 200 m) for the two cases are nearly equal because although the overturning is weaker for this case, it is located deeper in the water column, where the warmer water recirculation drives a significant percentage of the melt rate. By comparison, the discharge plume-only case only accounts for 40% of the reference case melt rate because the overturning is located at shallower depths. Note also that most of the discharge plume-driven melt occurs over the face-wide area instead of the area where the plume is in contact with the glacial face (see Fig. 4.3c).

The sensitivity of the overturning, recirculation, and melt rates to discharge strength, sill height, fjord depth and width, stratification, and tides are also important and similarly show a correlation between vertical profiles of overturning, recirculation, and melt rate (see Figs. J.2-J.5 in Appendix J of the parameter sensitivity cross-section plots of temperature, salinity, overturning, recirculation, and melt rates).

Decreasing the sill height removes barriers of warm water access to the fjord (Fig. J.2e) and increases melt rates by 20% for the case with no sill relative to the reference case (Fig. 4.4e). Increasing the fjord width from 6 km to 15 km approximately doubles the recirculation (Fig. J.5f) and also doubles the melt rates (Fig. 4.4f) for the $W = 25$ km case. Decreasing the fjord depth weakens the overturning circulation (Fig. J.4g) and melts a smaller cross-sectional glacial surface area, which results in a 25% decrease in melt rate for the shallow depth case ($H_{\mathrm{fj}} = 600$ m) compared to the reference case (Fig. J.5g). Increasing

the surface stratification slightly strengthens the deep overturning (Fig. J.4h), recirculation (Fig. J.5h), and therefore, melt rate (Fig. 4.4h). The strength of the tides can also amplify the overturning circulation at the glacial face at depths near the sill maximum depth and can lead to a 30% increase in overall melt rates (Fig. 4.4i) for a barotropic tidal amplitude of 0.1 m/s.

An important takeaway is that increasing the discharge strength leads to diminishing increases in circulation strength and melt, i.e., increasing discharge has a strong effect for weaker discharge rates, but a significantly weaker effect on melt rates beyond the discharge rate of $Q = 100$ m^3/s in the reference case. Increasing the discharge by an extreme factor of 10 (the $\mathrm{Q_{1000}M_P}$ case) relative to the reference case increases the overturning by a factor a 2.5, but this only increases the melt rate by 30%. The reason for the diminished importance of discharge-driven melt is that increases in discharge primarily amplifies the shallow overturning and recirculation, which has a smaller impact on the overall melt rate due to the colder waters present at these depths.

4.4 Linking Fjord Renewal, Horizontal Circulation, and Melt

In order to understand the sensitivity of glacial melt rates to fjord parameters, we extend previous theories (Zhao et al., 2021a) to relate the fjord overturning, recirculation, and melt to the parameters studied in Sect. 4.3.

4.4.1 Overturning Theory

Our theory for the overturning circulation uses the sum of the discharge plume entrainment and the melt plume entrainment (Morton et al., 1956; Cowton et al., 2015; Straneo and Cenedese, 2015):

$$\psi(x=0,z) \approx \beta_p B^{1/3}(z-z_B)^{5/3} + \beta_m W \left(\frac{\rho_w g_0'}{\rho_i}\right)^{1/3} M_0^{1/3}(z-z_B)^{4/3}\,. \tag{4.4}$$

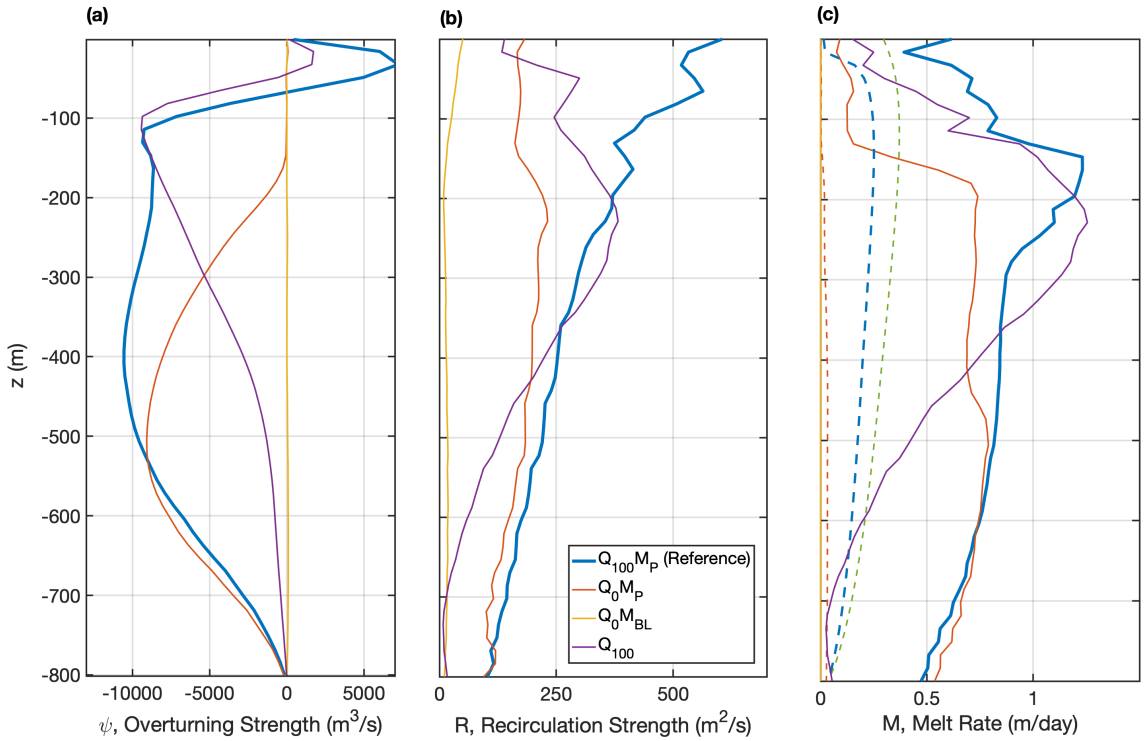

Figure 4.3: Profiles of (a) meridionally-integrated overturning streamfunction, (b) recirculation strength (as defined in Sect. 4.2.2), and (c) meridionally-averaged melt rate for the reference case ($Q_{100}M_P$), a melt plume only case (Q_0M_P), a boundary layer melt parameterization case (Q_0M_{BL}), and subglacial discharge only case (Q_{100}). The dotted lines in the melt rate panel show the direct contribution of the subglacial discharge plume to the meridionally-averaged melt rate.

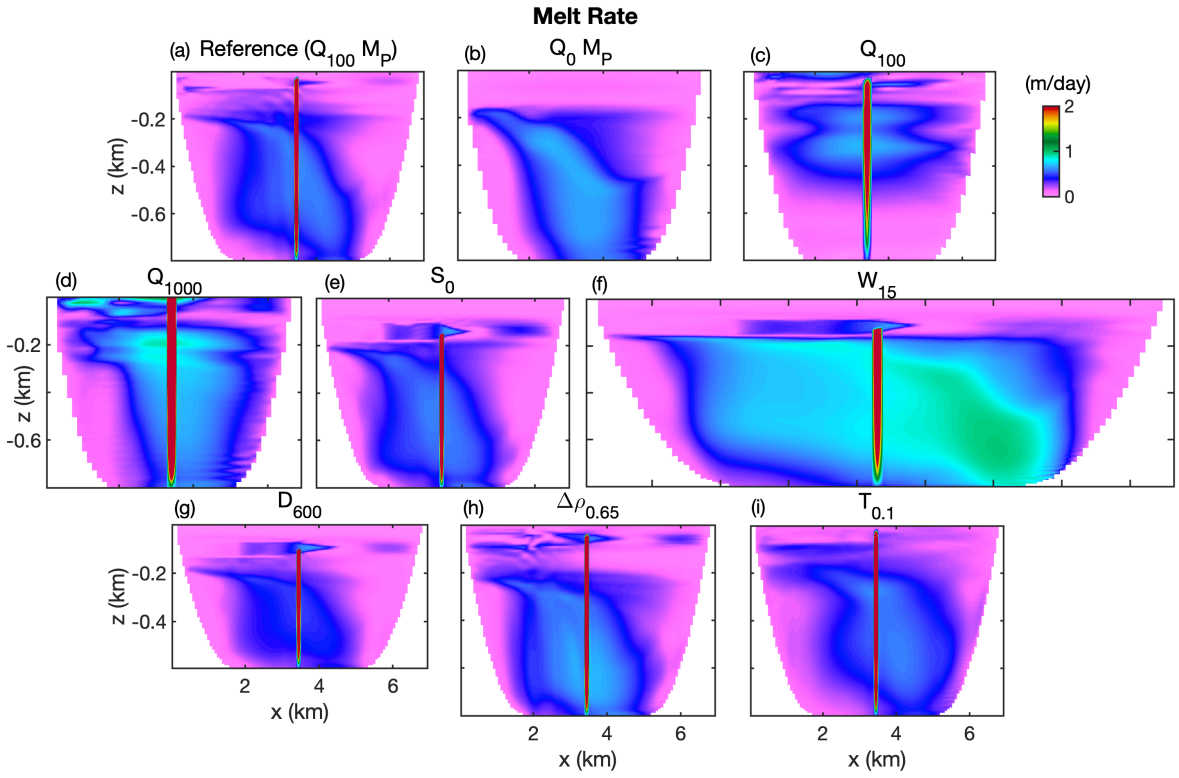

Figure 4.4: (a)-(i) Time-averaged melt rates (m/day) at the glacial face for 9 experiments with varying parameters (see the table in Appendix J for the specific parameters for each case).

Here, $\beta_p = (6/5)(9/5)^{1/3}\pi^{1/3}\epsilon^{4/3}$ (entrainment factor for a half-cone plume) and $\beta_m = (3/4)(4/5)^{1/3}\epsilon^{2/3}$ (entrainment factor for a sheet plume), which depend on an experimentally-derived entrainment coefficient, $\epsilon = 0.13$ (Linden, 2000). Additionally, M_0 is the melt rate (assumed to be constant with depth in the uniform density region) and ρ_w and ρ_i are the density of fresh water and ice, respectively. The discharge plume buoyancy flux $B(z) = g'Q$ varies with depth, but assuming an approximately uniform background density (ρ) below the neutral buoyancy depth yields $B \approx B_0 = g'_0 Q_0$, where B_0 is the buoyancy flux at the plume source, Q_0 is the subglacial discharge rate, and the reduced gravity is $g'_0 = g(\rho - \rho_w)/\overline{\rho}$. The neutral buoyancy depth of the discharge plume is primarily dependent on background stratification and weakly sensitive to the water mass transformation rates.

The melt plume buoyancy flux (last term in Eq. (4.4)) uses a simplified depth-constant melt rate M_0, but this can be extended to a depth-varying melt rate $M(z)$ and both the discharge plume and melt plume buoyancy flux contributions may be extended to depth-varying background density and solved numerically (see Appendix H for further details). Our simulations suggest that the depth variation of $M(z)$ is proportional to the time-mean near-glacier along-face velocity $\overline{v}(z)$ via the relationship $M(z) \approx k_M \overline{v}(z)$ for a proportionality constant $k_M \approx 0.035$, which is further discussed in Sect. 4.3. This relationship suggests a potential feedback between melt, overturning, and horizontal recirculation.

4.4.2 Recirculation Theory

In order to understand the relationship between overturning and recirculation, we apply the scaling arguments from Zhao et al. 2021a based on the vorticity balance. This shows that below the neutral buoyancy depth (which can be predicted using plume theory; see Appendix H), vorticity generated by water mass transformation due to the glacial boundary conditions (both the melt plume and discharge plume) is primarily balanced by the curl of bottom drag (as evidenced by Fig. J.6 in Appendix J).

Based on an approximate balance between these two vorticity terms, we derive the fol-

lowing scaling relationship between the overturning streamfunction and recirculation

$$\langle \psi(x,z) \rangle_x \approx \frac{C_F C_d}{f L_r^2 H_b^2} \left(\int_{-H}^{z} R(z')\, \mathrm{d}z' \right)^2 . \tag{4.5}$$

Here, $C_\mathrm{F} = 2(W + x_S)$ is the circumference of the fjord recirculation region, $C_d = 2 \times 10^{-3}$ is the bottom drag coefficient, and the boundary current width L_r is empirically approximated by $L_r \sim (L_\mathrm{d} + W/2)/2$ for a deformation radius L_d. We use the zonal average of the overturning streamfunction $\langle \psi(x,z) \rangle_x$ over the near-plume region $0 < x < L_r$ as a numerical approximation to the plume-driven overturning $\psi(x = 0, z)$ from Eq. (4.4). The water column thickness of the recirculation region below the neutral depth is $H_b = H - |z_N|$, where z_N is the neutral depth and H is the depth of the fjord. See Zhao et al. 2021a for a more detailed discussion of this scaling theory.

4.4.3 Melt Rate Theory

In order to extend our predictions of recirculation to total melt rate, we apply another scaling approximation from Zhao et al. 2021a that relates the time-mean horizontal tangential velocity $\overline{v}(z)$ at the glacial face to the horizontal recirculation, expressed as $\overline{v}(z) \approx 2R(z)/(L_r H_b)$. Assuming that the melt rates are primarily driven by horizontal velocities, which is true for the majority of the glacial surface area, the 3-equation thermodynamics (using e.g., Hellmer and Olbers 1989, Holland and Jenkins 1999 and assuming ice temperatures that are close to boundary layer ocean temperatures) allows us to simplify this relationship to a linear melt rate $M(z)$ (in m/s) that is approximately proportional to $\overline{v}(z)$ (and thus, $R(z)$),

$$M(z) = \frac{c_w(T_p - T_b)}{L_i + c_i(T_b - T_i)} C_d^{1/2} \Gamma_T \sqrt{\overline{v^2} + \overline{w^2}} \approx \underbrace{\frac{c_w(T_p - T_b)}{L_i} C_d^{1/2} \Gamma_T}_{\equiv k_M} |\overline{v}| \tag{4.6}$$

where $L_i = 3.35 \times 10^5$ J kg^{-1} is the latent heat of fusion of ice, $c_i = 2 \times 10^3$ J kg^{-1} K^{-1} is the specific heat capacity of ice, $c_w = 3.974 \times 10^3$ J kg^{-1} K^{-1} is the specific heat capacity of water, $C_d = 2 \times 10^{-3}$ is the bottom drag coefficient, $\Gamma_T = 2.2 \times 10^{-2}$ is the thermal transfer constant (corresponding to a thermal Stanton number $C_d^{1/2}\Gamma_T = 10^{-3}$), and T_b, T_p, T_i are

the boundary layer, plume, and ice temperature, respectively. For further discussion on this melt rate approximation, see Appendix K.

4.4.4 Summary of Theories

We can rewrite the relationships in Eqs. (4.4)-(4.6) and the plume theory (in Appendix H) as a priori predictions for the bulk overturning, recirculation, and melt rate explicitly in terms of the subglacial discharge, fjord width and depth, stratification, and near-glacier horizontal velocity.

The bulk overturning strength prediction (i.e., the overturning streamfunction in Eq. (4.4) evaluated at the neutral buoyancy depth z_N) can be expressed as

$$\psi(z_N) \approx \beta_p (g_0' Q_0)^{1/3} (z_N - z_B)^{5/3} + \beta_m W \left(\frac{\rho_w g_0'}{\rho_i} \right)^{1/3} (k_M \langle \overline{v} \rangle_z)^{1/3} (z_N - z_B)^{4/3} . \tag{4.7}$$

Fig. 4.5a and 4.5b show the predicted vs. simulation-diagnosed values of the neutral buoyancy depth based on plume theory and the overturning strength, respectively. These two comparisons show that over the range of parameters, the neutral buoyancy depth is well-approximated by plume theory (see e.g., Turner 1979), with a squared correlation coefficient of 0.92; similarly, overturning strength is well-approximated by Eq. (4.7), with a squared correlation coefficient of 0.89.

Using Eq. (4.5) and (4.7), we can express the depth-averaged recirculation below the neutral buoyancy depth in terms of the bulk overturning strength

$$\langle R \rangle_z \approx \left(\frac{\psi(z_N) f L_r^2}{C_F C_d} \right)^{1/2} , \tag{4.8}$$

or less accurately (as was used in the melt rate theory in Eq. (4.6)), the depth-averaged along-face zonal velocity

$$\langle R \rangle_z \approx L_r (H + z_N) \langle \overline{v} \rangle_z / 2 . \tag{4.9}$$

We note that equating the approximations in Eq. (4.8) and (4.9) allows us to relate the bulk

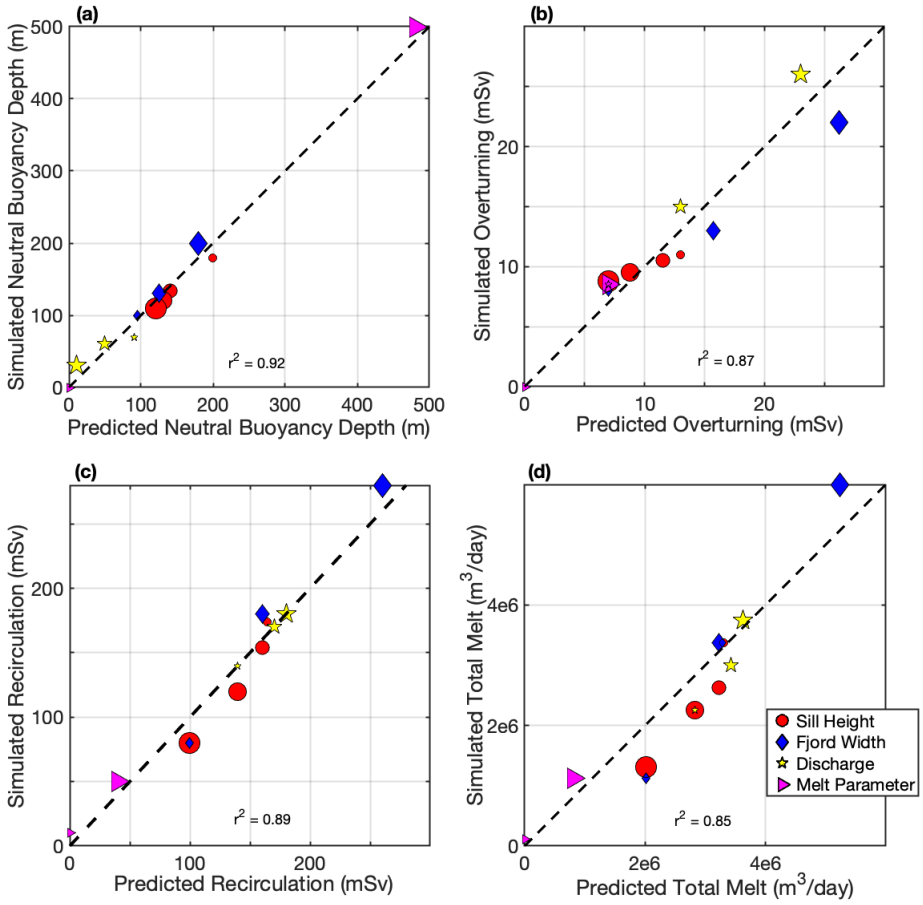

Figure 4.5: Simulation-diagnosed vs. theoretical predictions for (a) the neutral buoyancy depth based on plume theory, (b) the overturning circulation based on plume theory (Eq. (4.7)), (c) the depth-averaged recirculation based on the bulk overturning strength (Eq. (4.8)), and (d) the overall glacial melt rate based on the recirculation theory (Eq. (4.11)).

overturning to the depth-averaged near-glacier along-face velocity,

$$\langle \overline{v} \rangle_z \approx \frac{2f\psi(z_N)}{C_F C_d (H + z_N)}\,, \tag{4.10}$$

thereby removing the dependence of these theories on $\langle \overline{v} \rangle_z$, which is an essential (albeit less accurate) step to making the melt theory fully predictive i.e., without requiring a priori knowledge of the along-glacier velocity.

Fig. 4.5c shows a comparison between the predicted depth-averaged recirculation below the neutral buoyancy depth using Eq. (4.8) and the corresponding simulation-diagnosed recirculation using Eq. (4.2). The recirculation above the neutral buoyancy depth is not included since vorticity advection primarily balances water mass transformation above this depth and the assumptions used for the scaling arguments used to derive Eqs. (4.5) and (4.8) no longer apply. Additionally, the melt rates in this region only account for a small percentage of the overall melt rate since the outflowing glacially-modified water masses are much colder. However, the recirculation at depths between the sill maximum and the neutral buoyancy depth are taken into account in Eqs. (4.5) and (4.8). Fig. 4.5c shows that over the range of parameters, recirculation varies over a large range, but is well-approximated by this simple scaling argument, with a squared correlation coefficient of 0.89.

Finally, the depth-averaged melt rate can be expressed as

$$\langle M \rangle_z \approx k_M \langle \overline{v} \rangle_z\,. \tag{4.11}$$

Fig. 4.5d shows a comparison between the predicted depth-averaged melt rate calculated from Eq. (4.11) multiplied by the glacial surface area and the corresponding value diagnosed from the simulation by integrating the melt rate over the entire glacial face. This shows that over the range of parameters, melt rate varies significantly, but is relatively well-approximately by this simple scaling argument. Although the prediction of total melt rate is less accurate (with a squared correlation coefficient of 0.85) than the predicted recirculation, this is likely because the melt rate theory requires additional approximations and assumptions. The melt

rate can also be (less accurately) related to the bulk overturning strength or depth-averaged recirculation using Eqs. (4.10) and (4.9), respectively, to remove the dependence on the the near-glacier along-face velocity. The fully predictive theory for the total melt rate in terms of the overturning streamfunction by substituting Eq. (4.10) in Eq. (4.11) is compared with the simulation diagnosed melt rate in Fig. J.7 (which has a squared correlation coefficient of 0.72).

4.5 Discussion and Conclusion

In this chapter, we use a high-resolution idealized model (see Sect. 4.2) to analyze the sensitivity of glacial melt to fjord circulation (in Sect. 4.3) and address an important gap in scientific understanding: how fjord circulation and glacial melt co-influence each other and how to predict their bulk values as a function of fjord parameters. To achieve this, we extended previous theories (in Sect. 4.4) to predict the overturning, recirculation, and melt rates as functions of the model fjord parameters. These relationships are summarized in Eqs. (4.7)-(4.11), which explicitly express the sensitivity of the circulation and melt to each of the fjord parameters and illustrate the melt-circulation feedback, using the near-glacier velocity as a common link.

We found that a majority of the glacial melt occurs over the entire glacial front, instead of being localized to the discharge plume. For the highest discharge case ($Q_{1000}M_P$), the discharge plume region accounts for only 26% of the overall melt (and only 18% for the reference case) even though it increases the peak overturning strength by a factor of 2.5, because it confines this overturning to a narrow depth range near the neutral buoyancy depth. Most of the parameter variations we studied had a significant impact on the overall melt rate (see Fig. 4.4 for a figure showing the sensitivity of glacial melt distributions to fjord characteristics). These variations in melt can be theoretically related to the recirculation and overturning circulation, which in turn have two drivers: a face-wide melt plume and a

discharge plume.

The discharge plume drives a shallower overturning than the face-wide melt plume and, therefore, the face-wide melt plays a significantly larger role in glacial melt because it provides a greater proportion of the deep overturning. In this deep overturning circulation, warm water masses flow toward the glacial face at a range of depths primarily in the deeper half of the fjord, and flows away in the upper half (see the Q_0M_P case in Fig. 4.2a). Our results show that over most of the fjord parameter range studied, the deep overturning within fjords is primarily driven by melt, and the overall melt is primarily driven by recirculation at depth, which is correlated with the deep overturning circulation. This glacial melt seems to be concentrated at depth due to the warm water available at these depths, where the stratification is weaker. Additionally, the warm-water renewal in the deeper waters of the fjord is more strongly controlled by face-wide melt compared to the subglacial discharge plume. This potentially has implications that fjords with weak subglacial discharge year-round or in wintertime conditions can still have substantial melt rates as long as warm water is present within the fjord. There is observational evidence that suggests this may occur in some fjords (Wood et al., 2018), but more wintertime glacial melt rate observations are needed to confirm this phenomenon.

There are numerous caveats in this chapter due to the limitations of our simple model configuration. These include the simplicity of fjord geometry, atmospheric forcing, vertical mixing representation, the lack of sea ice, mélange, and icebergs, which can supply substantial buoyancy input (Enderlin et al., 2016). As a result of the high-resolution fjord-only domain, a caveat is the prescription of the eastern open-ocean boundary. The eastern boundary in our model is nudged to the open-ocean stratification, which is fixed for our simulation, so the boundary likely does not capture all of the variability that a fjord-shelf system would be able to include; there can be a shelf current-induced increase/ decrease in the exchange between the fjord and shelf (Zhao et al., 2021a). We also do not consider the effect of winds, which likely exhibits a larger effect on the shelf region via fjord

overturning driven by coastal upwelling (not included in our domain), but may also directly drive fjord circulation/renewal for strong enough katabatic wind events (Zhao et al., 2021a; Spall et al., 2017). Although this choice is an imperfect one, the eastern boundary is nudged to fjord mouth observations (from Gladish et al. 2015); in reality, a domain that includes the shelf would likely establish a balance between the shelf stratification and near-glacial stratification to set the stratification at the fjord mouth (e.g., Zhao et al. 2021a). Also, in our glacial boundary parameterization, the melt rates are calculated using the closest grid point of horizontal and vertical fjord velocities, which is an imperfect representation; in general, a better understanding and representation of the ice-ocean boundary layer needed to improve glacial melt rate estimates.

CHAPTER 5

Realistic Fjord Geometry and the Existence of Standing Eddies

5.1 Introduction

The recent acceleration of outflowing marine-terminating glaciers at the margins of the Greenland Ice Sheet and Antarctic Ice Sheet has received widespread attention (van den Broeke et al., 2016). In the Greenland Ice Sheet, the primary cause of the accelerated melting is postulated to be the warming of deep ocean currents that come into contact with the termini of tidewater glaciers (Holland et al., 2008; Straneo and Heimbach, 2013; Wood et al., 2018; Cowton et al., 2018). This submarine melt at the sides of marine-terminating glaciers drives glacial retreat and also amplifies iceberg calving depending on the properties of the glacier and fjord (Slater et al., 2021; Wood et al., 2021; Morlighem et al., 2016; Chauché et al., 2014; Fried et al., 2018; Rignot et al., 2015; Wagner et al., 2016). The submarine melt rate consists of ambient face-wide melt and discharge plume-driven melt (Straneo and Cenedese, 2015; Jackson et al., 2019). Although subglacial discharge plumes have the potential to drive a melt rate of more than a meter per day in the glacial area near the plume, it only occupies a small fraction of the glacial face (Cowton et al., 2015; Slater et al., 2018). By comparison, face-wide melting occurs along the entire glacial face as a result of either convection (Magorrian and Wells, 2016) or fjord circulation (Bartholomaus et al., 2013).

The focus of previous 2D and 3D simulations of the shelf-to-fjord system has been to understand the sensitivity of glacial melt and the overturning circulation/fjord renewal to

various fjord characteristics and atmospheric/oceanic drivers (e.g., Gladish et al. (2015), Sciascia et al. (2013), Xu et al. (2012), and Jackson et al. (2018)). Along with the relative scarcity of ocean observations near marine-terminating glaciers, only recently has the horizontal recirculation within fjords and their sensitivity to fjord and forcing parameters received attention in models (Zhao et al., 2019, 2021a), which has been suggested to have an influence on the face-wide melt rates (Slater et al., 2018; Jackson et al., 2019; Zhao et al., 2021a; Carroll et al., 2017). Existing melt parameterizations either do not take into account horizontal near-glacier velocities (e.g., Sciascia et al. (2013), Xu et al. (2012)) or do not resolve the horizontal flows necessary for accurate melt rate predictions (e.g., Cowton et al. (2015), Carroll et al. (2017)).

To better understand these processes in the context realistic fjord geometries, we conduct high-resolution fjord simulations of three major Greenland deep-water fjords and compare the emergent dynamics to results from previous studies. We will use simple dynamical theories of overturning circulation, horizontal recirculation in the fjord interior, and glacial melt rate from previous studies (Zhao et al., 2021a,b) to understand the model behavior. Using these results, we address a gap in understanding of how 3D fjord circulation drives melt in realistic fjord geometries, which has important implications for glacial retreat at the oceanic margins of ice sheets.

In Sect. 5.2, we present our model setup, configuration, and design philosophy. We also present an overview of the phenomenology and dynamics of the three representative regional fjord simulations used in our chapter: Ilulissat, Sermilik, and Kangerdlugssuaq. In Sect. 5.3, we present the discovery of multiple long-lived standing eddies for each fjord simulated. As a representative example with important melt implications, we discuss the properties of the standing eddy near the Ilulissat glacial face, its spinup, transport, mergers with other eddies, and its influence on Lagrangian and Eulerian residence times within the fjord. We also briefly discuss the properties of the other eddies in our three regional simulations and their preferred locations relative to fjord bathymetry. In Sect. 5.4, we discuss the vorticity

balance within Ilulissat fjord, which demonstrates the importance of the standing eddies to the integrated vorticity budget and use this to develop a scaling theory for the vertical profile of the near glacial horizontal velocity. We use this theory to predict the vertical profile of melt rate and discuss how standing eddies influence and in some cases, potentially amplify glacial melt. In Sect. 5.5, we summarize and discuss the major implications and caveats of our findings and suggest future avenues of research.

5.2 Setup of Regional Models

The design of our model setup is primarily motivated by the need for an improved understanding of the 3D circulation within warm, deep-water fjords with realistic geometries. Various characteristics of the 3D circulation were previously shown to be an important factor in determining glacial melt rates (Zhao et al., 2021b).

Fig. 5.1 shows the bathymetry around Greenland using the Bedmachine V3 bathymetric dataset (Morlighem et al., 2017). Along the perimeter, glacial fjords connect marine-terminating glaciers to the ocean on the continental shelf. The zoomed-in panels show the three Greenlandic fjord-shelf domains (Ilulissat, Kangerdlugssuaq, and Sermilik) selected for this chapter that are some of the widest and longest of Greenland's warm, deep-water fjords. Because these three fjords generally have a larger flux of solid ice and freshwater into the ocean and can be more easily resolved, they are chosen to be the subject of our regional fjord simulations; however, many more are planned in future studies. For each of these regional simulations, our primary aim is to capture the key drivers of the steady-state fjord circulation and to ignore time-varying and secondary effects or those that we cannot currently adequately represent. We anticipate that these models will greatly benefit from the inclusion of parameterizations of unresolved ice-ocean processes and have significant room for improvement in the future. The model configuration specifics are described in the following two subsections.

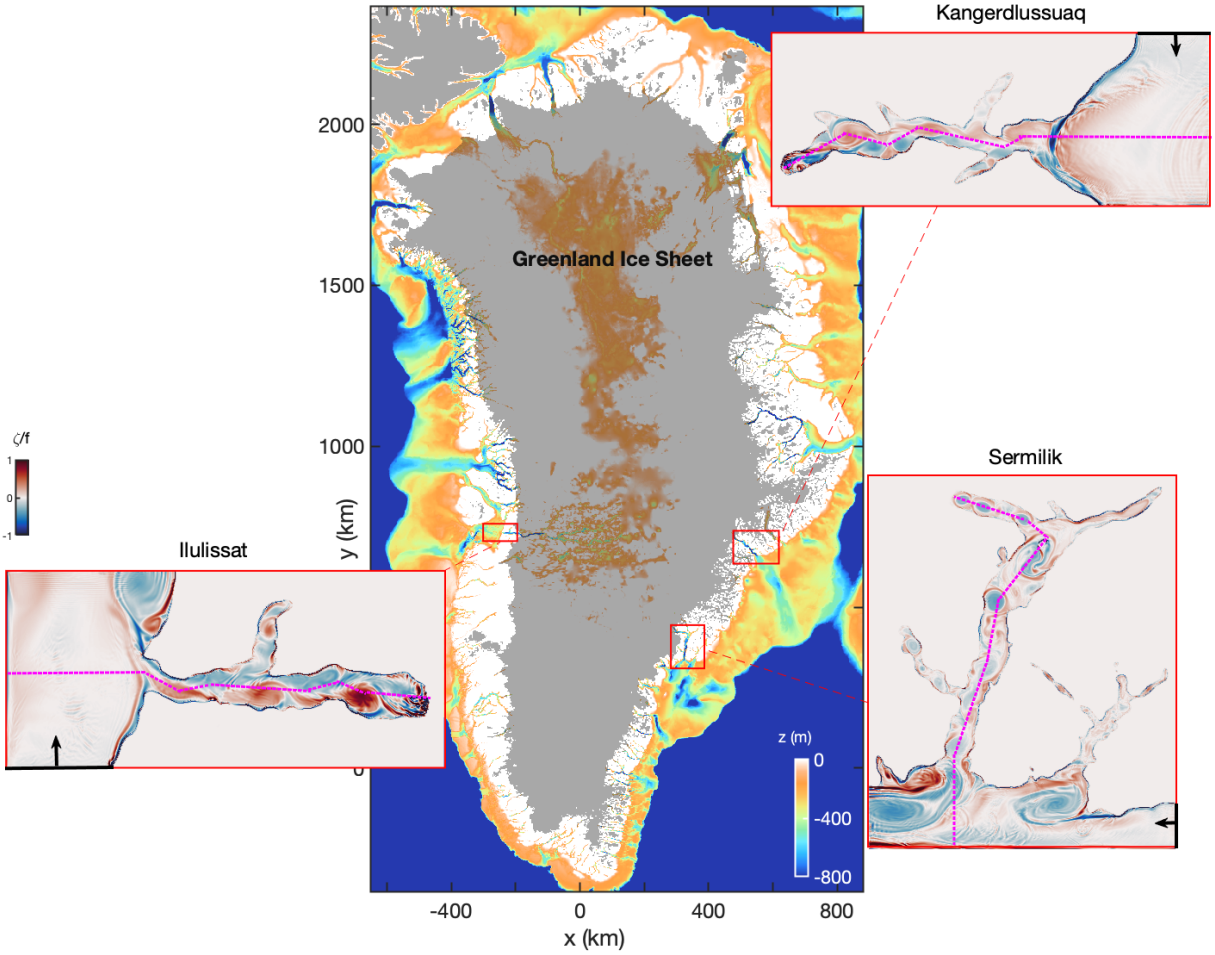

Figure 5.1: A map of Greenland bathymetry and ice sheet extent (shown in gray). The zoomed-in panels of three regional model domains show a near-surface (z = - 90 m) instantaneous vorticity at day 100. The piecewise-linear transects used in model diagnostics are shown in dotted pink and the boundary with imposed inflowing conditions (forced by velocity, temperature, and salinity) are shown in black. The bathymetry data shown uses Bedmachine V3 data (Morlighem et al., 2017).

5.2.1 Model Configuration

The model used in the chapter is the Massachusetts Institute of Technology General Circulation Model (MITgcm) (Marshall et al. 1997; see data availability statement). Using this model, we solve the hydrostatic, Boussinesq primitive equations with a nonlinear equation of state based on Jackett and McDougall (1995) in three high-resolution configurations of Ilulissat, Sermilik, and Kangerdlugssuaq fjords and a small area of the adjacent shelf for each simulation.

The model bathymetry for each of the three regions uses the Bedmachine V3 data (Morlighem et al., 2017), which has a 150 m horizontal resolution (see Fig. 5.1). The bathymetry shallower than 20 m were changed to dry cells and the entire bathymetry field was slightly smoothed with a 5 gridpoint Gaussian filter to reduce spurious sources of vorticity. The model domain dimensions $L \times W \times H$ vary by region and are presented for each region separately in Sect. 5.2.3. The model horizontal resolution is 150 m (the same as bathymetry data) and the vertical resolution varies slightly for each region. We use a Smagorinsky biharmonic horizontal viscosity and the K-Profile Parameterization (KPP) of the vertical viscosity and diffusivity (Smagorinsky, 1963; Large et al., 1994), in addition to a background vertical diffusivity of 10^{-6} m^2 s^{-1}. There is quadratic bottom drag with a coefficient of 2×10^{-3}. We use an f-plane approximation with a representative Coriolis parameter of $f = 1.31 \times 10^{-4}$ s^{-1}, which approximately corresponds to the latitude of the fjords in this chapter. The model experiments are run for 1 year because the fjord recirculation adjusts slowly and requires multiple months of spinup.

5.2.2 Boundary Conditions and Simplified Forcing Choices

Our boundary conditions allow us to achieve a fully spun-up steady-state 3D circulation within each fjord in as simplified a way as possible. The buoyancy drivers in our simulations are supplied by the open ocean and the glacial face boundary conditions, which makes their

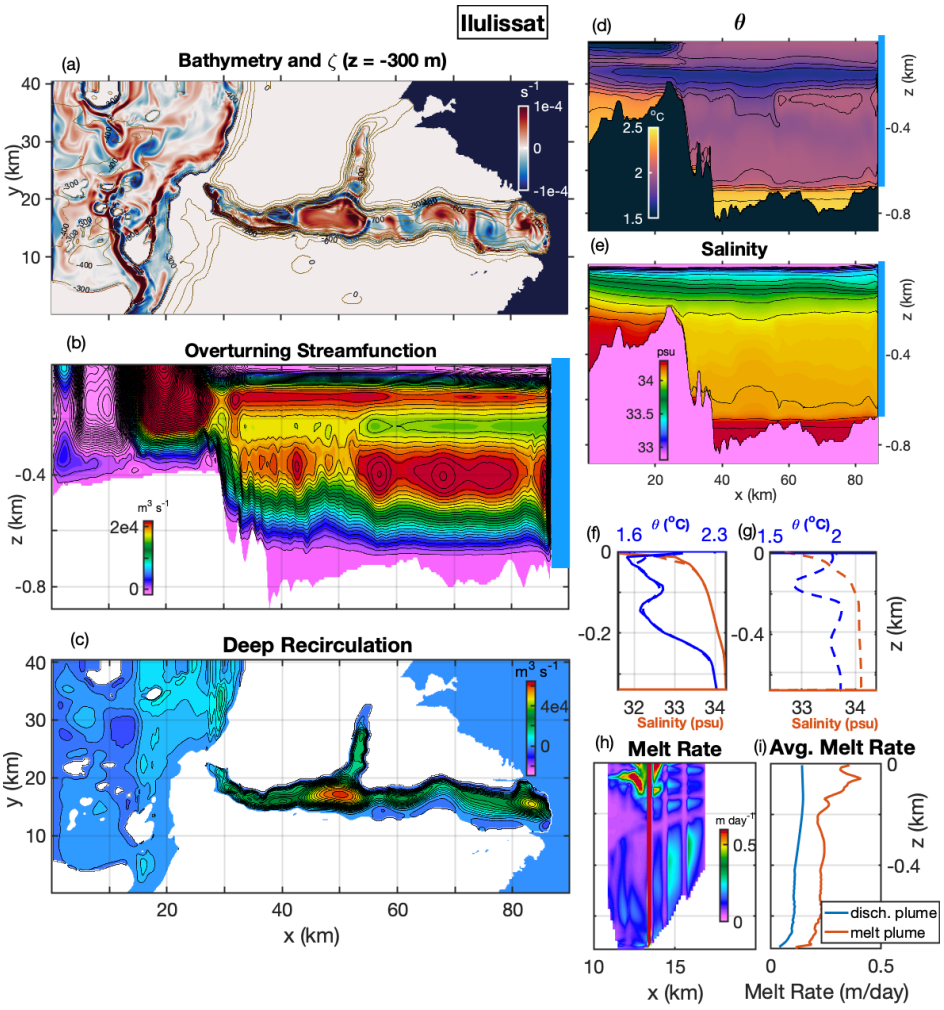

Figure 5.2: Ilulissat fjord at day 300, (a) snapshot of vorticity at $z = -300$ m on bathymetric contours, time-averaged (days 270 to 300) fields of (b) merdionally-integrated overturning streamfunction (using Eq. (5.1)), (c) depth-integrated recirculation (horizontal streamfunction using Eq. (5.2)) below $z = -300$ m, (d) along-transect (see the mid-fjord pink line from Fig. 5.1) potential temperature, (e) along-transect salinity, (f),(g) salinity and temperature profiles outside the fjord and inside the fjord, respectively, from OMG data (solid lines) and model output (dashed lines). (h) melt rate at the glacial face (Ilulissat Glacier, formerly Jakobshavn), (i) merdionally-averaged melt rate decomposed between discharge plume and melt plume. The contour spacings are 10^3 m^3/s, 4 $\times 10^3$ m^3/s, 0.1 °C, and 0.1 psu for (b)-(e), respectively.

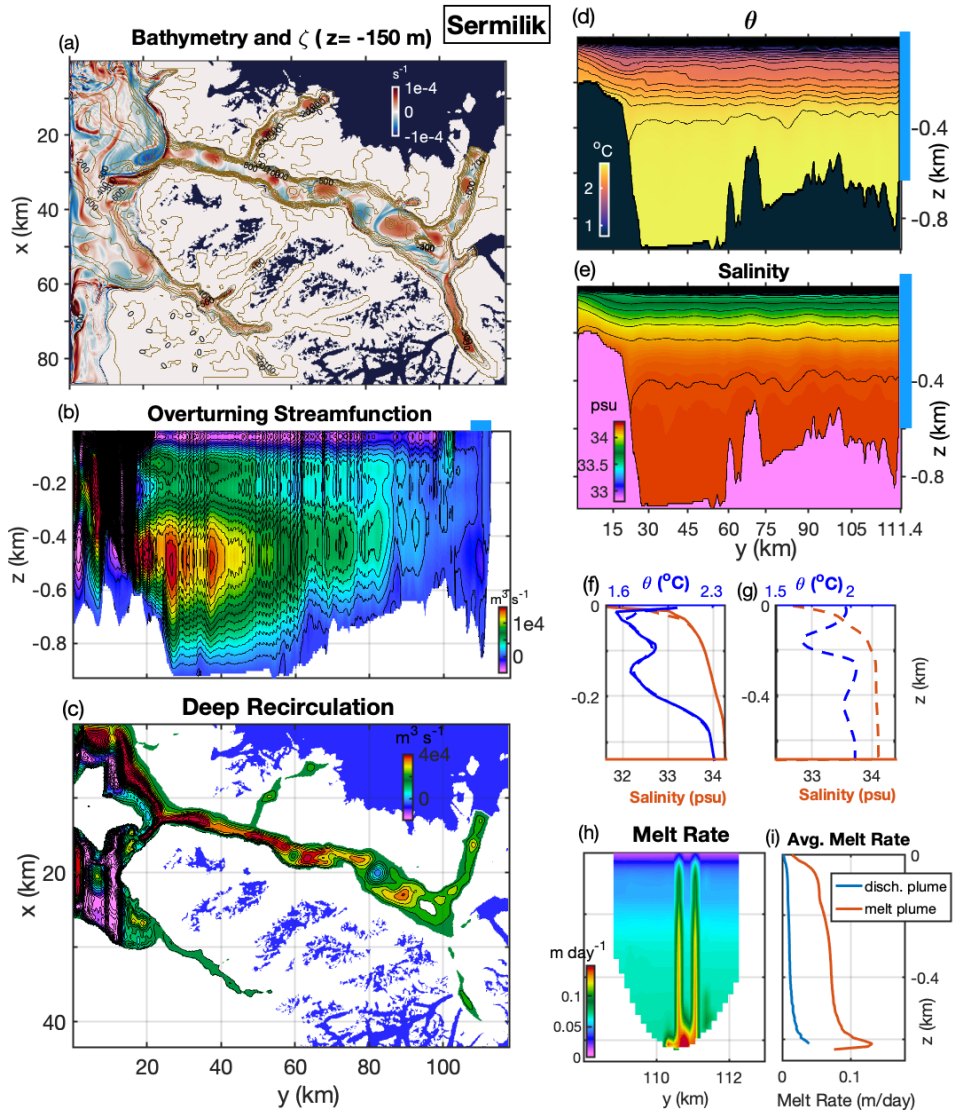

Figure 5.3: Sermilik fjord at day 300, (a)-(h) the same fields as Fig. 5.2 with (a) snapshot of vorticity at $z = -150$ m, and (g),(h) melt rates at Helheim Glacier. Note the rotation of axes and the stretching of the y-axis in (d)-(f) to approximately preserve along-fjord distance.

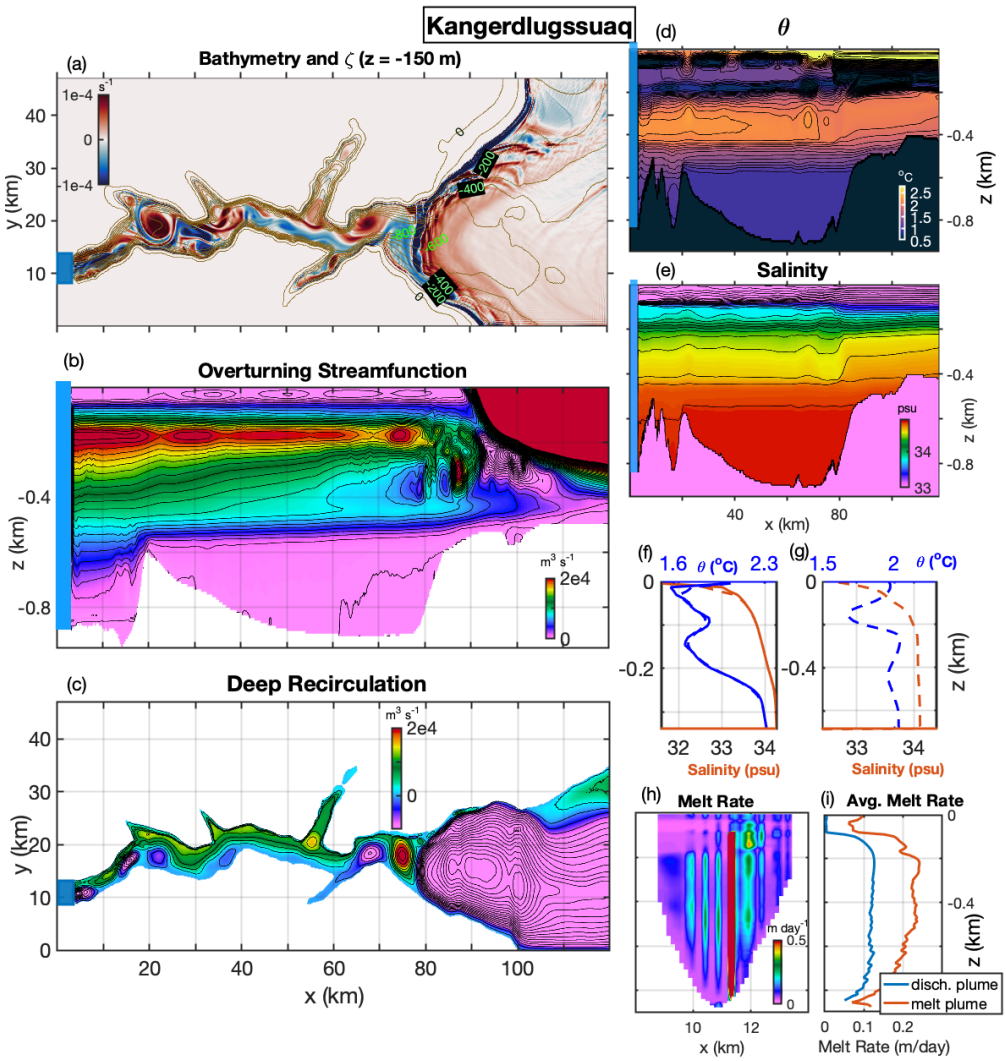

Figure 5.4: Kangerdlugssuaq (East Greenland) fjord at day 300, (a)-(h) the same fields as Fig. 5.2 with (a) snapshot of vorticity at $z = -150$ m, and (g),(h) melt rates at Kangerdlugssuaq Glacier.

representation critical in our simplified forcing. In this subsection, we discuss the following: first, the open-ocean forcing, second, the glacial face forcing, and finally, the choice of not implementing surface forcing.

Each of the domains has three open-ocean boundaries on the shelf region with one inflow boundary on the shelf. These inflow boundaries are forced by an inflow of a constant temperature, salinity, and velocity. The inflow boundaries are the southern, eastern, and northern boundaries of Ilulissat, Sermilik, and Kangerdlugssuaq, respectively (see Fig. 5.1 for the inflow boundaries in each domain). All other boundaries used the Orlanski radiation boundary conditions (Orlanski, 1976), which is implemented in MITgcm. The inflow temperature and salinity uses the Oceans Melting Greenland (OMG) AXCTD (Airborne eXpendable Conductivity Temperature Depth) data (Fenty et al. 2016; see data availability statement for individual AXCTDs used). For each fjord, the AXCTDs used correspond to those that were positioned closest to the shelf region within each domain during the 2020 summer season (July to September).

The velocity is imposed as a constant over the full cross-sectional area at the inflowing open-ocean boundary and is derived from approximations of the along-coast integrated transport, which has broadband temporal variability, but for our idealized setup is assumed to constant during the summer months. The integrated transport is motivated by a combination of Estimating the Climate and Circulation of the Ocean (ECCO) Version 5, Release alpha ($\approx$ 11 km horizontal resolution) (Zhang et al., 2018) coastal transport, existing data (Gladish et al. 2015, Sutherland et al. 2014, Straneo and Cenedese 2015, and references therein), and near-coast ($\approx$ 10 km offshore in these domains) sea surface height gradients from the Making Earth System Data Records for Use in Research Environments (MEaSUREs) dataset (Zlotnicki et al., 2019). None of these methods provide high accuracy of the near-coast integrated transport near these fjords, which are specified for each domain in the following subsection. However, we did not find strong sensitivities of the fjord circulation to deviations in the barotropic coastal transport and future iterations would benefit from

improved representation of the mean and variability of the coastal circulation. In particular, realistic temporal variability is likely to lead to flushing events, which we do not explore in this chapter.

Subglacial discharge exits at the base of the glacier and is typically 100s of m^3/s in the summer (ranging sporadically from 0 to 2000 m^3/s) and nearly zero in winter (Straneo and Cenedese, 2015; Chu, 2014). Areas of elevated mixing within the fjord-to-shelf region are primarily forced by subglacial and ambient melt plumes as they are a dominant mode of mixing for the majority of Greenland's fjords (Carroll et al., 2017; Gladish et al., 2015; Magorrian and Wells, 2016). We therefore use plume parameterizations for both the discharge plume and the melt plume across all ocean-glacial boundaries. The glacial geometry/interfaces used Bedmachine V3 data.

The plume parametrizations that we use are based on buoyant plume theory, as described in Cowton et al. (2015). The plume parameterization solves 1-dimensional equations for mass and momentum conservation vertically along the plume, and temperature/salinity evolve in response to advection, entrainment of ambient waters, and the turbulent transfer to the ice face Hellmer and Olbers (1989). The plume is coupled to the circulation and stratification in the MITgcm model configuration and is a slightly modified version of that proposed by Cowton et al. (2015), optimized to work efficiently in high resolution simulations (see data availability statement). This is identical to the parameterization package detailed in Cowton et al. (2015), except that we redistribute the buoyancy anomalies from the solutions to the discharge plume equations over a 5-gridpoint radius semi-circle in the horizontal and apply a 3-gridpoint smoothing in the vertical while conserving the overall buoyancy anomaly and entrainment. This prevents prohibitive restrictions set by the Courant-Friedrichs-Lewy (CFL) condition on the model timestep in our high resolution simulations as well as spurious mixing caused by sharp gradients in the forcing at the gridscale. The subglacial discharge uses a steady 2-month time average of summer discharge averaged over the years 2017 to 2019 based on the outflow locations and discharge magnitudes from the Mankoff et al. (2020)

dataset.

Lastly, we discuss briefly the choice of no surface boundary conditions. We note that these simplified fjord-shelf regional configurations are not intended to fully represent the dynamics of Greenland's fjords, but rather to capture a few salient features that include more realism not present in previous studies (Gladish et al., 2015; Carroll et al., 2017; Zhao et al., 2021a,b). However, we did test the sensitivity of our regional simulations to steady winds (stresses of up to 0.15 $\mathrm{N/m^2}$), a thin layer of static ice throughout the domain, and mean summer atmosphere forcing (temperature and freshwater fluxes), which did not have a noticeable influence on the fjord circulation below 100 m. Intermittent, strong katabatic winds are likely important for fjord dynamics as they may lead to flushing events (e.g., Spall et al. 2017), but the temporal variability of fjord dynamics is not investigated in the present chapter. One reason for this is that most of the coastal Greenland air-sea interaction (atmospheric temperature, air-sea freshwater fluxes, winds, floating ice) occurs in the abutting shelf seas rather than the fjords themselves since the area of a fjord is comparatively very small. Therefore, most of the air-sea interaction within fjords are advected into the fjord rather than exchanged at the surface waters of a fjord. Thus, we do not anticipate these factors to qualitatively change our findings.

5.2.3 Regional Case Studies

In this subsection, a phenomenological description of the hydrography, circulation, and melt is presented for three major Greenlandic fjords (Ilulissat, Sermilik, and Kangerdlugssuaq; see locations in Fig. 5.1). In these regional case studies, we quantify the fjord overturning circulation via the overturning streamfunction, which is calculated as

$$\psi(x,z) = \int_0^W \int_{z_B(x,y)}^z \overline{u}\ \mathrm{d}z'\,\mathrm{d}y'\,. \tag{5.1}$$

Here, $\overline{u}$ is the time-averaged velocity in the x-direction (and defined to be 0 below bathymetry), W is the width of the domain in the y-direction, and $z_B(x,y)$ is the bathymetric elevation.

To quantify the horizontal recirculation, we use the horizontal quasi-streamfunction

$$\Psi(x, y, z) = \int_0^y \overline{u}\, \mathrm{d}y' \,, \tag{5.2}$$

which is an approximation to the 3D streamfunction, and is further discussed in Appendix I.

5.2.3.1 Ilulissat

Ilulissat fjord in central-west Greenland has been discussed in many previous studies (e.g., Gladish et al., 2015; Khazendar et al., 2019; Beaird et al., 2017). In our setup, we use a model domain $L \times W \times H = 90$ km $\times$ 40 km $\times$ 886 m, force the inflowing open-ocean boundary using OMG data with a total barotropic coastal transport of 250 mSv, and use an summer mean discharge of 400 m^3/s.

In Fig. 5.2, we present a series of diagnostic fields that capture the dynamics of Ilulissat fjord: a vorticity snapshot, mean overturning calculated using Eq. (5.1), deep recirculation using Eq. (5.2) (integrated below $z = -300$ m), along-transect (see the mid-fjord pink line from Fig. 5.1) potential temperature, salinity, temperature and salinity profiles on the shelf and within the fjord in our model results vs. OMG measurements, glacial melt rates at the Jakobshavn/Ilulissat glacial face, and the horizontally-averaged melt rates decomposed into the melt within the discharge-plume driven region and the region outside the discharge-plume (melt plume).

Fig. 5.2a shows the mid-depth ($z = -300$ m) vorticity where the eddy variability on the shelf and within the fjord are apparent. On the shelf, the bathymetry guides the warm-water pathways, which have high vorticity and generate both cyclonic and anticyclonic eddies on the shelf. Inside the fjord, large cyclonic vorticity signatures are visible at three distinct locations ($x = 48, 68, 82$ km). Fig. 5.2b shows the overturning circulation, which shows two overturning cells: a deep overturning centered at $z = -400$ m and a shallow overturning cell centered at $z = -100$ m, both with deeper inflow and surface outflow. The deep recirculation

(below $z = -300$ m) shows large cyclonic recirculation cells co-located with 2 of the 3 regions of high vorticity. The along-transect profiles of potential temperature and salinity show a sharp transition of shelf waters to relatively well-mixed fjord waters. Specifically, the access of waters below 2 °C and above 34 psu are significantly limited by the sill at the fjord mouth. Fig. 5.2f,g show the observation-constrained boundary conditions at the southern shelf boundary and the interior fjord properties, respectively. Fig. 5.2h,i show the melt rate at the glacial face and the meridionally-averaged melt rate (comparing the discharge plume only and total melt), respectively. Although this fjord has one of the largest discharge rates in Greenland, over a half of the total melt occurs outside of the discharge plume.

Due to the shallow sill at the fjord mouth, the sill overflow is hydraulically controlled i.e., the Froude number of the $\sigma = 28.5$ kg/m^3 density layer is approximately critical using the definition in Eq. (3.16b) for the layer below σ (not shown). As a result, the melt and subglacial plumes drive an overturning (primarily the deeper melt-plume driven overturning) that is limited to density classes up to this threshold. This lower warm water availability within the fjord due to the hydraulically-controlled sill overflow results in lower glacial melt rates. However, a smaller range of density variation leads to a stronger overturning and recirculation strength for a fixed buoyancy flux forcing (acting on a weaker overall stratification), which leads to higher melt rates overall due to the stronger velocities at the ice face. See Zhao et al. (2019) for additional discussion on hydraulically-controlled fjord overturning and Pratt and Whitehead (2007) for background on hydraulically-controlled flows.

5.2.3.2 Sermilik

Sermilik fjord in southeast Greenland has been discussed in multiple previous studies (e.g., Straneo et al., 2011; Straneo and Cenedese, 2015). In our setup, we use a model domain $L \times W \times H = 120$ km $\times$ 85 km $\times$ 937 m, which has been rotated 81 degrees clockwise in this figure for ease in visualizing the overturning. We force the inflow open-ocean boundary using OMG data with a coastal transport of 200 mSv and use a summer mean discharge of

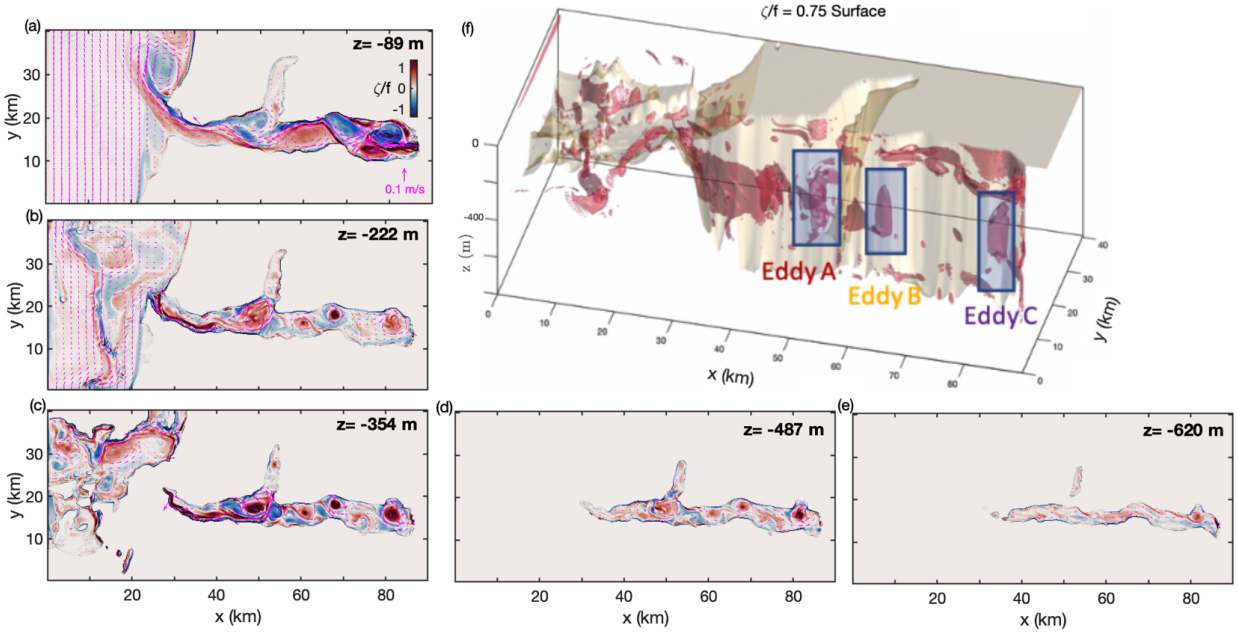

Figure 5.5: (a)-(e) Snapshots of vorticity at various depths and (f) 3D vorticity surface (ζ/f = 0.75) at day 100 showing the existence of three distinct eddies and their vertical structure in Ilulissat fjord.

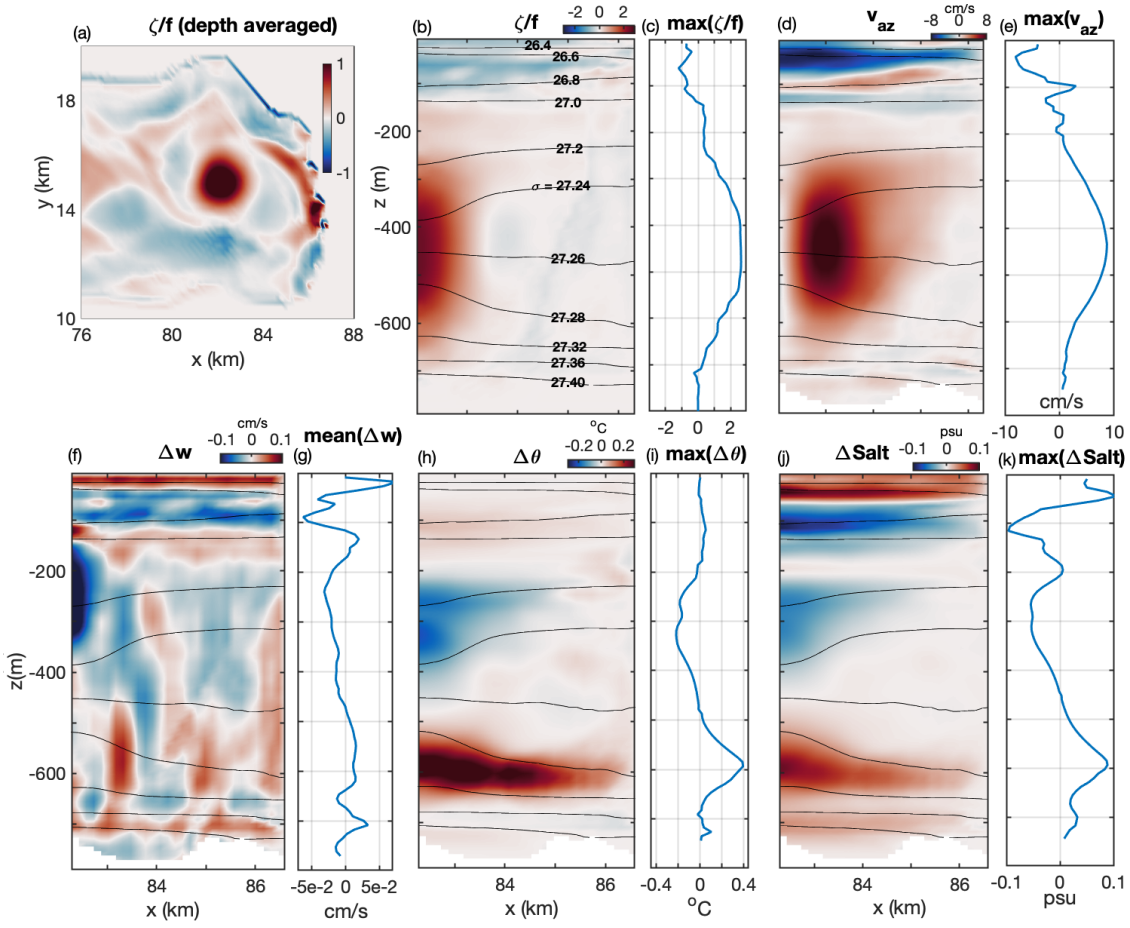

Figure 5.6: (a) Snapshot (day 200) of depth-averaged (below $z = -200$ m) nondimensionalized vorticity zoomed-in on near-glacier eddy region, at day 200, (b),(c) azimuthally-averaged vorticity and vertical profile of maximum vorticity, (d),(e) azimuthally-averaged azimuthal velocity v_{az} (positive is clockwise) and vertical profile of maximum azimuthal velocity, (f),(g) azimuthally-averaged vertical velocity anomaly and vertical profile of mean vertical velocity anomaly, (h),(i) azimuthally-averaged potential temperature anomaly and vertical profile of maximum potential temperature anomaly, and (j),(k) azimuthally-averaged salinity anomaly and vertical profile of maximum salinity anomaly. The anomalies in (f)-(k) were calculated relative to an azimuthal average just outside the domain shown (between a radial distance 4.5 to 6 km from the center of the eddy). Note the uneven spacing of potential density contours, which are shown for panels (b), (d), (f), (h), and (j).

230 m^3/s.

In Fig. 5.3, we present a series of diagnostic fields for Sermilik fjord and Helheim glacier melt rates similarly to Fig. 5.2. Fig. 5.3a shows the shallow ($z = -150$ m) vorticity where the eddy variability on the shelf and within the fjord are apparent but weaker than the Ilulissat fjord interior. A strong coastal current crosses the fjord mouth (with a cyclonic vorticity signature). Inside the fjord, cyclonic vorticity signatures are visible at multiple locations. Fig. 5.3b shows the overturning circulation, which is organized in two main cells: a deep cyclonic overturning centered at $z = -500$ m and a shallow anticyclonic overturning cell centered at $z = -120$ m. Neither the overturning nor recirculation extend all the way to Helheim glacier since this fjord has a weaker discharge and a more winding geometry compared to the other fjords tested, which results in an overturning circulation that is partially driven by water mass transformation within the fjord's tributaries. The along-transect profiles of potential temperature and salinity show well-mixed fjord properties below $z = -400$ m. Fig. 5.2f,g show the observation-constrained boundary conditions at the eastern shelf boundary and the interior fjord properties, respectively. Fig. 5.2h,i show the melt rate at the glacial face and the meridionally-averaged melt rate (comparing the discharge plume only and total melt), respectively. The melt distribution shows the elevated melt at depth due to the unimpeded access of warm-salty Atlantic Water from the shelf.

5.2.3.3 Kangerdlugssuaq

Finally, we discuss Kangerdlugssuaq fjord in central-east Greenland (e.g., Sutherland et al., 2014; Straneo and Cenedese, 2015). In our setup, we use a model domain $L \times W \times H = 120$ km $\times$ 46 km $\times$ 947 m, which has been rotated 45 degrees counterclockwise in this figure for ease in visualizing the overturning. We force the inflow open-ocean boundary using OMG data with a coastal transport of 150 mSv, and use an summer mean discharge of 200 m^3/s.

In Fig. 5.4, we present a series of diagnostic fields for Kangerdlugssuaq fjord and the corresponding glacier melt rates similarly to Fig. 5.2. Fig. 5.4a shows a snapshot of the

shallow ($z = -150$ m) vorticity, which has a signature of a strong coastal current that crosses the fjord mouth, which sets up a meridional baroclinic pressure gradient (suggested by the gradients in temperature and salinity near the fjord mouth at $x = 80$ km in Fig. 5.4d,e). This is a much stronger pressure gradient than the those that occur across the Sermilik and Ilulissat fjord mouths. Inside the fjord, cyclonic vorticity peaks are visible at multiple locations. Fig. 5.4b shows the overturning circulation, which shows mainly one overturning cell: a shallow overturning centered at $z = -150$ m. The along-transect profiles of potential temperature and salinity show well-mixed fjord properties below $z = -400$ m. Fig. 5.4f,g show the observation-constrained boundary conditions at the eastern shelf boundary and the interior fjord properties, respectively. Fig. 5.4h,i show the melt rate at the glacial face and the meridionally-averaged melt rate (comparing the discharge plume only and total melt), respectively. The near-glacier circulation and melt rates are strong influenced by the series of bathymetric sills near the grounding line (particularly near the mid-fjord along-transect, as seen in the $0 < x < 20$ km region of Fig. 5.4d,e). This weakens the access of warm waters, which then weakens the overturning and recirculation below $z = -500$. This is partly the reason this fjord has fairly weak undercutting rates for a deep-water fjord (see Fig. 5.4g,h), with melt rates that peak at mid-depth. Likely as a result, the glacial retreat in this fjord is not as strongly influenced by ocean-driven melt and undercutting; calving/ice dynamics are comparatively more important (Wood et al. 2021).

5.3 Standing Eddies in Fjords

In the model results presented in Sect. 5.2, the distinctive and previously unobserved phenomenon is the existence of long-lived standing cyclonic eddies within each fjord. Previous simulations (e.g., Gladish et al. 2015, Xu et al. 2012, Carroll et al. 2017) likely have not captured this effect due to a combination of bathymetric complexity, model resolution, and spinup time. Observations have likely missed these dynamically-significant features due to

their small-scale and temperature/salinity anomalies being less apparent (but still observable) compared to anomalies in the less-sampled velocity and vorticity fields because the eddies appear to exist primarily in the well-mixed fjord interior. In addition, although these are standing eddies, they do move periodically over distances larger than their radii, making them harder to observe.

In this section, we primarily discuss the properties of eddies within Ilulissat fjord, with a particular focus on the standing eddy near the Ilulissat glacier face, its spinup, transport, mergers with other eddies, and its influence on Lagrangian and Eulerian residence times within the fjord. We end this section with a discussion of the other eddies in all three fjords modeled and the relationship of eddy location to fjord bathymetry.

5.3.1 Eddy Properties and Spinup

In the simulation of Ilulissat fjord discussed in Sect. 5.2, there are three long-lived eddies (labeled Eddy A, B, and C) that are observed within the fjord, which are highlighted in the 2D vorticity fields and 3D vorticity surface in Fig. 5.5. These three eddies have different sizes and vertical vorticity profiles, but all emerge and begin spinning up around day 50 into the simulation around mid-depth ($z = -200$ to -400 m). Specifically, their emergence occurs as an apparent axisymmetrization of along-isobath flow that forms a series of gyre-like recirculation cells with alternating vorticity sign along the fjord (not shown but similar to the surface recirculation cells in Figs. 5.2a). This axisymmetrization and early eddy merger process results in the three long-lived cyclonic eddies (A, B, and C), and intermittent/short-lived anticycylonic eddies. Following this early axisymmetrization, the eddies grow in their vertical extent, primarily downwards to the seafloor over a period of 150 days – in Eddy C, this coincides with the spinup of the along-glacier face velocity discussed below.

Fig. 5.5f illustrates the 3D cyclonic vorticity surface ($\zeta/f = 0.75$), which shows that in addition to these eddies, there is a positive vorticity source from the sill overflow region, which is connected to and advects vorticity into Eddy A, and a positive vorticity source

at the glacier face near Eddy C, which intermittently interacts with Eddy C, but primarily flows out of the fjord in the surface 125 m. Note that these eddies do not extend to the surface region where the vorticity field is dominated by the strong outflow interacting with bathymetry along the fjord sides (e.g., in Fig. 5.5a). However, there are occasional instances of vertical alignment of the outflowing eddies in the surface 150 m with the deep-water eddies that are the focus of this chapter.

In Fig. 5.6, we show the azimuthally-averaged properties of the near-glacier eddy (Eddy C) at day 200. This eddy is located near the Ilulissat (formerly Jakobshavn) glacial face and is of particular importance due to its influence on the near-glacier velocity field and melt rate. Fig. 5.6a shows a snapshot of depth-averaged vorticity in the near-glacier region, which shows a clear radially-symmetric cyclonic eddy core centered at approx. $x = 82$ km in addition to a positive vorticity region near the glacier face. In the panels of Fig. 5.6b-e, we observe that the azimuthally-averaged vorticity, azimuthal velocity, and isopycnal structure are consistent with an oceanic cyclonic eddy, as discussed in previous literature (e.g., McWilliams, 1990). In particular, the stronger stratification at the core of the eddy drives a geostrophic circulation and a cold, fresh anomaly at the top of the eddy, which is consistent with the downward vertical velocity, and a warm, salty anomaly at the base of the eddy (in panels f through k). Both of these anomalies extend to but are much weaker at the glacier face in this snapshot.

Fig. 5.7a-d shows the spinup of the temperature, circulation, melt rates, and PV anomaly at the glacier face. These panels show that as the melt and circulation spin up, the pool of warm water in the deep fjord is consumed via mixing and export, which over time contributes to a lower melt rate. However, the circulation (overturning and recirculation) strengthens during this time, which compensates the cooler waters such that the overall melt rate does not change significantly – however, the total melt does increase slightly (by $\approx 10\%$) over this time. In Ilulissat fjord, the spinup process of the standing eddies and fjord recirculation takes approx. 3-6 months based on the near-glacier circulation and melt rate. The spinup time depends on the renewal rate of deep fjord waters, which depend on the fjord volume

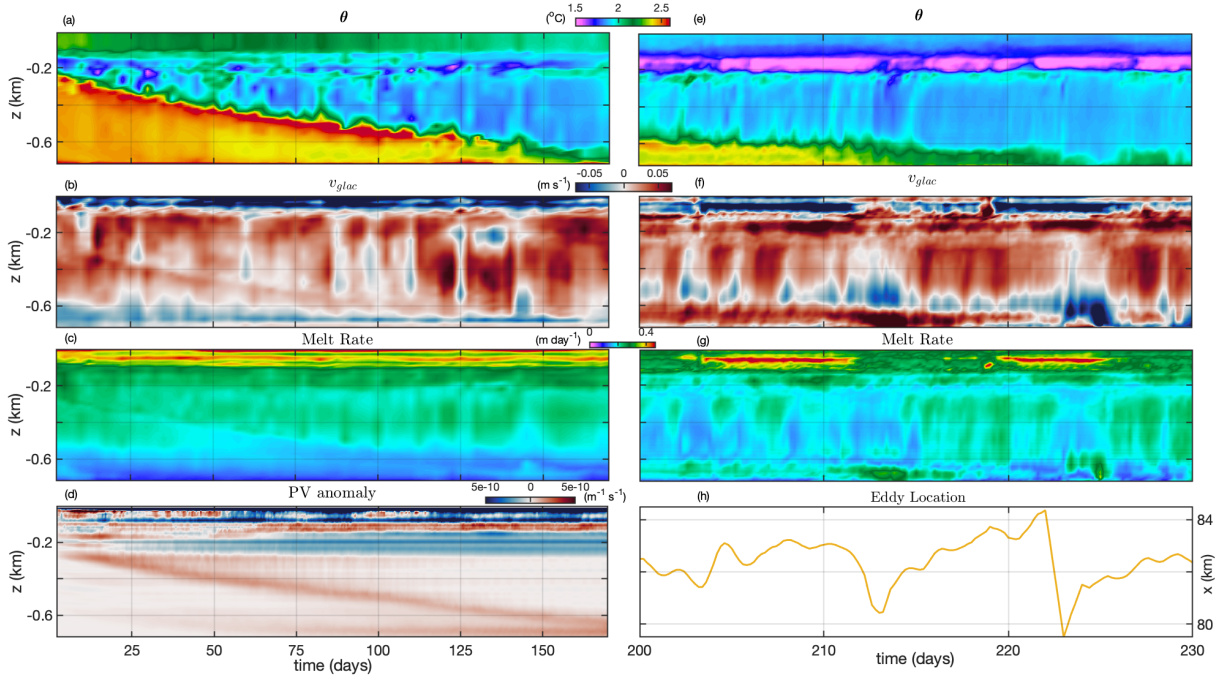

Figure 5.7: Time evolution of the along-glacier face average showing the spinup (over the first 170 days) of the (a) potential temperature, (b) meridional velocity, (c) melt rate, and (d) PV anomaly. Panels (a)-(d) use the 5-day time averages. The shorter time-scale variability (over days 200 to 230) of the instantaneous along-glacier face average of (e) potential temperature, (f) meridional velocity, and (g) melt rate, compared to the zonal eddy location.

below a given depth and the overturning circulation (driven primarily by the buoyancy flux from the glacier at depth). However, there is also a spinup time associated with the tendency of the vorticity balance, which is discussed further in the next section.

It is worth noting that the melt and near-glacier velocity deepens over this time period, which is important for accurate predictions of rates of glacial undercutting (see Zhao et al. 2021b for further discussion on the melt-circulation feedback in fjords). Due to this long duration, the temporal response/adjustment of the fjord circulation forcing variability on seasonal timescales (such as 1-2 month peak in summer subglacial freshwater discharge and seasonal winds) are important to take into account in an observational context because circulation may take months to spin up or spin down following a warm water renewal or summer subglacial discharge. It is possible then that these eddies do not fully spin up during a melt season. However, although the timescale associated with a full eddy spinup process is longer than the melt season (as Zhao et al. 2021b suggests) the subglacial discharge-driven circulation acts to trigger and potentially accelerate the melt-circulation feedback. This feedback then dominates the deep circulation (below the neutral buoyancy depth of the subglacial discharge plume) and lasts for a much longer time period. In the absence of subglacial discharge, the melt-driven circulation would take longer to spin up the eddies, but they would likely still exist.

Fig. 5.7e-h shows the influence of the Eddy C's location on the temperature, meridional velocity, and melt rate. Over a 30 day time-period (days 200 to 230), the eddy core shown in Fig. 5.7h ranges from 2 to 6 km away from the ice face (based on $x = 86$ km as the approximate location of the glacier face). The distance between the eddy and the glacier face has an effect on both the temperature (panel e) and velocity (panel f) at the glacier face. The total integrated melt rates when the eddy is closest to the ice face (defined here as periods where eddy core location > 83 km) is approximately 10% higher than the remainder of the time series. This effect on the melt rate is primarily due to the eddy-induced velocity field rather than the eddy-influenced temperature field since the horizontal velocities also

increase by approximately 10% during these time periods.

5.3.2 Eddy Transport and Mergers

Although eddy mergers do not have a significant effect on fjord overturning or heat transport (eddy momentum and heat transport terms are weak compared to the mean transport terms, which is not shown), they do have a significant effect on the maintenance of these standing eddies via vorticity advection, which is further discussed in Section 5.4.

In Fig. 5.8a-c, we show a Hovmöller diagram of the meridionally averaged vorticity, which highlights the preferred locations of the standing eddies in Ilulissat fjord and merger activity at various depths. Compared to Eddy A and C, Eddy B has a larger range and participates in more mergers (with C). Eddy A and C have strong deep vorticity signatures while Eddy A and B also have near-surface vorticity signatures and exhibit more clear instances of vertical alignment between the surface and deeper eddies. For the deeper eddy dynamics (below 125 m, panels b and c), Eddy B periodically propagates eastward and merges with Eddy C, and we can see that the signal of Eddy B is weak in time periods following these propagation events. In addition, there is an eastward propagation of vorticity from the region near Eddy A to Eddy B, although this signature is partially due to the vorticity advection from the near sill region (see Fig. 5.5f). The eastward propagation velocities are approximately 1 km/day and are consistent with the meridionally- and depth-averaged horizontal mean flow.

For the surface eddies (above 125 m, panel a), Eddy B periodically propagates westward with a propagation velocity of 1.25 km/day and merges with Eddy A, while Eddy A occasionally exits westward (out of the domain) where the vorticity is advected/diffused by the strong exiting flow. The periodical eddy mergers occur approximately every 30 days for the deeper eddies and it occurs approximately every 70 days for the surface eddies.

In the remainder of this chapter, we ignore the surface eddies, which are not standing eddies and do not strong influence the fjord circulation, vorticity balance, or melt rates

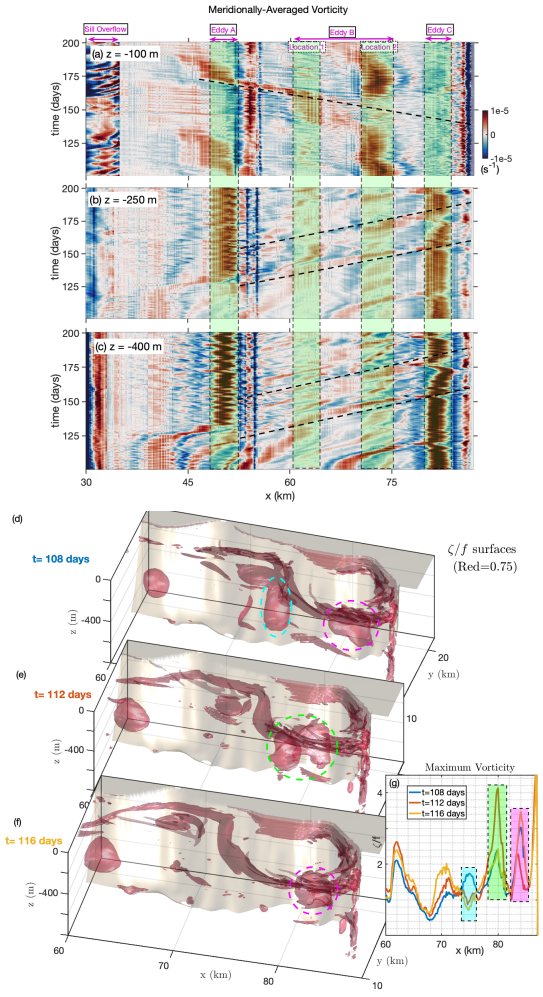

Figure 5.8: Hovmöller diagram of meridionally averaged vorticity vs. time for (a) z= -100 m, (b) z= -250 m, (c) z= -400 m, which show the preferred locations of Eddy A and C and two preferred locations for Eddy B in shaded light green. The propagation velocity (dotted black line) correspond to estimates of (a) 1.25 km/day, (b) 0.97 km/day, and (c) 1.04 km/day. Vorticity surface ($\zeta/f = 0.75$) at days (d)-(f) 108, 112, 116, respectively, and (g) the maximum vorticity as a function of x. The color outlines highlight the mergers of the Eddy B and C in panels (d)-(f), where cyan is the initial location of Eddy B, pink is the initial and final location of Eddy C, and lime is the merger location. The corresponding vorticity maxima are also highlighted with the same colors in panel (g).

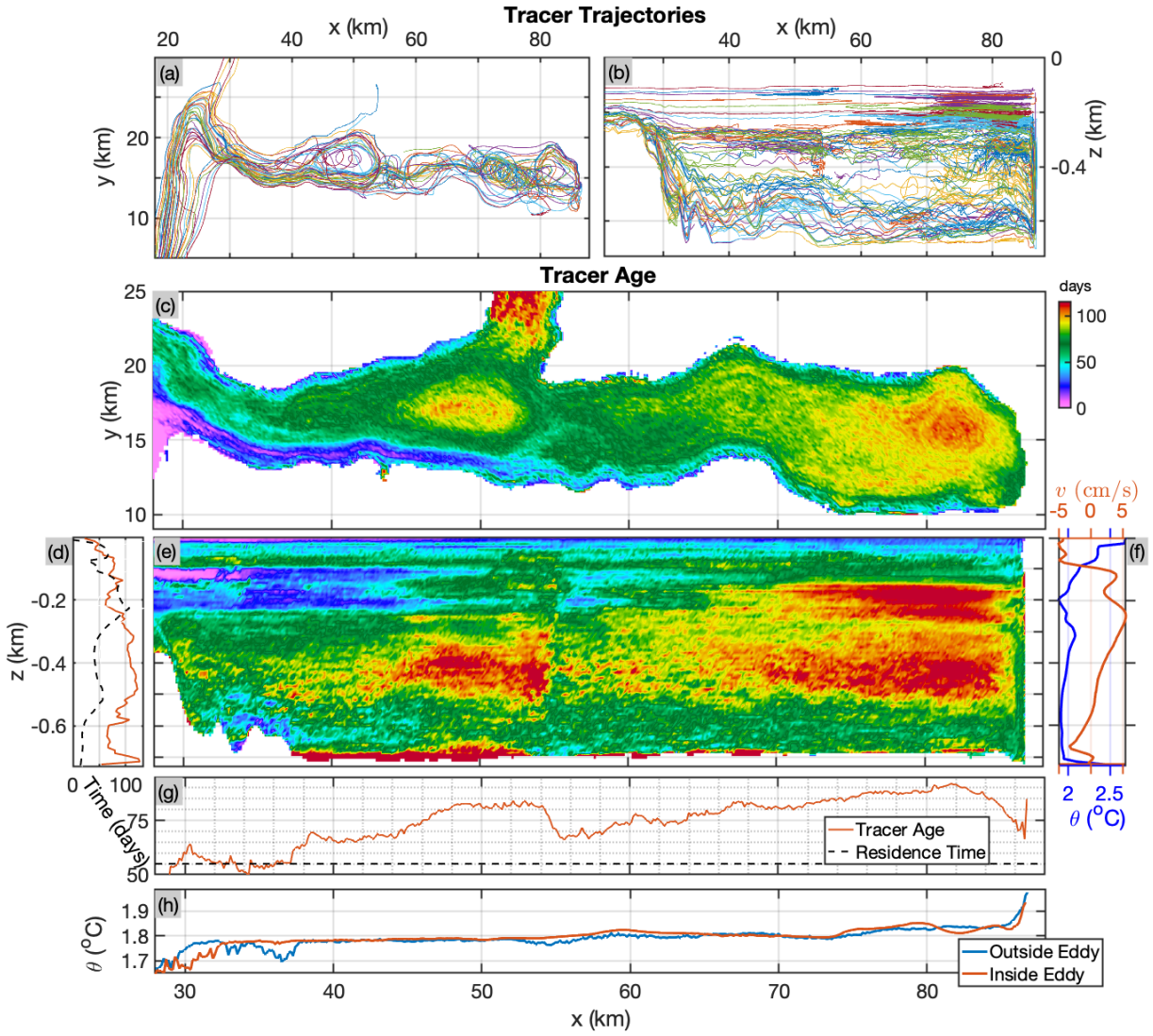

Figure 5.9: (a) Top view and (b) side view of a representative sample of 100 Lagrangian tracer trajectories that enter the fjord, (c) vertically-averaged and (e) meridionally-averaged residence time of the tracers, (d) zonally-averaged and (g) vertically-averaged profiles of panel (c) compared to the mean Eulerian age (calculated from the overturning circulation), (f) the near-glacier potential temperature and along-glacier meridional velocity, and (h) the vertically-averaged temperature below $z = -150$ m for tracers that leave the fjord within 50 days (those that are not trapped within eddies) vs. those that spend longer than 50 days within the fjord (those that are trapped inside eddies).

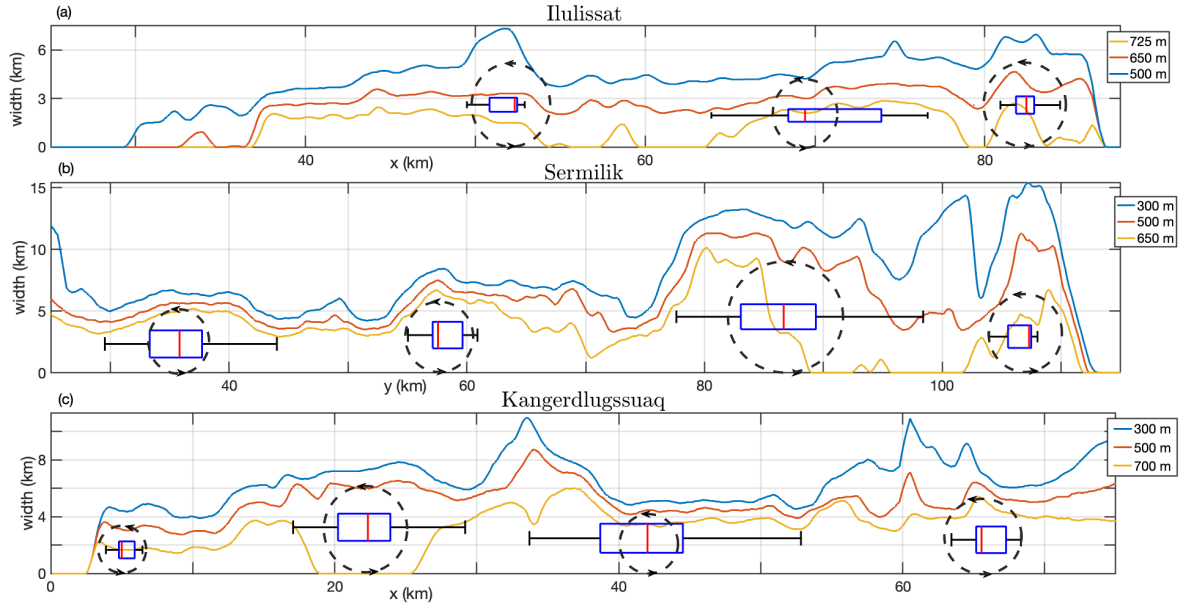

Figure 5.10: Time-mean eddy size (represented by the width of the dotted circles in the y-axis dimension) and box plot of eddy location (along the x-axis dimension) compared to the across-fjord width at various depths for (a) Ilulissat, (b) Sermilik, and (c) Kangerdlugssuaq fjords. The time-mean eddy size and location statistics were calculated using the AMEDA algorithm (see Sect. 5.3.4 for further discussion).

as much as the deeper standing eddies. In addition, these surface eddies are likely to be strongly influenced by the surface forcing (e.g., drag against sea ice/mélange), which is not represented in these model configurations. In contrast, the deeper eddies are by comparison are much less likely to be influenced by the surface forcing.

Fig. 5.8d-f shows the 3D vorticity surface ($\zeta/f = 0.75$) at days 108, 112, and 116, highlighting an eddy merger event between Eddy B (cyan) and C (pink) and their merger (lime green). The maximum vorticity over the course of the merger is shown in Fig. 5.8g that results in a peak vorticity for Eddy C that is approx. 60% greater than the pre-merger peak vorticity. Note the existence of an outflowing surface eddy in these panels (centered at $x = 70$ km, $z = -100$ m).

5.3.3 Lagrangian Standing Eddy Circulation/Trapping

Lagrangian tracer experiments have been informative in fjord and estuaries in both observations and numerical simulations (Pawlowicz et al., 2019). However, near glacier fjords, these simulations have only tested the fjord outflow on shelves instead of within the fjords themselves, e.g., in the West Antarctic Peninsula (Pinones et al., 2011) and Kangerdlugssuaq regions (Gelderloos et al., 2017). To better understand the influence of these eddies on tracers and residence times within these fjords, we use a tracer release experiment within the Ilulissat fjord simulation.

We deploy 100,000 tracer particles over a period of 20 days (5000 per day) starting at day 100 at even spacings in the x and z directions at the inflow boundary condition (50 tracers in the vertical direction and 100 tracer in the horizontal direction). The particle trajectories were not sensitive to the deployment rate because those that stay within the fjord spend a much longer period of time trapped within the fjord than the deployment duration. Fig. 5.9a,b shows the tracer trajectories from a top and side view, which highlights the trapping of tracers primarily within Eddy C (the near-glacier eddy) with weaker trapping in Eddy A and the weakest trapping in Eddy B. A few particles in panel a show an eastward spiral

movement of particles trapped in Eddy B, which coincides with an eddy merger event with Eddy C.

Fig. 5.9c,e shows the vertically- and meridionally-averaged tracer age (over all particles) at day 200, respectively, which highlights the high residence times within the eddy at $x = 50$ km and the near-glacier eddy, as well as at the deepest depths, where the circulation is weak. Fig. 5.9d,g show a comparison between expected Eulerian residence time (calculated from the overturning circulation magnitude divided by the depth-integrated fjord volume) and the zonal and vertical deviations as a result of standing eddies, and Fig. 5.9f,h shows the resulting colder bias of older water masses within the eddy at the glacier face.

Based on our tracer release experiment, approximately 7.5% of shelf tracers enter the fjord (consistent with Eulerian streamfunction). After 100 days, half of the tracers still remain in the fjord, where a majority of the tracers are near or within one of the three eddies. A key takeaway from this experiments is that the along-fjord and vertical deviations from the mean fjord residence time suggest that melt rates inferred from tracer concentration measurements within fjords such as noble gas and oxygen isotope measurements might be biased higher than actual melt rates. This is especially the case if they are within the near-glacier eddies where they may be trapped for a substantially longer time than the average Eulerian residence time.

5.3.4 Eddy Locations and Bathymetry

We also investigate and track the position of each individual eddy over time. To do so, we use the Angular Momentum for Eddy Detection and tracking Algorithm (AMEDA) (Vu et al., 2018). This detection and tracking algorithm has been effectively used in both numerical simulations and satellite data (Morvan et al., 2020). The algorithm uses gridded velocity, deformation radius, and a few user-defined tuning parameters as inputs and tracks individual eddy locations and radii over time. The algorithm uses this to find eddy centers that correspond to an extremum of the local normalized angular momentum that is contained

within a closed streamline. The streamlines surrounding this center are then computed and the eddy mean radius is defined as the equivalent radius of a disc with the same area as one delimited by the closed streamline with the maximum area.

In our implementation of this algorithm, we use the depth-averaged horizontal velocity field below the discharge plume neutral buoyancy depth (approximately $z = -150$ m for all three fjords), a deformation radius of 4 km that is approximately representative of all three fjord interiors, and the default tuning parameters from the algorithm (our results were not sensitive to these parameters). In addition to the cyclonic eddies, the algorithm also detected smaller anticyclonic eddies, but these were short-lived eddies with weaker cores and are therefore not included in the discussion in the remaining sections.

Fig. 5.10 shows the time-mean eddy radii (over days 200 to 300) and box plots of eddy locations compared to the width of the three fjords at selected depths. For all three fjords, there is a suggestive visual correlation of eddy locations with the widest parts of the fjords. Most of the eddy radii are contained within the $z = -500$ m isobath and the eddies are fairly evenly spaced with no two preferred eddy locations within 10 km (a few eddy radii) of each other. A few of the eddy positions have a large horizontal extent (e.g., Ilulissat Eddy B), which seem to occur when the fjord width does not change much in the along-fjord direction. These same eddies also undergo eddy mergers more frequently (as discussed in Sect. 5.3.2). Importantly, there are eddies (with varying properties) positioned near the glacier face in all three of the fjords tested, which has implications for glacial melt rate. However, the near-glacier eddies in the Sermilik and Kangerdlugssuaq fjords are much weaker than the one in Ilulissat because these fjords have a weaker subglacial discharge.

5.4 Vorticity and Glacial Melt Rates

Recent modeling results show that the horizontal recirculation plays an important and potentially dominant role in glacial melt rates in deep-water fjords (Zhao et al., 2021b). Specif-

ically, the near-glacier horizontal velocity, which owes its magnitude to the horizontal recirculation within the fjord, plays an important role in driving ambient front-wide glacial melt and may be comparable to the subglacial discharge-driven melt (Slater et al. 2018, Jackson et al. 2019). While the horizontal velocity can be locally complicated (e.g., within the standing eddies and near topographic features), we take an overall view that focuses on the fjord-scale recirculation, for which a dynamical analysis of the circulation (i.e., the horizontally-integrated vorticity balance) is the appropriate diagnostic. In order to develop scaling theories for the recirculation and near-glacier horizontal velocities, we present a vorticity balance analysis using Ilulissat fjord as an example. We then use this to develop a simple theory to predict the near-glacier horizontal velocities and glacial melt-rate, which builds on the theory from Zhao et al. (2021b).

5.4.1 Fjord Vorticity Balance

To provide a theoretical scaling prediction for the near-glacier horizontal velocity, we first diagnose the fjord vorticity balance. We start with the horizontal inviscid momentum equations using the Boussinesq approximation on an f-plane,

$$\partial_t \mathbf{u}_h + (\mathbf{u}\cdot\nabla)\mathbf{u}_h + f\hat{\mathbf{z}}\times\mathbf{u}_h = -\frac{1}{\rho_0}\nabla_h p - \boldsymbol{F}_{\text{fric}}\,, \tag{5.3}$$

for bottom friction parameterized as $\boldsymbol{F}_{\text{fric}} = \partial_z\boldsymbol{\tau}$ for a stress

$$\boldsymbol{\tau} = \begin{cases} C_d|\mathbf{u}_h|\mathbf{u}_h, & \text{at } z = z_b \text{ (bathymetry)},\\ 0, & \text{otherwise}, \end{cases} \tag{5.4}$$

where $C_d = 2\times10^{-3}$ is the bottom drag coefficient. The stress in the interior includes viscous terms parameterized by the K-Profile Parameterization (Large et al., 1994), but this is negligible in our simulations. Note the difference in notation used here for the 2D velocity vector and Laplacian operator $\mathbf{u}_h = (u, v)$, $\nabla_h = (\partial_x, \partial_y)$, and the 3D velocity vector and Laplacian operator $\mathbf{u} = (u, v, w)$, $\nabla = (\partial_x, \partial_y, \partial_z)$.

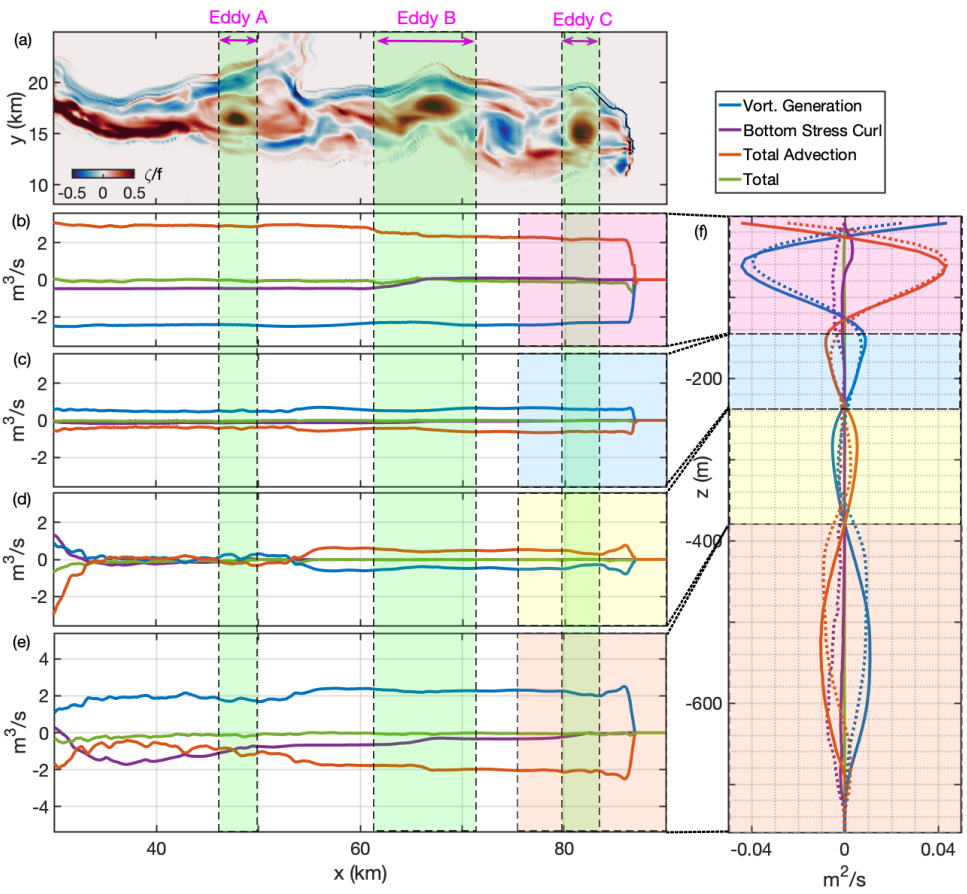

Figure 5.11: (a) The depth-averaged vorticity at day 210 for Ilulissat fjord with zonal eddy extent over days 200 to 220 (shaded green area). Time-averaged (days 200 to 220) meridionally-integrated zonal-cumulative integrals (starting from the glacial face and integrating westward) of the labeled terms in Eq. (5.5) vertically-integrated between four separate depth bands, (b) $-125 < z$ m, (c) $-235 < z < -125$ m, (d) $-380 < z < -235$ m, and (e) $z < -380$ m. (f) The time-averaged area integral of the near-glacier recirculation region ($x > 75$ km) for each of the labeled terms in Eq. (5.6) (pink, light blue, light yellow, light orange shaded regions correspond to the regions in (b)-(e)). Additional dotted lines in panel (f) correspond to the vorticity generation, total vorticity advection, and bottom stress curl terms integrated in a larger full-fjord region ($x > 40$) km (the total does not deviate significantly from the $x > 75$ km region).

Taking the horizontal curl of Eq. (5.3), we obtain the equation for the vertical component of vorticity

$$\underbrace{\partial_t \zeta}_{\text{tendency}} + \underbrace{\nabla \cdot (\mathbf{u}\zeta) - \zeta \partial_z w - [(\partial_z u)(\partial_y w) - (\partial_z v)(\partial_x w)]}_{\text{total vort. advection}} - \underbrace{f \partial_z w}_{\text{vort. generation}} = - \underbrace{\nabla_h \times \boldsymbol{F}_{\text{fric}}}_{\text{bottom stress curl}} . \tag{5.5}$$

Fig. 5.11b-e shows the time-averaged meridionally-integrated zonal-cumulative integrals of each term in Eq. (5.5) vertically-integrated over four distinct depth bands. We use a zonal-cumulative integral, which starts at zero at the glacial face and is integrated westward, to visually reduce noisy vorticity sources generated by bathymetry. The terms in this balance shown in Fig. 5.11 include the vorticity generation, bottom stress curl, and total vorticity advection (including horizontal and vertical vorticity advection, vorticity stretching, and tilting). The vortex tilting terms are comparatively much smaller than the other terms and grouped with this total vorticity advection term. The four depth bands are chosen based on the sign of $\partial_z w$ (which is consistent with the two overturning cells in Fig. 5.2b) and correspond to the inflow/outflow of the melt plume-driven overturning ($z < -380$ m, $-380 < z < -235$ m) and the inflow/outflow of the discharge plume-driven overturning ($-235 < z < -125$ m, $-125 < z$ m), which is more apparent in the near-glacier area integral discussed below.

Starting in the bottom layer, the near-glacier region converts vorticity generation to total vorticity advection, which is primarily balanced by the bottom stress curl over the entire fjord (with a near compensation between the advection and stretching terms). We primarily use the approximate balance between the vorticity generation and bottom stress curl in the bottom layer to develop our scaling prediction for the melt rate in the next subsection. In the other three layers, the vorticity generation is predominantly balanced by total vorticity advection over most of the fjord.

We now calculate vertical profiles of the terms in Eq. (5.5) over a defined region of the

fjord by taking an area-integral and applying the Stokes' and divergence theorems

$$\underbrace{\iint f\partial_z\overline{w}\,\mathrm{d}A}_{\text{vorticity generation}} - \underbrace{\oint_{\partial A}\partial_z\overline{\tau}\cdot\hat{\mathbf{t}}\,\mathrm{d}s}_{\text{bottom stress curl}}$$
$$= \underbrace{\oint_{\partial A}\left(\overline{\mathbf{u}_h\zeta}\right)\cdot\hat{\mathbf{n}}\,\mathrm{d}s - \iint\overline{\zeta\partial_z w} + \text{`}\overline{\text{vortex tilting}}\text{'}\,\mathrm{d}A}_{\text{total vort. advection}}, \tag{5.6}$$

where $\hat{\mathbf{n}}$ is the unit vector normal to and $\hat{\mathbf{t}}$ is the unit vector tangential to the boundary of area A and the vortex tilting refers to the last component of the total vorticity advection term in Eq. (5.5). Fig. 5.11e shows the vertical profiles of each of the terms in Eq. (5.6) integrated over two regions: the near-glacier recirculation area (bounded by $x = 75$ km and the glacial face) in the solid lines and the entire fjord region excluding the sill (bounded by $x = 35$ km and the glacial face) in the dotted lines. Note that over the near-glacier region, the vorticity generation in the bottom layer is balanced by total vorticity advection while bottom stress curl is weak. However, the bottom stress curl is the dominant term in the bottom 200 m when integrated over the full fjord domain.

5.4.2 Implications for Glacial Melt

In order to understand the sensitivity of glacial melt rates to fjord parameters, we extend previous theories (Zhao et al., 2021a) to relate the vorticity balance to glacial melt.

Based on the vorticity balance in the bottom layer in Eq. (5.5) and Fig. 5.11, we calculate a prediction for the along-isobath velocity by balancing the area-integrated bottom stress curl and vorticity generation terms from Eq. (5.6). An underlying assumption is that this along-isobath velocity is assumed to be approximately constant around the isobath, which includes the near-glacier region as part of its circuit. This assumption allows us to predict vertical profiles of horizontal velocity at the glacier face. The vorticity generation term is defined as

$$fQ(z),\ \text{where } Q(z) \equiv \iint \overline{w}_z\,\mathrm{d}A\,. \tag{5.7}$$

The bottom stress curl term

$$\oint_{\partial A} \partial_z \overline{\tau} \cdot \hat{\mathbf{t}} \, \mathrm{d}s \approx \mathcal{C} \underbrace{C_d H_{\mathrm{eff}}^{-1}}_{\equiv C_\tau} |v_{\mathrm{bdy}}| v_{\mathrm{bdy}} \,, \tag{5.8}$$

can be approximated by using a mean along-isobath velocity, v_{bdy}, which approximates the path integral with a boundary perimeter length $\mathcal{C}$ circumscribing region A using an along-path averaged velocity scale $v_{\mathrm{bdy}} = \mathcal{C}^{-1} \oint_{\partial A} \mathbf{u}_h \cdot \hat{\mathbf{t}} \, \mathrm{d}s$ within a bottom boundary layer scale height, H_{eff}. In the simplified boundary layer parameterization using a bulk drag coefficient (in MITgcm with an unresolved bottom boundary layer), $C_\tau \equiv C_d(\Delta z)^{-1}$ and v_{bdy} is evaluated at the deepest wet grid cell just above bathymetry. This is used as the prediction of the mean along-perimeter horizontal velocity at each depth in the discretized vertical grid, which we denote as v_{theory}.

Setting the terms from Eqs. (5.7) and (5.8) equal, we have a prediction for the near-glacier velocity

$$v_{\mathrm{theory}} \approx \mathrm{sgn}(Q(z)) \left(\frac{f|Q(z)|}{\mathcal{C} C_\tau} \right)^{1/2} . \tag{5.9}$$

We compare the prediction of the vertical profile of horizontal velocity to the simulated results of Ilulissat fjord. Fig. 5.12a,b show the near glacier circulation, which is consistent with the near-glacier eddy discussed in previous sections. However, the along-face horizontal velocity in Fig. 5.12b,c exhibit complex meridional and vertical structure. Fig. 5.12d shows that the depth-averaged velocity based on Eq. (5.9) compared to the meridionally-averaged along-glacier velocities diagnosed from simulations. The differences between the theoretical depth-averaged along-glacier velocity and simulated velocity profiles are substantial at most depths. Specifically, in the bottom layer, the small recirculation region in the southeast corner leads to a southward along-glacier velocity, which is not captured in our theory. This negative (clockwise) recirculation region accounts for the difference between our theory over $-620 < z < -400$ m. Below these depths, the specific pathways of currents guided by bottom bathymetry dominates the near-glacier velocity. However, in the bottom layer the

theoretical prediction of the depth-averaged along-glacier velocity is within 10% (greater) of the simulation-diagnosed value. This prediction is not expected to be accurate in the other depth bands because the vorticity generation is balanced by the total vorticity advection term instead of bottom stress curl.

Using this prediction of the near-glacier velocity magnitude, we develop predictions for the glacial melt rate. Assuming that the melt is primarily driven by horizontal velocities external to the discharge plume and vertical velocities within the discharge plume, we use the 3-equation thermodynamics (using e.g., Hellmer and Olbers 1989, Holland and Jenkins 1999) and assume ice temperatures that are approximately freezing. This allows us to simplify this relationship to a linear melt rate M (in m/s) that is approximately proportional to $\overline{v}_{\text{theory}}$ for the melt rate external to the plume as

$$M_{\text{v,theory}} = \frac{c_w(T_a - T_b)}{L_i} C_d^{1/2} \Gamma_T |\overline{v}_{\text{theory}}| \,, \tag{5.10}$$

where $L_i = 3.35 \times 10^5$ J kg^{-1} is the latent heat of fusion of ice, $c_w = 3.974 \times 10^3$ J kg^{-1} K^{-1} is the specific heat capacity of water, $\Gamma_T = 2.2 \times 10^{-2}$ is the thermal transfer constant, and $T_b = T_f$ and T_a are the boundary layer (assumed to be at freezing temperature) and ambient temperature, respectively. The vertical ambient temperature profile is diagnosed from the model over near-glacier region, $x > 85$ km.

The total melt rate is the sum of the region outside of the plume (from Eq. (5.10)) and the region within the plume

$$M_{\text{total,theory}} = M_{\text{v,theory}} + \frac{c_w(T_a - T_b)}{L_i} C_d^{1/2} \Gamma_T |\overline{w}| \,, \tag{5.11}$$

where the vertical velocities are predicted used plume dynamics (Morton et al., 1956), which is used in the parameterization of plume entrainment in our model (Cowton et al., 2015) and can be diagnosed directly (or explicitly included in the theory).

The melt rate predictions, $M_{\text{v,theory}}$ and $M_{\text{total,theory}}$, are shown in Fig. 5.12e compared to the simulation-diagnosed meridionally-averaged melt rate. Within the bottom layer, the

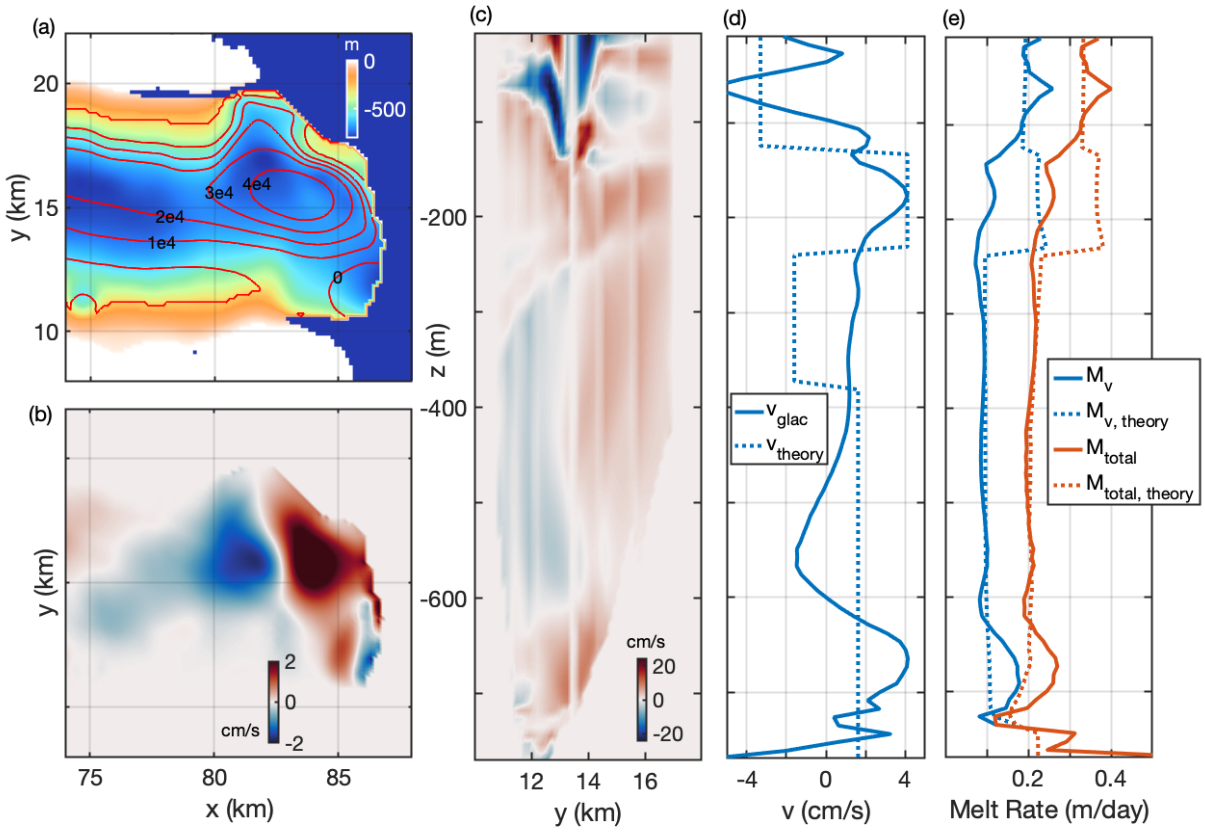

Figure 5.12: Time-averaged (days 200 to 220) (a) depth-integrated (below $z = -300$ m) horizontal streamfunction contours over bathymetric depth zoomed-in on the near-glacier region, (b) depth-averaged meridional velocity, (c) meridional velocity at the glacier face, (d) meridionally-averaged meridional velocity and the theoretical prediction (dotted line), and (e) glacial melt rates based on the horizontal velocity only (M_v) and the horizontal and vertical velocities (M_{total}) with corresponding theoretical predictions (dotted lines).

melt rate is well predicted by the theory in Eq. (5.11), with the vertical and horizontal velocity components each driving approximately half of the melt rate in both the theory and simulations. This improved accuracy compared to the near-glacier velocity is due to the fact that the temperature profile is diagnosed from the model results. Note that this theory only accounts for thermal contribution to the elevated melt rates near the grounding line (leading to glacial undercutting) and not the increased along-glacier velocity at the grounding line since it uses a layer-averaged velocity. However, this only demonstrates a partial success of the theory as shown in Fig. 5.12d,e. For the profiles shapes in Fig. 5.12d, the theory for the third layer provides an accurate prediction of near-glacier velocity, and in Fig. 5.12e the second layer is an inaccurate prediction for melt rate due to advection playing a significant role in the vorticity balance in Fig. 5.11. On the other hand, the general magnitudes of velocity and melt rate are still reasonable.

In summary, we find that vertical profiles of velocity and melt at the glacial face are dependent on complex bathymetric features and restricts/guides access of dense warm water near the grounding line. The melt rate is strongly influenced by a complicated flow that is not easily captured in our simple theories. However, a simple vorticity balance and melt rate prediction can aid with the interpretation of realistic simulations to better understand how circulation drives glacial melt.

5.5 Conclusions

In this chapter, we use a high-resolution numerical model with realistic geometry to simulate the fjord circulation within three major Greenlandic fjords (Section 5.2, Figs. 5.2–5.4). These simulation results support the discovery of multiple standing eddies in each fjord (see Fig. 5.5). We discuss the properties of these eddies and their role in fjord circulation, tracer advection, and the role of bathymetry in determining their preferred locations (Section 5.3, Figs. 5.6, 5.9, 5.10). To understand the influence of eddies and the resulting circulation

within realistic fjord geometries, we analyze the fjord vorticity balance, which allows us to extend previous theories for the glacial melt rate (Section 5.4).

We find that eddies within glacial fjords are generated by a combination of two vorticity sources (see Fig. 5.11): (1) vorticity generation from the subglacial discharge and meltwater plumes at the glacial face and (2) vorticity advection into the fjord through the fjord mouth at mid-depths. These eddies take months to spin up (Fig. 5.7) and eventually reach a steady state with bottom stress curl balancing/dissipating the vorticity input at depth. The eddies are large perturbations on the horizontal streamfunction within the fjord, undergo mergers with other eddies (Fig. 5.8), and significantly increase the Lagrangian and Eulerian residence times within the fjord (see Fig. 5.9). These eddies prefer deep and wide regions within the fjords (see Fig. 5.10).

Most important, when these eddies are close to the ice face, they serve to amplify glacial melt rates (as shown in Fig. 5.12). To develop a scaling theory for the vertical melt rate, we used the vorticity balance in Section 5.4.1. In this balance, the eddies play an important role in the vorticity budget at deeper depths, where the near-eddy regions dissipate the majority of the vorticity through bottom stress curl. Although the near-eddy circulation is not entirely set by the eddy dynamics, the aggregation of most eddies near the deepest and widest portions of the fjord occurs where the along-isobath circulation dissipates most of the vorticity beneath these eddies. Our results show the existence of long-lived eddies for all three of the fjords studied. However, standing eddies are also likely to exist in many of the other deep-water fjords around Greenland.

There are numerous caveats in this chapter due to the limitations of our model configuration. These include the absence of atmospheric fluxes, simple vertical mixing representation, the lack of sea ice, mélange, and icebergs, which can supply substantial buoyancy input (Enderlin et al., 2016). Another caveat is the prescription of a time-invariant open-ocean boundary, which limits the shelf variability within our simulations; there can be a shelf current-induced increase/decrease in the exchange between the fjord and shelf (Zhao et al.,

2021a). We also do not consider the effect of winds, which likely exhibits a larger effect on the shelf region via fjord overturning driven by coastal upwelling (not included in our domain), but may also directly drive fjord circulation/renewal for strong enough katabatic wind events (Zhao et al., 2021a; Spall et al., 2017). Also, in our glacial boundary parameterization, the melt rates are calculated using the closest grid point of horizontal and vertical fjord velocities, which is an imperfect representation; in general, a better understanding and representation of the ice-ocean boundary layer needed to improve glacial melt rate estimates. Another caveat is that much of the analysis in this chapter is specific to Illulisat, which can be extended to more fjords in the future.

CHAPTER 6

Conclusions

In this chapter, we conclude the thesis with a summary of the results in Chapters 2–5 and review the progress on the primary science questions presented in Section 1.3. We then provide a brief synopsis of recent and ongoing work that targets unanswered aspects of these science questions as well as new ones that have emerged. Finally, we close with long-term aspirations inspired by this thesis work.

6.1 Summary

The projects that constitute this thesis seek to investigate the ocean circulation in fjords and ice-shelf cavities using idealized modeling with the goal of simulating and understanding phenomena that may be useful in guiding future observations. As a result, we have discovered the existence of multiple previously-unobserved phenomena in fjords and ice shelf cavities such as boundary currents, transient and standing eddies, hydraulic-control and the shocks they establish, eddy-driven/drag-dominated/diabatically-driven recirculations, and complex 3D overturning circulation pathways. We have developed simple theories for their dynamics and although the simplifications and idealizations in our studies come with numerous caveats, there is evidence for such phenomena in recent data (Kimura et al., 2016) and regional modeling (Dutrieux et al., 2014). These phenomena are much more easily understood in an idealized model setup, which allows them to be more easier identified in isolation. One goal of this work is to encourage future observations of these phenomena to better understand their role in fjord and ice-shelf cavity circulation and glacial melt.

In Chapter 2, we study the role of bathymetric sills in ocean-filled cavities in West Antarctica and northern Greenland using a simple 2-layer isopycnal model with a channel geometry. We find that bathymetric sills (such as the one below Pine Island ice shelf) can be shallow enough to obstruct the overturning circulation (which supplies the warm water access to glacier faces) and thereby modulate glacial melt rates. We also find that bottom roughness/drag can influence the circulation patterns, but not the overturning strength. The use of an idealized model informs our interpretation of the dynamics, which include eddies, boundary currents, recirculation regions, and hydraulic jumps. We develop theories for the strength of the overturning circulation to explain the simulation results, which are important for determining the role of cavity-circulation on glacial melt rates. Future open questions involve understanding how these dynamics interact with the evolving ice shelf and its impact on the cavity geometry and glacial melt rates. Additional considerations, including the variability of tidal and external currents, winds, accurate bathymetry, ice shelf geometry, and continuous stratification are all important next steps for the community to consider.

In Chapter 3, we investigate how the following parameters control the warm water access to glacier faces: fjord width, sill height, open-ocean stratification, wind direction and strength, and subglacial discharge. We use a 3-layer isopycnal model of a fjord with a plume parametrization and an attached periodic ocean shelf, which is an idealized representation of many fjord-shelf systems in Greenland and the West Antarctic peninsula. This work helps us quantify the relative importance of geometric and oceanic/atmospheric forcing parameters on the control of the volume and heat exchange rate between fjords and the open ocean. We develop theories supported by simulation results for a priori estimates of glacial melt rates based on the parameters explored. Following this work, there are a number of open questions that require further study. Additional observational and modeling work is needed to investigate ice-ocean boundary layer processes to close the gap between our simple melt rate parameterizations based on plume theory and in-situ melt rate observations. In addition,

measurements of fjord recirculation and spatial density variations at depth are lacking and are critically needed to compare with our findings in the hopes of improve our understanding of fjord circulation and their influence on glacial melt rates.

In Chapter 4, we study intra-fjord circulation using an idealized MITgcm configuration with unprecedented resolution at the full-fjord scale. We investigate how the internal fjord variability and circulation responds to the parameter variations studied in Chapter 3 and more important, how the resulting circulation influences the spatial distribution of melt rate at the glacial face. The main findings of the chapter are that: (a) glacial melt in fjords is primarily driven by recirculation at depth for most fjord parameters, which is in turn driven by overturning; (b) front-wide glacial melt at depth dominates the overall melt and rate of undercutting compared to the shallower discharge plume-driven melt; and (c) front-wide glacial melt drives a stronger warm-water overturning and recirculation at depth, leading to a melt-circulation feedback. Following this study, there are a number of open questions that require further attention. Additional work is needed to investigate the submesoscale phenomenology and the distribution of mixing within the fjord. Another future avenue is to investigate boundary layer parameterizations at the glacial face and the interaction of submesoscale-microscale dynamics. A final avenue is to investigate the interaction between circulation and melt in more realistic regional models and the co-interaction of multiple neighboring fjords.

In Chapter 5, we present high-resolution numerical simulations of three glacial fjords (Ilulissat, Sermilik, and Kangerdlugssuaq) forced by NASA OMG (Estimating the Circulation and Climate of the Ocean) observations, which exhibit along-fjord overturning circulations similar to previous studies. However, multiple standing eddies emerge in each of the simulated fjords and owe their existence to realistic fjord geometry. These standing eddies are long-lived, take months to spin up, and prefer locations over the widest regions of deep-water fjords, with some that periodically merge with other eddies. The residence time within these eddies are significantly larger than waters outside of the eddies. These eddies are most

significant for two reasons: (1) they account for a majority of the vorticity dissipation required to balance the vorticity generated by discharge and meltwater plume entrainment and act to spin down the overall recirculation; (2) if the eddies prefer locations near the ice face, their azimuthal velocities can significantly increase melt rates. Therefore, the existence of standing eddies are an important factor to consider in glacial fjord circulation and melt rates and should be taken into account in models and observations. Additional work is needed to investigate individual fjords at higher resolution as well as a larger sample of Greenlandic fjords.

6.2 Progress on Addressing Science Questions

In Section 1.3, we asked: *Why do existing ice-ocean parameterizations underpredict observed glacial melt rates by an order of magnitude? Is it due to a limitation in ice-ocean paramterizations or missing physics?*

A partial answer to this conundrum that emerges in the work leading up to Chapter 4 (and remaining valid in the regional simulation results in Chapter 5) is that melt plumes can account for a significant portion of the overall melt in Greenland fjords. This has been hinted at in previous simulations and observations (Slater et al., 2018), but Chapter 4 provides the first dynamical explanation for why this is the case. In Chapter 4, we showed that a melt-circulation feedback may exist and in deep, warm water fjords, this accounts for a doubling of the melt rate from 150m horizontal resolution to 15m horizontal resolution (see e.g., Fig. 4.1c,f). This suggests that the fine-scale details of fjord circulation are far more important than previously appreciated. Although this melt-circulation feedback is an important newly-recognized dynamical process in fjords and ice-shelf cavities, there is still a significant gap between observed and simulated melt rates, which is the subject of possible future work discussed in Section 6.3.

In addition to this central conundrum, we present a brief overview on the progress on the

science questions posed in Section 1.3.

Primary Science Questions:

- *What are the relevant parameters in constraining the overturning circulation that brings warm water masses towards and away from marine-terminating glaciers?* In Chapters 2–5, we find that both subglacial discharge and melt-driven circulation are primary drivers of the overturning circulation and in the absence of a substantially tall sill or strong forcing, the buoyancy flux at the glacier face can be used to make an accurate prediction of the overturning circulation. However, warm-water access, winds, and bathymetry can all play a role in the overturning circulation by influencing the near-glacier stratification.

- *What are the most important physical/dynamical processes in shelf-fjord and shelf-cavity exchange?* In Chapters 2 and 3, we find that in addition to the overturning circulation, the strength of the horizontal recirculation (and the resulting horizontal velocities near the glacier face) is a critical component of the 3D fjord circulation. This horizontal recirculation is set by a vorticity balance between diabatic generation at the glacier face, bottom stress, and vorticity advection into and out of the fjord or ice-shelf cavity.

- *What are the relevant submesoscale phenomena within fjords/ice shelf cavities and what role do they play in the mixing and export of freshwater?* In Chapter 4, we discover a fjord circulation that is very energetically active at the submesoscale. We partially answer this question by showing that the submesoscale variability can account for a significant increase in melt rate for the highest resolution simulation results, which is in part caused by an increase in the high-frequency submesoscale variability within the fjord.

- *Are there significant feedbacks between fjord circulation and glacial melt rate due to stratification and subglacial plume entrainment and how do these vary over the relevant*

parameter regimes? In Chapter 4, we find that there is nearly a two-fold increase in melt rate between the coarse (150 m horizontal resolution) and highest resolution (15 m horizontal resolution) simulation results. At the highest resolution, the melt-circulation feedback results from an interaction between the horizontal recirculation and melt-driven plume (leading to an increased buoyancy flux) and is particularly strong for fjords with high melt or high subglacial discharge. This feedback exists due to a strengthening of the recirculation over time due to a strengthening of the melt-driven plume over time.

- *How does realistic geometry in fjords influence circulation and glacial melt rate and does this lead to any new dynamical phenomena?* In Chapter 5, we find that realistic geometry can significantly alter the gyre-like circulation observed in previous chapters into a series of standing eddies that prefer wide and deep regions within fjords. These eddies play a significant role in the fjord vorticity balance and can amplify melt rates if they are positioned close to the glacier face.

6.3 Recent and Ongoing Developments

To tackle the remaining science questions and new ones that have emerged as a result of the work in this thesis, we provide a brief synopsis of two follow-up projects that are currently in progress.

6.3.1 Simulating Greenland's Deep-Water Fjords

Preliminary work has begun on the development of a comprehensive suite of high-resolution simulations of all of Greenland's fjords – the GRIFFIN (Greenland Regional Intra-Fjord Fluxes and Interactions Numerics) project (see Fig. 6.1a). A first version of GRIFFIN will use the same framework of regional fjord simulations developed in Chapter 5. Currently,

the simulations in Fig. 6.1a only use the NASA OMG hydrography data. Over time, I plan to iteratively improve this modeling framework to include additional ice-ocean physics, more realistic time-varying surface and boundary forcing conditions, and data assimilation capabilities. In the long term, these fjord-resolving simulations can be used in conjunction with coarse-resolution climate models to improve projections of glacial retreat and sea level rise.

6.3.2 Observations of a Standing Eddy in Torsukataq Fjord, Greenland

Recently, in collaboration with the NASA OMG project, we have made the first observational evidence of a standing eddy within a glacial fjord. Fig. 6.1b shows the locations where Expendable Bathythermographs were deployed in Torsukataq Fjord in Central-West Greenland in Summer 2021. Preliminary results in Fig. 6.1c show temperature profile measurements that provide evidence for the existence of a standing eddy similar to those in the model results presented in Chapter 5. The search for the Torsukataq Fjord eddy was motivated and guided by a model configuration of this fjord similar to the regional models in Chapter 5 and Fig. 6.1a.

6.4 Looking Ahead

In my future work, I plan to conduct Large Eddy Simulations that can resolve both the fjord scale and the discharge plumes. To complement this, I plan to conduct observational work near marine-terminating glaciers with a particular focus on the ice-ocean boundary layer processes. It is likely that an improved understanding of fine-scale processes at and near the boundary layer will offer promising paths towards resolving the major conundrum only partially addressed in this work.

In addition to the goal of leveraging the outcomes of this work to improve climate projections (sea level rise, retreat of ice sheets, regional changes in ocean circulation, etc.), I

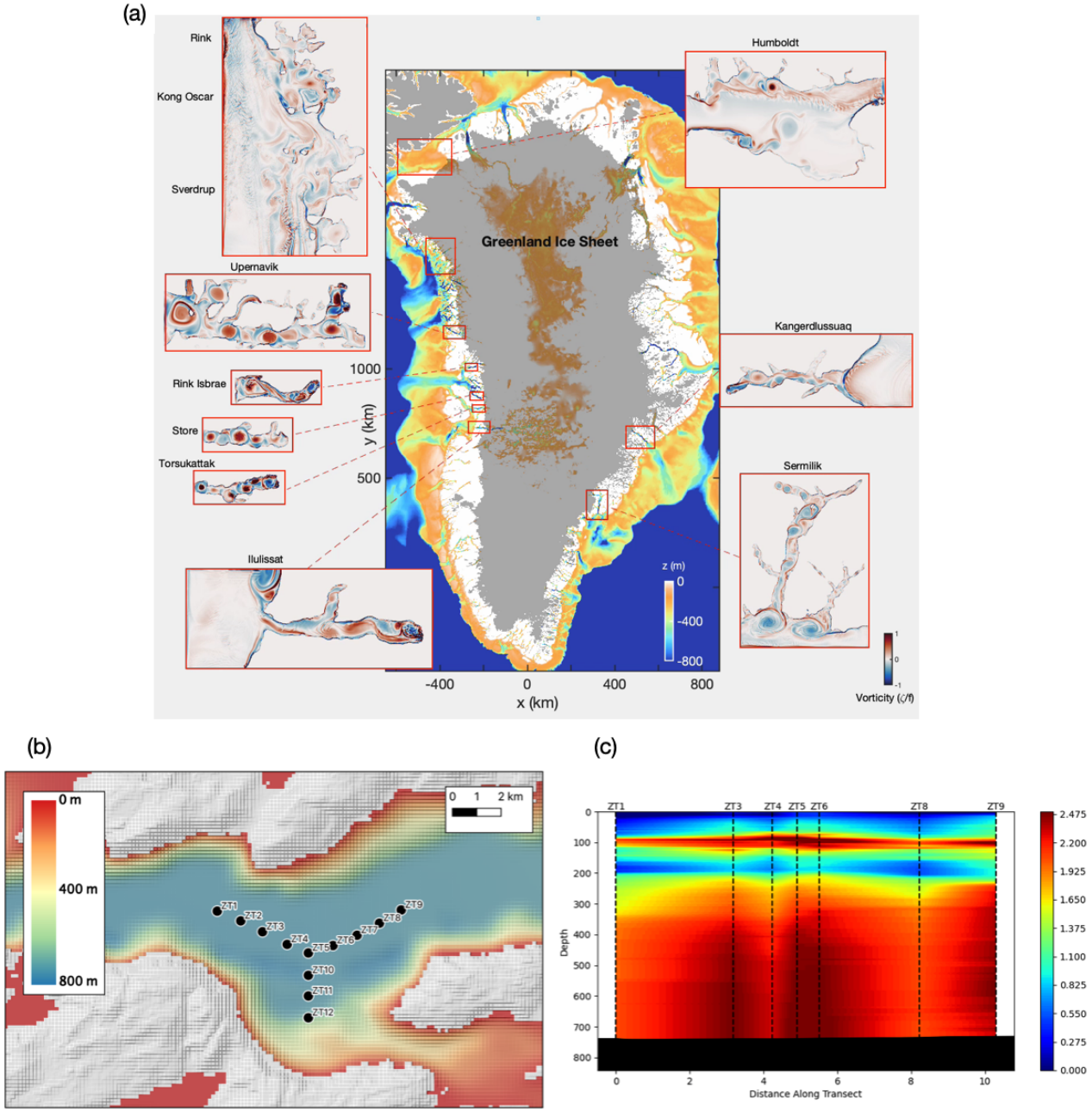

Figure 6.1: Ongoing work on the (a) The GRIFFIN project, a comprehensive suit of high--resolution simulations of Greenland's deep-water fjords, and (b) measurement locations and (c) temperature profiles showing observational evidence of a standing eddy in Torsukataq Fjord, Greenland.

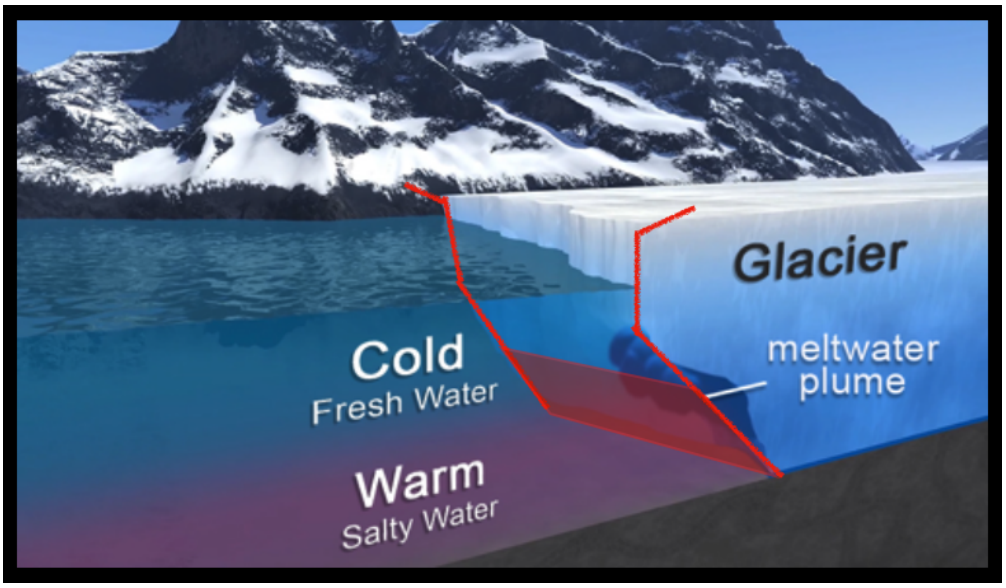

Figure 6.2: An preliminary, untested design sketch for a proposed submarine glacial tarp (in red) to prevent undercutting and slow the retreat of marine-terminating glaciers. (Background image courtesy of NASA OMG.)

propose a related radical glacier geoengineering idea that I believe is worthy of serious consideration and exploration in the spirit of creative climate mitigation solutions (as mentioned in Chapter 1.1).

Fig. 6.2 shows a high-risk high-reward aspirational concept idea for a submarine glacial tarp loosely inspired by the tarps used in mountain glaciers (Huss et al., 2021) and a potentially more cost-effective alternative to existing glacier geoengineering ideas (Moore et al., 2018). In glacial retreat and ice sheet mass balance, the rate of undercutting at the terminus of marine-terminating glaciers is of first order importance. In addition, Chapters 4 and 5 showed that the along-front melt at depth is substantially influenced by a melt-circulation feedback, which would be substantially weakened with a submarine tarp, effectively slowing down glacial retreat. This would be accomplished by serving as a barrier to prevent warm water from reaching the ice and entraining into the meltwater plumes. However, this tarp will likely need to avoid the rapid flowing subglacial discharge regions and many challenges

will need to be overcome to design an effective way of securing the tarp to the ice (perhaps via a grid of ice stakes or multiple moored tethers).

Support for a highly multidisciplinary collaboration including extensive modeling, laboratory experiments, engineering, and small-scale test deployments would be necessary to design and implement a submarine tarp that would mitigate glacial retreat without negatively influencing the glacier stability or biological productivity. Although this idea is highly risky, if effective, these tarps may be deployed at the most critical rapidly-retreating marine-terminating glaciers around Greenland and delay the retreat of the Greenland ice sheet until global greenhouse gas emissions can be sufficiently reduced.

APPENDIX A

Model Sensitivities

Although we have reduced the scope of Chapter 2 to heavily idealized cases, we can determine the sensitivity of the model results with three additional considerations: horizontal grid spacing, top topography, and quadratic friction. We find that in all cases the dynamics remain qualitatively unchanged, and our results may be expected to translate well to more realistic cavity configurations.

We find empirically that the transport, interface, velocity, and sill crossing location are not sensitive to horizontal grid spacings higher than $dl = 250$ m, indicating this resolution is sufficient for the statistical flow properties presented in main text. Fig. A1 shows a comparison of bottom layer PV for four different grid spacings. Even at lower resolutions, the qualitative features of the flow are similar, but there are significant differences in boundary current velocity and transport. Both the overall and gyre-like recirculation strength time-averaged over the last 100 days between resolution $dl = 250$ m and $dl = 125$ m vary by less than 10% and shows a reasonable degree of convergence for $dl = 250$ m.

In the main text of Chapter 2, we restricted our attention to flat-topped rigid lids for simplicity. Therefore, these results are also applicable to the free surface exchange flows since the surface wave effects are negligible for our chosen parameters. However, we can test varying cases of top topographies, as shown in Fig. A2, which does not significantly impact the observable dynamics of the flows, except in extreme cases, which are possible since ice shelf drafts can vary by over hundreds of meters in domains with bathymetry comparable to ours. Top topography is defined using $H_2^S = H - \Delta H_T$ with the top slope starting at

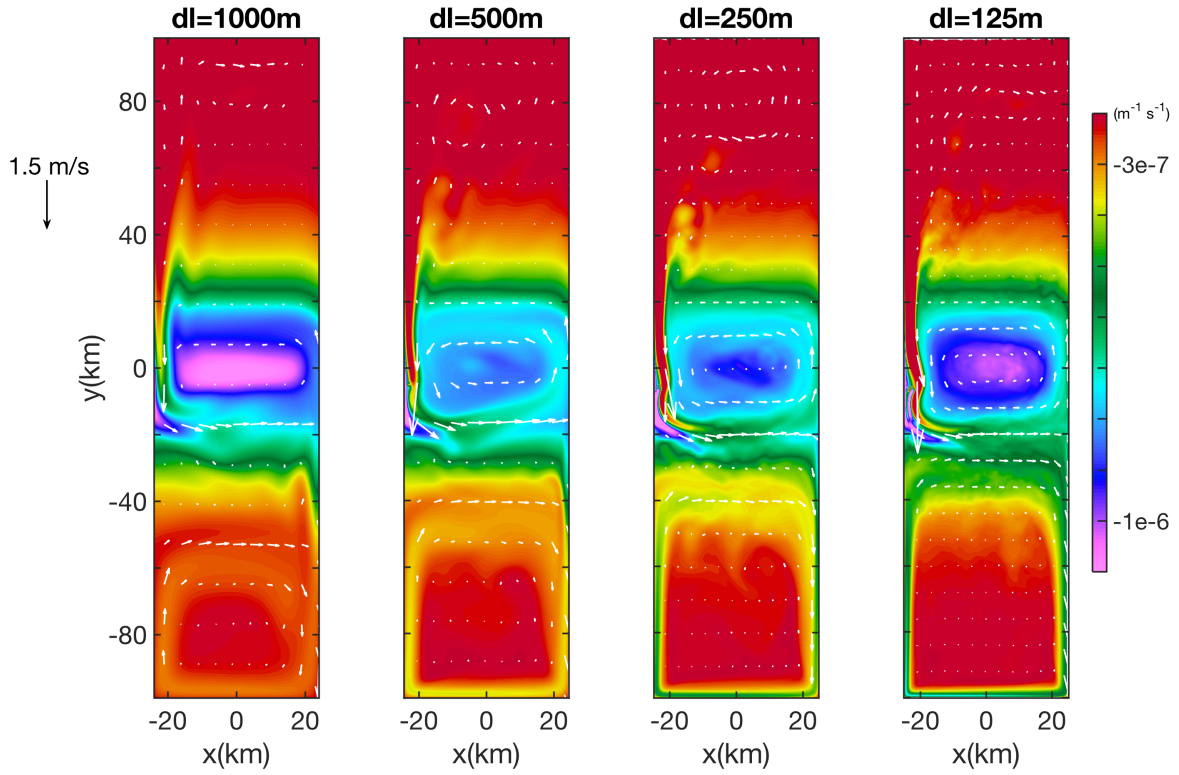

Figure A.1: Resolution sensitivity plot of bottom layer potential vorticity (Eq. (2.11b)) for the case $S_{400}r_5F_{100}$, averaged over last 100 days. The EKE increases and converges at higher resolution, which intensifies the western boundary current, the gyre-like recirculation around the sill maximum, and the boundary gyre in the southern region of the domain. This impacts the central near-sill PV minimum region due to an increase in eddy PV flux convergence also establishes sharper boundary currents. The thickness-weighted average velocity vectors are shown in white for each case.

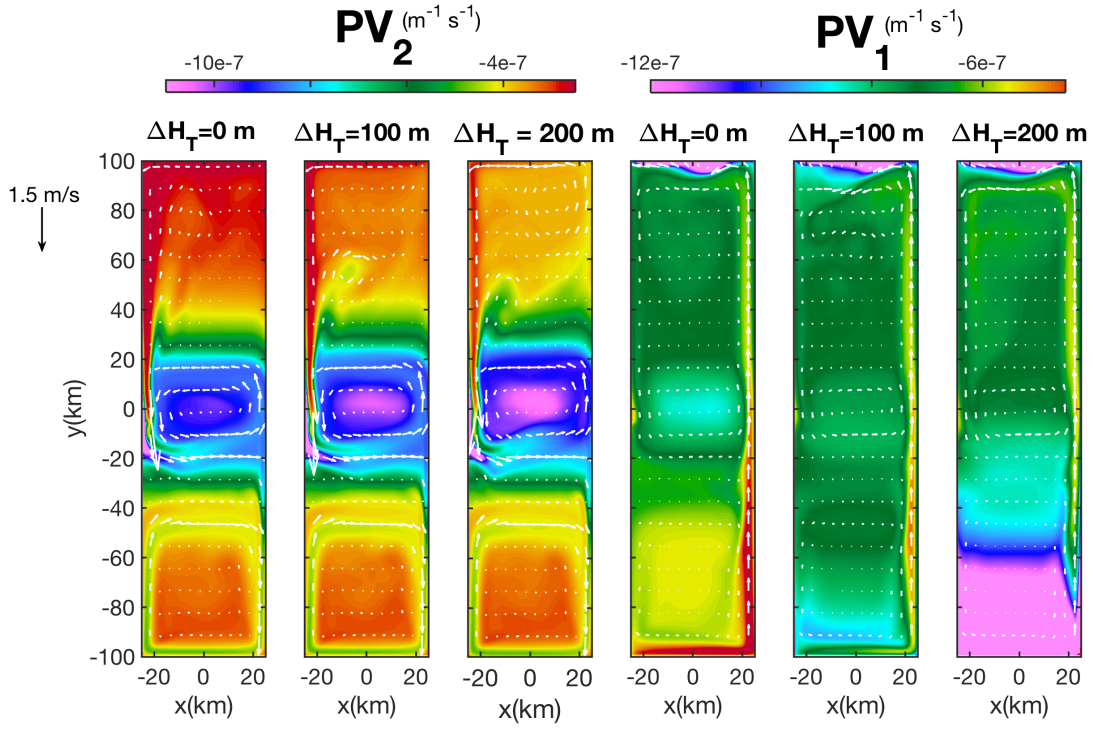

Figure A.2: Sensitivity plot of top and bottom layer thickness-weighted average potential vorticity (PV_1 and PV_2, respectively) (Eq. (2.11b)) for case $S_{400}r_5F_{100}$ with top slopes $\Delta H_T = 0, 100, 200$ m, averaged over last 100 days. This demonstrates that top topography has a small effect on the overall dynamics of both the bottom and top layer. The thickness-weighted average velocity vectors are shown in white for each case.

the midpoint $y = 0$ and is flat north of this, which is a crude approximation for the PIG geometry (Kimura et al., 2016). We found no significant differences as long as the sill's topographic beta is much larger than the top topographic beta, which is true except for very gentle sills.

We also tested longer domains and bathymetry for varying sill width scale L_{Sill} using meridionally stretched domains. These results did not show any qualitative difference when mapped back onto the regular domain except in the HF regime, where the boundary layer widens, a result consistent with our theory that $L_{\mathrm{St}} \propto L_{\mathrm{Sill}}$.

Finally, we tested the effect of a realistic quadratic friction with a dimensionless coefficient of 2×10^{-3}, in contrast with the range of linear friction coefficients we have explored in the main text. With this quadratic friction, we observe the same dynamical regimes discussed in this study for equivalent values of friction depending on the specified pressure head. For example, with a pressure head of $\Delta H_2 = 100$ m and $H_{\mathrm{sill}} = 400$ m, the quadratic solution exhibits a similar mean and RMSD transport to the linear friction case with $\hat{r} = 0.1$, as shown in Fig. 2.2.

APPENDIX B

Forward-Backward Time-stepping in a Rigid Lid

We present a method for finding a convergent, accurate pressure field at the top surface for the Forward-Backward time-stepping scheme. A similar approach can also be taken for the generalized Forward-Backward time-stepping scheme.

Traditionally, in the Forward-Backward time-stepping scheme with a free-surface, each layer depth h is calculated forward in time based on the velocity fields u and v at a time t i.e. $h^{t+1} = f(u^t, v^t, h^t)$, while the velocities are calculated backward in time based on h^{t+1} as

$$\begin{aligned} h^{t+1} &= h^t + \Delta t[\nabla \cdot (h\mathbf{u}^t)]\,, \\ u^{t+1} &= u^t + \Delta t G_u(h^{t+1}, u^t, v^t)\,, \\ v^{t+1} &= v^t + \Delta t G_v(h^{t+1}, u^{t+1}, v^t)\,, \end{aligned} \tag{B.1}$$

where $\mathbf{G} = \partial_t \mathbf{u}$ is the momentum tendency from Eq. (3.2a). The meridional velocity v benefits from a backward Coriolis term due to u^{t+1} and to minimize errors, this process alternates the term that is updated first.

However, with a rigid lid implementation, the velocities are only partially updated via an explicit time step, and are then corrected to include the tendency due to the surface pressure gradient. Specifically, the velocity vector $\mathbf{u}^t$ for each layer is updated so that $\mathbf{G}^* = \mathbf{G} - \nabla\phi_1$, using the definition for the top layer Montgomery potential $\phi_1 = p_T/\bar{\rho}$, so all the forces in the momentum balance are included except surface pressure gradient. This results in a force decomposition $\partial_t \mathbf{u} = \mathbf{G} - \nabla\phi_1$ where

$$\mathbf{u}^{t+1} = \mathbf{u}^t + \Delta t \mathbf{G}(\mathbf{u}^t, h^{t+1}) - \Delta t \nabla \phi_1^{t+1} = \mathbf{u}^* - \Delta t \nabla \phi_1^{t+1}\,. \tag{B.2}$$

The initial velocity u^t after a partial update, including all forces except pressure gradient, becomes u^*, and after including the surface pressure gradient force, becomes u^{t+1}. This is calculated for each time-step in the order

$$h^{t+1} = h^t + \Delta t[\nabla \cdot (h\mathbf{u}^t)]\,, \tag{B.3a}$$

$$u^* = u^t + \Delta t G_u(u^t, v^t, h^{t+1})\,, \tag{B.3b}$$

$$v^* = v^t + \Delta t G_v(u^t, v^t, h^{t+1})\,, \tag{B.3c}$$

$$\phi_1^{t+1} \text{ s.t. } \nabla \cdot (H\nabla\phi_1^{t+1}) = \nabla \cdot (HG_{u,v}(u^t, v^t, h^{t+1}))\,, \tag{B.3d}$$

$$u^{t+1} = u^t + \Delta t G_u(h^{t+1}, v^*, \nabla\phi_1^{t+1})\,, \tag{B.3e}$$

$$v^{t+1} = v^t + \Delta t G_v(h^{t+1}, u^*, \nabla\phi^{t+1})\,. \tag{B.3f}$$

In Eq. (B.3c), the half-updated velocity v^* can no longer include the backwards Coriolis contribution from u^*, since continuity must be satisfied at full steps t and $t+1$ and not half steps i.e. $\nabla \cdot (h^{t+1}\mathbf{u}^{t+1})$ and $\nabla \cdot (h^t\mathbf{u}^t) = 0$ are satisfied, but $\nabla \cdot (h^{t+1}\mathbf{u}^*) = 0$ is not necessarily satisfied. Therefore, v^{t+1} can not be updated using u^{t+1} since continuity is satisfied for $\nabla\phi_1^{t+1}$, calculated based on (u^*, v^*), while it is not necessarily satisfied for (u^{t+1}, v^*).

The velocities with the fully updated pressures must have zero depth-integrated divergence, satisfying the continuity equation at every gridpoint in the horizontal plane. Thus, the pressure gradient $\nabla\phi_1^{t+1}$ is constrained in terms of the known partially-updated variables.

APPENDIX C

Thickness-weighted PV Balance

In our problem, the PV balance allows us identify the dominant mechanisms that facilitate cross-sill exchanges in various parameter regimes.

By taking the curl of the momentum equation, the mean shallow water thickness-weighted PV equation for a homogeneous fluid layer with friction and viscosity is

$$\frac{\partial \overline{h_n q_n}}{\partial t} + \nabla \cdot (\overline{h_n q_n \mathbf{u}_n}) = -\nabla \times \overline{\left(\frac{r\mathbf{u}_n}{h_n} \right)} + \overline{h \nabla \times (\upsilon S_n)} \,. \tag{C.1}$$

This equation is time-averaged and advection can be partitioned into mean and eddy components of PV flux with the thickness-weighted identity

$$\overline{h_n q_n \mathbf{u}_n} \;=\; \overline{h_n} \langle q_n \mathbf{u}_n \rangle \;=\; \overline{h}_n \langle [\langle q_n \rangle + q_n^\dagger][\langle \mathbf{u}_n \rangle + \mathbf{u}_n^\dagger] \rangle \;=\; \overline{h}_n [\langle \mathbf{u}_n^\dagger q_n^\dagger \rangle + \langle \mathbf{u}_n \rangle \langle q_n \rangle] \,, \tag{C.2}$$

where we define the thickness-weighted average and deviations from that average in Eq. (2.26). This allows Eq. (C.1) to be written as

$$\frac{\partial}{\partial t}(\overline{h}_n \langle q_n \rangle) + \nabla \cdot [\overline{h}_n (\langle \mathbf{u}_n \rangle \langle q_n \rangle + \langle \mathbf{u}_n^\dagger q_n^\dagger \rangle)] \;=\; -\nabla \times \overline{\left(\frac{r\mathbf{u}_n}{h_n} \right)} + \overline{h \nabla \times (\upsilon S_n)} \,. \tag{C.3}$$

The diabatic terms $\langle q_n \rangle (\partial_t \overline{h}_n + \nabla \cdot \overline{h_n \mathbf{u}_n})$ can be grouped together under the continuity equation in Eq. (3.2b) as

$$\overline{h}_n \frac{\partial \langle q_n \rangle}{\partial t} + \overline{h}_n \langle \mathbf{u}_n \rangle \cdot \nabla \langle q_n \rangle + \nabla \cdot [\overline{h}_n \langle \mathbf{u}_n^\dagger q_n^\dagger \rangle] = - \nabla \times \overline{\left(\frac{r\mathbf{u}_n}{h_n} \right)} + \overline{h \nabla \times (\upsilon S_n)} - \varpi_n \langle q_n \rangle \,. \tag{C.4}$$

This equation states that in a frame following the thickness-weighted average velocity, the thickness-weighted PV is modified by eddy PV flux convergence, torques imposed by friction and viscosity, and stretching imposed by diabatic velocities.

APPENDIX D

Rotating 2-Layer Uniform PV Solution

In addition to the rotating 1-layer zero PV solution provided in Section 2.7, we present a rotating 2-layer uniform PV solution following Pratt and Armi (1990). This discussion is restricted to isopycnal layers of inviscid fluid flowing due to pressure and gravity in a channel of slowly varying cross-section. The 2-layer channel flow solution over bathymetry assumes uniform PV for each layer n

$$q_n = \frac{f}{H_{i\infty}} = \frac{f + \dfrac{\partial v_n}{\partial x}}{h_n}\,, \tag{D.1}$$

where $H_{n\infty}$ is the upstream layer thickness. The Bernoulli functions for the two-layer case are defined as

$$B_1(\psi_1) = \frac{v_1^2}{2} + \frac{p_T}{\bar{\rho}} + B_{1\infty}\,, \tag{D.2a}$$

$$B_2(\psi_2) = \frac{v_2^2}{2} + \frac{p_T}{\bar{\rho}} + g'(h_2 + h_B) + B_{2\infty}\,, \tag{D.2b}$$

and are constant along streamlines. The prescribed integration constants $B_{1\infty}$ and $B_{2\infty}$ are defined as fixed potentials infinitely upstream and are chosen based on the interface depth for a quiescent flow. The analog of this for our finite domain is defined using the thicknesses at the northern boundary conditions H_1^N, H_2^N.

Using Eqs. (D.1) – (D.2b) and Eqs. (2.30a) – (2.30c), the general form of solutions for thickness and along-channel velocity are

$$h_n(x) = \overline{D}_n e^{k_d x} + \hat{D}_n e^{-k_d x} + \overline{U}\,, \tag{D.3a}$$

$$v_n(x) = \overline{V}_n e^{k_d x} + \hat{V}_n e^{-k_d x} + Cx + \overline{U}\,, \tag{D.3b}$$

where $\overline{D}_n, \hat{D}_n, \overline{V}, \hat{V}, C,$ and $\overline{U}$ are constants that can be determined in terms of $H_{i\infty}$ and h_B analytically (Pratt and Armi, 1990). Our analytical predictions for the critical transport based on this theory were calculated iteratively by finding the Bernoulli constants that exceeded the threshold for critical velocities at the sill maximum.

As prescribed pressure head increases, the analytical solution reaches a critical and eventually a supercritical state, which generally leads to PV adjustment processes that cause the breakdown of semigeostrophic theory and uniform PV becoming a poor assumption (Pratt and Armi 1990, Dalziel 1991). Therefore, there must be nonuniform PV effects, otherwise the cross-channel velocity gradient would result in a flow that would be highly supercritical for channel widths greater than $\sim L_d$, due to the barotropic cross-channel shear necessary to maintain uniform PV. Specifically, in our numerical solutions, we find that uniform PV is a reasonable approximation in the wide channel limit only within a western boundary layer of scale width $\sim L_d$, and the flow transitions to a smaller PV in the quiescent interior. This is also supported by analytical non-uniform PV models and laboratory experiments. For instance, Borenas and Whitehead (1998) demonstrated in laboratory experiments that upstream recirculation with flow reversals are necessary for flow separation and maintain criticality due to the recirculatory flow. Either recirculation or nonuniform PV are therefore unsurprising in the wide limit to maintain hydraulically-controlled states since highly supercritical flows are unlikely to remain steady.

APPENDIX E

Rotating Uniform PV Layer-Grounding Theory

In Chapter 2, layer-grounding occurs for sufficiently high sills with supercritical flow. Here, we derive a theoretical estimate for the boundary current transport necessary to achieve this state using the 1-layer Eqs. (2.30a) – (2.30c) for a boundary current of uniform PV of width $w_{\mathrm{BC}}(y)$ to be determined, that evolves in the along-stream direction, adjacent to a stagnant interior. We consider an inflow coming from the northern boundary, between the western wall $x = -W/2$ and $x = -W/2 + w_{\mathrm{BC}}(y)$. Implicitly, $h + h_B = H_\infty$ at $x = -W/2 + w_{\mathrm{BC}}(y)$ from Eq. (2.30c). The boundary conditions for the western boundary current are

$$v[-W/2 + w_{\mathrm{BC}}(y)] = 0\,, \tag{E.1a}$$

$$\psi[-W/2 + w_{\mathrm{BC}}(y)] = 0\,, \tag{E.1b}$$

$$\psi[-W/2] = Q\,, \tag{E.1c}$$

where $Q = -\int_{-W/2}^{x} hv dx'$ is the along-channel transport.

The boundary conditions in Eqs. (E.1a) and (E.1b) combined with Eqs. (2.30a) – (2.30c) allows us to write the solutions for h and v as a function of h_B and x

$$h = -h_B \cosh\left(\frac{x + w_{\mathrm{BC}}}{L_d}\right) + H_\infty\,, \tag{E.2a}$$

$$v = -\frac{g' h_B}{f L_d} \sinh\left(\frac{x + w_{\mathrm{BC}}}{L_d}\right)\,. \tag{E.2b}$$

Applying the third boundary condition in Eq. (E.1c), the expression involving transport can be written as

$$\frac{Qf}{g' h_B H_\infty} - \frac{h_B}{2H_\infty} \sinh^2\left(\frac{w_{\mathrm{BC}}}{L_d}\right) + \cosh\left(\frac{w_{\mathrm{BC}}}{L_d}\right) = 1\,, \tag{E.3}$$

which yields two solutions for the boundary current width

$$w_{\mathrm{BC}}(y) = L_d \cosh^{-1}\left(\frac{H_\infty \pm \sqrt{H_\infty^2 - 2H_\infty h_B + h_B^2 + 2Qf/g}}{h_B}\right), \tag{E.4}$$

which is $\mathcal{O}(L_d)$ and changes as a function of bathymetric height, upstream forcing, and transport, reaching a minimum at the sill maximum. Layer-grounding can occur when $h = 0$ using Eq. (E.2a), but the solution branch $w_{\mathrm{BC}} \geq L_d \cosh^{-1}(H_\infty/H_{\mathrm{Sill}})$ can be excluded since the thickness is always negative somewhere.

Therefore, the condition that predicts layer-grounding is when the discriminant in (E.4) becomes negative

$$Q_{\mathrm{ground}} \geq \frac{g(H - H_{\mathrm{Sill}})^2}{2|f|}. \tag{E.5}$$

This represents a sharp transition of a boundary current of width $w_{\mathrm{BC}} = L_d \cosh^{-1}(H_\infty/h_B)$ to a boundary of undefined width i.e. grounding. This appropriately represents the behavior observed in our simulations since boundary currents have width $\mathcal{O}(L_d)$ immediately before layer-grounding, instead of a width that approaches zero.

APPENDIX F

Plume Parameterization in an Isopycnal Model

We derive a point-source plume solution with a piecewise-constant background density, which can be used in isopycnal models such as BEOM. This is a special case of plume theory in a continously-stratified fluid (see e.g., Turner 1979).

The traditional theory of plumes with uniform background density predicts that buoyant plumes are largely controlled by the buoyancy forcing, which sets the entrainment and mixing of the plume with the ambient fluid (Morton et al., 1956). An axisymmetric turbulent plume can be defined based on the parameters B (buoyancy flux), z (height above the source), and R (radial length scale). For a constant background density, it is often assumed that the profiles are self-similar and dimensional analysis can be used to find the vertical velocity w, reduced gravity g', and R as a function of z.

The conservation of mass, momentum, and buoyancy flux can be written as (Turner, 1979)

$$\frac{\partial m}{\partial z} = 2\alpha m/R\,, \tag{F.1a}$$

$$\frac{\partial mw}{\partial z} = mg'/w\,, \tag{F.1b}$$

$$\frac{\partial mg'}{\partial z} = -mN^2(z)\,, \tag{F.1c}$$

for a mass defined as $m = R^2 w$. For the specific case of piecewise-uniform density, the buoyancy flux (third equation) can be simplified to

$$B = mg'\,. \tag{F.2}$$

B is constant within each layer, but changes at each interface according to this definition, which is discontinuous since g' is discontinuous. We implement a simple first-order Euler scheme for R and w, which converges for small interval size $\Delta z \sim 0.1$ m. We use this to solve for $R(z)$ and $g'(z) = B/m$ at each step in z. At interfaces, we solve for the jump in B and g' as $\Delta B = B_+ - B_-$ and $\Delta g' = g'_+ - g'_-$ before solving for m and w. These jumps are defined as

$$\Delta B = \pi R^2 w g(\rho_+ - \rho_-)/\bar{\rho}\,, \tag{F.3a}$$

$$\Delta g' = g(\rho_+ - \rho_-)/\bar{\rho}\,. \tag{F.3b}$$

This density of the plume can therefore be defined as

$$\rho_P(z) = -g'\bar{\rho}/g + \rho(z)\,, \tag{F.4}$$

which is continuous since

$$\rho_{P+} - \rho_{P-} = -(g'_+ - g'_-)\bar{\rho}/g + (\rho_+ - \rho_-) = 0\,. \tag{F.5}$$

For the 3-layer isopycnal model, the overturning circulation is determined by buoyancy fluxes and mass entrainment driven by either a point source or line source. The mass flux and density flux relationships can be determined in multiple ways. Fig. F.1 illustrates one way to partition control volumes to determine the overall bulk water mass transformations, which are defined in terms of the two unknowns: volume transport in the bottom and top layers, Q_3 and $-Q_1$. The volume transport in the middle layer must compensate the transport in the other two layers. The density flux conservation equations for the overall system can then be written as (with mass conservation already applied)

$$(Q_3 - Q_0)\rho_3 + Q_0\rho_0 = Q_3\rho_3^P\,, \tag{F.6a}$$

$$Q_1\rho_1 + (Q_3 - Q_1)\rho_2 = Q_3\rho_3^P\,. \tag{F.6b}$$

We can solve for the unknowns as

$$Q_3 = \frac{Q_0(\rho_3 - \rho_0)}{\rho_3 - \rho_3^P}\,, \tag{F.7a}$$

$$Q_1 = \frac{Q_3(\rho_2 - \rho_3^P)}{\rho_2 - \rho_1}\,, \tag{F.7b}$$

where ρ_3^P is found using Eq. (F.4) evaluated at the interface between between layers 2 and 3.

We choose W_{nudg} and L_{nudg} to be the width and length of the nudging region. In our simulations, we define our nudging region to be 5 km so the diabatic flux is resolved and distributed over at least 10 grid points, whereas the plume radius would be sub-gridscale. The thickness nudging due to plume entrainment corresponding to the diagram in Fig. F.1 can be expressed as

$$\varpi_{1,\text{p}} = \left(\frac{\partial h_1}{\partial t}\right)_{\text{p}} = \frac{Q_1}{W_{\text{nudg}} L_{\text{nudg}}}\,, \tag{F.8a}$$

$$\varpi_{2,\text{p}} = \left(\frac{\partial h_2}{\partial t}\right)_{\text{p}} = \frac{Q_3 + Q_0 - Q_1}{W_{\text{nudg}} L_{\text{nudg}}}\,, \tag{F.8b}$$

$$\varpi_{3,\text{p}} = \left(\frac{\partial h_3}{\partial t}\right)_{\text{p}} = -\frac{Q_3 + Q_0}{W_{\text{nudg}} L_{\text{nudg}}}\,. \tag{F.8c}$$

We can alternatively express Eq. (F.7a) as two cases (depending on the plume exit depth),

$$Q_{\text{plume}} = Q_3 = \begin{cases} Q_0(\rho_3 - \rho_0)(\rho_3 - \rho_3^P)^{-1}, & \text{if } \rho_3^P < \rho_2 \\ Q_0(\rho_3 - \rho_0)(\rho_3 - \rho_2)^{-1}, & \text{if } \rho_3^P \geq \rho_2 \end{cases} \tag{F.9a}$$

$$\text{where } \rho_3^P = -g'_{5/2}\rho_2/g + \rho_3\,. \tag{F.9b}$$

For the second case in Eq. (F.9a), where $\rho_3^P \geq \rho_2$, the overturning circulation reduces to the Knudsen relations in the bottom two layers, which depends only on the stratification and the discharge strength. However, each of the parameters we consider can potentially lead to the first case ($\rho_3^P < \rho_2$), which decreases the overturning strength by a factor of $(\rho_3 - \rho_2)(\rho_3 - \rho_3^P)^{-1} < 1$. In the simulations discussed in Sect. 3, this was readily achieved

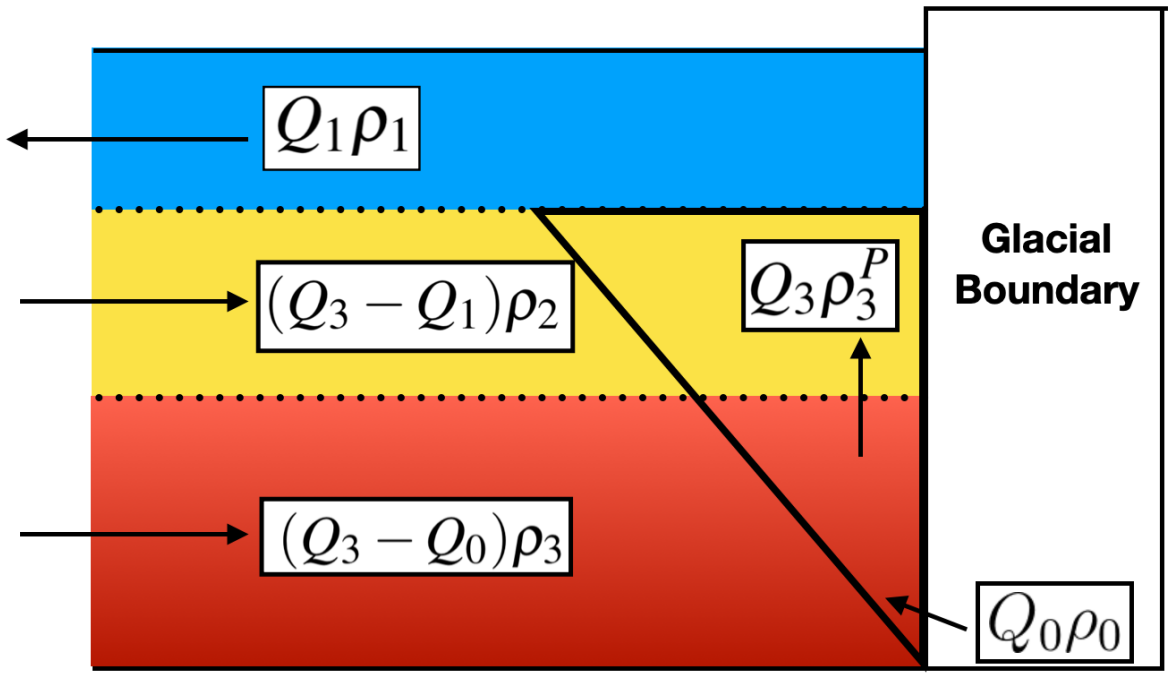

Figure F.1: A diagram of bulk water mass transport in our BEOM plume parameterization used in Chapter 3.

for greater sill heights and deeper offshore AW, but this is also achievable for other parameters as well, especially a denser top layer and shallower fjord.

Similarly, a line plume parameterization with varying source width is implemented and test in our model. For a small discharge width (50 m or less), there is a negligible difference between the terminal volume flux of a point plume and line plume parameterization. For larger plume source widths, the overturning strength and neutral depth of the plume are quantitatively different, but the overturning still varies proportionally to the discharge.

APPENDIX G

Circulation-Aware Glacial Melt Rate Estimates

An important implication for fjord overturning and horizontal recirculation is the submarine melt rate implied by our simulation results and theory. The purpose of this appendix is to draw a posteriori melt rate inferences from the overturning and recirculation strengths diagnosed from our simulations. We calculate the melt rates using a front-wide ambient melt (including a line plume) in the warm bottom layer area in contact with the glacial face as well as the melt rate within the half-cone subglacial discharge-driven plume over a much smaller area of the glacial face.

All along the glacial face, the melt rate per unit area can be solved using a combination of the depth-dependent plume equations (discussed in Appendix A) and the three-equation system (Hellmer and Olbers, 1989; Holland and Jenkins, 1999), which describes the thermodynamical equilibrium at the ice-ocean interface. This equilibrium can be expressed using approximate heat and salt conservation and the linearized freezing temperature of seawater,

$$q(L_i + c_i(T_b - T_i)) = \gamma_T c_w (T_p - T_b) \tag{G.1a}$$

$$qS_b = \gamma_S (S_p - S_b)\,, \tag{G.1b}$$

$$T_b = \lambda_1 S_b + \lambda_2 + \lambda_3 z\,. \tag{G.1c}$$

Here, q (m s^{-1}) is the glacial melt rate per unit area, $L_i = 3.35 \times 10^5$ J kg^{-1} is the latent heat of fusion of ice, $c_w = 3.974 \times 10^3$ J kg^{-1} K^{-1} is the specific heat capacity of water, $c_i = 2 \times 10^3$ J kg^{-1} K^{-1} is the specific heat capacity of ice, T_p and S_p are the plume temperature and salinity, $T_i = -10$ °C is the ice temperature, T_b and S_b are the boundary layer temperature and salinity, γ_T and γ_S are the turbulent thermal and salt transfer coefficient, and $\lambda_1 =$

-5.73×10^{-2} °C psu^{-1}, $\lambda_2 = 8.32 \times 10^{-2}$ °C, and $\lambda_3 = 7.61 \times 10^{-4}$ °C m^{-1} are the freezing point slope, offset, and depth. These empirical values are consistent with those used in previous studies (Sciascia et al., 2013; Cowton et al., 2015).

Although previous parameterizations of the turbulent transfer coefficients used constant values (Hellmer and Olbers, 1989), more recent work shows that a dependence on ocean velocities near the boundary are in better agreement with submarine melt rate measurements (Jenkins et al., 2010)

$$\gamma_T = C_d^{1/2} \Gamma_T \sqrt{v^2 + w^2}\,, \tag{G.2a}$$

$$\gamma_S = C_d^{1/2} \Gamma_S \sqrt{v^2 + w^2}\,, \tag{G.2b}$$

where $C_d = 2.5 \times 10^{-3}$ is the drag coefficient, $\Gamma_T = 2.2 \times 10^{-2}$ and $\Gamma_S = 6.2 \times 10^{-4}$ are the thermal and salt transfer constants, and v and w are the tangential horizontal and vertical velocities at the glacier boundary. For our simulations, the plume vertical velocity (at 100 m above the discharge source) ranges from 0 m/s (no subglacial discharge) to 3.7 m/s (greatest discharge) and the horizontal velocity $v = v_{\max}$ in the gridpoint adjacent to the glacier face in the lower layer ranges from 0.05 to 0.3 m/s.

Although the vertical velocities (in the plume) are much larger than the horizontal velocities near the glacial face, recent work suggests that the ambient melt dynamics driven by the horizontal recirculation may be as important as the subglacial discharge-driven melt (Slater et al. 2018, Jackson et al. 2019). This is partly due to the fact that ambient melt affects a much larger area of the glacial face. Studies have also noted that ambient melt rates from the plume melt parameterizations are unrealistically low compared to the total ice flux at the terminus, but have not determined which melt processes produce these high melt rates (Jackson et al., 2019; Straneo and Cenedese, 2015; Carroll et al., 2016; Fried et al., 2015).

For Jakobshavn Glacier, using a subglacial discharge of 1700 m^3/s (based on assuming all runoff enters as subglacial discharge in Beaird et al. 2017), our theory predicts an overturning circulation of 85 mSv and horizontal recirculation strength of 300 mSv. Here, the plume

vertical velocity at the mid-depth point of the bottom layer (predicted to be 440 m thick) is 2.7 m/s and the horizontal velocity at the glacier boundary is 0.34 m/s. Using a bottom layer ambient temperature and salinity of 4 ^{o}C and 34.0 psu (Gladish et al., 2015), we can calculate the plume temperature and salinity at mid-depth in the bottom layer. Using Eqs. (G.1a)-(G.1c), this allows us to find the boundary layer temperature and salinity and the melt rates. Our predicted maximum discharge plume-driven melt rate (or rate of undercutting) is 8.7 m/day and the predicted ambient melt rate over the rest of the terminus in contact with the bottom layer AW is 1.1 m/day. However, due to its much larger area, the ambient melt accounts for 80% of the total volume melt and is $\sim$1.0 km^3/year based on a bottom layer thickness of 400 m and fjord width of 8 km.

We note that the ambient melt rate is dictated by $v_{\max}$, since it is $\sim$30 times larger than the vertical velocity of the distributed line plume predicted by plume theory (Jenkins, 2011). Thus, the ambient melt rate including the horizontal velocity is approximately 30 times larger than the one using only the vertical line plume velocity. Since our melt rate estimate uses the discrete density profile from our 3-layer model and is only an approximation to the realistic vertical structure of temperature and salinity, it is only able to capture an approximate bulk melt rate estimate.

The ratio of areas covered by the discharge plume and ambient melt plume depends on the mean width of the discharge plume source and the vertical rise distance. The mean width for a point/cone plume is half of its radius at neutral buoyancy ($R_{\max}/2$) and for a truncated-line plume with a finite width w_{s} discharge source, the mean width is the mean of w_{s} and $R_{\max}/2$ (Cowton et al. 2015, Jackson et al. 2017). For a truncated-line plume of $w_{\mathrm{s}} = 200$ m at the source (which best fits Greenland's fjords, as shown in Jackson et al. 2017), our simulation results for the Jakobshavn test case suggests a subglacial discharge plume that occupies $\sim$3% of the surface area of the face, but accounts for 20% of the meltwater supply. However, the buoyancy forcing is likely dominated by the freshwater from subglacial discharge rather than the meltwater production.

Recently, it has been argued that the empirical coefficients C_d and Γ_T are untested in tidewater glaciers and larger values are more consistent with observations, i.e. $C_d = 1 \times 10^{-2}$, $\Gamma_T = 4.4 \times 10^{-2}$, which would result in melt rate estimates that are 4 times greater (Jackson et al., 2019).

APPENDIX H

MITgcm Model Setup and Plume Parameterizations

The model used in Chapter 4 is the Massachusetts Institute of Technology General Circulation Model (MITgcm). Using this model, we solve the hydrostatic, Boussinesq primitive equations with a nonlinear equation of state based on Jackett and McDougall 1995. For the cases with tides (see the table in Appendix J), we use a barotropic tidal velocity (with magnitudes of 0 to 0.1 m/s) with a semi-diurnal frequency.

The plume parameterizations that we implement in the MITgcm model configuration is a slightly modified version of that proposed by Cowton et al. 2015, optimized to work efficiently in high resolution simulations, and is available at: *https://github.com/zhazorken/MITgcm_FJ*. This is identical to the parameterization package detailed in Cowton et al. 2015, except for an important distinction: we redistribute the buoyancy anomalies from the solutions to the discharge plume equations over a 10-gridpoint radius semi-circle in the horizontal and apply a 3-gridpoint smoothing in the vertical while conserving the overall buoyancy anomaly and entrainment. This prevents prohibitive restrictions set by the Courant-Friedrichs-Lewy (CFL) condition on the model timestep in our high resolution simulations as well as spurious mixing caused by sharp gradients in the forcing at the gridscale. The effects of the buoyancy forcing from this modified plume parameterization can be seen in the first 10 near-glacier gridpoints ($0 < x < 380$ m) near the glacier in the overturning streamfunction plots (Figs. 4.2e and J4). The sensitivity of the model diagnostics to the number of gridpoints of the plume forcing (between 5- and 15-gridpoint radii) was very weak, but 10 gridpoints provided a significant (4x) improvement to the model timestep limitation.

The basic formulas for the vertical volume flux via entrainment for a point source plume (representing the discharge plume) and a sheet plume (representing the distributed melt plume) that are used in these plume parameterizations (as well as the theory in Section 4.4) can be derived from classic self-similarity and entrainment assumptions (see e.g., Morton et al. 1956). To provide context for our theory, the following is a brief overview of the fundamental aspects of plume theory.

An idealized axisymmetric turbulent plume can be defined in terms of parameters B (buoyancy flux) and r (radial length scale), which are functions of z (height above the source). For a constant background density, it is often assumed that plume profiles are self-similar and dimensional analysis can be used to find the vertical velocity w, reduced gravity g', and r as a function of z. Alternatively, for background density profiles that vary with height, and the plume parameterization used in our model configuration, the vertical properties of the plume are found numerically by solving a set of differential equations, i.e., the conservation of mass, momentum, and buoyancy flux (based on Turner 1979):

$$\frac{\partial m}{\partial z} = 2\alpha m/r\,, \tag{H.1a}$$

$$\frac{\partial mw}{\partial z} = mg'/w\,, \tag{H.1b}$$

$$\frac{\partial mg'}{\partial z} = -mN^2(z)\,, \tag{H.1c}$$

for a plume entrainment mass flux $m = r^2 w$. A similar set of equations can also be derived for the front-wide melt plume by imposing a distributed buoyancy flux and can also be solved numerically (see Turner 1979). For a more complete plume formulation which includes temperature, salinity, and density profiles that vary with depth (such as the one implemented in our model), see Cowton et al. 2015.

In order to arrive at the simplifications to the overturning theory discussed in Section 4 (which are discharge- and melt plume-driven), we can approximate the solution to Eqs. (H.1a)-(H.1c) by assuming an approximately uniform density below the depth of neutral

buoyancy (which is a fairly accurate approximation given the weak stratification below the neutral buoyancy depth in many of Greenland's fjords; see e.g., Straneo and Cenedese 2015). This approximation allows the buoyancy flux equation (Eq. (H.1c)) to be simplified to

$$B = mg' \,, \tag{H.2}$$

which results in the self-similar discharge plume solutions used in Section 4.1 (see Straneo and Cenedese 2015 for a discussion). The melt rate that is used for the buoyancy flux of the melt-driven plume can be approximated to be uniform with depth for simplicity (approximately a vertical mean) for the simplified overturning circulation approximation theory in Section 4.1, which allows for a similarity solution for the melt plume component used in Eq. (4.4).

APPENDIX I

Quasi-Streamfunction Discussion

We note that the quasi-streamfunction defined in Eq. (4.3) is only approximately equal to the 3D streamfunction, which can be defined via the relationship $(u, v, w) = \nabla \times \Psi_3$. The horizontal velocity field (u, v) is unlikely to be exactly nondivergent anywhere, but over most of the fjord, the horizontal velocity field is approximately nondivergent, i.e., the x- and y-components of the streamfunction vector are approximately zero and the flow is approximately described by the z-component of the streamfunction. The lack of boundary-incident streamlines in Fig. 4.2e and Fig. J.4 suggests that the horizontal velocity field is indeed approximately nondivergent. Since the calculation of this quasi-streamfunction is calculated by taking the integral in the across-fjord direction, the interior quasi-streamfunction is largely unaffected by the eastern and western boundary nudged regions.

APPENDIX J

Fjord Circulation and Melt Sensitivity to Discharge Plume Strength, Geometry, Stratification, and Tides

This section provides additional exposition of the dependence of the fjord circulation and melt on the various model control parameters discussed in Section 4.3. Figs. J.2-J.5 shows the time-averaged meridionally-averaged temperature and salinity, overturning circulation, and vertically-integrated horizontal recirculation, and glacial melt rates for 9 endmember cases. All of the parameter variations seen here substantially influence the circulation and/or melt rate and suggest that these properties are all likely to be important when considering overturning, recirculation, and melt rates in real fjord systems.

The overturning circulation in the greatest discharge strength case $Q_0 = 1000$ m^3/s (Fig. J.4d) increases by a factor of 2.5 compared to the $Q_0 = 100$ m^3/s case (Fig. J.4c), but the overall melt rate only increases by 30% (Fig. 4.4c, d). Similarly to the reference case, the discharge plume and melt plume with a high discharge ($Q_0 = 1000$ m^3/s) is also additive, but the discharge-driven shallow overturning cell dominates the peak overturning strength (Fig. J.4d). The increase in discharge primarily increases the magnitude of the shallow overturning circulation, which increases the shallow recirculation. An important takeaway is that at these depths, the recirculation (in Fig. J.5d) has a much smaller impact on the overall melt rate.

Name	*Parameter*	*Test Cases*	*Test Name*	*Units*
Sill Height	H_S	[0, **150**, 200, 250]	[S_0, - , S_{150}, S_{200}, S_{250}]	m
Fjord Width	W_{fj}	[4,**6**,9,15]	[W_4, - , W_9, W_{15}]	km
Fjord Depth	H_{fj}	[600, **800**, 1000]	[D_{600}, - , D_{1000}]	m
Fjord Length (constant)	L_{fj}	25		km
Subglacial Discharge	Q_0	[0, **100**, 300, 1000]	[$Q_0, Q_{100}, Q_{300}, Q_{1000}$]	m^3/s
Melt Parameterization		[No melt, Boundary Layer Melt, **Melt Plume**]	[- , M_{BL}, M_P]	
Stratification	$\rho_3 - \rho_2$	[0.25, **0.45**, 0.65]	[$\Delta\rho_{0.25}$, - , $\Delta\rho_{0.65}$]	kg/m^3
Tidal Amplitude	u_{tide}	[**0**, 0.05, 0.1]	[- , $T_{0.05}$, $T_{0.1}$]	m/s

TABLE 1. Summary of key fjord parameters and test cases for the numerical simulations. All variables are independently varied relative to the reference case (in bold text).

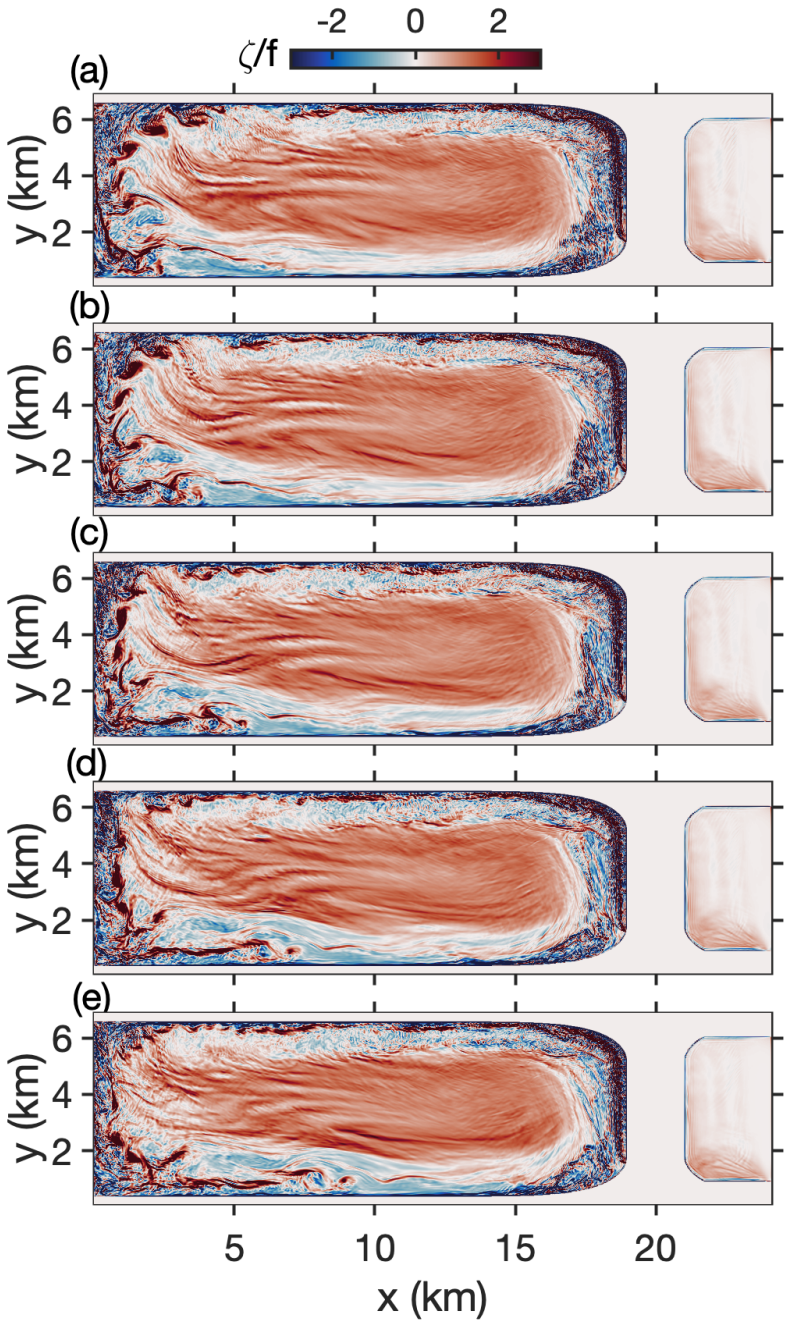

Figure J.1: Snapshots of normalized vorticity of the reference simulation at $z = -320$ m at time (a) 90.0, (b) 90.1, (c) 90.2, (d) 90.3, (e) 90.4 days, showing a sequence of eddies being shed into the interior horizontal recirculation.

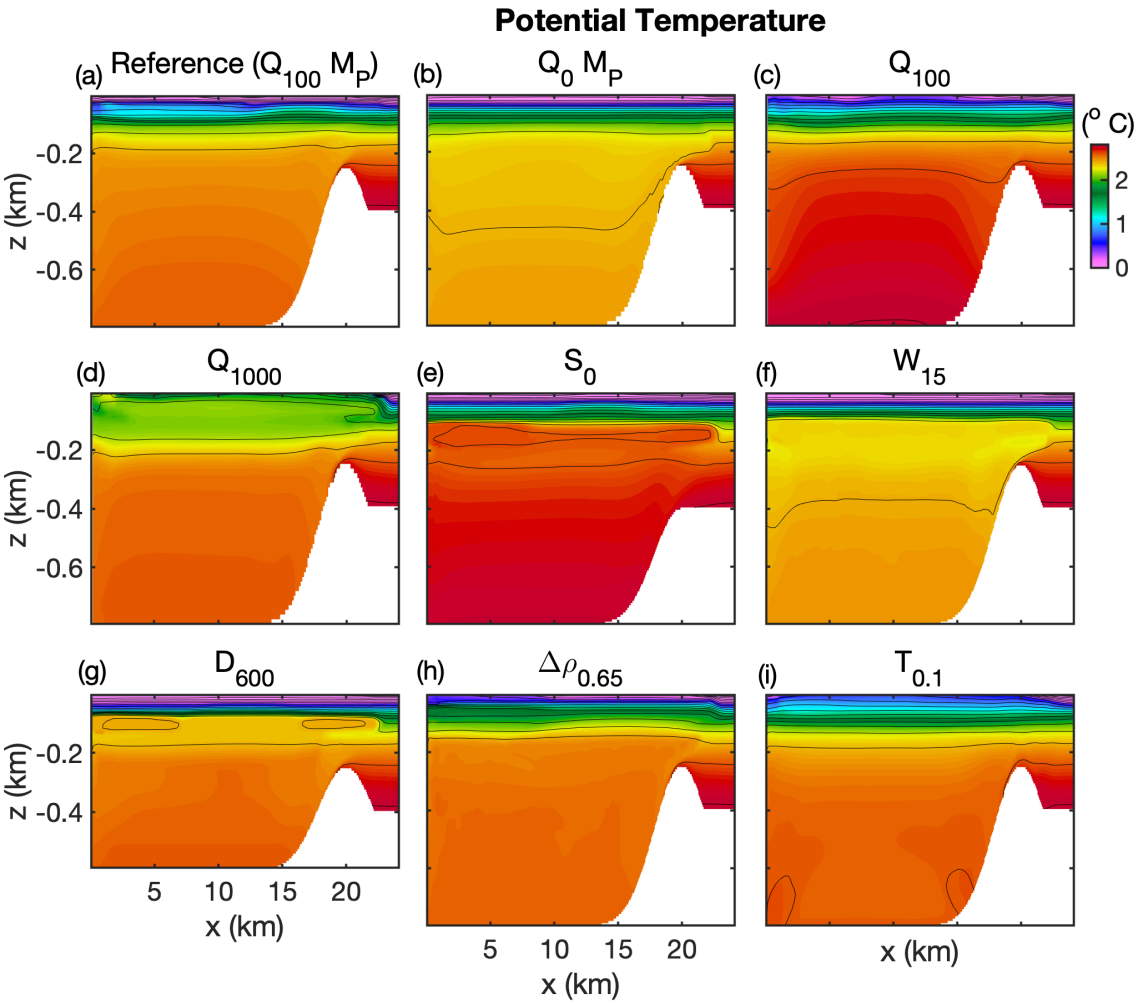

Figure J.2: (a)-(i) Time- and meridionally-averaged potential temperature profiles for 9 experiments with varying parameters (see the table in Appendix J for specific parameters for each case). The contour spacing is 0.2 °C.

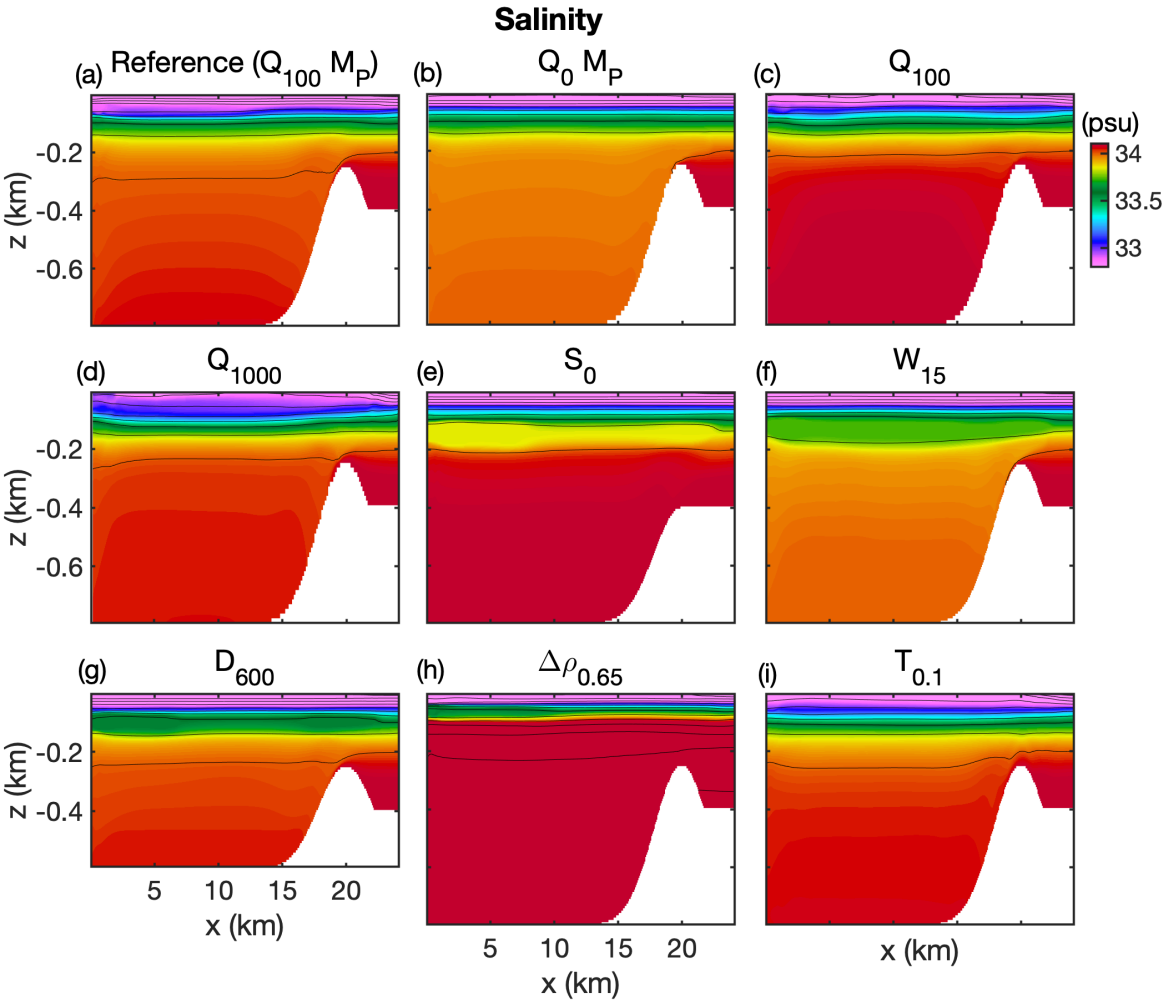

Figure J.3: (a)-(i) Time- and meridionally-averaged salinity profiles for 9 experiments with varying parameters (see the table in Appendix J for specific parameters for each case). The contour spacing is 0.2 psu.

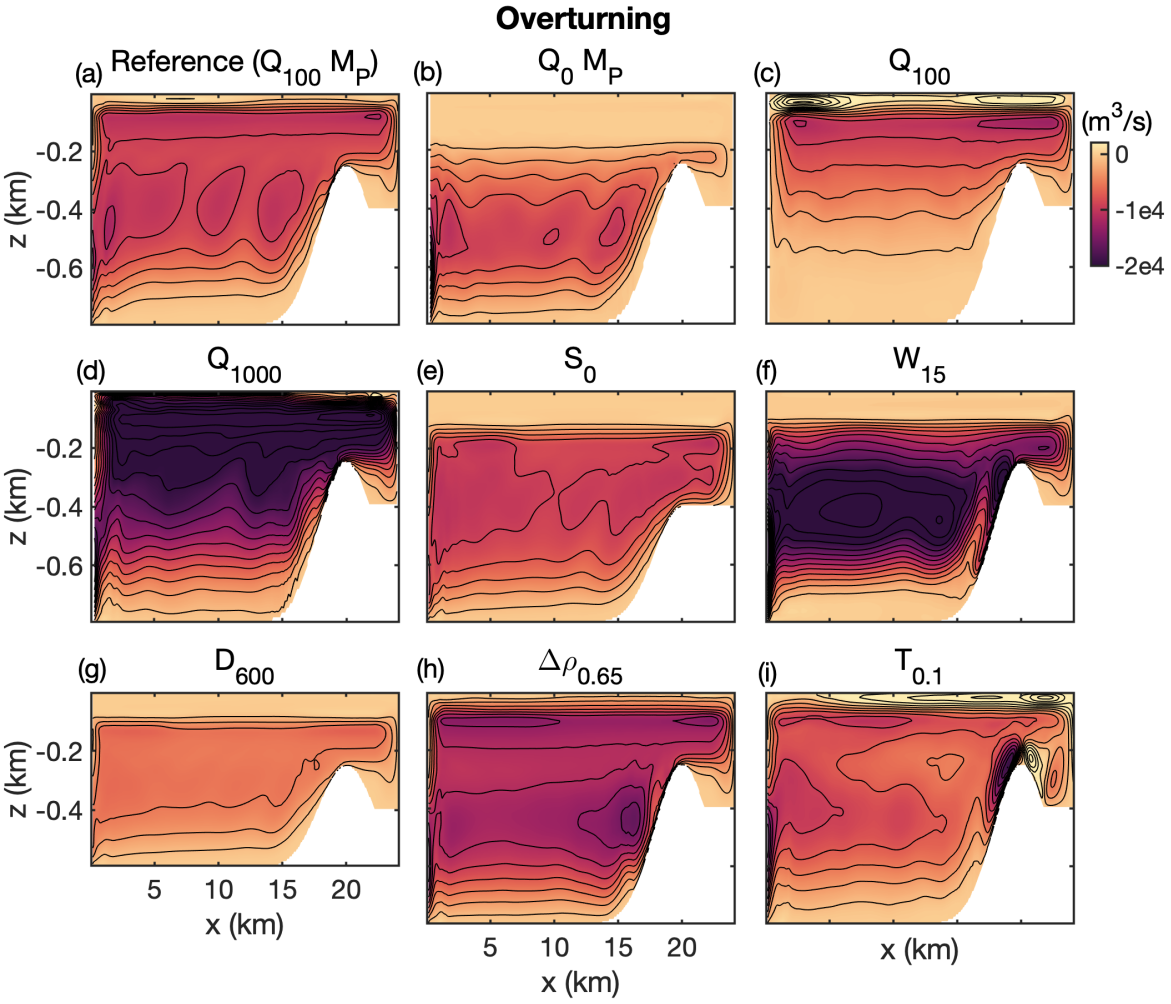

Figure J.4: (a)-(i) Time-averaged overturning circulation for 9 experiments with varying parameters (see the table in Appendix J for specific parameters for each case). The contour spacing is 2×10^3 m^3/s.

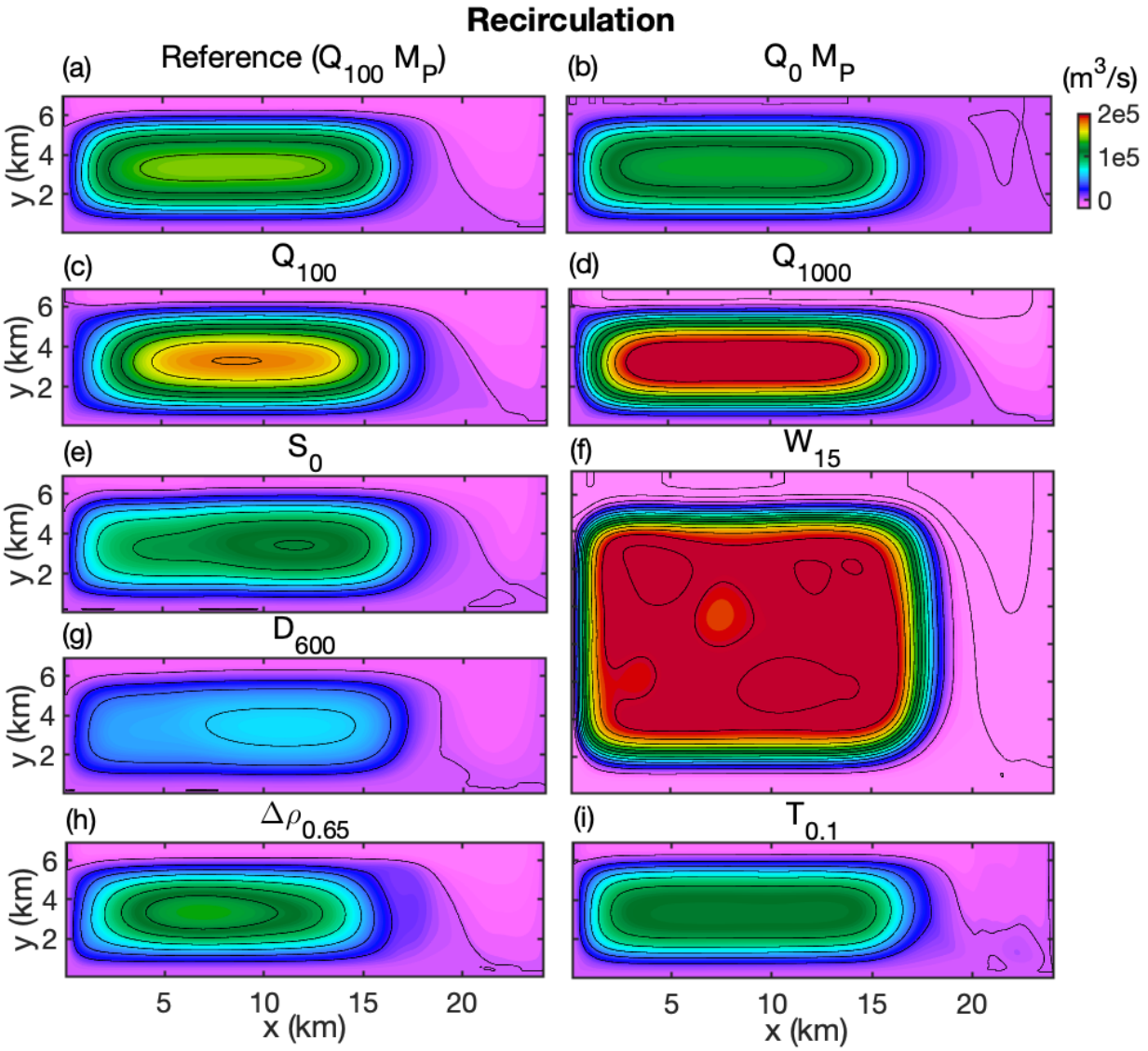

Figure J.5: (a)-(i) Time-averaged horizontal recirculation integrated over depth (excluding circulation above the neutral buoyancy depth) for 9 experiments with varying parameters (see the table in Appendix J for specific parameters for each case). The contour spacing is 2×10^4 m^3/s.

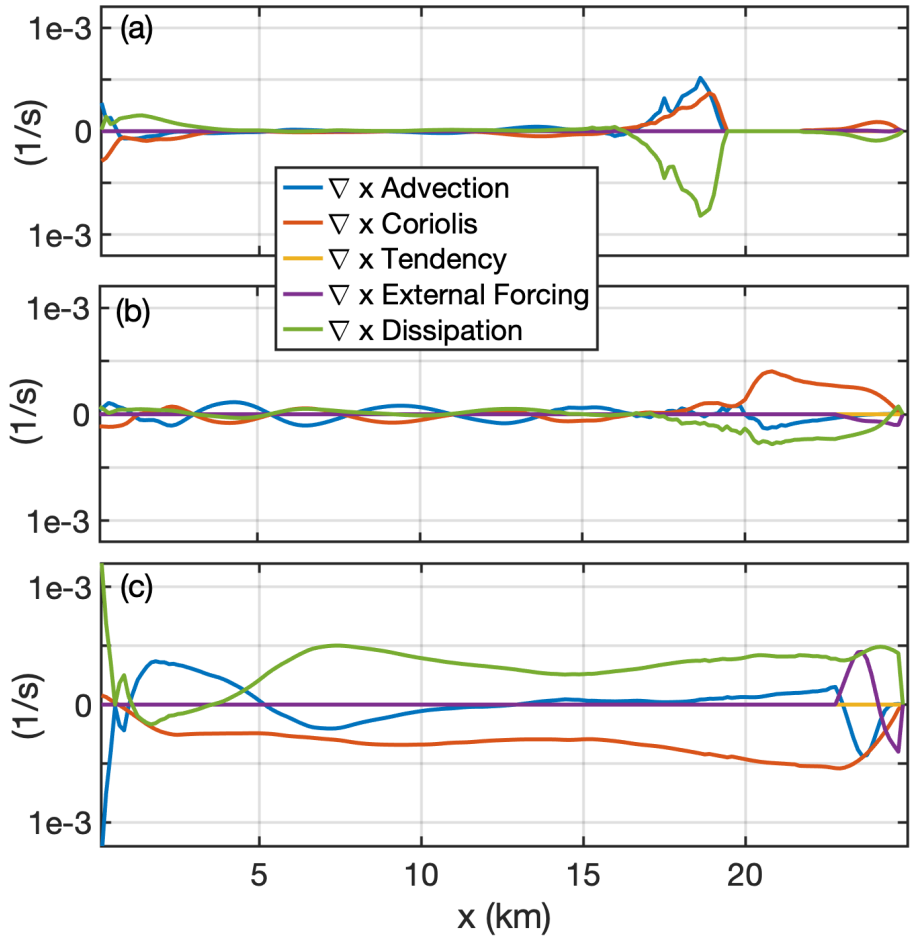

Figure J.6: Vorticity balance in our reference experiment showing the depth-integrated meridionally-integrated curl of the momentum equation terms, cumulatively-integrated w.r.t. x starting from $x = 0$ in (a) the top 200 m, (b) -400 m $< z < -200$ m, and (c) the bottom 400 m. See Zhao et al. 2021a for a derivation of the terms used in the vorticity balance.

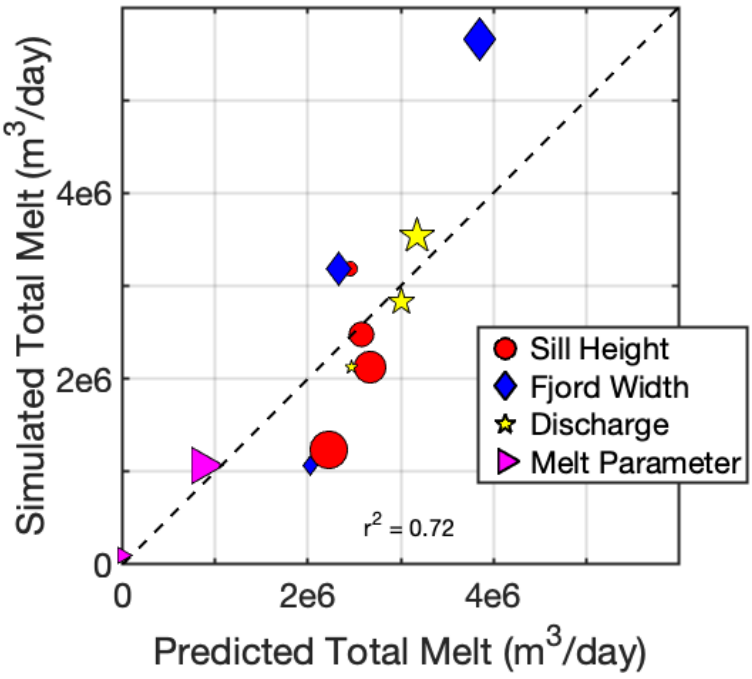

Figure J.7: Simulation-diagnosed vs. theoretical predictions for the overall glacial melt rate based on the overturning and recirculation theory (Eqs. (4.11) and (4.10)).

APPENDIX K

Melt Rate Theory Approximations

The expressions and approximations used in Section 4.3 on the melt rate theory are a variation of the three-equation system of equations (Hellmer and Olbers, 1989; Holland and Jenkins, 1999) which describes the thermodynamical equilibrium at the ice-ocean interface. This equilibrium can be expressed using approximate heat and salt conservation and the linearized freezing temperature of seawater,

$$M(L_i + c_i(T_b - T_i)) = \gamma_T c_w (T_p - T_b) \tag{K.1a}$$

$$MS_b = \gamma_S (S_p - S_b)\,, \tag{K.1b}$$

$$T_b = \lambda_1 S_b + \lambda_2 + \lambda_3 z\,, \tag{K.1c}$$

where $M, L_i, c_w, c_i, C_d, T_b, T_i, T_p$ are defined in Section 4.3, S_p is the plume salinity, S_b is the boundary layer salinity, γ_T and γ_S are the turbulent heat and salt transfer coefficients, respectively, and $\lambda_1 = -5.73 \times 10^{-2}$ °C psu^{-1}, $\lambda_2 = 8.32 \times 10^{-2}$ °C, and $\lambda_3 = 7.61 \times 10^{-4}$ °C m^{-1} are the freezing point slope, offset, and depth. These empirical values are consistent with those used in previous studies (Sciascia et al., 2013; Cowton et al., 2015). Recent parameterizations of the turbulent transfer coefficients (Jenkins et al., 2010) express the turbulent transfer coefficients in terms of near-glacial ocean velocities as

$$\gamma_T = C_d^{1/2} \Gamma_T \sqrt{v^2 + w^2}\,, \tag{K.2a}$$

$$\gamma_S = C_d^{1/2} \Gamma_S \sqrt{v^2 + w^2}\,, \tag{K.2b}$$

with C_d, Γ_T, v, w as defined in Section 4.3, and $\Gamma_S = 6.2 \times 10^{-4}$ is the salt transfer constant.

For simplicity, our theory in Section 4.3 for the melt rate M only uses Eqs. (K.1a) and (K.2.a), since the plume and boundary layer temperature can be evaluated in our model directly (and does not vary significantly over the cases tested). We can then integrate the melt rate outside the discharge plume regions (which allows us to simplify $\sqrt{v^2 + w^2}$ to v) since this is where the majority of the melt occurs.

Bibliography

Aiki, H., X. Zhai, and R. Greatbatch, 2016: Energetics of the global ocean: The role of mesoscale eddies. *Indo-Pacific Climate Variability and Predictability. Asia-Pacific Weather and Climate*, World Scientific, chap. 4, 109–134.

Bamber, J. L., A. J. Tedstone, M. D. King, I. M. Howat, E. M. Enderlin, M. R. van den Broeke, and B. Noel, 2018: Land Ice Freshwater Budget of the Arctic and North Atlantic Oceans: 1. Data, Methods, and Results. *J. Geophys. Res. Oceans*, **123 (3)**, 1827–1837, doi:10.1002/2017JC013605.

Bartholomaus, T. C., C. F. Larsen, and S. O'Neel, 2013: Does calving matter? Evidence for significant submarine melt. *Earth Planet. Sci. Lett.*, **380**, 21–30, doi:10.1016/j.epsl.2013.08.014.

Bartholomaus, T. C., and Coauthors, 2016: Contrasts in the response of adjacent fjords and glaciers to ice-sheet surface melt in West Greenland. *Ann. Glaciol.*, **57 (73)**, 25–38, doi:10.1017/aog.2016.19.

Beaird, N., F. Straneo, and W. Jenkins, 2017: Characteristics of Meltwater Export from Jakobshavn Isbrae and Ilulissat Icefjord. *Ann. Glaciol.*, **58 (74)**, 107–117, doi:10.1017/aog.2017.19.

Beckmann, J., , M. Perrette, and A. Ganopolski, 2018: Simple models for the simulation of submarine melt for a Greenland glacial system model. *The Cryosphere*, **12**, 301–323.

Borenas, K., and J. Whitehead, 1998: Upstream separation in a rotating channel flow. *J. Geophys. Res.*, **103**, 7567–7578.

Cai, C., E. Rignot, D. Menemenlis, and Y. Nakayama, 2017: Observations and modeling of ocean-induced melt beneath Petermann Glacier Ice Shelf in northwestern Greenland. *Geophys. Res. Lett.*, **44**, 8396–8403, doi:10.1002/2017GL073711.

Carroll, D., D. A. Sutherland, E. Shroyer, J. D. Nash, G. Catania, and L. A. Stearns, 2017: Subglacial discharge-driven renewal of tidewater glacier fjords. *J. Geophys. Res. Oceans*, **122**, 6611–6629.

Carroll, D., and Coauthors, 2016: The impact of glacier geometry on meltwater plume structure and submarine melt in greenland fjords. *Geophys. Res. Lett.*, **43 (18)**, 9739–9748, doi:10.1002/2016GL070170.

Chauché, N., A. Hubbard, J. C. Gascard, J. E. Box, R. Bates, and e. a. Koppes, M., 2014: Ice-ocean interaction and calving front morphology at two west greenland tidewater outlet glaciers. *Cyrosphere*, **8**, 1457–1468, doi:doi.org/10.5194/tc-8-1457-2014.

Chu, V. W., 2014: Greenland ice sheet hydrology: A review. *Progress in Physical Geography: Earth and Environment*, **38 (1)**, 19–54, doi:10.1177/0309133313507075.

Cook, A. J., P. R. Holland, M. P. Meredith, T. Murray, A. Luckman, and D. G. Vaughan, 2016: Ocean forcing of glacier retreat in the western Antarctic Peninsula. *Science*, **353 (6296)**, 283–286.

Cottier, F., F. Nilsen, R. Skogseth, V. Tverberg, J. Skardhamar, and H. Svendsen, 2010: Arctic fjords: A review of the oceanographic environment and dominant physical processes. *Geological Society of London Special Publications*, **344**, 35–50, doi:10.1144/SP344.4.

Cowton, T., D. Slater, A. Sole, D. Goldberg, and P. Nienow, 2015: Modeling the impact of glacial runoff on fjord circulation and submarine melt rate using a new subgrid-scale parameterization for glacial plumes. *J. Geophys. Res. Oceans*, **120**, 796–812.

Cowton, T. R., A. J. Sole, P. W. Nienow, D. A. Slater, and P. Christoffersen, 2018: Linear response of east greenland's tidewater glaciers to ocean/atmosphere warming. *Proc. Natl. Acad. Sci. (USA)*, **115 (31)**, 7907–7912, doi:10.1073/pnas.1801769115.

Dalziel, S., 1991: Two-layer hydraulics: a functional approach. *J. Fluid Mech.*, **223**, 135–163.

De Rydt, J., and G. Gudmundsson, 2016: Coupled ice shelf-ocean modeling and complex grounding line retreat from a seabed ridge. *J. Geophys. Res. Earth Surf.*, **121**, 865–880, doi:10.1002/2015JF003791.

De Rydt, J., P. R. Holland, P. Dutrieux, and A. Jenkins, 2014: Geometric and oceanographic controls on melting beneath Pine Island Glacier. *J. Geophys. Res. Oceans*, **119**, 2420–2438, doi:10.1002/2013JC009513.

Dutrieux, P., J. D. Rydt, A. Jenkins, P. R. Holland, H. K. Ha, S. H. Lee, E. J. Steig, Q. Ding, E. P. Abrahamsen, and M. Schroder, 2014: Strong sensitivity of Pine Island ice-shelf melting to climatic variability. *Science*, **343**, 174–178.

Enderlin, E. M., G. S. Hamilton, F. Straneo, and D. A. Sutherland, 2016: Iceberg meltwater fluxes dominate the freshwater budget in Greenland's iceberg-congested glacial fjords. *Geophys. Res. Lett.*, **43**, 11,287–11,294, doi:10.1002/2016GL070718.

Farmer, D., and H. Freeland, 2021: The physical oceanography of fjords. *Prog. Oceanogr.*, **12**, 147–220.

Federov, A. V., and W. K. Melville, 1996: Hydraulic jumps at boundaries in rotating fluids. *J. Fluid Mech.*, **324**, 55–82.

Fenty, I., and Coauthors, 2016: Oceans Melting Greenland: Early results from NASA's ocean-ice mission in Greenland. *Oceanography*, **29 (4)**, 72–83, doi: doi.org/10.5670/oceanog.2016.100.

Fraser, N. J., M. E. Inall, M. G. Magaldi, T. W. Haine, and S. C. Jones, 2018: Wintertime Fjord-Shelf Interaction and Ice Sheet Melting in Southeast Greenland. *J. Geophys. Res. Oceans*, **123 (12)**, 9156–9177, doi:10.1029/2018JC014435.

Fried, M. J., G. A. Catania, L. A. Stearns, D. A. Sutherland, T. C. Bartholomaus, E. Shroyer, and J. Nash, 2018: Reconciling drivers of seasonal terminus advance and retreat at 13

central west greenland tidewater glaciers. *J. Geophys. Res. Earth Surface*, **123 (7)**, 1590–1607, doi:doi.org/10.1029/2018JF004628.

Fried, M. J., G. A. Catania, T. C. Bartholomaus, D. Duncan, M. Davis, L. A. Stearns, J. Nash, E. Shroyer, and D. Sutherland, 2015: Distributed subglacial discharge drives significant submarine melt at a greenland tidewater glacier. *Geophys. Res. Lett.*, **42 (21)**, 9328–9336, doi:10.1002/2015GL065806.

Gelderloos, R., T. W. N. Haine, I. M. Koszalka, and M. G. Magaldi, 2017: Seasonal variability in warm-water inflow toward kangerdlugssuaq fjord. *Journal of Physical Oceanography*, **47 (7)**, 1685 – 1699, doi:10.1175/JPO-D-16-0202.1.

Gent, P. R., 2011: The Gent–McWilliams parameterization: 20/20 hindsight. *Ocean Modelling*, **39 (1)**, 2–9, doi:https://doi.org/10.1016/j.ocemod.2010.08.002.

Gent, P. R., and J. C. McWilliams, 1990: Isopycnal Mixing in Ocean Circulation Models. *J. Phys. Oceanogr.*, **20 (1)**, 150–155, doi:10.1175/1520-0485(1990)020¡0150:IMIOCM¿2.0.CO;2.

Geyer, W. R., and P. MacCready, 2014: The Estuarine Circulation. *Annu. Rev. Fluid Mech*, **46 (1)**, 175–197, doi:10.1146/annurev-fluid-010313-141302.

Gill, A., 1977: The hydraulics of rotating-channel flow. *J. Fluid Mech.*, **80**, 641–671.

Gladish, C. V., D. M. Holland, A. Rosing-Asvid, J. W. Behrens, and J. Boje, 2015: Oceanic Boundary Conditions for Jakobshavn Glacier. Part I: Variability and Renewal of Ilulissat Icefjord Waters, 2001–14. *J. Phys. Oceanogr.*, **45 (1)**, 3–32, doi:10.1175/JPO-D-14-0044.1.

Griffies, S., and R. Hallberg, 2000: Biharmonic friction with a Smagorinsky-like viscosity for use in large-scale eddy-permitting ocean models. *Mon. Wea. Rev.*, **128**, 2935–2946.

Gudmundsson, G. H., 2013: Ice-shelf buttressing and the stability of marine ice sheets. *The Cryosphere*, **7**, 647–655.

Gudmundsson, G. H., J. Krug, G. Durand, L. Favier, and O. Gagliardini, 2012: The stability of grounding lines on retrograde slopes. *The Cryosphere*, **6**, 1497–1505.

Hallberg, R., and P. Rhines, 1996: Buoyancy-driven circulation in an ocean basin with isopycnals intersecting the sloping boundary. *J. Phys. Oceanogr.*, **26**, 913–940.

Helfrich, K. R., A. C. Kuo, and L. J. Pratt, 1999: Nonlinear Rossby adjustment in a channel. *J. Fluid Mech.*, **390**, 177–222.

Hellmer, H. H., and D. J. Olbers, 1989: A two-dimensional model for the thermohaline circulation under an ice shelf. *Antarctic Science*, **1 (4)**, 325–336, doi: 10.1017/S0954102089000490.

Hogg, A. M., W. K. Dewar, P. Berloff, and M. L. Ward, 2011: Kelvin wave hydraulic control induced by interactions between vortices and topography. *J. Fluid Mech.*, **687**, 194–208, doi:10.1017/jfm.2011.344.

Holland, D. M., and A. Jenkins, 1999: Modeling Thermodynamic Ice-Ocean Interactions at the Base of an Ice Shelf. *J. Phys. Oceanogr.*, **29 (8)**, 1787–1800, doi:10.1175/1520-0485(1999)029¡1787:MTIOIA¿2.0.CO;2.

Holland, P. R., 2017: The transient response of ice shelf melting to ocean change. *J. Phys. Oceanogr.*, **47 (8)**, 2101–2114, doi:10.1175/JPO-D-17-0071.1.

Holland, P. R., A. Jenkins, and D. M. Holland, 2008: The response of ice shelf basal melting to variations in ocean temperature. *J. Climate*, **21**, 2258–2272, doi: 10.1175/2007JCLI1909.1.

Huss, M., U. Schwyn, A. Bauder, and D. Farinotti, 2021: Quantifying the overall effect of artificial glacier melt reduction in switzerland, 2005–2019. *Cold Regions Science and Technology*, **184**, 103 237, doi:https://doi.org/10.1016/j.coldregions.2021.103237.

Inall, M. E., and P. A. Gillibrand, 2010: The physics of mid-latitude fjords: a review. *Geological Society of London Special Publications*, **344**, 17–33.

Inall, M. E., T. Murray, F. R. Cottier, K. Scharrer, T. J. Boyd, K. J. Heywood, and S. L. Bevan, 2014: Oceanic heat delivery via Kangerdlugssuaq Fjord to the south-east Greenland ice sheet. *J. Geophys. Res. Oceans*, **119 (2)**, 631–645, doi:10.1002/2013JC009295.

IPCC, 2019: *IPCC, 2019: IPCC Special Report on the Ocean and Cryosphere in a Changing Climate. H.-O. Portner, D.C. Roberts, V. Masson-Delmotte, P. Zhai, M. Tignor, E. Poloczanska, K. Mintenbeck, A. Alegría, M. Nicolai, A. Okem, J. Petzold, B. Rama, N.M. Weyer (eds.)*. In Press.

IPCC, 2021: *Climate Change 2021: The Physical Science Basis. Contribution of Working Group I to the Sixth Assessment Report of the Intergovernmental Panel on Climate Change, eds. Masson-Delmotte, V., P. Zhai, A. Pirani, S.L. Connors, C. Pean, S. Berger, N. Caud, Y. Chen, L. Goldfarb, M.I. Gomis, M. Huang, K. Leitzell, E. Lonnoy, J.B.R. Matthews, T.K. Maycock, T. Waterfield, O. Yelekçi, R. Yu, and B. Zhou*. Cambridge University Press, Cambridge, U.K.

Jackett, D. R., and T. McDougall, 1995: Minimal adjustment of hydrographic profiles to achieve static stability. *J. Atmos. Ocean. Technol.*, **14 (4)**, 381–389.

Jackson, R., J. Nash, C. Kienholz, D. Sutherland, J. Amundson, R. Motyka, D. Winters, E. Skyllingstad, and E. Pettit, 2019: Meltwater intrusions reveal mechanisms for rapid submarine melt at a tidewater glacier. *Geophys. Res. Lett.*, doi:10.1029/2019GL085335.

Jackson, R. H., S. J. Lentz, and F. Straneo, 2018: The Dynamics of Shelf Forcing in Greenlandic Fjords. *J. Phys. Oceanogr.*, **48 (11)**, 2799–2827, doi:10.1175/JPO-D-18-0057.1.

Jackson, R. H., E. L. Shroyer, J. D. Nash, D. A. Sutherland, D. Carroll, M. J. Fried, G. A. Catania, T. C. Bartholomaus, and L. A. Stearns, 2017: Near-glacier surveying of

a subglacial discharge plume: Implications for plume parameterizations. *Geophys. Res. Lett.*, **44 (13)**, 6886–6894, doi:10.1002/2017GL073602.

Jacobs, S. S., A. Jenkins, C. F. Giulivi, and P. Dutrieux, 2011: Stronger ocean circulation and increased melting under Pine Island Glacier ice shelf. *Nat. Geosci.*, **4**, 519–523.

Jakacki, J., A. Przyborska, S. Kosecki, A. Sundfjord, and J. Albretsen, 2017: Modelling of the Svalbard fjord Hornsund. *Oceanologia*, **59 (4)**, 473–495, doi: https://doi.org/10.1016/j.oceano.2017.04.004.

Jenkins, A., 2011: Convection-Driven Melting near the Grounding Lines of Ice Shelves and Tidewater Glaciers. *J. Phys. Oceanogr.*, **41 (12)**, 2279–2294, doi:10.1175/JPO-D-11-03.1.

Jenkins, A., P. Dutrieux, S. Jacobs, S. McPhail, J. Perrett, A. Webb, and D. White, 2010: Observations beneath Pine Island Glacier in West Antarctica and implications for its retreat. *Nat. Geosci.*, **3**, 468–472.

Joughin, I., R. B. Alley, and D. M. Holland, 2012: Ice-Sheet Response to Oceanic Forcing. *Science*, **338**, 1172–1176.

Joughin, I., B. E. Smith, and B. Medley, 2014: Marine ice sheet collapse potentially under way for the Thwaites Glacier Basin, West Antarctica. *Science*, **344**, 735–738.

Khazendar, A., I. Fenty, and D. e. a. Carroll, 2019: Interruption of two decades of Jakobshavn Isbrae acceleration and thinning as regional ocean cools. *Nat. Geosci.*, **12**, 277–283, doi: https://doi.org/10.1038/s41561-019-0329-3.

Kimura, S., A. Jenkins, P. Dutrieux, A. Forryan, A. Garabato, and Y. Firing, 2016: Ocean mixing beneath Pine Island Glacier ice shelf, West Antarctica. *J. Geophys. Res. Oceans*, **12**, 8496–8510, doi:10.1002/2016JC012149.

Konrad, H., L. Gilbert, S. L. Cornford, A. J. Payne, A. Hogg, A. Muir, and A. Shepherd, 2017: Uneven onset and pace of ice-dynamical imbalance in the Amundsen Sea Embayment, West Antarctica. *Geophys. Res. Lett.*, **44**, 910–918, doi:10.1002/2016GL070733.

Large, W. G., J. C. McWilliams, and S. C. Doney, 1994: Oceanic vertical mixing: A review and a model with a nonlocal boundary layer parameterization. *Reviews of Geophysics*, **32 (4)**, 363–403, doi:10.1029/94RG01872.

Lee, T., D. E. Waliser, J.-L. F. Li, F. W. Landerer, and M. M. Gierach, 2013: Evaluation of CMIP3 and CMIP5 Wind Stress Climatology Using Satellite Measurements and Atmospheric Reanalysis Products. *J. Climate*, **26 (16)**, 5810–5826, doi:10.1175/JCLI-D-12-00591.1.

Lindeman, M. R., F. Straneo, N. J. Wilson, J. M. Toole, R. A. Krishfield, N. L. Beaird, T. Kanzow, and J. Schaffer, 2020: Ocean Circulation and Variability Beneath Nioghalvfjerdsbrae (79 North Glacier) Ice Tongue. *J. Geophys. Res. Oceans*, **125 (8)**, e2020JC016 091, doi:10.1029/2020JC016091.

Linden, P. F., 2000: *Convection in the environment. In Perspectives in Fluid Dynamics, ed. GK Batchelor, HK Moffat, MG Worster.* Cambridge University Press, Cambridge, U.K., 289 – 345 pp.

Little, C. M., A. Gnanadesikan, and R. Hallberg, 2008: Large-Scale Oceanographic Constraints on the Distribution of Melting and Freezing under Ice Shelves. *J. Phys. Oceanogr.*, **38 (10)**, 2242–2255, doi:10.1175/2008JPO3928.1.

Lorenz, E. N., 1955: Available potential energy and the maintenance of the general circulation. *Tellus*, **2**, 157–167.

Magorrian, S. J., and A. J. Wells, 2016: Turbulent plumes from a glacier terminus melting in a stratified ocean. *J. Geophys. Res. Oceans*, **121 (7)**, 4670–4696, doi:10.1002/2015JC011160.

Mankoff, K. D., B. Noël, X. Fettweis, A. P. Ahlstrøm, W. Colgan, K. Kondo, K. Langley, S. Sugiyama, D. van As, and R. S. Fausto, 2020: Greenland liquid water discharge from 1958 through 2019. *Earth System Science Data*, **12 (4)**, 2811–2841, doi:10.5194/essd-12-2811-2020.

Marshall, J. A., C. Hill, L. Perelman, and C. Heisey, 1997: A finite-volume, incompressible navier stokes model for studies of the ocean on parallel computers. *J. Geophys. Res.*, **102 (C3)**, 5753–5766.

Mayer, C., N. Reeh, F. Jung-Rothenhäusler, P. Huybrechts, and H. Oerter, 2000: The subglacial cavity and implied dynamics under Nioghalvfjerdsfjorden Glacier, NE-Greenland. *Geophys. Res. Lett.*, **27**, 2289–2292.

McWilliams, J., 1990: The vortices of two-dimensional turbulence. *J. Fluid. Mech.*, **219**, 361–385, doi:10.1017/S0022112084001750.

Moffat, C., 2014: Wind-driven modulation of warm water supply to a proglacial fjord, Jorge Montt Glacier, Patagonia. *Geophys. Res. Lett.*, **41 (11)**, 3943–3950, doi:10.1002/2014GL060071.

Moffat, C., B. Owens, and R. C. Beardsley, 2009: On the characteristics of Circumpolar Deep Water intrusions to the west Antarctic Peninsula Continental Shelf. *J. Geophys. Res. Oceans*, **114 (C5)**, doi:10.1029/2008JC004955.

Moore, J. C., R. G. andThomas Zwinger, and M. Wolovick, 2018: Geoengineer polar glaciers to slow sea-level rise. *Nature*, **555**, 303–305, doi:https://doi.org/10.1038/d41586-018-03036-4.

Morlighem, M., J. Bondzio, H. Seroussi, E. Rignot, E. Larour, A. Humbert, and S. Rebuffi, 2016: Modeling of store gletscher's calving dynamics, west greenland, in response to ocean thermal forcing. *Geophys. Res. Lett.*, **43**, 2659–2666, doi:doi.org/10.1002/2016GL067695.

Morlighem, M., and Coauthors, 2017: BedMachine v3: Complete Bed Topography and Ocean Bathymetry Mapping of Greenland From Multibeam Echo Sounding Combined With Mass Conservation. *Geophys. Res. Lett.*, **44 (21)**, 11,051–11,061, doi: 10.1002/2017GL074954.

Morton, B. R., G. I. Taylor, and J. S. Turner, 1956: Turbulent gravitational convection from maintained and instantaneous sources. *Proceedings of the Royal Society of London. Series A. Mathematical and Physical Sciences*, **234 (1196)**, 1–23, doi:10.1098/rspa.1956.0011.

Morvan, M., X. Carton, P. L'Hégaret, C. de Marez, S. Corréard, and S. Louazel, 2020: On the dynamics of an idealised bottom density current overflowing in a semi-enclosed basin: mesoscale and submesoscale eddies generation. *Geophysical Astrophysical Fluid Dynamics*, **114:4-5**, 607–630.

Mouginot, J., E. Rignot, and B. Scheuchl, 2014: Sustained increase in ice discharge from the Amundsen Sea Embayment, West Antarctica, from 1973 to 2013. *Geophys. Res. Lett.*, **41**, 1576–1584, doi:10.1002/2013GL059069.

Nakayama, Y., R. Timmermann, M. Schröder, and H. Hellmer, 2014: On the difficulty of modeling circumpolar deep water intrusions onto the Amundsen Sea continental shelf. *Ocean Model.*, **84**, 26–34, doi:10.1016/j.ocemod.2014.09.007.

Nowicki, S. M. J., T. Payne, E. Larour, H. Seroussi, H. Goelzer, W. Lipscomb, J. Gregory, A. Abe-Ouchi, and A. Shepherd, 2016: Ice sheet model intercomparison project (ismip6) contribution to cmip6. *Geosci. Model Dev. Discuss.*, doi:10.5194/gmd-9-4521-2016.

Orlanski, I., 1976: A simple boundary condition for unbounded hyperbolic flows. *J. Comput. Phys.*, **21**, 251–269, doi:doi.org/1721.1/119821.

Pawlowicz, R., C. Hannah, and A. Rosenberger, 2019: Lagrangian observations of estuarine residence times, dispersion, and trapping in the Salish Sea. *Estuarine, Coastal and Shelf Science*, **225**, 106 246, doi:https://doi.org/10.1016/j.ecss.2019.106246.

Pinones, A., E. E. Hofmann, M. S. Dinniman, and J. M. Klinck, 2011: Lagrangian simulation of transport pathways and residence times along the western Antarctic Peninsula. *Deep Sea Research Part II: Topical Studies in Oceanography*, **58 (13)**, 1524–1539, doi: https://doi.org/10.1016/j.dsr2.2010.07.001, Understanding the Linkages between Antarctic Food Webs and the Environment: A Synthesis of Southern Ocean GLOBEC Studies.

Pörtner, H. O., and Coauthors, 2019: IPCC, 2019: IPCC Special Report on the Ocean and Cryosphere in a Changing Climate. In press.

Pratt, L., and L. Armi, 1990: Two-layer Rotating Hydraulics: Strangulation, Remote and Virtual Controls. *Pageoph*, **133**, 587–617.

Pratt, L. J., 1987: Rotating shocks in a separated laboratory channel flow. *J. Phys. Oceanogr.*, **17**, 483–491.

Pratt, L. J., K. R. Helfrich, and E. P. Chassignet, 2000: Hydraulic adjustment to an obstacle in a rotating channel. *J. Fluid Mech.*, **404**, 117–149.

Pratt, L. J., and J. A. Whitehead, 2007: *Rotating Hydraulics*. Springer.

Pritchard, H. D., and D. G. Vaughan, 2007: Widespread acceleration of tidewater glaciers on the Antarctic Peninsula. *J. Geophys. Res. Earth Surf.*, **112 (F3)**, 1–10, doi: 10.1029/2006JF000597.

Rignot, E., I. Fenty, Y. Xu, C. Cai, and C. Kemp, 2015: Undercutting of marine-terminating glaciers in west greenland. *Geophys. Res. Lett.*, **42 (14)**, 5909–5917, doi: doi.org/10.1002/2015GL064236.

Rignot, E., S. Jacobs, J. Mouginot, and B. Scheuchl, 2013: Ice-Shelf Melting Around Antarctica. *Science*, **341 (6143)**, 266–270, doi:10.1126/science.1235798.

Rignot, E., J. Mouginot, M. Morlighem, H. Seroussi, and B. Scheuchl, 2014: Widespread, rapid grounding line retreat of Pine Island, Thwaites, Smith, and Kohler glaciers,

West Antarctica, from 1992 to 2011. *Geophys. Res. Lett.*, **6**, 3502–3509, doi: 10.1002/2014GL060140.

Sadourny, R., 1975: The dynamics of finite-difference models of the shallow-water equations. *J. Atmos. Sci.*, **32**, 680–689.

Salmon, R., 2002: Numerical solution of the two-layer shallow water equations with bottom topography. *J. Marine Res.*, **60**, 605–638.

Schaffer, J., 2017: Ocean impact on the 79 North Glacier, Northeast Greenland. Ph.D. thesis, Univ. of Bremen, 206 pp., URL `:nbn-resolving.de/urn:nbn:de:gbv:46-00106281-12`.

Schaffer, J., T. Kanzow, W. von Appen, L. von Albedyll, J. E. Arndt, and D. H. Roberts, 2020: Bathymetry constrains ocean heat supply to Greenland's largest glacier tongue. *Nat. Geosci.*, **13**, 227–231, doi:10.1038/s41561-019-0529-x.

Schodlok, M., D. Menemenlis, E. Rignot, and M. Studinger, 2012: Sensitivity of the ice-shelf/ocean system to the sub-ice-shelf cavity shape measured by NASA IceBridge in Pine Island Glacier, West Antarctica. *Ann. Glaciol.*, **53 (60)**, 156–162, doi: 10.3189/2012AoG60A073.

Schoof, C., 2007: Ice sheet grounding line dynamics: Steady states, stability, and hysteresis. *J. Geophys. Res. Earth Surf.*, **112 (F3)**, 2156–2202, doi:10.1029/2006JF000664.

Sciascia, R., F. Straneo, C. Cenedese, and P. Heimbach, 2013: Seasonal variability of submarine melt rate and circulation in an East Greenland fjord. *J. Geophys. Res. Oceans*, **118**, 2492–2506.

Seroussi, H., M. Morlighem, E. Rignot, E. Larour, D. Aubry, H. Ben Dhia, and S. Kristensen, 2011: Ice flux divergence anomalies on 79 North Glacier, Greenland. *Geophys. Res. Lett.*, **38**, L09 501, doi:10.1029/2011GL047338.

Seroussi, H., Y. Nakayama, E. Larour, D. Menemenlis, M. Morlighem, E. Rignot, and A. Khazendar, 2017: Continued retreat of Thwaites Glacier, West Antarctica, controlled by bed topography and ocean circulation. *Geophys. Res. Lett.*, **44**, 6191–6199, doi:10.1002/2017GL072910.

Shchepetkin, A. F., and J. C. McWilliams, 1998: Quasi-monotone advection schemes based on explicit locally adaptive dissipation. *Mon. Wea. Rev.*, **126**, 1541–1580.

Shchepetkin, A. F., and J. C. McWilliams, 2005: The regional oceanic modeling system (ROMS): a split-explicit, free-surface, topography-following-coordinate oceanic model. *Ocean Modelling*, **9**, 347–404.

Slater, D. A., D. I. Benn, T. R. Cowton, J. N. Bassis, and J. A. Todd, 2021: Calving multiplier effect controlled by melt undercut geometry. *J. Geophys. Res. Earth Surf.*, **n/a (n/a)**, e2021JF006 191, doi:https://doi.org/10.1029/2021JF006191.

Slater, D. A., F. Straneo, S. B. Das, C. G. Richards, T. J. W. Wagner, and P. W. Nienow, 2018: Localized Plumes Drive Front-Wide Ocean Melting of A Greenlandic Tidewater Glacier. *Geophys. Res. Lett.*, **45 (22)**, 12,350 – 12,358, doi:10.1029/2018GL080763.

Spall, M. A., R. H. Jackson, and F. Straneo, 2017: Katabatic Wind-Driven Exchange in Fjords. *J. Geophys. Res. Oceans*, **122 (10)**, 8246–8262, doi:10.1002/2017JC013026.

St-Laurent, P., 2018: Back of Envelope Ocean Model (BEOM). URL `www.nordet.net/beom.html`, accessed 1 April 2018.

St-Laurent, P., J. M. Klinck, and M. S. Dinniman, 2013: On the Role of Coastal Troughs in the Circulation of Warm Circumpolar Deep Water on Antarctic Shelves. *J. Phys. Oceanogr.*, **43 (1)**, 51–64, doi:10.1175/JPO-D-11-0237.1.

St-Laurent, P., J. M. Klinck, and M. S. Dinniman, 2015: Impact of local winter cooling on the

melt of Pine Island Glacier, Antarctica. *J. Geophys. Res. Oceans*, **120 (10)**, 6718–6732, doi:10.1002/2015JC010709.

Stern, M., 1974: Comment on rotating hydraulics. *Geophys. Fluid Dyn.*, **6 (2)**, 127–130, doi:10.1080/03091927409365791.

Stewart, K., A. Hogg, S. Griffies, A. Heerdegen, M. Ward, P. Spence, and M. England, 2017: Vertical resolution of baroclinic modes in global ocean models. *Ocean Modelling*, **113**, 50–65, doi:https://doi.org/10.1016/j.ocemod.2017.03.012.

Stigebrandt, A., 1981: A mechanism governing the estuarine circulation in deep, strongly stratified fjords. *Estuar. Coast. Mar. Sci.*, **13**, 197–211.

Stommel, H., 1948: The westward intensification of wind-driven ocean currents. *Trans. Amer. Geophys.*, **29**, 202–206.

Straneo, F., and C. Cenedese, 2015: The Dynamics of Greenland's Glacial Fjords and Their Role in Climate. *Annu. Rev. Mar. Sci.*, **7 (1)**, 89–112, doi:10.1146/annurev-marine-010213-135133.

Straneo, F., R. Curry, D. Sutherland, G. Hamilton, and C. e. a. Cenedese, 2011: Impact of fjord dynamics and glacial runoff on the circulation near Helheim Glacier. *Nat. Geosci.*, **4**, 322–327.

Straneo, F., and P. Heimbach, 2013: North Atlantic Warming and the Retreat of Greenland's Outlet Glaciers. *Nature*, **504 (7478)**, 36–43, doi:https://doi.org/10.1038/nature12854.

Sutherland, D. A., F. Straneo, and R. S. Pickart, 2014: Characteristics and dynamics of two major Greenland glacial fjords. *J. Geophys. Res. Oceans*, **119 (6)**, 3767–3791, doi:10.1002/2013JC009786.

Sutherland, D. A., R. H. Jackson, C. Kienholz, J. M. Amundson, W. P. Dryer, D. Duncan, E. F. Eidam, R. J. Motyka, and J. D. Nash, 2019: Direct observations of submarine

melt and subsurface geometry at a tidewater glacier. *Science*, **365 (6451)**, 369–374, doi: 10.1126/science.aax3528.

Towns, J., and Coauthors, 2014: XSEDE: Accelerating scientific discovery. *Computing in Science & Engineering*, **16 (5)**, 62–74, doi:10.1109/MCSE.2014.80.

Turner, J. S., 1979: *Buoyancy effects in fluids. Cambridge University Press Paperback.* 368 pp.

Vallis, G. K., 2006: *Atmospheric and Oceanic Fluid Dynamics*. Cambridge University Press, Cambridge, U.K., 745 pp.

van den Broeke, M. R., E. M. Enderlin, I. M. Howat, P. K. Munneke, B. P. Y. Noël, W. J. van de Berg, E. van Meijgaard, and B. Wouters, 2016: On the recent contribution of the Greenland ice sheet to sea level change. *The Cryosphere*, **10**, 1933–1946, doi:10.5194/tc-10-1933-2016.

Visbeck, M., J. Marshall, T. Haine, and M. Spall, 1997: Specification of Eddy Transfer Coefficients in Coarse-Resolution Ocean Circulation Models. *J. Phys. Oceanogr.*, **27 (3)**, 381–402, doi:10.1175/1520-0485(1997)027¡0381:SOETCI¿2.0.CO;2.

Vu, B. L., A. Stegner, and T. Arsouze, 2018: Angular momentum eddy detection and tracking algorithm (ameda) and its application to coastal eddy formation. *Journal of Atmospheric and Oceanic Technology*, **35 (4)**, 739 – 762, doi:10.1175/JTECH-D-17-0010.1.

Wagner, T. J. W., T. D. James, T. Murray, and D. Vella, 2016: On the role of buoyant flexure in glacier calving. *Geophys. Res. Lett.*, **43 (1)**, 232–240A, doi: doi.org/10.1002/2015GL067247.

Whitehead, J. A., A. Leetmaa, and R. Knox, 1974: Rotating hydraulics of strait and sill flows. *Geophysical Fluid Dynamics*, **6 (2)**, 101–125, doi:10.1080/03091927409365790.

Wood, M., E. Rignot, I. Fenty, D. Menemenlis, R. Millan, M. Morlighem, J. Mouginot, and H. Seroussi, 2018: Ocean-Induced Melt Triggers Glacier Retreat in Northwest Greenland. *Geophys. Res. Lett.*, **45 (16)**, 8334–8342, doi:10.1029/2018GL078024.

Wood, M., and Coauthors, 2021: Ocean forcing drives glacier retreat in Greenland. *Science Advances*, **7 (1)**, doi:10.1126/sciadv.aba7282.

Xu, Y., E. Rignot, D. Menemenlis, and M. Koppes, 2012: Numerical experiments on subaqueous melting of Greenland tidewater glaciers in response to ocean warming and enhanced subglacial discharge. *Ann. Glaciol.*, **53 (60)**, 229–234.

Zhang, H., D. Menemenlis, and I. Fenty, 2018: ECCO LLC270 Ocean-Ice State Estimate. *ECCO Consortium*, doi:doi.org/1721.1/119821.

Zhao, K. X., A. L. Stewart, and J. C. McWilliams, 2019: Sill-Influenced Exchange Flows in Ice Shelf Cavities. *J. Phys. Oceanogr.*, **49 (1)**, 163–191, doi:10.1175/JPO-D-18-0076.1.

Zhao, K. X., A. L. Stewart, and J. C. McWilliams, 2021a: Geometric Constraints on Glacial Fjord–Shelf Exchange. *J. Phys. Oceanogr.*, **51 (4)**, 1223–1246, doi:10.1175/JPO-D-20-0091.1.

Zhao, K. X., A. L. Stewart, and J. C. McWilliams, 2021b: Linking Overturning, Recirculation, and Melt in Glacial Fjords. *Submitted to Geophys. Res. Lett.*

Zhao, K. X., A. L. Stewart, J. C. McWilliams, I. Fenty, and E. Rignot, 2021c: Standing Eddies in Glacial Fjords and their Role in Fjord Circulation and Melt. *Manuscript in preparation.*

Zlotnicki, V., Z. Qu, J. Willis, R. Ray, and J. Hausman, 2019: JPL MEASURES Gridded Sea Surface Height Anomalies Version 1812. *PO.DAAC, CA, USA.*, **Dataset accessed [2021-05-03] at**, doi:https://doi.org/10.5067/SLREF-CDRV2.